On the scaling and ordering of columnar joints

by

Lucas Goehring

A thesis submitted in conformity with the requirements
for the degree of Doctor of Philosophy
Graduate Department of Physics
University of Toronto

Omar al-Khayyam, Rubaiyat 42

You asked 'What is this transient pattern?'
If we tell the truth of it, it will be a long story;
It is a pattern that came up out of an ocean
And in a moment returned to that ocean's depth.

Abstract

On the scaling and ordering of columnar joints

Lucas Goehring
Doctor of Philosophy
Graduate Department of Physics
University of Toronto
2008

Columnar jointing is a fracture pattern, best known from locations such as the Giant's Causeway, or Fingal's Cave, in which cracks self-organize into a nearly hexagonal arrangement, leaving behind an ordered colonnade. In this thesis observations of columnar jointing are reported from both a controlled laboratory setting, and in cooled lava flows. Experiments were performed in slurries of corn starch and water, which form columnar joints when dried. This drying process is examined in detail, and it is shown how desiccation leads to the propagation of a sharp shrinkage front. In general, but with some significant exceptions, the size of columnar joints is inversely dependent on the speed of this shrinkage front during their formation. The exceptions, which include sudden jumps in column scale, show that hysteresis is also important in choosing the column scale. Novel observations of the 3D structure of joints in starch show that columnar joints do not settle down to a perfect hexagonal pattern, but rather mature into a continuously evolving dynamic pattern. This pattern is scale invariant, and the same statistical distribution of column shapes applies equally to joints in both starch and lava. Field work was performed to study columnar jointing in the basalts of the Columbia River Basalt Group and the island of Staffa, and the more heterogeneous lava flows of Southwestern British Columbia. The widths of columns and the heights of striae (chisel-like markings that record details of cooling) were examined in detail, and these length scales are shown to be inversely proportional to each other. An additional length scale, that of wavy columns, is also first reported here. Based on these measurements, empirical advective-diffusive models are developed to describe the transport of water in a drying starch-cake, and the transport of heat in a cooling lava flow. These models have only a single scaling parameter, the Péclet number, which relates the fracture front velocity times the column size to the (thermal or hydraulic) diffusivity. In both cases, the formation of columnar joints occurs at a Péclet number of about 0.2. This model explains the hundred-fold differences in scale between columnar joints in starches and lavas, and can be used as a tool for the interpretation of joint patterns in the field.

Acknowledgements

The resources available at the University of Toronto have contributed greatly to the success of this project. Laser diffraction particle sizing was performed at the Aqueous Process Engineering and Chemistry Group. Optical particle sizing was performed with the assistance of Chris Charles. Electron microscopy was done using facilities in the Geology Department. Micro-computed Tomography was done at the Mouse Imaging Centre (MICe) at Sunnybrook Hospital. Finally, attempts were made at the Lassonde Institute to perform seismic study of fracture, with the friendly help of Ben Thompson.

The aid that I had in the field was important for the geological component of my research. Pierre-Yves Robin, Sandy Cruden, and Mark Jellinek gave me invaluable advice while I was planning my field expeditions, and especially helped me put together the first trip to the Columbia Plateau. I am indebted to the friendship of Catherine Duquette, who accompanied me into the field for two years, and who braved perilous cliffs, venomous rattlesnakes and fearsome heat in order to help me measure the size of thousands of silly little markings on rocks. I am also thankful for the assistance of Brian Goehring, who helped survey the Columbia Plateau for suitable study sites, and for the skills of Robert Mehew who organized a very successful interdisciplinary expedition to Staffa. Thanks also are extended to Historic Scotland, who kindly gave permission for the extended scientific stay on their island of Staffa, and to Massey College, who provided an unprecedentedly large travel grant to pay for my wanderings.

Before beginning this project I was completely untrained in any aspects of geology or geophysics. Credit for my sparking my interest in exploring the geology of columnar jointing should be extended to my teachers in geophysics and geodynamics: Jerry Mitrovica, Richard Bailey, David Dunlop, and especially Richard Peltier.

Special thanks should also go to Pierre-Yves Robin, who was always available for consultation, and who often patiently explained many a (for me) confusing piece of geological lore.

The discussion and perspective of the so-called Cracking Club, a focussed group of scientists and engineers who are collectively questioning the origin and properties of cracks in simple systems, has also been of significant help. In particular, I am indebted to the advice of Eric Dufresne, L. Mahadevan, Bill Russell, and Alex Routh.

I also greatly thank my partner, Eric Bond, who has put up with me all summer while this thesis was written.

Finally, I wish to thank my supervisor, Stephen Morris, who helped make all this possible.

Contents

List of Tables

List of Figures

Chapter 1

Introduction

Staffa is a small, windswept, uninhabited island that is exposed to the Atlantic surge, in the Hebrides of Scotland. It would be totally unremarkable, save perhaps as a sanctuary for migrating bird populations, were it not for Fingal's Cave. This cave is carved deep into 60 million year old lava by the wave action of the rough Atlantic sea. Its walls are formed by great pillars of rock, and its roof by gracefully curving ribs of basalt, giving visitors the impression of a natural cathedral. The tall cliffs in its vicinity, shown for example in Figure 1.1, appear almost as a rock forest, with trunk-like columns supporting a finely jointed upper layer.

The names associated with spots like this, such as the Giant's Causeway (N. Ireland), the Devil's Postpile (California), the Devil's Tower (Wyoming) or Samson's Ribs (Edinburgh), reflect the impression that the regularity of the rock patterns at these sites could not be caused by nature, but only by supernatural agents. As will be described here, this is far from true. The features common to all these sites, columnar joints, formed there by the cracking of cooling lava flows. In this thesis, it will be shown how these inspiring patterns organize, how they scale, and how they can be created in the laboratory.

1.1 A history of the study of columnar jointing

Columnar jointing has been studied since the Giant's Causeway was first reported to the Royal Society in the 17th Century, when travelers' reports excited speculation as to what mechanism could produce such a startling, seemingly unnatural display of order and symmetry [14, 27, 68]. This formation, in which long vertical prismatic columns cover a coastline in Northern Ireland, remains one of the most well known outcrops of columnar jointing in the world.

Figure 1.1: Colonnade and entablature of the Fingal's lava, Staffa (Scotland), to the west of Fingal's Cave. The colonnade is 15-20 m thick, overlies a coarse ash layer, and cooled from the ash-lava contact upwards. The entablature, above, is about of equal thickness, and is part of the same flow unit that cooled downwards from the exposed upper surface.

Columnar features were subsequently identified at many sites around the world, as columnar jointing is fairly common. A colonnade near Fingal's Cave is shown in Figure 1.1, for example. These features in lava can vary from small centimeter-sized columns [77] to large columns several meters across [79], and can occur in a wide range of lava types.

Although the origin of joints in basalt featured strongly in the 18th century debate between the competing theories of the Neptunists, who believed that basalt had formed from the sea, and the Plutonists, who believed that it was of volcanic production, the true cause of columnar joints remained largely a mystery for several hundred years [105]. It was Victorian geologist Robert Mallet who finally convincingly argued that columnar joints arise from the stresses due to thermal contraction in cooling lava [62].

Mallet showed how a hot lava flow would cool and crack in a way that could consistently produce a columnar pattern. By applying linear elasticity and heat conduction theory to this problem, he worked out, qualitatively, how joints form as the result of a front of ordered contraction cracks propagating into a cooling lava flow, accompanying a thermal contraction front [62]. This model was able to accurately predict the shape of curving or inclined columns formed in unusual geometries (such as in a small valley).

A series of models of the hexagonal pattern of columnar jointing can also be traced back to Mallet. He argued that a shrinking isotropic film, such as the cooling surface of a lava flow, would break into symmetric plates that tile the plane [62]. In a manner that is reminiscent of Griffith fracture theory (which was not to be developed until nearly 50 years later [35]), the stresses that build up in centers of triangular, square, and hexagonal plates were compared to the stress released by the breaking of their perimeters. Assuming that the areas of the three types of regular shapes were equal, then the perimeter of the hexagonal tile is the largest. Even when the perimeter lengths are weighted with an estimate of their expected contribution to stress release at the center of the tile, it follows that the ratio of stress release to stress buildup is also largest in a hexagonal tiling. Mallet thus predicted that the cooling film would fracture into this arrangement before it could fracture into any other regular tiling. Columns would then be formed by the gradual extension of these initial forms into the cooling mass. Similar ideas were presented by Tomkeieff, who described columnar jointing as arising from equally spaced 'centers of attraction' [105], and by Smalley, who considered instead randomly distributed 'stress centers' [100].

Around the time of Mallet, a survey of the Giant's Causeway was conducted by O'Reilly [75], covering 201 columns, as shown in Figure 1.2. To this day it remains the largest survey of columnar joints in the field, and it has been mined many times

for statistical studies [13, 31, 51, 110]. It should be noted, however, that none of the previously mentioned geometric models accurately describe its features, as these models all describe the propagation of a unchanging fracture network. Since the fracture pattern at the surface of a lava flow is known to have mostly rectilinear joints [79], rather than hexagonal ones, some dynamical mechanism needs to be identified in order to explain the shapes in the fracture pattern.

It was not until the late 1970s that the dynamics of columnar joints began to be investigated. As will be described in detail in Section 1.3, the fractures forming the sides of igneous columns advance in individual abrupt steps that are recorded by chisel-like markings called *striae* [89]. Aydin and DeGraff described how this sequential advance of striae allows the evolution of the fracture pattern of columnar joints, and showed how the ordering of a basalt colonnade on Hawaii occurs in the first two meters away from the cooling surface [2]. The columnar pattern can thus be thought of as a dynamic 2D fracture network that leaves a columnar record of itself as it advances in the third direction. Current models of this behavior, such as those of Jagla *et al.* [50, 51, 92] or Budkewitsch and Robin [13], all emphasize this dynamic quality during the initial evolution of columnar joints, and attempt to describe how a disordered surface pattern relaxes into an ordered, static, mature state. However, as will be shown in Section 2.5, the pattern of columnar joints does not, in fact, approach a static final state, but continues to evolve constantly throughout the colonnade.

Following these key insights, research performed in the 1980s and 90s filled in a consistent picture of the cooling dynamics and of the mechanics of the intermittent fracture advance [13, 19, 59, 60, 90], as will be described in Section 1.3. However, despite a considerable understanding of how columnar joints form, at least two significant problems still remain open – the question of the quantitative scaling behavior of columnar joints, and the question of how, and why, columns order. These two problems are the focus of the research presented in this thesis.

1.2 Columnar jointing in the laboratory

Columnar jointing is a remarkably robust phenomenon. Columnar joints of some kind are found in many igneous rock types such as basalt (including lunar basalt [52]), rhyolite, andesite, and dacite. They have been reported in other geological materials, such as sandstone and coal, and in man-made materials such as smelter slag, glass, chemically laced vitrified ice, and certain types of drying starches [19, 28, 66, 71, 95]. There has been much recent interest in this last example, that of a drying starch-water slurry

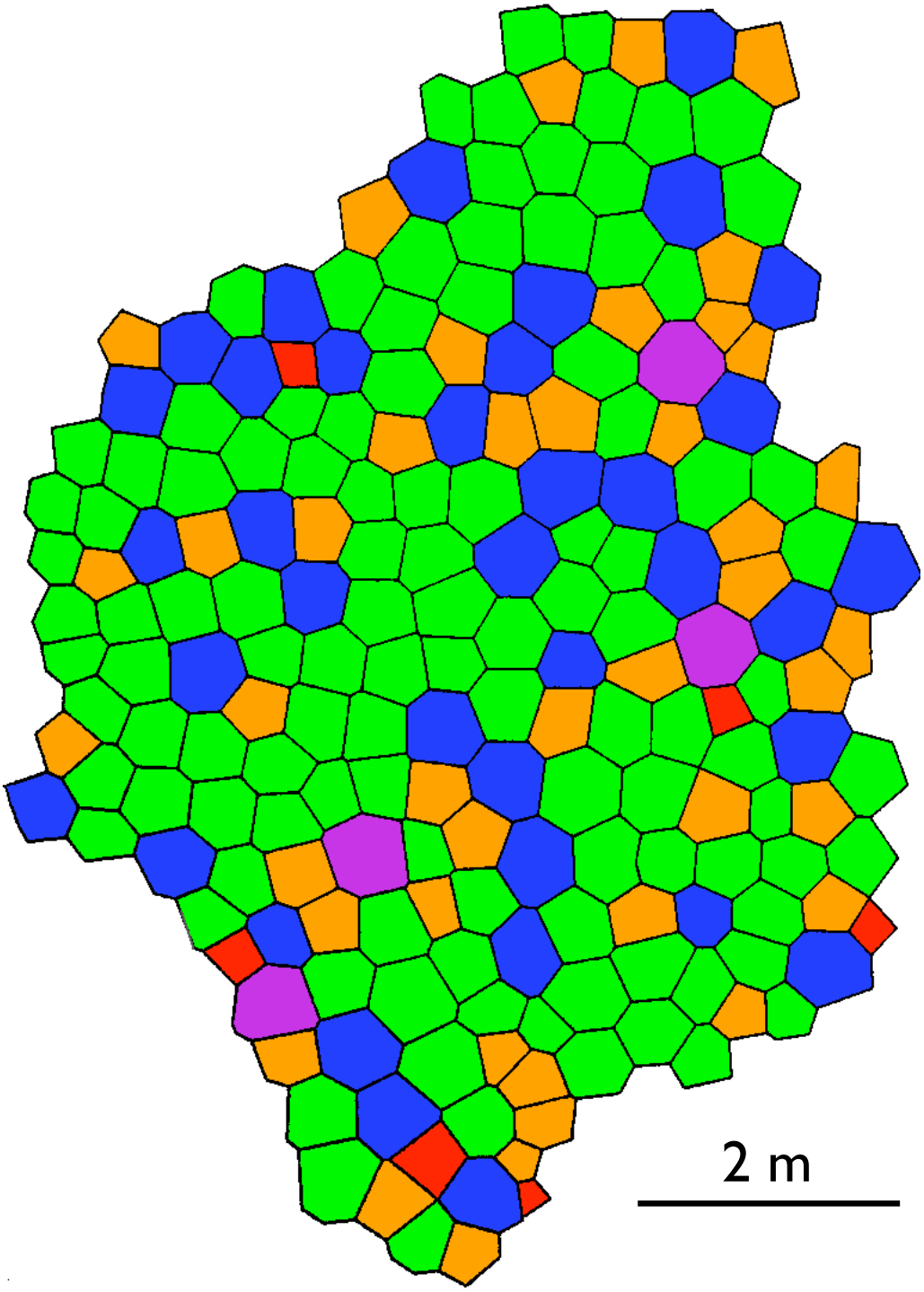

Figure 1.2: O'Reilly's survey of a section of the Giant's Causeway, adapted from reference [75]. Columns are colored according to the number of their neighbors. Quadrilaterals are colored red, pentagons orange, hexagons green, heptagons blue, and octagons purple.

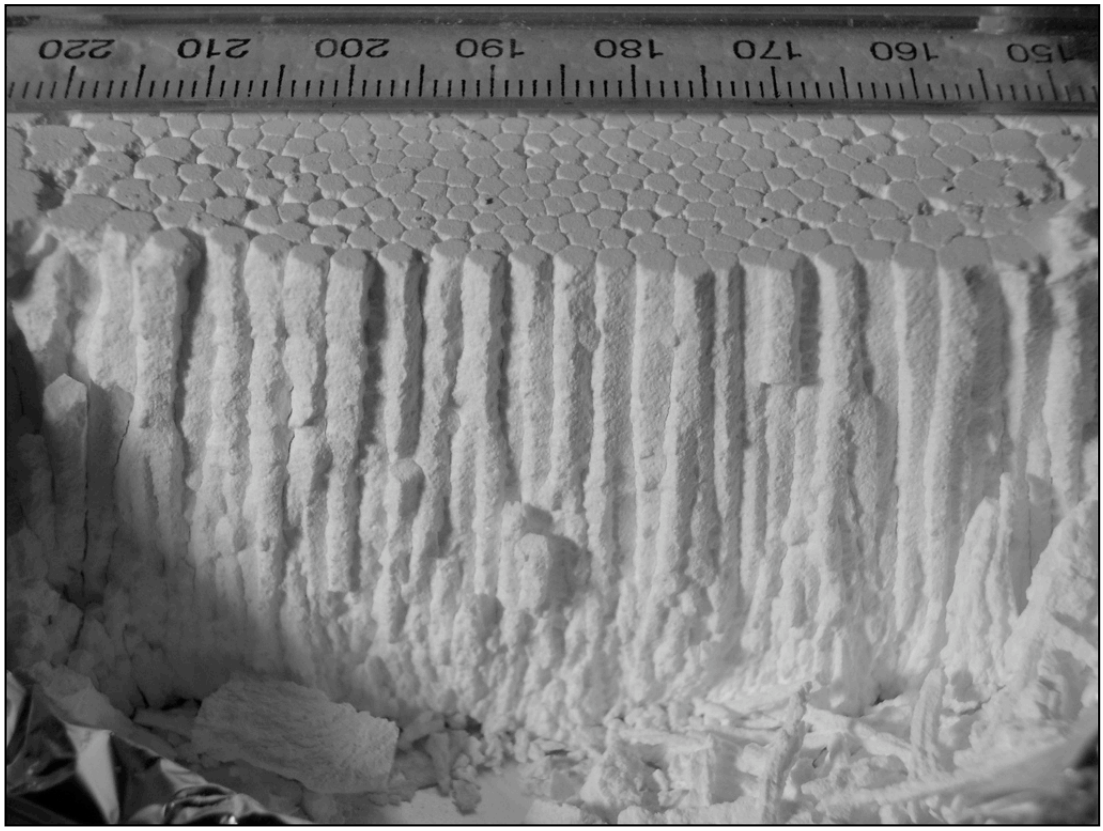

Figure 1.3: An example of columnar jointing in starch. The sample is shown inverted, with the drying surface positioned at the bottom of the image.

[29, 30, 31, 67, 70, 71, 72, 74, 106]. Experiments on the formation of columnar joints in starch are the subject of Chapter 2 of this thesis.

Drying starch was first systematically studied by Müller [71], although its propensity to form columnar joints had apparently been known since at least Victorian times [28, 47, 105]. In starches, columns are usually between 1-10 mm in diameter, as demonstrated in Figure 1.3, and are therefore about two orders of magnitude smaller than joints typically found in lava. In this case, it is the propagation of a sharp shrinkage front, due to desiccation, which drives the ordering of contraction cracks, as is shown in Figure 1.4, and as will be demonstrated in Section 2.2.

If allowed to dry freely, a starch slurry will form a colonnade in which the columns slowly increase in scale throughout the drying layer [31, 67, 71]. This coarsening is due to changes in the shrinkage front, which slows down as it propagates away from the drying surface, as is demonstrated in Section 2.4.1. If the desiccation is controlled in such a way that the shrinkage front propagates at a fixed speed, a case more analogous to cooling lava, then the coarsening of the colonnade is halted, as will be shown in Section 2.4.3.

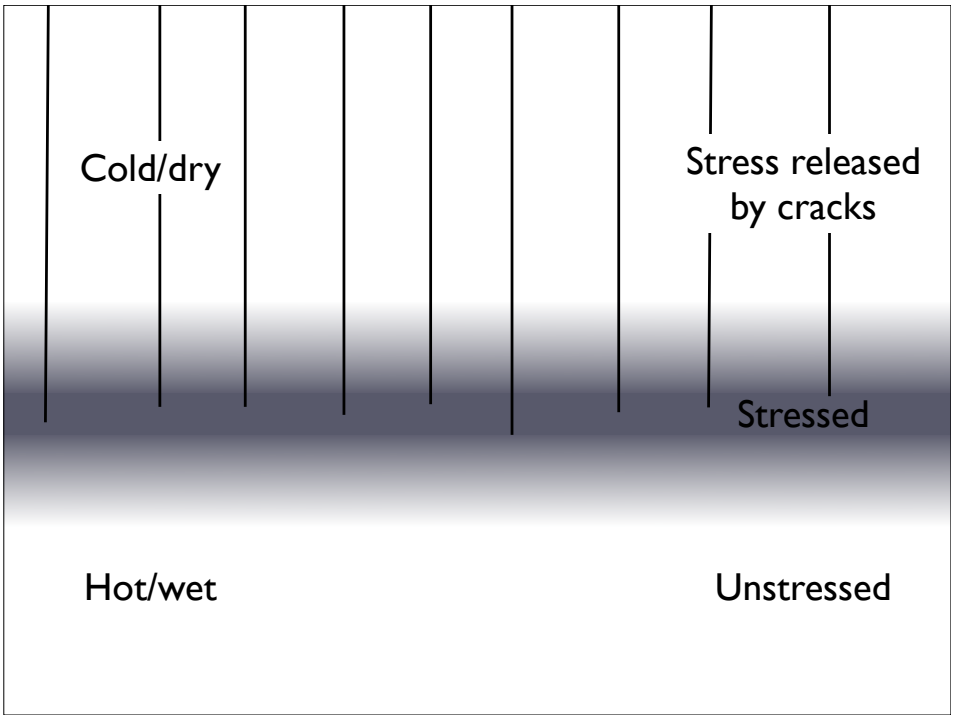

Figure 1.4: In both drying and cooling systems, columnar joint tips are confined to a thin elastic layer. To one side, elastic stresses are released by existing cracks, while on the other side, elastic stresses do not form.

The pattern of columnar jointing is difficult to study in the field, due to the requirement of visualizing large landscapes in 3D. In the absence of strong observational constraints, a number of distinct theories have been developed to explain columnar joints. In general these studies are interested in either scaling (*e.g.* [38, 85]), or ordering (*e.g.* [13, 50, 51]). The laboratory exploration of columnar jointing offers an unusual opportunity to do modern, controlled experiments that can shed light on this classic problem of geomorphology. The experiments presented in Chapter 2 contain the first observations of the 3D structure of columnar joints ever made, and are used in Chapter 4 to develop a theory of the scaling of columnar joints that can explain both the scale selection processes in starch and lava joints, and the differences in scale between these two joint patterns.

1.3 Jointing processes in lavas

Igneous columnar joints form as a result of a cooling front moving from some cooling surface into a lava, such as from the exposed surface of a lava lake or flood basalt flow [62]. As is shown in Figure 1.4, stress only builds up to significant levels in a thin

elastic layer which is near the glass transition temperature T_g. Here, T_g refers to the temperature at which a cooling lava can begin to sustain tensile stress, a temperature that only depends weakly on the cooling rate, and which is significantly cooler than the temperature at which the melt begins to solidify [90]. On one side of the elastic layer, stress is relaxed by viscous or plastic deformation, while on the other side stress is relieved by the widening of existing cracks. Throughout cooling, all the active crack tips of the columnar joints will be confined to this thin, moving elastic layer. Observations of the Kilauean lava lakes indicate that cracks begin to form at the surface of a lava lake at around 900°C. However, within a cooling colonnade Ryan and Sammis have shown that T_g is much lower, approximately 750°C [90].

The columnar crack tips do not advance smoothly with the motion of the intruding elastic layer, but rather advance intermittently, leaving striae on the sides of columns [89]. These striae, which look somewhat like chisel-marks, are typically an alternation of a relatively smooth surface caused by a crack advancing in an elastic medium, and a rough fracture surface that shows the termination of a crack tip in a more plastic environment [89]. Subsequent striae are not exactly coplanar, and often the later crack bends a little to meet the earlier one at right angles, as is shown in Figure 1.5(b,e). This slight curvature can be used to infer the direction of crack propagation, and hence the direction of cooling [19]. Observations of striae will be discussed in detail in Chapter 3. Plumose structure (also known as hackle) appears as a light feathering pattern on the surface of striae, as shown in Figure 1.5(a,d,e). This pattern of lines, which form perpendicular to the leading edge of a growing crack tip, can be used to deduce the fracture initiation point of a stria, as well as its direction of crack propagation [19]. Unfortunately, the delicate features of both plumose and striae are easily erased by weathering.

As cooling can occur from both the upper and lower surfaces of a roughly planar lava flow (or from *any* surface in a more complex geometry), there are typically at least two distinct structures in each flow unit [21, 59, 62]. Frequently, these structures are as simple as two colonnades: an upper colonnade cooling from the top down, and a lower colonnade cooling from the bottom up. However, cooling lavas can also support another less regular jointing pattern, known as *entablature* [105]. This highly disorganized pattern usually has a smaller scale than columnar joints, and frequently occurs in a band between the upper and lower colonnades (although this is likely simply due to a mismatch of the joints propagating from the separate colonnades). In many other cases entablature partially or entirely replaces the upper colonnade. These three types of fracture patterns, upper colonnade, lower colonnade, and entablature, are all displayed in Figure 1.6. The mechanisms that distinguish between ordered columnar jointing and

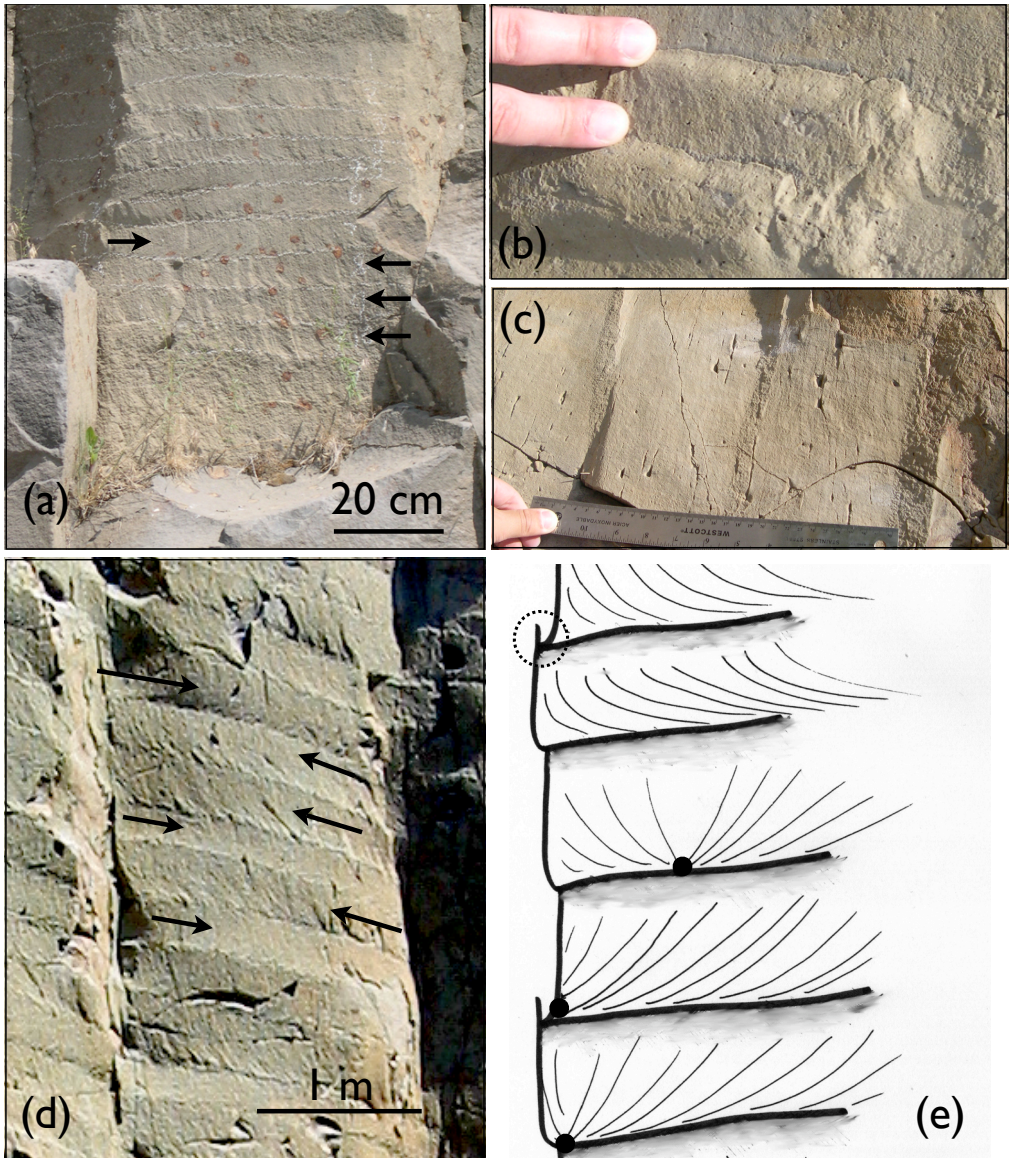

Figure 1.5: Stria and plumose features. (a) shows chalked demarkations of individual striae, with some feathery plumose structure visible. (b) shows the curvature of several striae that imply that this column cooled from the top of the picture downwards. (c) shows alternating rough and smooth regions that can be used to measure stria heights. (d) shows large stria and plumose features. (e) shows a schematic representation of striae, with the crack initiation points shown as black dots, plumose shown as thin lines, stria edges as thick lines, and the alternation of smooth and rough surfaces as surface shading. A dashed circle in the upper left corner emphasizes how subsequent striae often curve slightly in order to intersect at right angles. In (a),(d) arrows show the inferred direction of crack propagation within individual striae.

disordered entablature are not understood, although crystal textures in entablature are finer than in colonnades from the same flow unit [59]. This implies that the smaller scale entablature probably cooled more quickly than the colonnades [59].

The observations of Hardee [41] on the cooling of a Hawaiian lava lake showed that, after an initial period of diffusively-dominated cooling, heat was efficiently extracted through the upper surface of the lava lake by two-phase convection of water and steam occurring within the joints. This idea was developed by Budkewitsch and Robin [13], and is generally accepted, at least for cooling from the upper surface. The first evidence that this mechanism is also active in the lower colonnade is presented here in Section 4.2.5. It will be argued there that this style of convection maintains a constant heat flux with a value proportional to the crack cross-sectional density. A series of novel, analogous experiments, where a constant evaporation rate is actively maintained during the drying of a starch-cake, is presented in Section 2.4.3.

Exposed outcrops of columnar joints often exhibit an uncanny degree of regularity which can appear unnatural to the casual observer. Columnar joints meet at Y-junctions, with joint angles close to 120°, and the columns are usually all quite close to being equal in their cross-sectional areas, as was shown in Figure 1.2. However, the cracks on the exterior surface of a flow containing a colonnade are much less regular, and more like conventional mud crack patterns [79]. This surface pattern is mostly composed of T-junctions, and shows a wide distribution of polygon areas [79]. It is remarkable that most of the ordering process that gives rise to columnar joints – the evolution of T-junctions into Y-junctions, and the narrowing of the cross-sectional area distribution – occurs within a meter or two of the flow margin [2]. The forces driving this ordering process are still poorly understood. However, the regularity of the interior of a colonnade is often overstated; even the most well-ordered formations, such as the Giant's Causeway, which is many tens of meters thick, still retain a significant number of penta-hepta defects. This is emphasized by the coloring scheme adopted in Figure 1.2. As will be shown in Sections 2.5 and 3.5, a statistical description of the pattern of columnar joints shows the same level of disorder in desiccated starch, the survey of O'Reilly, and lavas across the Columbia Plateau. Any explanation of the ordering process of columnar joints must also account for this residual disorder.

The origin of the size, and the overall scaling of columnar joints, has long been an unresolved issue. Published measurements of stria heights have previously indicated that they usually vary in direct proportion to the average columnar side width [20, 38, 89]. This will be confirmed in Chapter 3. Furthermore, the small-scale entablature appears to cool more quickly than larger-scale colonnades [59]. A number of models

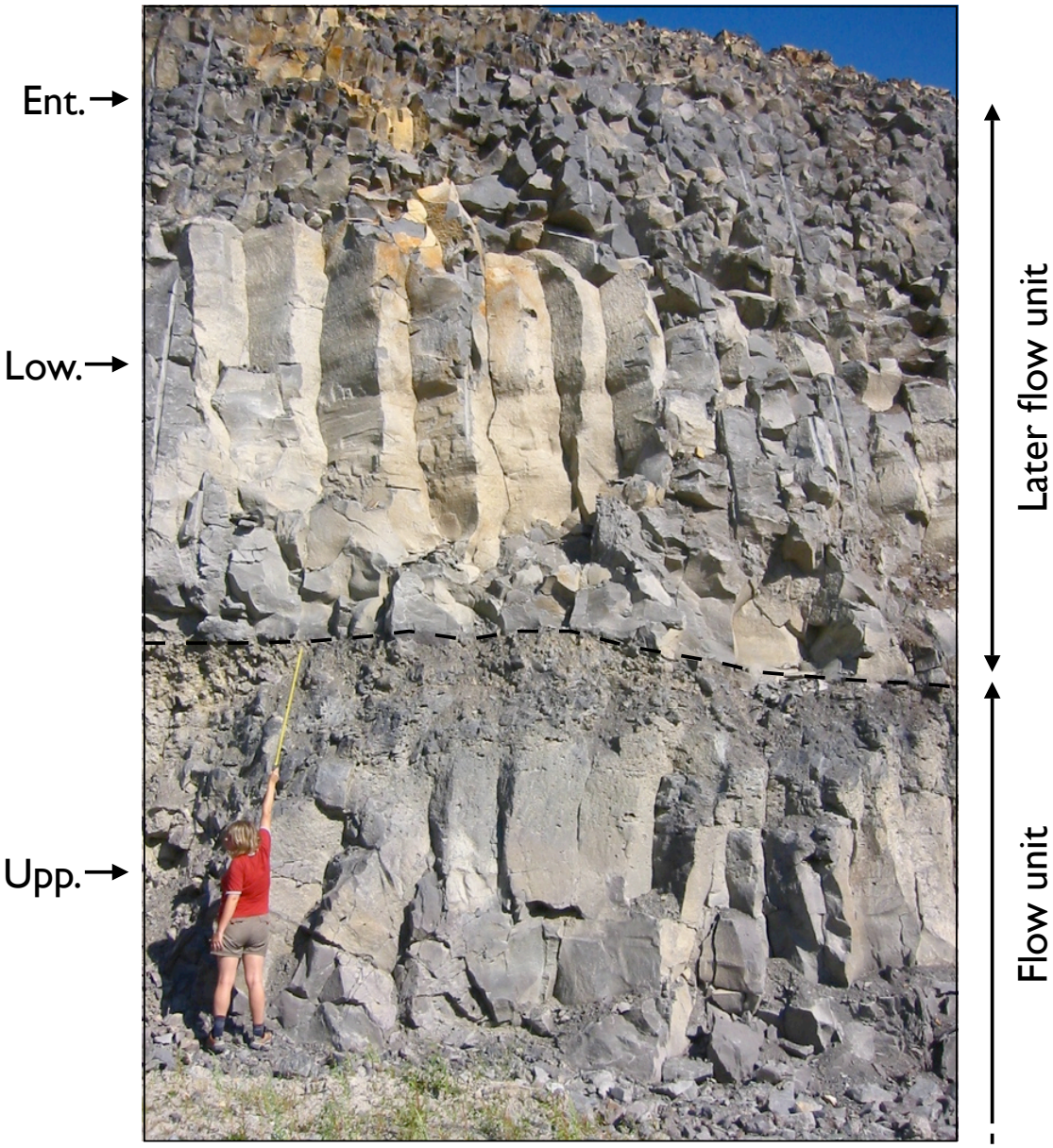

Figure 1.6: Examples of an upper colonnade (labeled Upp.), lower colonnade (Low.) and entablature (Ent.) in two flow units of the Cheakamus basalts. The terms upper and lower here refer to the direction in which the colonnades cooled. The boundary between the two flow units is marked by a dashed line overlying the vesicular surface of one flow. A second, unexposed, lower colonnade is presumably present beneath the ground level.

have been presented in which the scaling of joints is discussed in light of these suggestive observations [13, 20, 33, 38, 60, 85, 92]. It is generally accepted that larger columns result from more slowly cooled lavas, but there is currently little consensus on the details of this relationship. The new observational insights presented in this thesis will solve the long-standing problem of fracture spacing in columnar joints.

1.4 Analogs to columnar jointing

It has been suggested that there is a close relationship between a number of different types of fracture patterns in which the fracture network is able to evolve [19, 31, 50]. Thin isotropic media undergoing brittle fracture due to shrinkage typically display fracture networks which have predominantly 90° junctions and four-sided polygonal patterns of cracks [8, 97]. Evolved, or iterative patterns, on the other hand, often contain 120° junctions and hexagonal shapes. For example, ice-wedge polygons, which cover much of the polar terrain of the Earth [57], and also appear to cover significant areas of Mars [65], are seasonal thermal contraction cracks in permafrost. These cracks open during the winter and heal during summer as water and/or detritus fills in the fissures [57]. This annual cycle allows the cracks to move slightly between years, and it has been observed that young ice-wedge networks contain more four-sided polygons than older crack networks, which are hexagonal on average [99]. Septarian concretions, roughly spherical bodies which have been fractured and filled in with another material, also can display a similar hexagonal joint pattern [94]. A phase field model of columnar jointing has recently been constructed that claims to apply equally to all of these cases [50]. This generality suggests that the detailed description of columnar jointing presented in this thesis could have applicability to a wide number of fields.

Additionally, columnar jointing is related to a number of interesting model problems that test the current understanding of fracture mechanics. The initiating pattern at the free surface of columnar jointing should be similar to that of a uniformly drying thin film (or mud crack pattern), which scales with the thickness of the layer [8, 36, 97]. Furthermore, the directional propagation of columnar joints into a medium is analogous to the two-dimensional problem of directional fracture in thin layers, which produces an analogous dynamic ordering of fractures [1, 18, 23, 45, 97, 117]. These two fracture problems are important in many engineering applications of coatings and thin colloidal films, such as paints and glazes, and are currently the subject of intensive study. Some conclusions of this thesis which are of relevance to these patterns are given in Section 4.4.3.

1.5 Outline of thesis

Following this introduction, Chapter 2 will present experiments performed in desiccating corn-starch slurries. After a brief summary of experimental methods, the physical properties of a drying starch-cake are described. It will be shown that drying proceeds by the formation of a sharp drying front, analogous to the dynamics of cooling described in Section 1.3. Several types of experiment will be described, including those where the starch-cake dries naturally, and those where feedback is used to manipulate the evaporation rate. These experiments represent a level of control over the formation of columnar joints that has never previously been achieved. Data from these trials are collected through X-ray tomography and destructive sampling techniques, representing the first record of columnar jointing that has probed all three dimensions of this pattern. In this chapter, the dynamical evolution of a columnar jointing pattern is examined.

Results from experiments are contrasted in this thesis with field measurements of columnar joints in lava flows. These observations, reported in Chapter 3, were made across the Columbia Plateau and Southwestern British Columbia, and on the island of Staffa. These measurements focussed on striae, and show how the height of striae depends on the size of the colonnade on which they form, their position within the flow unit, and the size and shape of their neighbors, both vertically and horizontally. A novel feature of igneous columnar joints, wavy columns, is also described, which represents a coherent mode of the evolution of the columnar pattern.

In Chapter 4 the formation of columnar joints in both starch and lava is considered. The transport of moisture in a drying starch-cake is described in detail, and shown to reduce to a linear advection-diffusion problem in the vicinity of the fracture front. A single dimensionless parameter, the Péclet number, which is the ratio of the fracture front velocity times the size of the average column to the diffusivity, controls the scaling of starch columns. Similarly, measurements of stria height are used to put constraints on an advection-diffusion model of the cooling of a lava flow. In both cases some hysteresis is present, but the Péclet number is 0.2 ± 0.1. The scale selection question can thus be explained by differences in the thermal diffusivity of basalt, and the hydraulic diffusivity of a starch-cake, and in the velocity of the fracture front.

Chapter 5 briefly summarizes the most important results and conclusions of this thesis. It is followed by appendices describing the numerical methods used during analysis, and the field sites visited during the course of this research.

Chapter 2

Experimental observations

This chapter will describe experimental observations of desiccating starch suspensions, and the formation of columnar joints in this material. Section 2.1 describes the general experimental setup that was used, including the design of a feedback controlled apparatus, and the methods used to image columnar joints. Following this, Section 2.2 details a series of experiments that were performed in order to determine the physical properties of desiccating starch, along with their results. Section 2.3 explains the algorithms that were developed to measure the mean cross-sectional area of a starch colonnade, and the position and velocity of the fracture front as it moves during desiccation. Finally, the results of experiments on the scaling of columnar joints in starch are presented in Section 2.4.

Most of the results described in this chapter have been previously published, or submitted for publication, in References [29, 30, 31]. The majority of Section 2.2 is unpublished, but is being prepared for an article on the physics of the drying of colloidal starch [32].

2.1 Experimental setup and conditions

2.1.1 Experimental methods

Experiments were performed in mixtures of corn starch and water, using methods similar to those described by Müller [70, 71, 72], who rediscovered the phenomenon of columnar jointing in dried starch layers. Other experimental groups [67, 106] have used similar techniques, although Toramaru and Matsumoto [106] used potato starch instead of corn starch.

Starch slurries initially composed of equal weights of dry corn starch (Canada brand)

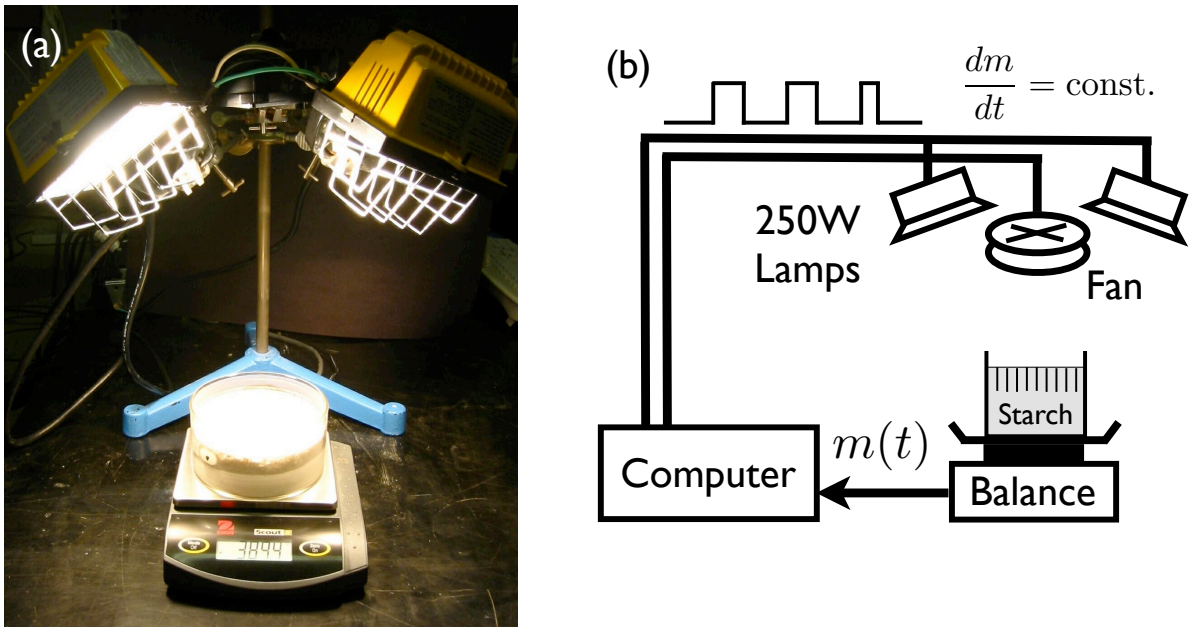

Figure 2.1: Experimental setup. (a) Pyrex dishes of starch-water slurries were dried under overhead heat lamps and a small fan. The displayed sample is partially dried, and cracks extend from the upper surface to the change in sample color (indicating the separation of the starch-cake from the container walls). (b) An automated scale was used to feedback control the evaporation rate by adjusting the duty cycle of overhead lamps and fan.

and water were desiccated in round flat-bottomed Pyrex dishes, or beakers. A range of dish sizes were used; most experiments were performed in dishes with an inner radius of 60 mm, and a height of 65 mm. Traces of bleach were added to the water before it was weighed out, in order to sterilize the experiments. No more than 10-20 ml of bleach per liter of water was necessary. Most samples had an initial thickness of approximately 40 mm, but samples were studied in the range of 3 - 100 mm initial thickness.

Slurries were dried under 250 W halogen heat lamps, while additional ventilation could be provided with a small computer fan. A typical experiment is depicted in Figure 2.1(a). There was otherwise no direct control on the room humidity or temperature, other than black cloth blinds surrounding the experimental setup about 30 cm from the drying sample. Under these conditions, it usually took 1-7 days to dry the initial slurry into a fully fractured starch-cake. Deep samples could take as long as a month to fully dry.

Vacuum desiccation experiments on dry starch powder showed that starch is very hydrophilic, and contains about 4-5% water, by mass, as a dry reagent. Most of this water can be removed by leaving the starch under a heat lamp overnight, as well. It

is likely that the amount of the initial water bound to starch depends on the relative humidity in the air. Uncertainty in the initial moisture content of *dry* starch was the dominant experimental error involved in reproducing the initial conditions of the starch slurry.

2.1.2 Multi-stage fracture

The fracture of a drying corn starch-water mixture occurs in two distinct stages [8, 31, 71, 106]. Initially the sample dries homogeneously and a few first-generation cracks (also known as primary cracks), penetrating the full depth of the layer, break the starch-cake into large pieces. As shown in Figure 2.2(a) the plumose structure on these cracks show that they initiate at the upper drying surface, and quickly propagate vertically through the entire sample. The resulting disordered fracture network, shown for example in Figure 2.2(b), scales like that of an ordinary thin film, and has been studied as an example thereof [8, 9]. In particular, the average spacing between first generation cracks increases linearly with sample depth, and these cracks typically meet at 90° junctions [8, 9].

Once a sample has reached a water concentration of 0.3 g/cm^3 (see Section 2.2.3), the starch-cake begins to dry from the top down. A fracture pattern develops at the drying surface at this time, and further drying propagates the fracture tips into the sample. This leads to a moving fracture front that is a clearly delineated boundary between uncracked starch with a consistency of wet clay, and harder dry starch which has given way to columnar jointing. These two layers come apart easily when a partially dried sample is removed from its dish, as all the fracture tips are confined to a thin interface. Once the fracture front propagates all the way to the bottom of the sample, cracks appear in the base of the starch-cake that can be seen through the underside of the Pyrex container. When a starch sample is removed from its dish, by turning the dish over and gently tapping it, a counterpart of the final fracture pattern is still visible, attached to the dish.

2.1.3 Feedback control

Simple experimental control of the evaporation rate of starch-water mixtures was achieved by manually adjusting the height of the heat lamps and the level of ventilation provided by the fan between experiments. Hereafter, these runs will be referred to as "uncontrolled" experiments, and will be reported on in Section 2.4.1. The relative heating intensity can be measured with a photometer, or, since the evaporation rate is roughly constant in the initial part of the experiment, it can also be characterized by measuring the initial

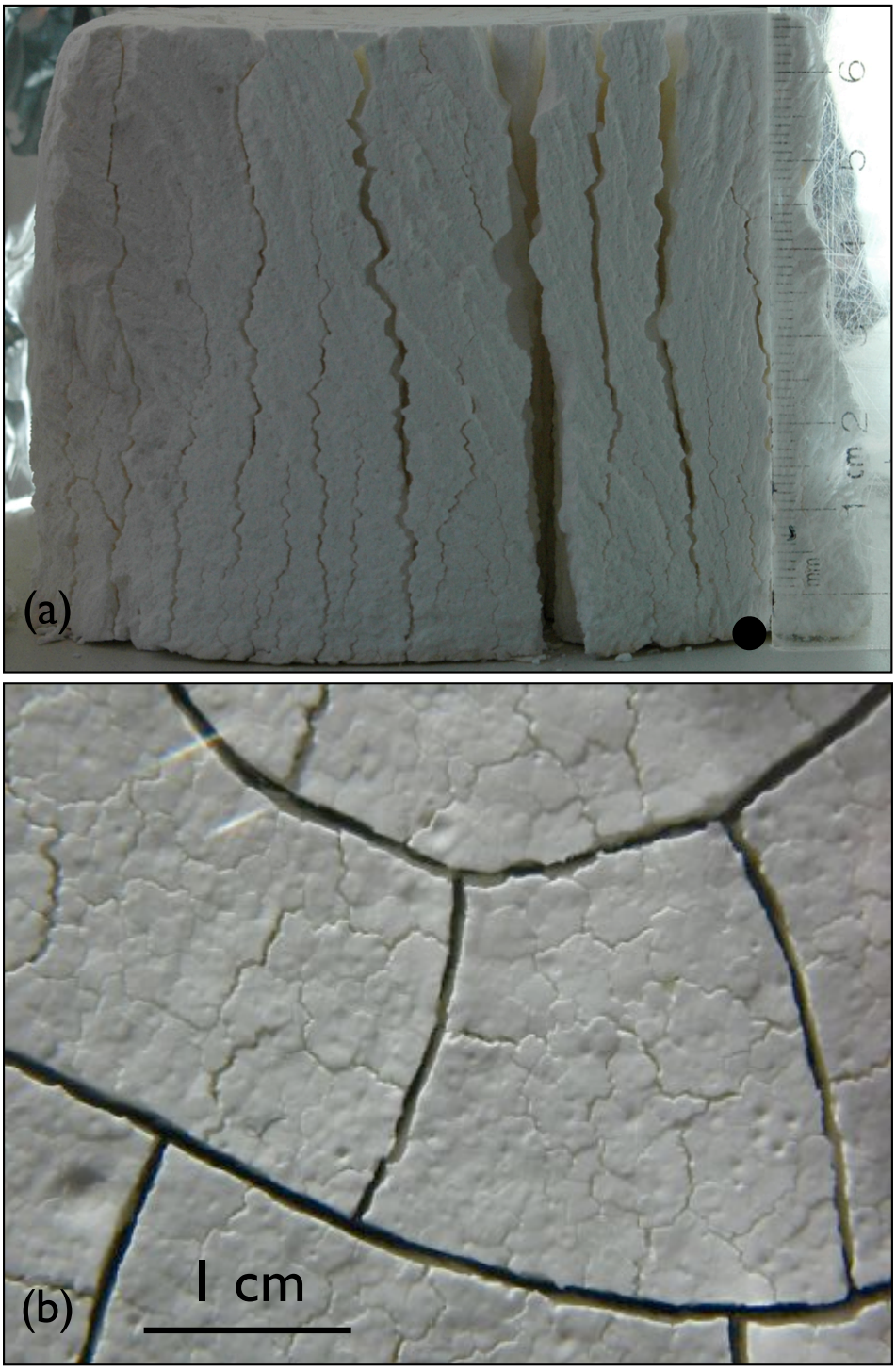

Figure 2.2: Examples of first-generation cracks in a dry starch-cake. (a) shows the surface of a first-generation crack (shown inverted, with the drying surface at the bottom of the image), where plumose lines can be seen radiating from the crack initiation point (black circle). Stria-like steps are visible in the record of columnar fractures that border this fracture face. (b) shows first-generation cracks in cross-section, at the drying surface.

evaporation rate. All other starch experiments, save those reported here, have used only this level of experimental control [28, 67, 70, 71, 72, 106].

To achieve more complete experimental control, samples were dried on digital scales (Ohaus Scout II and Scout Pro digital balances) which interfaced with the serial ports of a computer. Labview code was designed to accept and record the sample mass, $m(t)$, every minute, and to compute the evaporation rate $Q_m = \mathrm{d}m/\mathrm{d}t$ through a least-squares linear fit to the slope of $m(t)$ every half hour. In these experiments the transition between first-generation cracks and columnar jointing was observed to be accompanied by a change in the evaporation rate. This change appears as a kink in the mass-time graph of Fig. 2.3(a).

Since dishes of different sizes were used in these experiments, it is usually more convenient to report the measured evaporative mass flux $q_m = Q_m/A_d$, where A_d is the cross-sectional area of the pyrex dish.

The Labview based feedback loop which is sketched in Figure 2.1(b) was designed to control the evaporation rate in desiccation experiments. A set of six optically isolated triac switches were built and interfaced to a computer using a parallel port to control two identical experimental setups. These switches allowed Labview to turn the two overhead lamps, and one ventilating fan, on and off as desired for each setup. The duty cycle of the lamps and fan were adjusted in a feedback response to an error signal composed of the difference between the measured evaporation rate $Q_m(t)$, and the desired evaporation rate $Q_c(t)$. With a time-step of half an hour the optimal gain in the feedback loop was established experimentally to be between 0.1-0.2, to prevent ringing. The lamp/fan duty cycle was only one minute long, which is brief enough not to affect the drying dynamics with its periodicity. Care was taken to ensure that the overhead fans were cycled off before the sample was weighed, to prevent any breeze from interfering with accurate weighing. Several types of controlled experiment were developed, all involving variations in the form of $Q_c(t)$. In all cases, the control loop terminated when the sample was fully dried, or when the duty cycle on both the lamps and fan reached 100%, when the algorithm could no longer maintain an evaporation rate near Q_c.

Certain experiments were performed which could control the final evaporation rate Q_0, but which would allow the early parts of the desiccation to proceed naturally (see Figs. 2.3(d),(e)). For these experiments feedback control was only initiated after Q_m naturally decreased to be equal to Q_0. In practice this meant that for these "partially controlled" experiments, reported on in Section 2.4.2, the controlled evaporation phase began shortly after columnar jointing was initiated.

Other experiments required the control of the evaporation rate Q_c at all times through-

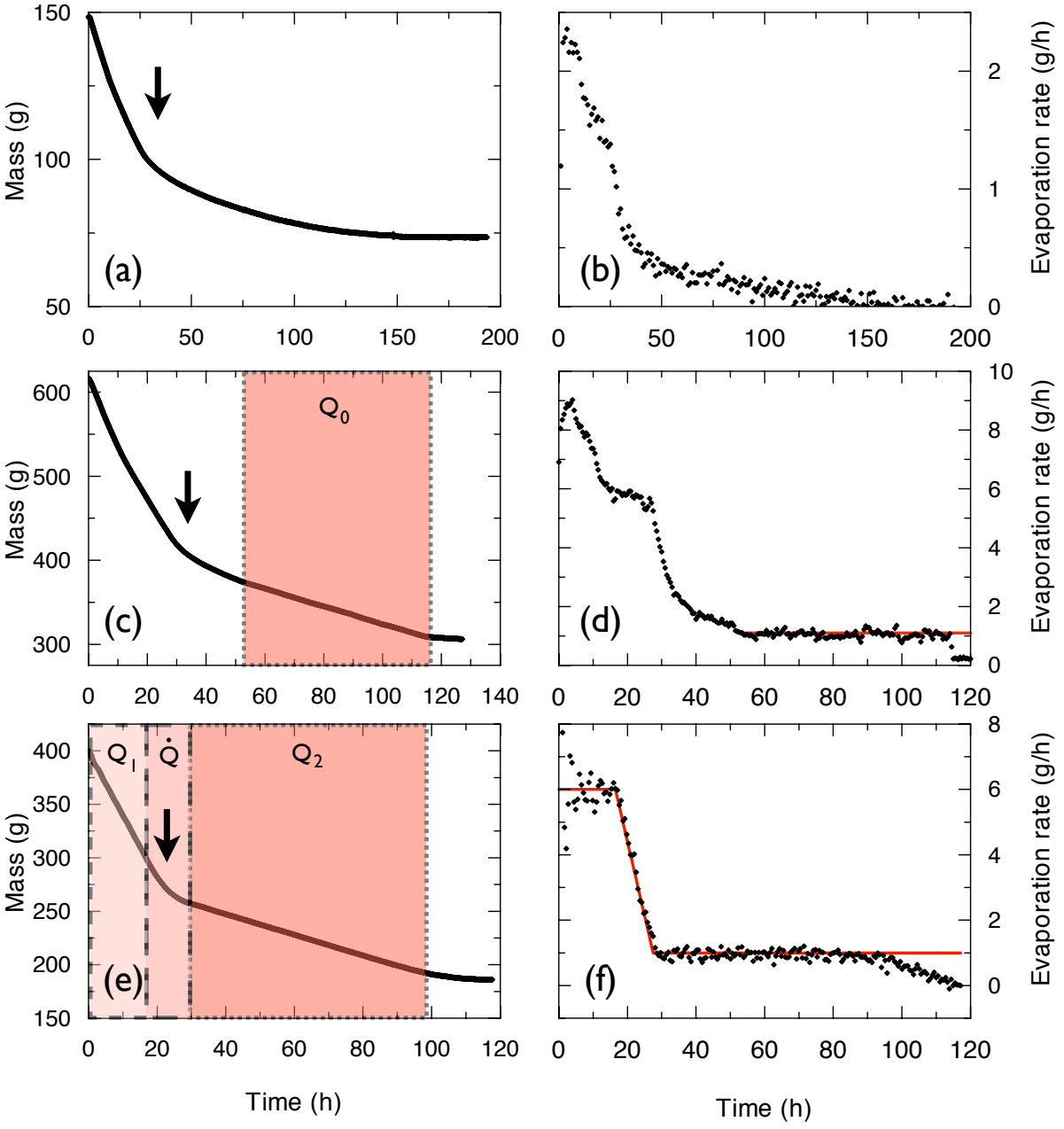

Figure 2.3: Experimental evaporation rate control. (a) Shows the total mass m versus drying time for an uncontrolled desiccation, with measured evaporation rate (b). (c) Shows a feedback controlled run in which the final drying rate in (d) is constant. The three stage feedback controlled desiccation shown in (e) and (f) was designed to initiate and develop columnar joints in a controllable way. Arrows in (a,c,e) point out a kink in the desiccation curve that occurs when the sample ceases to dry homogeneously. In (c)–(f) the red lines and shaded boxes indicate controlled parameters.

out the desiccation. A "fully controlled" experimental protocol was designed to mimic the early stages of the uncontrolled evaporation curve, while allowing the freedom to vary key evaporation rate parameters. This scheme began with a period of constant, rapid evaporation, followed by a ramp down to a controlled final evaporation rate. The algorithm had three free parameters: the initial drying rate Q_1, the final drying rate Q_2, and the slope of the transition between them, $\dot{Q}$. The $\dot{Q}$ ramp began after half of the initial water mass had evaporated. Columnar jointing began late in the ramp phase. Results from "fully controlled" experiments are presented in Section 2.4.3. A variation on this experimental protocol was also developed that replaced the constant Q_2 with an arbitrary $Q_c(m)$. This variant was used to run a series of exploratory tests which involved steps in the final evaporation rate, or short pulses of enhanced evaporation, as presented in Section 2.4.4.

2.1.4 3D visualization

Historically, columnar joints have only been studied in two dimensions. Field studies have focussed either on the pattern in cross-section, such as O'Reilly's 1879 survey of the Giant's Causeway [75], or on the exposed faces of colonnades (*e.g.* [19, 21]). A novel part of this thesis was the use of 3D visualization techniques to study columnar joints.

After a sample was dry, its pyrex container was inverted and the base lightly tapped to remove the starch-cake. A set of columns, chosen from the inner half of the sample's radius, and which did not include any columns that were adjacent to first-generation cracks, was removed to serve as the observational sub-sample.

In some cases, fully 3D volume-filling images were made of the experimental sub-sample using micro-computed X-ray tomography (MicroCT). The starch-cake density was reconstructed by observing the diffraction pattern of X-rays sent through it. This technique mapped small (approximately 2.5 cm diameter) cylinders of fractured starch with a voxel size of $\sim 30\ \mu\text{m}^3$, and a 1024^3 array of voxels. This resolution is about twice the diameter of the average starch grain (see Section 2.2.1). 10 samples were subjected to MicroCT, although only the two clearest samples were analyzed. One sample, which was used to characterize uncontrolled desiccation, had $q_m \sim 30$ mg/h cm^2 during the first few hours of drying. The other sample, used to characterize fully controlled desiccation, had the controlled evaporation rate $q_c = 8.8$ mg/h cm^2 during the Q_2 phase of control. Movies which show the evolution of columnar joints in these two samples are published as online supplements to Reference [29]. An example cross-sectional image from the tomogram of the sample from the uncontrolled experiment is shown in Figure 2.4

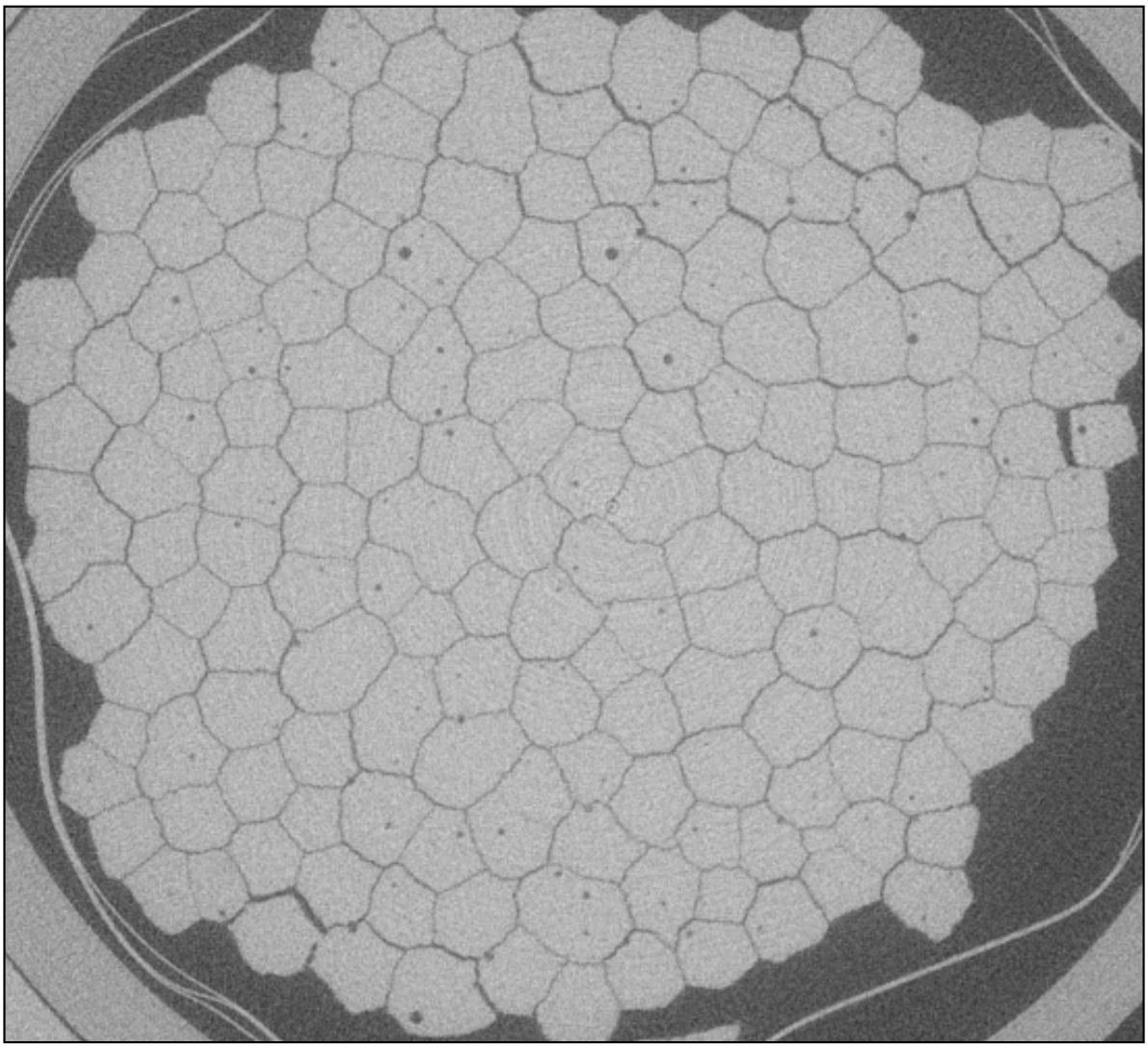

Figure 2.4: Example cross-sectional image taken from 13.5 mm deep into a 3D X-ray tomogram of a starch-cake dried in an uncontrolled experiment. The faint rings visible near the center of the picture are artifacts of the inversion process used to reconstruct the image from X-ray diffraction data. The small black dots are bubbles. The imaged window is 2.5 cm across. Movies which show the evolution of the cross-sectional pattern from two tomograms are available as online supplements to Reference [29].

In most cases, MicroCT was unnecessary, and overly expensive. Imaging was instead done directly through digital photography of column cross-sections. Layers of starch were successively and destructively removed by sawing away the surface of the sample. Fine black sand (<75 μm sieve cut) was rubbed into the exposed surfaces to improve the contrast of the cracks. Images were obtained of the surface after each cut, for later analysis (an example of such a cut surface is shown in Figure 2.17(a)). This destructive sampling technique produced useful measurements at 2-3 mm depth intervals, but was too aggressive to use closer than $\sim$5 mm from the drying surface, where the column structure was too delicate.

2.2 The physical properties of desiccating starch

In order to encourage physically based modeling, and to foster a theoretical understanding of the formation of columnar joints in starch, as well as to help interpret certain experimental results, investigations were made into several physical properties of desiccating starch slurries. The results presented here characterize the physical transport of water, and describe the microscopic origins of stresses, within a desiccating starch-cake.

2.2.1 Particle sizing

A disperse smear of starch grains on a glass plate was observed under a digital microscope. Images were thresholded to produce a binary image of starch grains, and the visible areas and the semi-major and semi-minor axes of 256 grains were measured. The average particle radius, $R_g = 5.9\pm0.3$ μm, was calculated by assuming spherical particles, as shown in Figure 2.5(a). The average grain eccentricity, calculated from the semi-major and semi-minor axes of grains, was 0.7 ± 0.1.

By employing a laser diffraction particle sizer (Malvern Mastersizer S) the particle size distribution of starch grains was more accurately measured. This device measures particle size by inverting the diffraction pattern of laser light shone through a suspension of particles in a fluid or air stream. The distribution of the radii of starch grains in water was found to be sharply peaked around a mean $R_g = 8.2$ μm, with a full-width-half-maximum of 3.2 μm, as shown in Figure 2.5(b). A small, broad, secondary peak between 0.1 and 1 μm may result from small detritus broken off of normal-sized particles. In air, particles tended to clump, yielding a broadened shoulder on the upper end of the main peak and a small peak at 100-200 μm radius.

The slightly different results obtained by the two particle sizing methods are due to

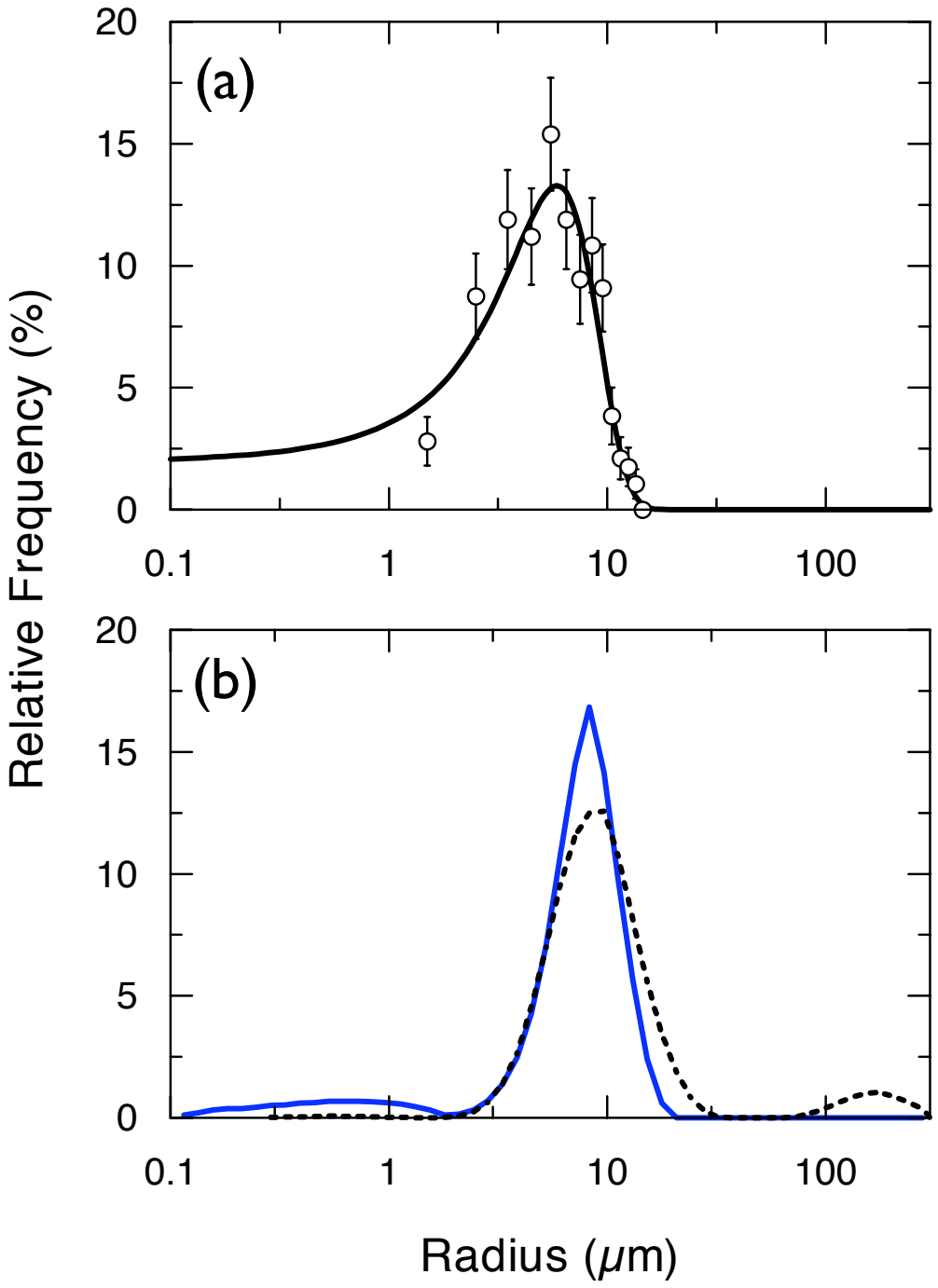

Figure 2.5: Particle sizing. (a) The particle size distribution (with a 1 μm bin size) obtained through optical microscopy techniques is fit by a gaussian distribution (solid line) with a mean radius $R_g = 5.9 \pm 0.3$ μm, and a standard deviation of 3.0 ± 0.2 μm. (b) The particle size distributions for starch grains in water (solid line) and in air (dashed line), using laser diffraction particle sizing, shows no evidence of particle swelling. In water the size distribution has a mean $R_g = 8.2$ μm and a full-width-half-maximum of 3.2 μm.

the different assumptions underlying each measurement. Visual particle sizing assumes that the grains are perfect spheres, which they are not. This assumption, along with the more limited statistics of visual methods, suggests that the laser diffraction particle sizing method is likely the most reliable of the two techniques.

The laser diffraction results also imply that starch grains do not swell when immersed in water. The particle size distributions of starch grains in air and water match exactly on the lower end of the main peak, a result that would not be affected by clumping, but that would be affected by any swelling of the particle size when wetted. Furthermore, the particle size distribution in water was measured eight times, from shortly after immersion to fifteen minutes later. There was no measurable difference in the particle size distribution between these trials.

In a drying sample, for low enough water concentrations, the surface tension across the water-air interface of water bridges between grains controls the flow of water, and leads to forces that scale inversely with R_g. The capillary pressure across this interface is given by

$$P_c(R_w) = -\frac{2\gamma_w}{R_w}, \tag{2.1}$$

where R_w is the radius of curvature of the water bridges connecting two grains, and γ_w is the surface tension of water. In a close-packed lattice of spheres R_w can reach a minimum of approximately $0.15R_g$ [23]. Using a surface tension of water of 0.072 N/m at 25°C [113], Equation 2.1 implies that there is a maximum achievable capillary pressure of approximately 120 kPa, caused by the capillary bridges.

2.2.2 Particle surface characteristics

Starch was observed under high magnification using electron microscopy. Dry starch was dusted onto a sticky sample holder, briefly sputtered with carbon to coat the grains, and exposed to the vacuum of a JEOL JSM-840 scanning electron microscope chamber. As shown in Figure 2.6(a) the starch grains are roughly uniform in size and typically somewhat spherical, but are also often possessed of angular corners. High-resolution images of single grains (see Figures 2.6(b,c)) show that starch grains have substructure. Pits and dimples appear on many, but not necessarily all, grains. When wetted these pits will fill with water and should contribute significantly to the porosity of any packing of grains. Many grains also appear to be covered by a fractured plate-like skin, as shown in Figure 2.6(c). It is uncertain if this is caused by the fracture of the sputtered carbon surface that was coated over the grains before they were observed, if it is some structure that formed when the starch was placed in vacuum, or if it is part of the original surface

of the starch grain.

A single column of starch was also observed in the electron microscope. Images of this column are shown in Figures 2.6(d-f). The column does not show any revealing surface patterning such as the striae or plumose that are typical of columnar jointing in lavas. The dried starch grains do not crystallize but rather appear to pack randomly. High-resolution images of grain-grain contacts (see Figure 2.6(f)) show that as they dry, grains can indent their neighbors and form slightly cohesive 'kissing' contacts. These contacts, or actually deformations of the grains, probably formed through the action of surface tension in water bridges that had previously connected the two grains.

2.2.3 Slurry density

Liquid starch-water mixtures were filled into a 100 ml volumetric flask and weighed to determine their density. Additional tests were performed in an oscillating U-tube densitometer (Anton Paar DMA 500), although for dilute samples the settling of starch out of suspension affected these density measurements. All values were corrected for an initial 5% moisture content, by mass, in the initial *dry* starch powder (see Section 2.1.1).

Suspensions of starch grains in water can be treated as a two-phase mixture of wet grains and water. Under the assumption that the starch and water phases do not interact with each other (such as through grains swelling, absorbing water, disassociating, or otherwise reacting with the liquid), the sample density ρ can be calculated by considering the relative volume and density of the two phases:

$$\rho = (1 - C/\rho_w)\rho_s + C, \tag{2.2}$$

where ρ_s and ρ_w are the densities of bulk starch and water, respectively, and C is the moisture concentration in the mixture.

To test for any observable disassociation of starch in water, 25 g of starch were mixed with 500 ml of water for 1 hour using a stir bar, at room temperature. The resulting suspension was left to settle overnight, and decanted. Measurements of the density of the supernate were indistinguishable from measurements of the density of tap-water, ρ_w = 0.997414 $\pm$0.000002 g/cm^3 at 25°C. As shown in Figure 2.7(a), there are no other indications of disassociation in liquid starch-water mixtures. A fit of all density data from starch grains suspended in water to Equation 2.2 gives $\rho_s = 1.57 \pm 0.01$ g/cm^3.

As it dries, a starch-water mixture completely solidifies when the grains have settled and are fully packed, when all the excess water has evaporated, and when air begins to intrude into the pores between grains. To find the density of solid mixtures, the

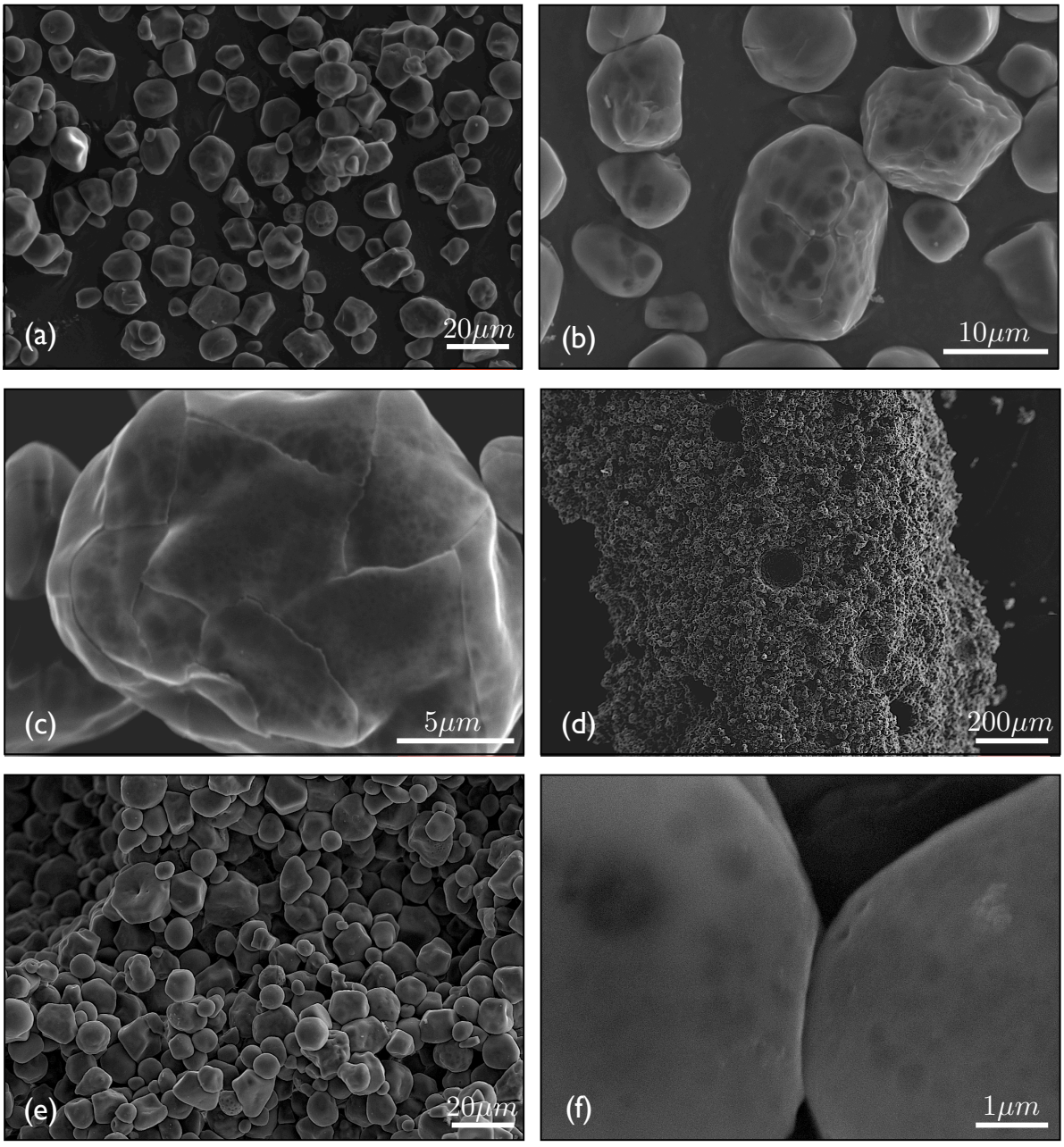

Figure 2.6: Scanning electron microscope images. (a) Grains are roughly uniform in size, and typically spherical, although blunt corners occur on many grains. (b) Starch grains display dimples, holes, and voids. (c) Their surface also shows a fractured plate-like structure. (d) An image of a single dried column, with a small prominent bubble near the centre and (e) a close-up near that bubble, show the random close-packing of dried grains. (f) The inspection of individual grain-grain contacts shows how grains deform into each other when dried, forming 'kissing contacts'.

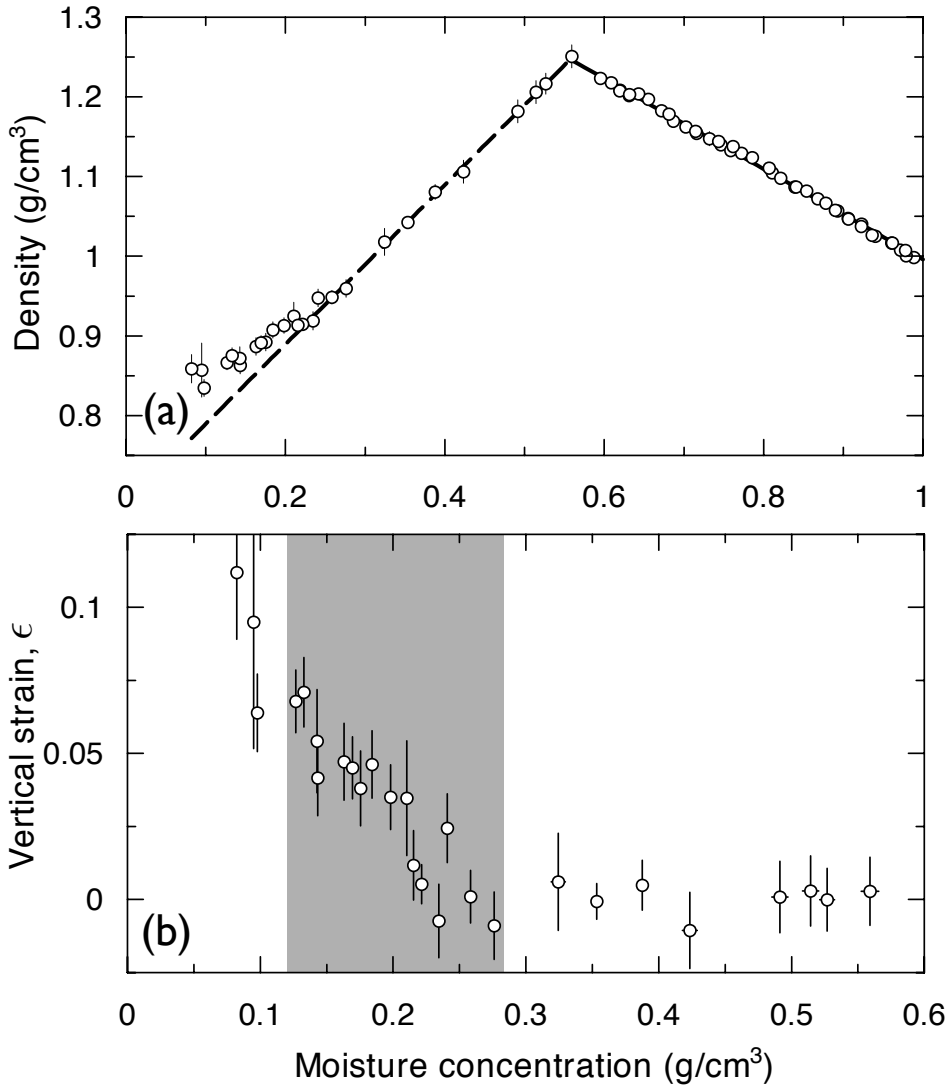

Figure 2.7: Density changes and strain develops during the drying of a starch-water mixture. (a) The measured density dependence (open circles) of starch-water mixtures is well modeled by a non-interacting mixture of starch and water (solid line, given by Equation 2.2) or starch, water and air (dashed line, given by Equation 2.3). (b) Below $C = 0.3$ g/cm^3 the density deviates from this model due to desiccation-induced strain. The grayed region indicates samples in which columnar jointing had been initiated, but where joints did not reach the base of the starch-cake.

thickness, diameter, and mass of partially dried starch-cakes were measured. These cakes were prepared by adding 100-300 g of an equal mixture of dry starch and water to Pyrex round-bottomed dishes, and drying them under heat lamps for some time. The inside of the dishes had been covered with a piece of wax paper cut to the size of the base of the dish and a tin foil ribbon cut to the size of the walls of the dish – allowing the gentle removal of the fragile partially dried starch-cake without breaking it. The mass of the removed starch-cake was measured on a digital balance, and the thickness and diameter were measured using calipers.

Once air begins to infiltrate the starch-cake, a three-phase model of density is necessary. During this period of drying, as long as there is no tensile strain in the starch-cake, the relative volume of the starch grains remains a constant. The sample density ρ can thus still be calculated by considering the relative contributions of starch and water, by

$$\rho = (1 - \phi)\rho_s + C, \tag{2.3}$$

where the porosity ϕ is the relative volume of the part of the sample *not* taken up by bulk starch. The cross-over between this model, and that of Equation 2.2 occurs when the pore space is entirely filled – when $C/\rho_w = \phi$. This no-strain model is accurate until columnar jointing starts, as is shown in Figure 2.7(a), and the cross-over point implies that the starch-cake porosity $\phi = 0.56 \pm 0.005$. This is unusually high for any random close packing. However, ϕ is the sum of the relative pore space between grains, and the relative volume contained in the holes and pits *within* grains. It may be that these intra-granular pores contribute a large portion of the porosity.

If there is strain in the drying sample, the horizontal component will be accommodated by fractures, both primary and columnar, which remained open when the starch-cake radius was measured. Instead, as is shown in Figure 2.7(b), only the vertical strain

$$\epsilon_{33} = -\frac{h - h_0}{h_0} \tag{2.4}$$

was measured, by comparing the thickness h of a starch-cake to the expected unstrained height h_0 (which can be calculated from Equation 2.3).

Since primary cracks open before columnar jointing begins, there must be some strain associated with their development. However this strain appears to be too small to be detected by the methods described here. Once columnar jointing begins, the total vertical strain increases as the depth of jointing increases. If the horizontal strains that lead to fracture formation are approximately equal to the measured vertical strain, $\epsilon_{ii} = \epsilon$, then

the total horizontal strain that develops during drying may be as high as 10%. Since measuring h only observes the integrated vertical strain across the entire starch-cake, it cannot be clearly said what form $\epsilon(C)$ takes. It may be that the strain uniformly increases with decreasing C, or it may be that all the strain is generated over a very narrow change in C.

2.2.4 Water transport

The experiments in this section were performed in order to determine how the water concentration C varies, both spatially and temporally, during drying. Starch slurries were poured into flat-bottomed dishes with an inner radius of 43.1 mm (90x50 mm Pyrex dishes), the insides of which were covered with a circle of wax paper and a ribbon of tin foil to facilitate the easy removal of the sample. 317.1 g of an equal mixture of starch and water, by mass, were added to each dish, which filled the dishes nearly up to the brim. Each sample was placed on an automated balance and subjected either to an uncontrolled experiment, with $q_m = 0.19$ g/cm^2 h initially, or to a controlled experiment with $Q_1 = 4$ g/h, $\dot{Q} = 0.5$ g/h, and $Q_2 = 1$ g/h ($q_c = 17$ mg/cm^2 h). After a certain time t had passed, the sample was removed. The uncontrolled experiment was performed 17 times, with t varying between 6 and 48 hours. The controlled experiment was performed 15 times, with drying lasting 20-80 hours. The average evaporative water fluxes during both sets of experiments are shown in Figure 2.8. This figure also shows that the controlled experiment was only able to sustain the desired evaporation rate through the first 65 hours of the experiment.

Immediately after a sample was removed from the balance and its dish, a sub-sample was selected and cut into 1-3 mm thick layers along the vertical z direction. The moisture concentration field $C(z,t)$ shown in Figure 2.9 was then sampled by comparing the weights of these layers before and after baking them dry, for each experiment.

The drying of a starch slurry occurs in three phases, as has been noticed on multiple occasions [8, 9, 29, 31, 67, 74, 106]. The desiccation experiments described in this thesis typically begin with equal masses of starch and water, in order to allow the mixture to be manipulated as a liquid. In this proportion $C = 0.6$ g/cm^3, and there is more water than pore space. The first phase of drying therefore occurs as the starch settles in a water column, and as water evaporates from the surface of a pool of supernatant liquid. This initial evaporation rate is virtually uniform, and can be used to characterize the effective drying power applied to the mixture [106]. During this phase the sample is not solid enough to dissect.

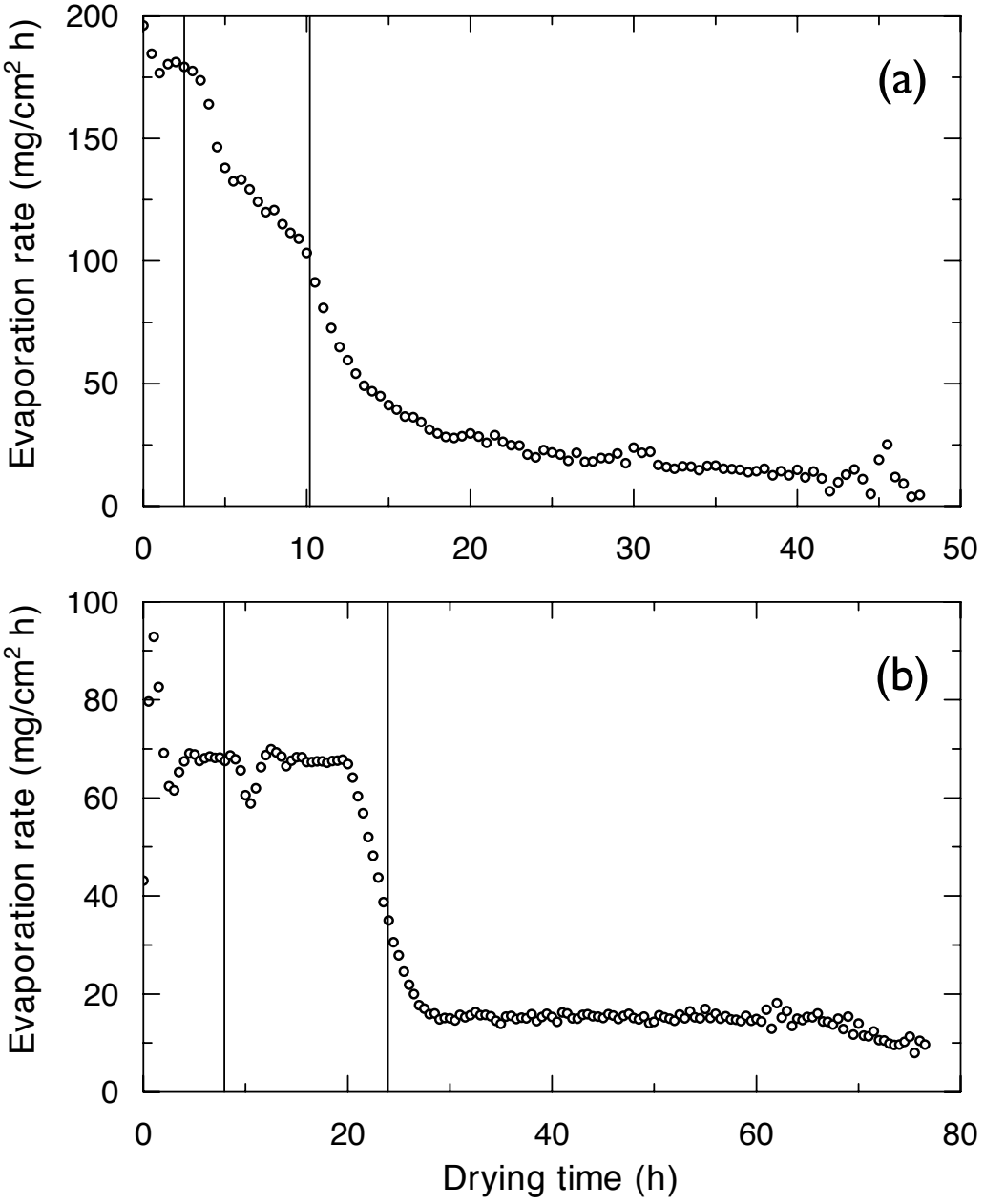

Figure 2.8: Evaporative flux for water transport experiments with (a) uncontrolled, and (b) controlled experimental conditions. Vertical lines show the transitions between two-phase drying, three-phase unstrained drying, and three-phase strained drying, as discussed in Section 2.2.3. After approximately 65 hours the control loop in (b) begins to fail.

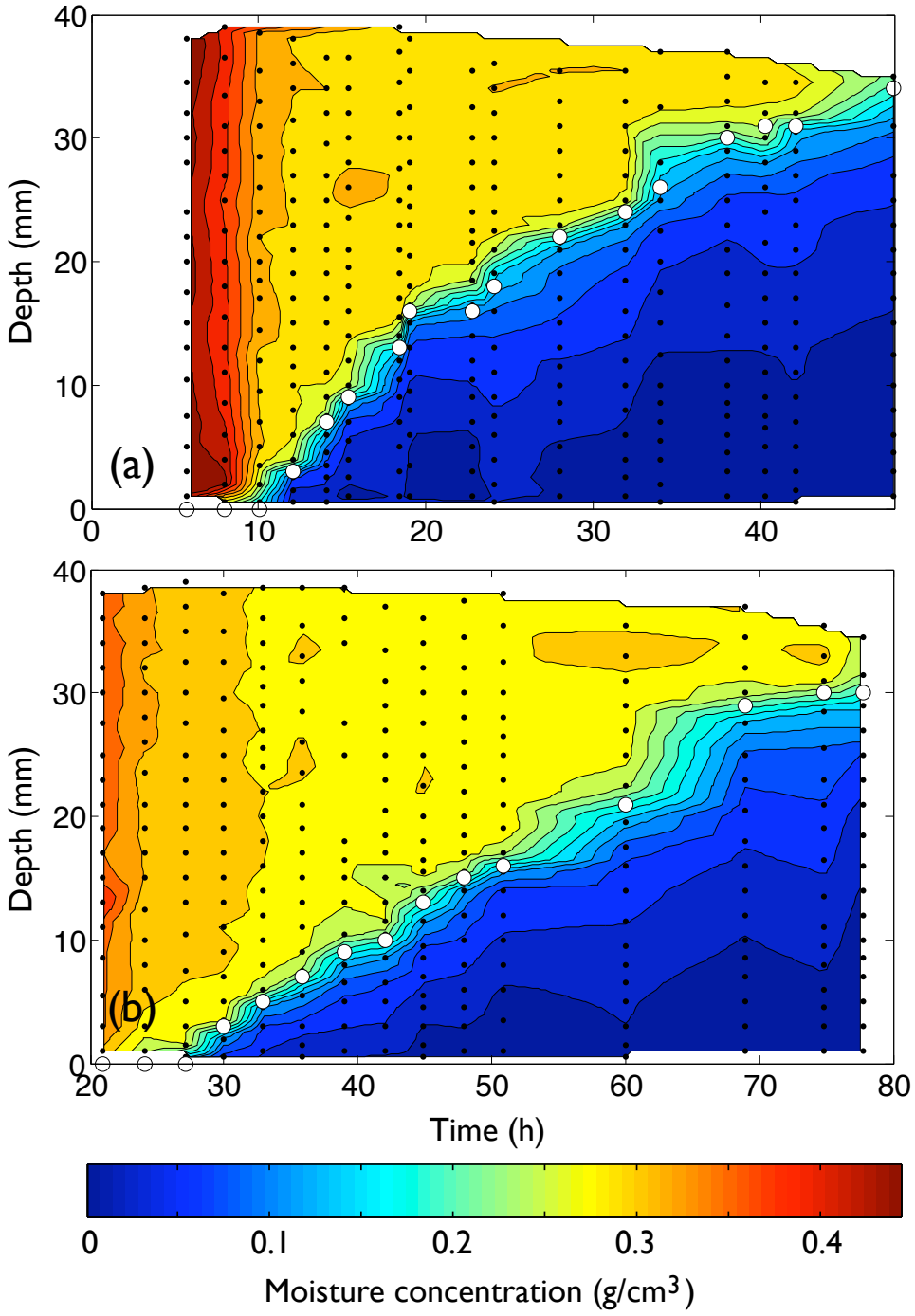

Figure 2.9: Moisture concentration in (a) uncontrolled and (b) controlled experiments, throughout desiccation. Black dots indicate data sampling times and locations, between which the colored C field is interpolated. White circles show the depth to which fractures have advanced, as described in Section 2.2.5.

When the water concentration reaches 0.56 g/cm^3, the starch grains are fully packed and further drying causes air to intrude into the cake. Drying in this second phase is slower than in the first phase, but capillary transport is efficient enough to continue to dry the entire sample uniformly. There is no concentration gradient across the thickness of the starch-cake. First-generation cracks open during this phase.

At a critical water concentration of 0.30 g/cm^3, a starch-cake starts to dry inhomogeneously, large strains begin to accumulate, and soon a fine-scaled fracture pattern is initiated at the drying surface. Further evaporation causes the growth of these cracks into the drying cake, accompanied by a large moisture gradient. Figure 2.10 shows how a moisture front develops and moves through the starch-cake during the final drying phase. Starch taken from below this front has a nearly uniform moisture concentration of $C = 0.30$ g/cm^3, while the moisture concentration of starch taken from above the moisture front has a strong depth dependence. It is important to note that, in contrast to a typical diffusive front, the curvature $\partial^2 C/\partial z^2$ is positive above the fracture front. The implications of this will be analyzed in Section 4.1.1. A similar sharp drying front has been seen in the directional drying of 2D suspensions [23], and has also been imaged in drying starch slurries using nuclear magnetic resonance techniques [67]. Such a front is expected when capillary forces become the dominant driving mechanism for water transport, and indicates a shift from flow-limited to evaporation-limited dynamics [23, 29, 74]. Water transport in this third phase is thus likely driven by vapor diffusion, rather than by capillary flow.

2.2.5 Fracture position

As seen in Figure 2.10 there is a clearly delimited boundary between nearly uniformly moist unfractured starch and starch which has given way to columnar jointing, during the third, and final, phase of drying. These two layers come apart naturally when a partially dried starch-cake is removed from its dish, as all the fracture tips are confined to a thin interface. Figure 2.11 shows the depth to which columnar jointing has progressed during the water transport experiments discussed in the previous section. As it intrudes into the starch-cake, the fracture front is actually slightly curved, as fractures (and presumably evaporation) lag slightly near the walls of the pyrex dish [71]. To eliminate this uncertainty the fracture depth near the center of the sample was used consistently.

In an uncontrolled experiment, the fracture front slows down as it advances into the sample, whereas in the controlled experiment, the fracture front advances at a roughly constant velocity. In both cases the vertical position of the fracture tips, $\chi(t)$, can be fit

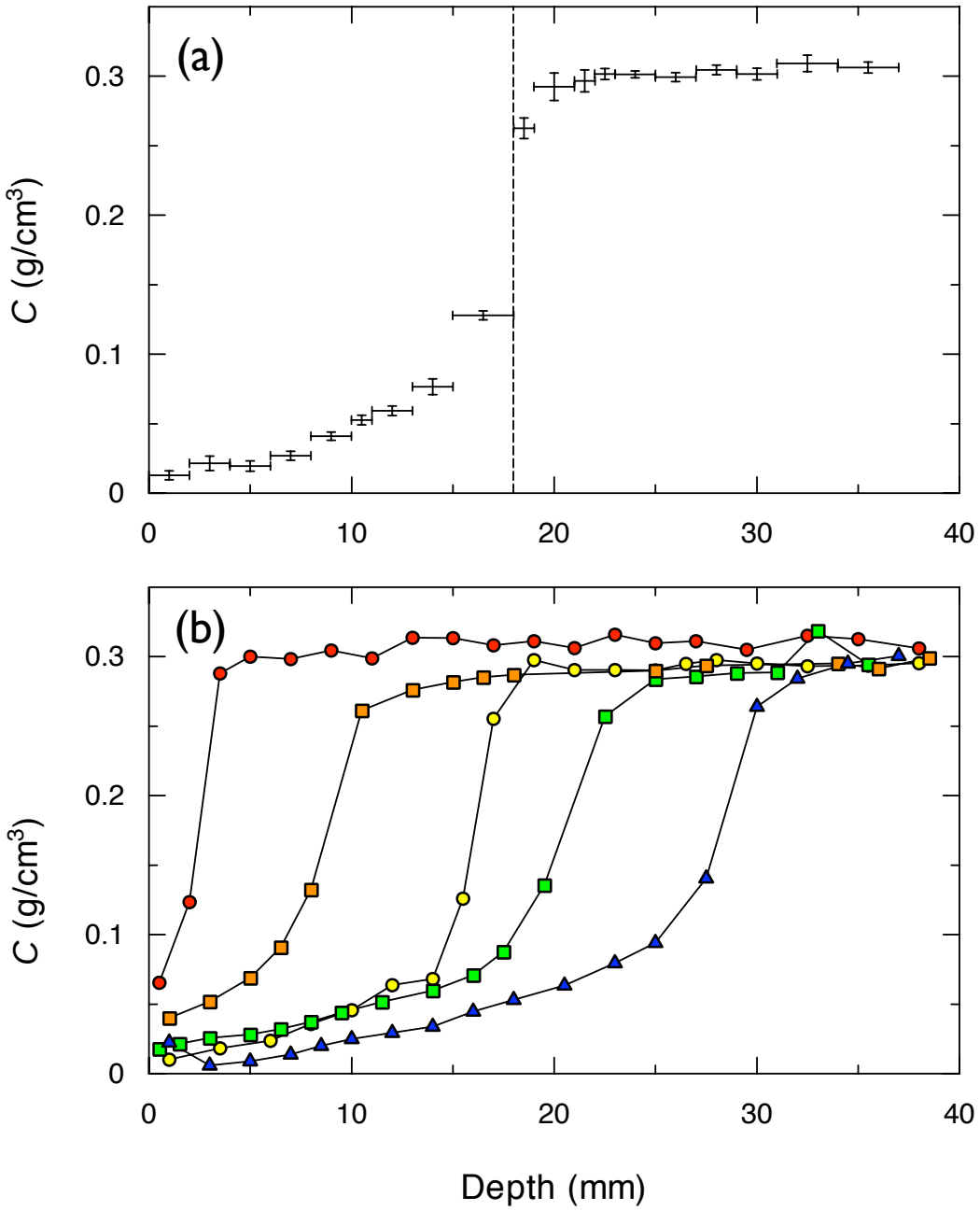

Figure 2.10: Moisture concentration in (a) an uncontrolled experiment after 24 hours of drying, and (b) a controlled experiment after 30 (red), 40 (orange), 50 (yellow), 60 (green) and 70 (blue) hours of drying. In (a), columnar jointing extends up to the vertical dashed line, and representative error bars are shown.

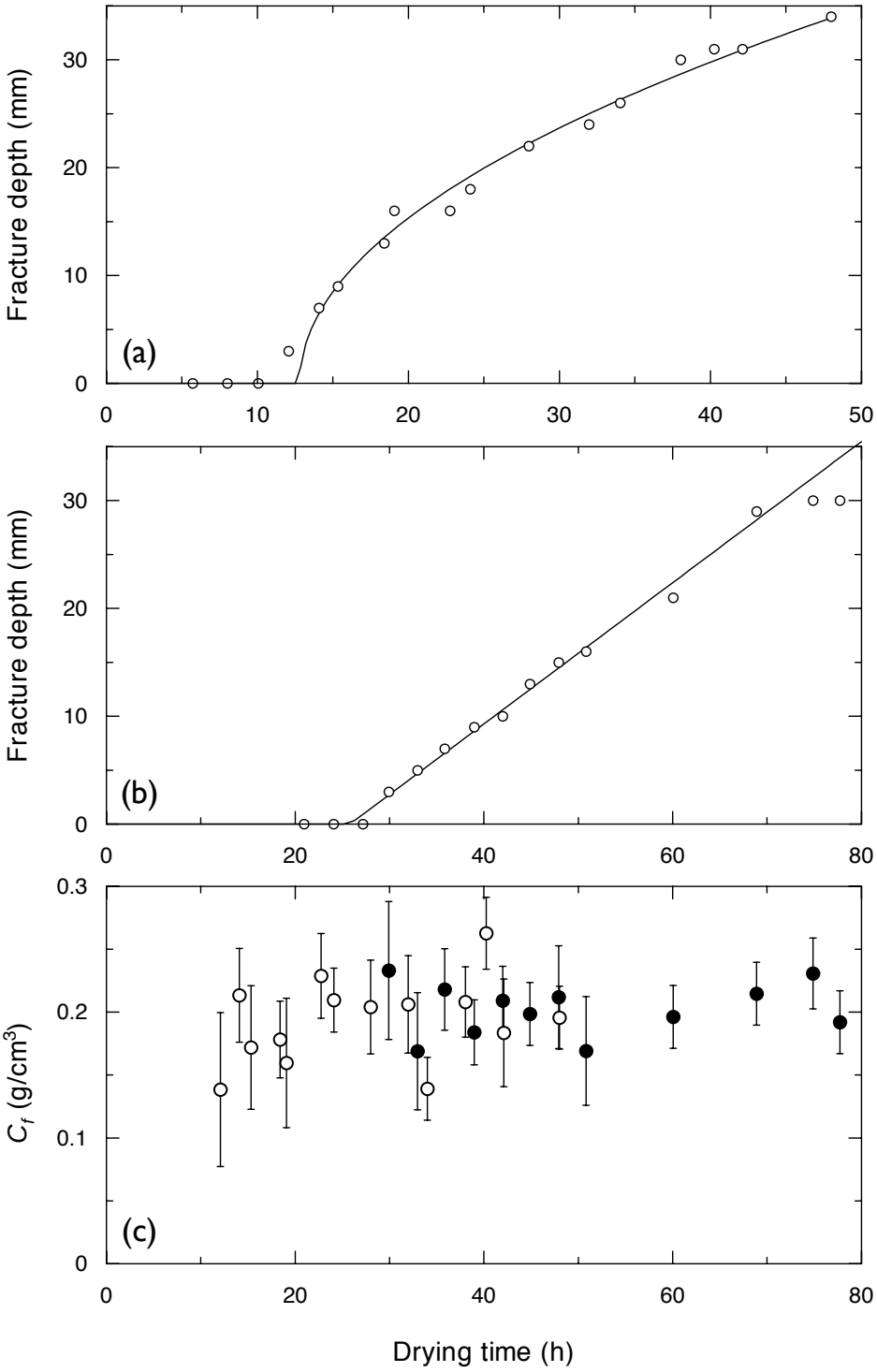

Figure 2.11: Fracture position in (a) uncontrolled and (b) controlled experiments. Errors in the fracture position are ± 0.5 mm, about the size of the data points. The line in (a) is a fit to a $t^{1/2}$ diffusive model, while the line in (b) is fit to a linearly advancing fracture front. (c) The water concentration at the fracture front is a constant in both the controlled (filled circles) and uncontrolled (open circles) experiments.

to a power-law function

$$\chi = a_0(t - t_0)^p \tag{2.5}$$

with three free parameters: the amplitude a_0, exponent p, and the intercept t_0 on the time axis.

The uncontrolled experiment has a fit exponent of $p = 0.58 \pm 0.03$, which indicates that the slowing fracture front *may* penetrate slightly faster than normal diffusion would predict. However, this fit only covers one decade of data, and should not be considered as conclusive evidence of anomalous diffusion. A normal diffusive model, where p is forced to be 1/2, cannot be reliably ruled out, as is shown in Figure 2.11(a). The amplitude of such a $t^{1/2}$ fit, $a_0 = 5.7 \pm 0.1$ mm/h$^{1/2}$, can be used to put a limit on the diffusivity of water near the fracture front, as is discussed in Section 4.1.

A free power-law fit for the data from the controlled experiment gives an exponent of 0.96 ± 0.06, indicating that the controlled evaporation rate successfully fixes the average speed of the fracture front. In this fit, the two data points after 70 hours have been neglected, as it was found that the control cycle began to fail after around 65 hours. If the fit is forced to $p = 1$ for the controlled data, as displayed in Figure 2.11(b), it shows that for $q_c = 17$ mg/cm^{2}h, the fracture front advances at a constant rate of 0.18 ± 0.01 μm/s.

In all cases, and at all times, the observed fracture front trails slightly behind the drying front discussed in the previous section, and appears to be locked to a constant value of the moisture concentration throughout drying, C_f. Figure 2.11(c) shows the values of C_f calculated by interpolating between the concentration data presented in Figure 2.9. Errors are estimated by assuming that there is a 0.5 mm uncertainty in the fracture front position, but assume a minimum error of 0.025 g/cm^3. The error weighted mean of these measurements gives a value of $C_f = 0.20 \pm 0.005$ g/cm^3. This concentration is about 0.1 g/cm^3 below the concentration at which inhomogeneous drying is initiated, and suggests that the starch experiments can accommodate a strain of at least a few percent before cracking. The stress-strain relationship of partially dried starch-cakes is discussed in the following section.

2.2.6 Rheology

Rheology experiments were done using an TA Instruments RA1000 rotating-head rheometer. This device consists of a flat base-plate, and a 40 mm diameter parallel plate rotatable head. A sample is placed in a variable gap between the head and the base-plate, which can be pressed together. The gap thickness, the head's shear rate, shear force

and total shear, and the sample's normal force and temperature can all be measured, or controlled, with remarkable precision by this instrument. The temperature of the sample is controlled by a peltier plate.

The rheology of a starch-water mixture is very complex. As a liquid slurry, this type of mixture behaves as a shear-thickening (dilatant) fluid. The viscosity μ_m exhibits a newtonian plateau at low shear stresses (<20 Pa applied across a 250 μm gap) but this plateau is strongly dependent on C, increasing from 0.1-1 Pa s for a $C = 0.63$ g/cm^3 slurry to 1-10 kPa s for a $C = 0.57$ g/cm^3 slurry. When solid samples with $C = 0.45$, 0.40, 0.37, and 0.32 g/cm^3 were tested for a viscous response to an applied shear stress, they all showed evidence that μ_m is of order 10^9 Pa s. As will soon be shown, this is likely due to a non-linear relaxation mechanism of a packed granular material, and not truly indicative of the sample viscosity.

To ensure that prolonged exposure to heat lamps was not slowly changing the rheology of a drying starch-cake, the temperature dependent viscosity of a starch-water slurry was measured. When heated above their gelation temperature T_{gel}, starch particles in suspension absorb large amounts of water, swell to many times their original size, and then release amylose molecules into the surrounding liquid [40, 98]. This causes a dramatic increase in μ_m due to the cross-linking of amylose, which can be useful in the preparation of foodstuffs (*e.g.* [98]). This effect was measured in a dilute suspension ($C = 0.94$ g/cm^3) of starch in water. Experiments were performed at different temperatures, across a 250 μm gap with either a controlled stress of 1 Pa (used for low μ_m fluids) or a controlled shear speed of 0.2 Hz (high μ_m fluids). Below 60°C μ_m did not increase noticeably over an hour long experiment. However, as shown in Figure 2.12(a), there are very profound changes to the slurry behavior once the temperature is brought above 60°C, as $T_{gel} = 62 \pm 1$°C.

Thermistor measurements made in drying starch-water mixtures showed that the temperature within the sample was never above 40°C, implying that gelation did not occur in any of the desiccation experiments.

To confirm that the viscosity of the water phase of a corn starch-water mixture is no different than that of tap-water, the shear viscosity of still tap-water, and a saturated solution of starch in water, prepared at room temperature as was described in Section 2.2.3, were measured. During these tests the temperature of the base-plate was increased at 1°C/min, starting from 22°C. The viscous responses of both liquids are shown in Figure 2.12(b), and agree with each other, within experimental uncertainty, until T_{gel} is reached. Above this temperature the saturated starch solution approximately doubles in viscosity, suggesting that there were some traces of amylose in the solution.

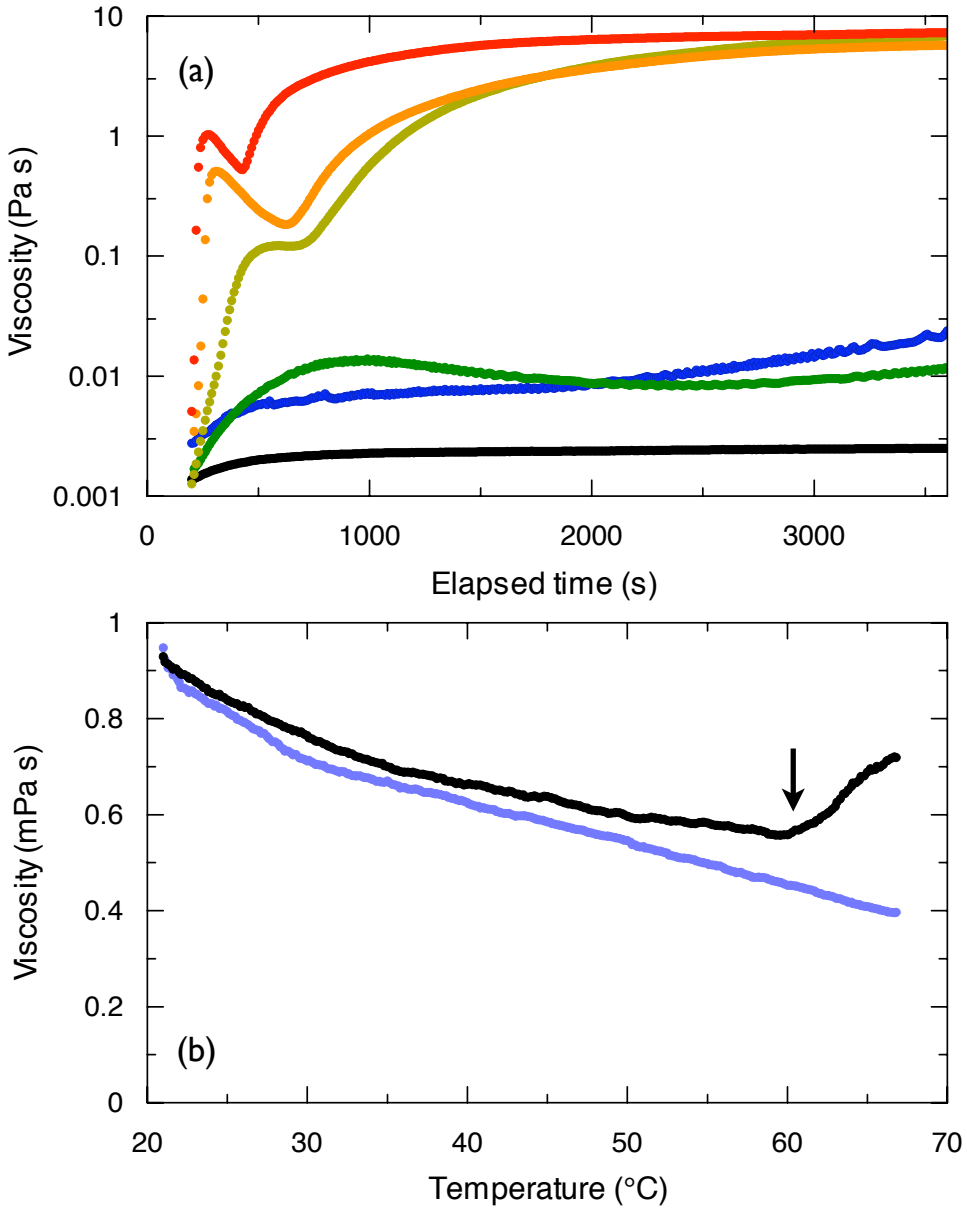

Figure 2.12: High-temperature dependence of starch rheology. (a) The time dependence of the shear viscosity $\mu_m(t, T)$ of a dilute suspension of starch in water, raised to 60°C (black), 61°C (blue), 62°C (green), 63°C (yellow), 64°C (orange), and 65°C (red). (b) The shear viscosity of tap water (blue curve) and a saturated starch solution (black curve), agree with each other, to within experimental reproducibility, below the gelation temperature (black arrow), but diverge above it.

As the temperature of a starch-water mixture never reaches T_{gel} in a typical desiccation experiment, the viscosity of the liquid phase of the mixture can be assumed to be that of water.

The elastic properties of partially dried starch-cakes were measured in small discs, prepared to fit into the 40 mm diameter gap of the rheometer. Liquid slurry was poured into a mould, leveled, and partially dried on a precision balance. Once a desired moisture concentration C was reached, the sample was carefully removed, and transferred to the rheometer. Compressional tests were done by slowly lowering and raising the rheometer head, and recording the normal force response of the sample. Due to limitations of the rheometer, data recorded while raising the head from a compressed state were clearer than data obtained by compressing a sample from an unstrained position. Figure 2.13(a) shows the normal force on the rheometer head as it is raised from a maximum pressure of approximately 70 kPa. Experiments were done over a range of strain rates (from 0.1–4 μm/s) and water concentrations (0.3-0.4 g/cm^3), although all tests generated experimentally identical stress-strain curves.

The elastic response of a starch-cake is well fit by a model of 3rd order elasticity. In its general form, this model adds the next-to-lowest order terms to linear elasticity, and estimates the total elastic energy density $\mathscr{E}$ as

$$\mathscr{E} = S\epsilon_{ik}^2 + \frac{1}{2}E\epsilon_{ll}^2 + \frac{1}{3}\mathrm{A}\epsilon_{ik}\epsilon_{il}\epsilon_{kl} + \mathrm{B}\epsilon_{ik}^2\epsilon_{ll} + \frac{1}{3}\mathrm{C}\epsilon_{ll}^3, \tag{2.6}$$

where A, B, and C are the Landau moduli [58], and S and E are the linear shear and Young's moduli. This model has been successfully applied to granular solids such as sandstones, and other sedimentary rocks [76, 116]. The higher order terms can be seen to follow naturally by considering the compression of two elastic spheres into each other. In the absence of any strain, the contact between the spheres occurs only at a single point. If an infinitesimal stress is applied to the spheres, it will be concentrated onto this single point, making the system infinitely deformable. In response to a finite stress, however, the contact area between the spheres increases as the particles deform. As it takes more and more stress to strain the spheres by the same amount, this leads to a stress-dependent increase in the stiffness of the system. An effective-medium theory for a granular solid can be constructed, with some slight modifications, from the sum of a large number of such elastic sphere interactions [76].

If there is no shear, Equation 2.6 can be directly differentiated to give the stress

$$\sigma_{ij} = E\epsilon_{ii}\delta_{ij} + \mathrm{C}\epsilon_{ii}^2\delta_{ij} \tag{2.7}$$

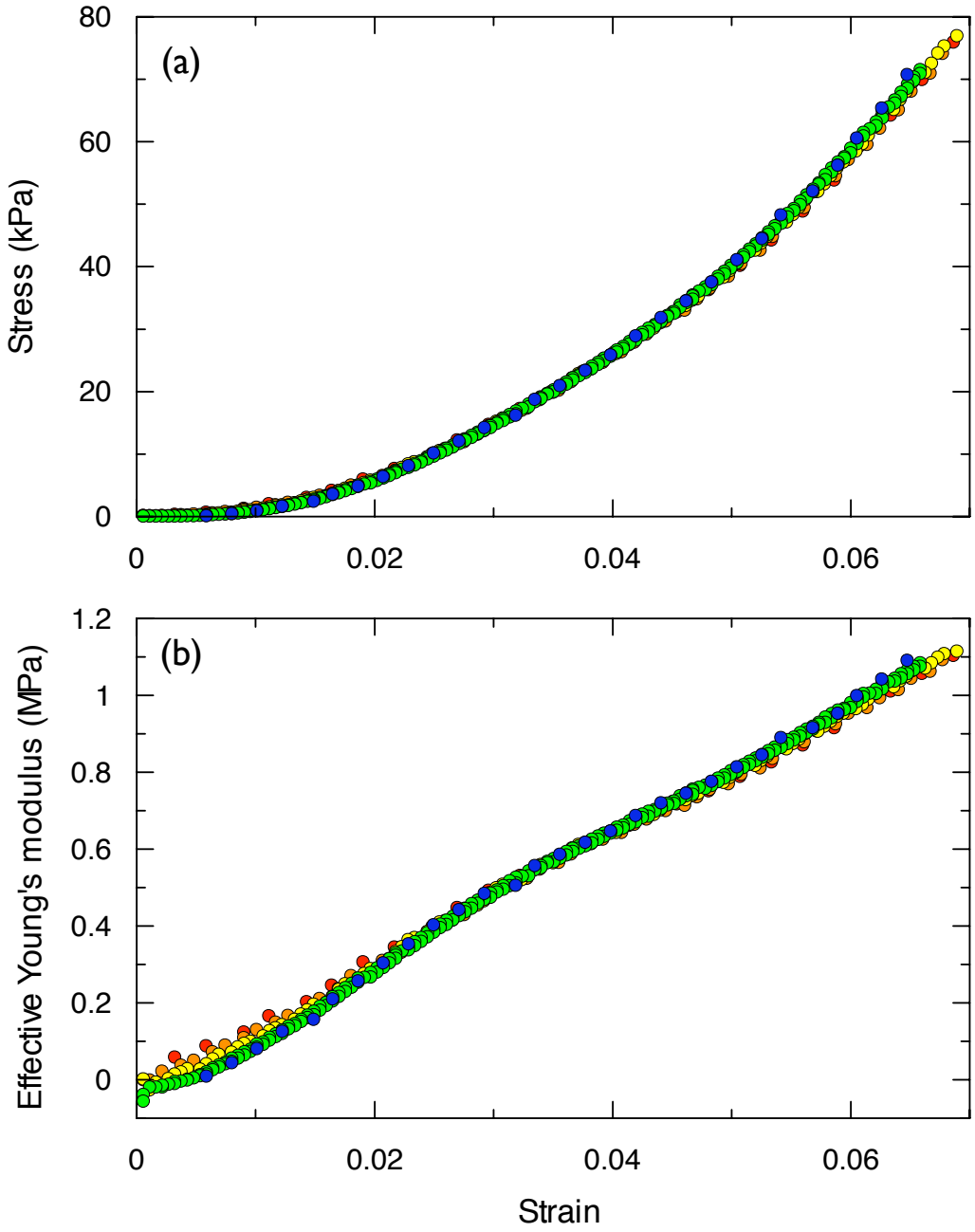

Figure 2.13: The elastic properties of a thin starch-cake when C=0.32 g/cm^3. The stress (a) and effective Young's modulus (b) are dependent on the strain, and agree with the predictions of 3rd order elastic theory. Data were collected at 5 different strain rates (different colors, from 0.1-4 μm/s), but the elastic response shows no dependence on the strain rate.

which only depends on the linear elastic modulus, E, and the Landau modulus C. Since the rheometer only applies a uniaxial strain, ϵ_{33}, the effective Young's modulus of the starch-cake

$$E' = \frac{\sigma_{33} - \sigma_0}{\epsilon_{33}} = E + \mathrm{C}\epsilon_{33}. \tag{2.8}$$

Here, the correction term σ_0, typically only a few hundred Pa, is the normal force observed by the rheometer head once it had been raised enough to lose contact with the starch sample, and σ_{33} is the measured vertical stress. Results for the effective Young's modulus are shown in Figure 2.13(b) for $C = 0.32$ g/cm^3. A fit to the 3rd order elastic model given in Equation 2.7 agrees with the prediction that the modulus E' is zero in the absence of any strain, and gives the Landau modulus C = 16±1 MPa. Additional tests were performed at a moisture concentration of 0.39 g/cm^3 with identical results.

An additional, unusual, feature of the rheology of granular solids is the lack of a well-defined relaxation time, or relaxation spectrum. Instead of viscous damping, there is a slow dynamical relaxation of stress, with no time constants: if a force is applied, the recovery is slow, but logarithmic in time [76]. This type of relaxation is shared by a number of superficially unconnected systems, such as the relaxation of the magnetization of spin glasses, and the dc susceptibility of granular magnetic media [102]. The slow-relaxation hypothesis was tested by compressing a moist starch disc to a fixed strain, and measuring the resulting normal force on the rheometer head as a function of time. The results from two such tests are shown in Figure 2.14, which shows that, indeed, partially dried starch does have a logarithmic recovery. In another test a small shear strain was applied to a sample for 5 minutes, and then the relaxation of the strain was monitored once the pressure was released. As shown in Figure 2.14, the strain also shows a logarithmic recovery in time. The cause of these slow dynamics are not understood, but they imply that newtonian relaxation is not significant in the rheological response of solid starch samples to stress. Any measurements of the viscosity of a starch-cake, such as were made previously in this section, are likely sampling this logarithmic stress relaxation, and should not be relied upon. However, these results also suggest that over the week-long course of a desiccation experiment, there should be at most only a small decrease in the drying-induced strain, due to any stress relaxation mechanism.

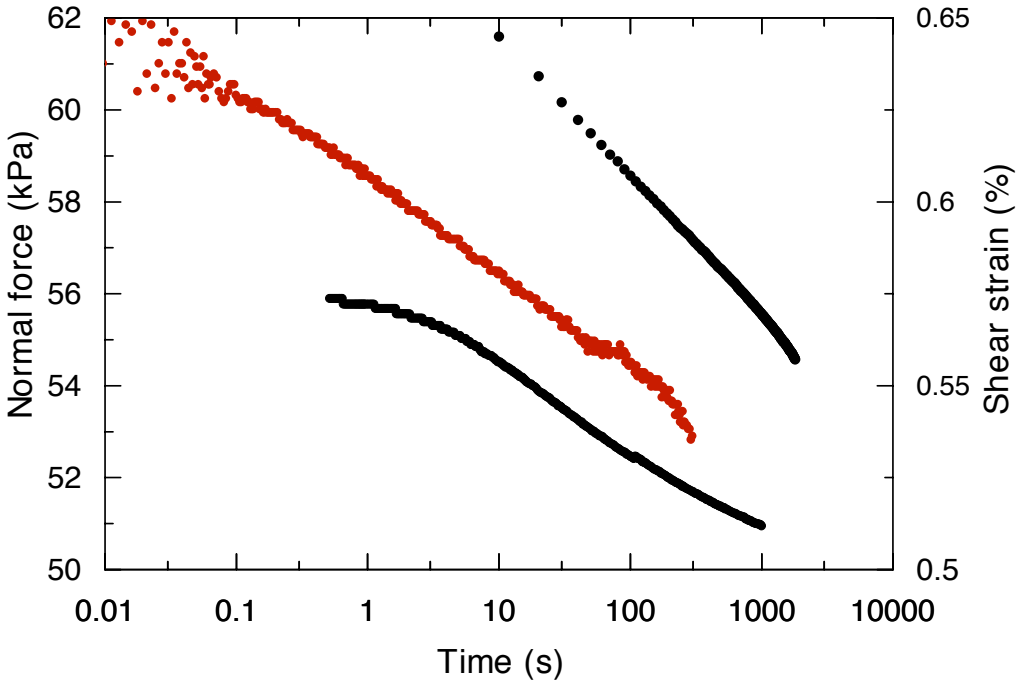

Figure 2.14: The logarithmic relaxation mechanism of corn starch is shown in response to applied normal forces (black circles, left axis) and an applied shear strain (red circles, right axis).

2.2.7 Permeability

The intrinsic permeability κ_w of a porous medium is defined through Darcy's law

$$J = -\frac{\kappa_w}{\mu}\frac{dP}{dz} \tag{2.9}$$

and describes the volumetric flow rate per unit area $J = q/\rho$, of a fluid of viscosity μ that will pass through a porous medium under a pressure gradient dP/dz.

To measure the saturated permeability of starch, long glass tubes with radii 1.4-2.2 cm were set up vertically. Discs of fine filter paper (Whatman type 42 ashless filter) were cut to size and glued to the lower open end of each tube. Starch slurry was poured in at the top of a tube and allowed to settle for 1-2 hours. Additional water was then added to the tube to increase the hydraulic head, the top end of the tube was plugged with a wet cloth, and the lower end was positioned so as to drip into a flask set on a digital balance. The flask mass was automatically recorded every minute, and the volumetric flow rate J was calculated every half hour. The lab temperature was measured several times during these experiments and found to be consistently 24±0.5°C, implying that the viscosity of water, $\mu_w = 0.91$ mPa [113]. Each permeability experiment typically

lasted 4-6 hours, although the long-term stability of a thick sample was tested through a multi-day experiment, as shown in Figure 2.15(a).

The effect of the filter paper on the permeability can be eliminated by considering the hydraulic resistance,

$$\Omega_h = \frac{\Delta P}{\mu J}, \tag{2.10}$$

which adds in series when liquid is forced through several sequential material layers by a total pressure drop ΔP. Measurements for a single filter paper give $\Omega_h = 0.3{\times}10^{14}$ m^{-3}, while for a filter covered with 4 mm of starch $\Omega_h = 1.8{\times}10^{14}$ m^{-3}. Thus, the effects of the filter paper on the permeability is equivalent to about half a mm of starch, and can be neglected for experiments more than a few mm thick.

Although each permeability experiment resulted in a well defined κ_w, which did not vary by more than a few percent over the course of the experiment, there was significant scatter between trials (see Figure 2.15(b)). This scatter may be attributable to slight variations in packing arrangements, although attempts to prove this were inconclusive. Averaging over all trials, the intrinsic permeability of saturated starch slurries can be estimated to be $4.5{\pm}1.5{\times}10^{-14}$ m^2.

The intrinsic permeability can be used as a probe of the connected porosity, which may differ from the total porosity $\phi = 0.56$. One common permeability model assumes a regular cubic array of pores separated by small throats of length $2R_g$, where R_g is the grain radius [108]. In this case

$$\kappa_w = \frac{R_g^2 \phi_p^2}{18\pi}, \tag{2.11}$$

where the connected porosity ϕ_p would only include the pore space between grains, but not the much smaller void spaces within individual grains. If $R_g = 8.2$ μm, then Equation 2.11 predicts that $\phi_p = 0.2{\pm}0.1$, which implies that the connected porosity is much lower than the total porosity.

2.2.8 Synthesis and summary of starch drying properties

The results of Sections 2.2.1 to 2.2.7 combine to give a coherent picture of the drying of a starch-water slurry into a solid starch-cake. This drying occurs occurs in three phases, as has been previously recognized [8, 9, 29, 31, 67, 74, 106]. Since most desiccation experiments begin with roughly equal masses of starch and water, in order to allow the mixture to be manipulated as a liquid, the moisture concentration C is initially about 0.6 g/cm^3. The first phase of drying occurs as the starch settles in the water column, and water evaporates from the surface of a pool of supernatant liquid. This initial

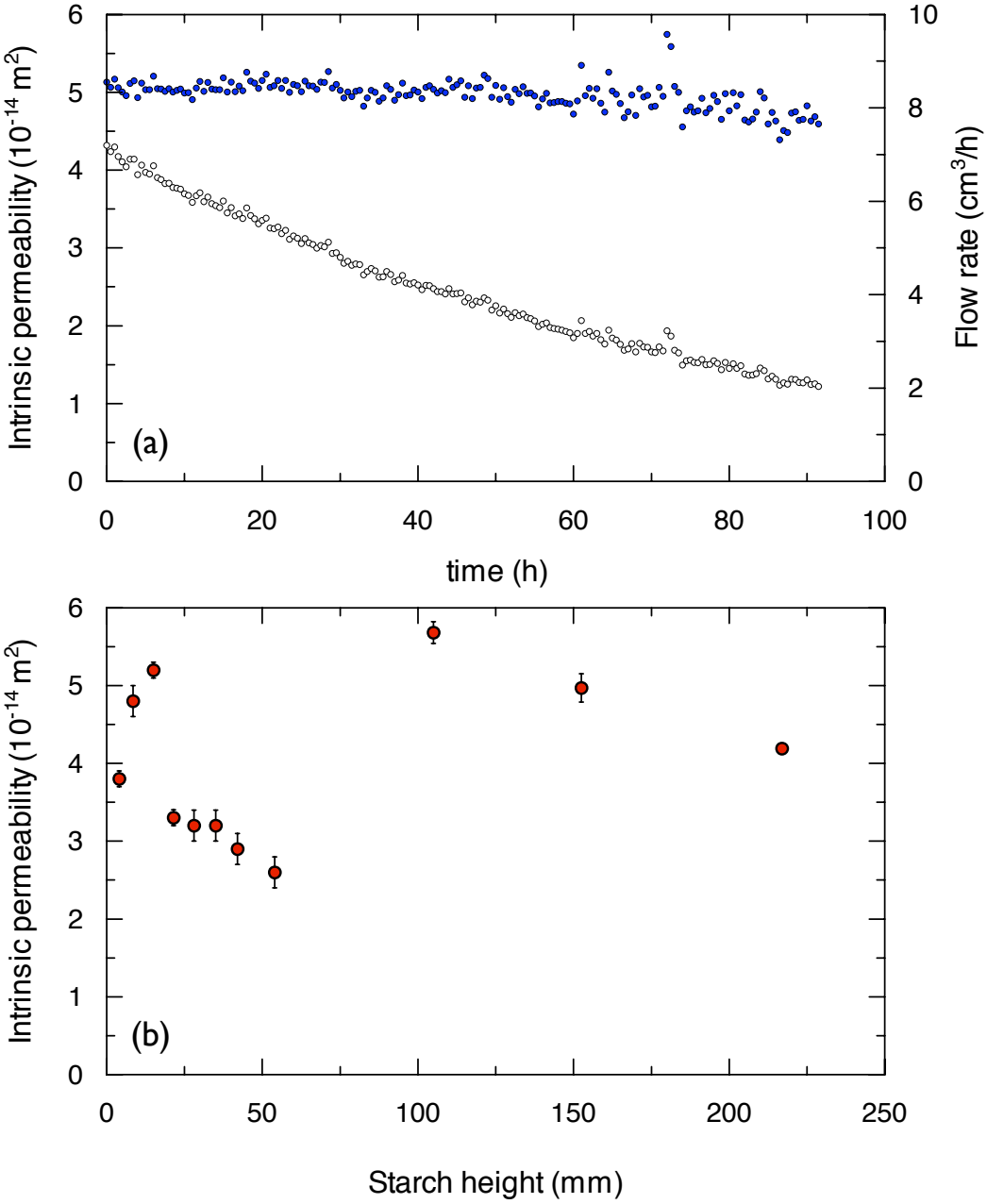

Figure 2.15: Intrinsic permeability measurements in saturated starch. (a) Permeability (blue points, left axis), and volumetric flow rate (open circles, right axis), were measured in a 155 mm thick saturated starch plug over 3.5 days. The permeability is very stable through the entire range of time, and over a large change in flow rate. (b) measurements of permeability in samples of different thickness, however, are scattered.

evaporation rate can be used to characterize the effective drying power applied to the starch-cake [106].

The remaining two stages of drying correspond to the stages of fracture discussed in Section 2.1.2. Once the starch-cake has reached $C = 0.56$ g/cm^3, air begins to infiltrate into the voids between the starch grains, and multi-phase flow begins to occur. The porosity of ϕ=0.56$\pm$0.005 of this mixture is unusually high, considering that the porosity for a random close packing of spheres is only 0.36, and that the porosity is even lower than this in random close packings of irregular shapes such as ellipsoids [22]. However, the results presented here are in relatively good agreement with a previously published value of $\phi = 0.51$ in corn starch [55].

In order to have such a large porosity, water must be distributed between two distinct, but connected, reservoirs: the gaps left between the closely packed grains (with porosity ϕ_p), and the smaller pores within individual grains (with porosity ϕ_g). The measured ϕ can be reconciled with known packing behavior if the pore space within the starch grains contribute a porosity of about $\phi_p = 0.3\pm0.05$. This agrees with an interpretation of the intrinsic permeability of saturated starch, which indicates that $\phi_p = 0.2\pm0.1$. As will be shown in Section 2.4.3, a comparison of the surface volumetric water flux to the fracture front velocity, during controlled experiments, further suggests that $\phi_g = 0.26\pm0.01$. This confirms that the complementary $\phi_p = 0.3\pm0.01$.

Since the large pores between grains will empty before the smaller pores within grains, they control the second phase of drying, which is dominated by capillary water transport. Their emptying corresponds to the phase of homogenous sample drying, which happens between $C = 0.56$ g/cm^3 and $C = 0.30$ g/cm^3. There is little or no measurable strain during this phase of drying, although a few primary cracks do appear. Up to this point, the starch-cake is very weak and brittle.

Once most of the water has been removed from the pore spaces between grains, some small amount will remain to form water bridges between individual grains. As C continues to decrease, there is a transition from a network of connected capillary bridges (the so-called *funicular* regime) to an unconnected network of bridges (the *pendular* regime). In the pendular regime, capillary flow will cease, and moisture is transported only through the diffusion of water vapor [74]. It is at this point that drying becomes nonuniform, and a drying front begins to intrude into the sample.

Normally the pendular regime would occur only at a very low water concentration. It can be shown that for a random packing of spheres, for example, the pendular regime begins at 13.6% of the saturated water concentration [26]. However, in the case of starch the presence of a reservoir of water within the starch grains increases the critical moisture

concentration of the transition between regimes. If $\phi_g = 0.26 \pm 0.01$ and $\phi_p = 0.30 \pm 0.01$, then the pendular regime should begin at approximately $\phi_g + 0.136\phi_p = 0.30 \pm 0.01$. This corresponds precisely with the initiation of nonuniform drying at $C = 0.30$ g/cm^3.

Once formed, the pendular water bridges give the partially dried starch-cake much of its cohesiveness, but also act to pull the starch grains together. During this final phase of drying, a total strain of up to 10% develops, which is equivalent to putting the sample under a uniform bi-axial tension of up to 160 MPa. This stress leads directly to the creation of columnar joints, as a fracture front forms that is linked to the drying front.

There is little evidence to distinguish whether the drying stresses are fully developed early into the nonuniform drying phase, or if the stress generation is spread out evenly over a wide range of C. If the water in capillary bridges is in equilibrium with the water within starch grains, then the capillary bridge radius will only slowly decrease as the grains dry out. The fracture front is apparently fixed at $C_f = 0.2$ g/cm^3, which indicates that the tensile stress must still be increasing at this water concentration. However, the stress required to break the capillary bridges cannot exceed their maximum capillary pressure of approximately 120 MPa. It has been shown in experiments on drying colloidal silica that fracture growth can be considered to be caused by the failure of water bridges between grains [23], and it seems likely that this is the case in starch as well. It is not unreasonable to suggest, therefore, that the great majority of strain develops between C=0.3 and C=0.2 g/cm^3.

The full details of the desiccation of starch, and the transport dynamics of water within a drying starch-cake, are complex processes, and have only partially been resolved here. However, the above description provides enough detail to develop tools to aid in the analysis of other experimental data on the scaling and ordering of columnar joints. It is also sufficient to identify the main drying forces, and to quantify the mechanisms and flow of liquid and vapor water within a drying starch-cake. These results may be of broad applicability to the behavior of other drying colloidal systems.

2.3 Fracture measurement methods

2.3.1 Measuring the cross-sectional area

The cross-sectional areas of columnar joints were analyzed manually in early experiments. Images of cracks were individually traced over, by hand, using Scion Image software. This software then allowed the semi-automatic measurement of certain properties of the traced crack networks, including the cross-sectional areas, perimeter lengths, and numbers of

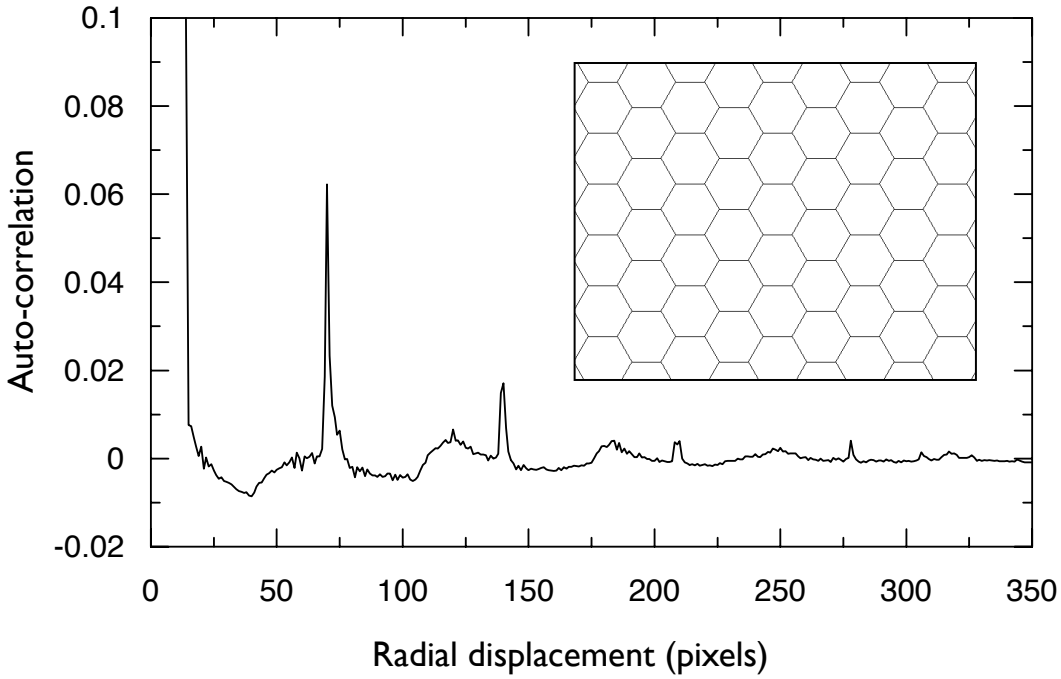

Figure 2.16: The radial auto-correlation function of a regular hexagonal network with edge lengths of 40 pixels each (shown in inset) has peaks at a radius of 70 pixels and its harmonics.

neighbors of columns, and the joint angles and lengths of edges, to be made. However, this method is exceedingly time consuming, as approximately 200-300 columns were traced in each image, in order to achieve a reasonable statistical average. Since over fifty desiccation experiments were run, and most were dissected to reveal at least 10 cross-sectional slices per sample, this method could not be reasonably applied to most of the experiments reported on in this thesis.

A fully automated method was developed to quickly measure the crack spacing of a fracture pattern. The autocorrelation function, a, of a data set $g(\mathbf{x})$ shows how related a data point is to points at some distance $\mathbf{x}'$ from it:

$$a(\mathbf{x}') = \frac{\langle g(\mathbf{x})g(\mathbf{x}+\mathbf{x}')\rangle - \langle g(\mathbf{x})\rangle^2}{\langle g(\mathbf{x})g(\mathbf{x})\rangle - \langle g(\mathbf{x})\rangle^2}, \tag{2.12}$$

where angled brackets represent averaging over all available data. Calculating a from Equation 2.12 is inefficient, however the auto-correlation function is also the fourier transform partner of the power spectrum of $g(\mathbf{x})$ - $\langle g(\mathbf{x})\rangle$. The power spectrum and its inverse fourier transform *can* be efficiently calculated, by fast fourier transform.

To find the crack spacing using auto-correlation methods, a rectangular selection is first cropped from an image of columnar joints in cross-section. The bitmap image

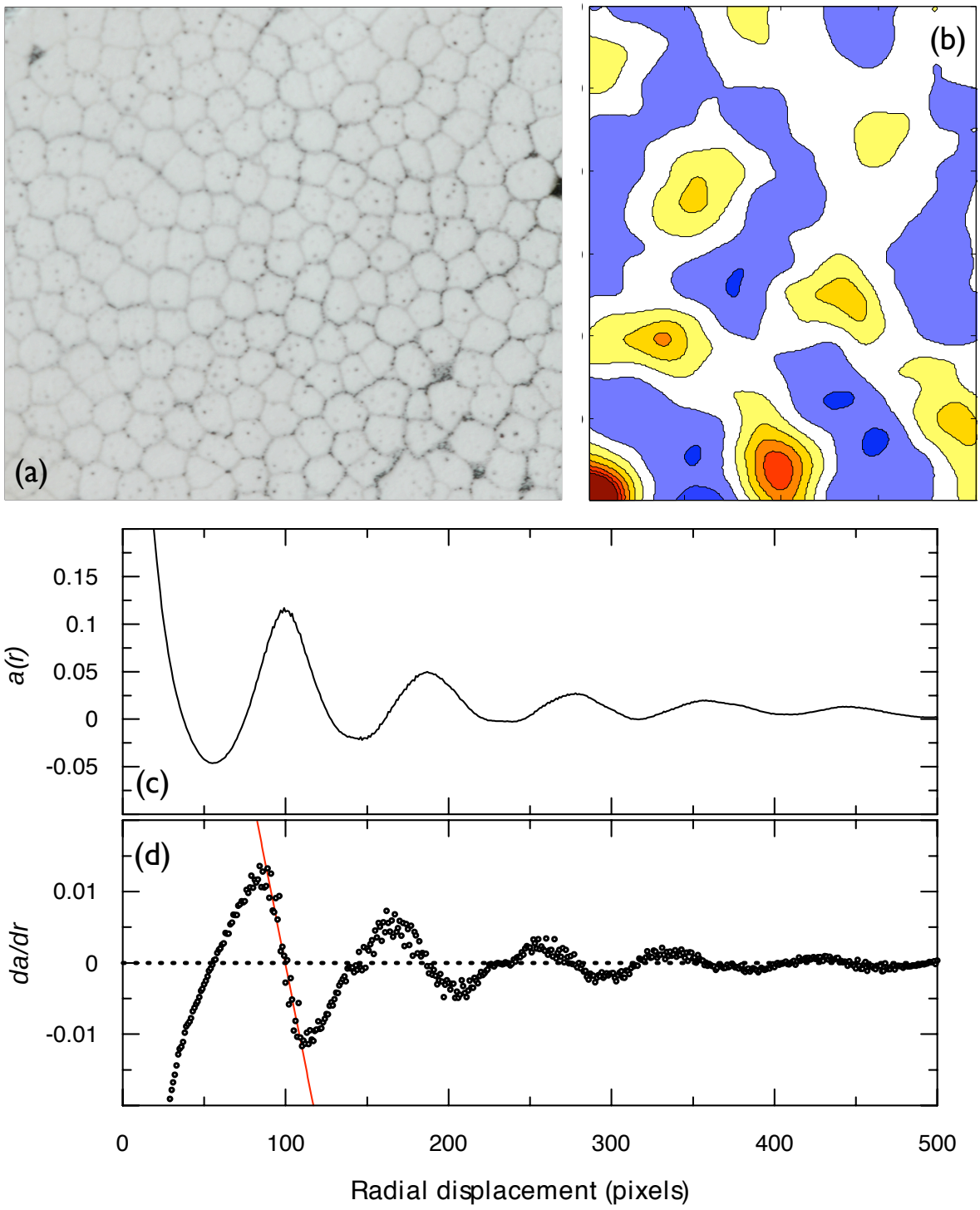

Figure 2.17: Auto-correlation methods applied to image data. (a) Example input cross-sectional image of starch columns. (b) The 2D auto-correlation function of the image in (a), near the origin (200×300 pixels are shown, with the origin at the bottom left corner), showing positive correlation in yellow and red, and negative correlation in blue. (c) The radial auto-correlation function $a(r)$ computed for the input image, and (d) its derivative da/dr. In (d) a dashed line shows the zero-axis, and a red line displays how the intercept is found.

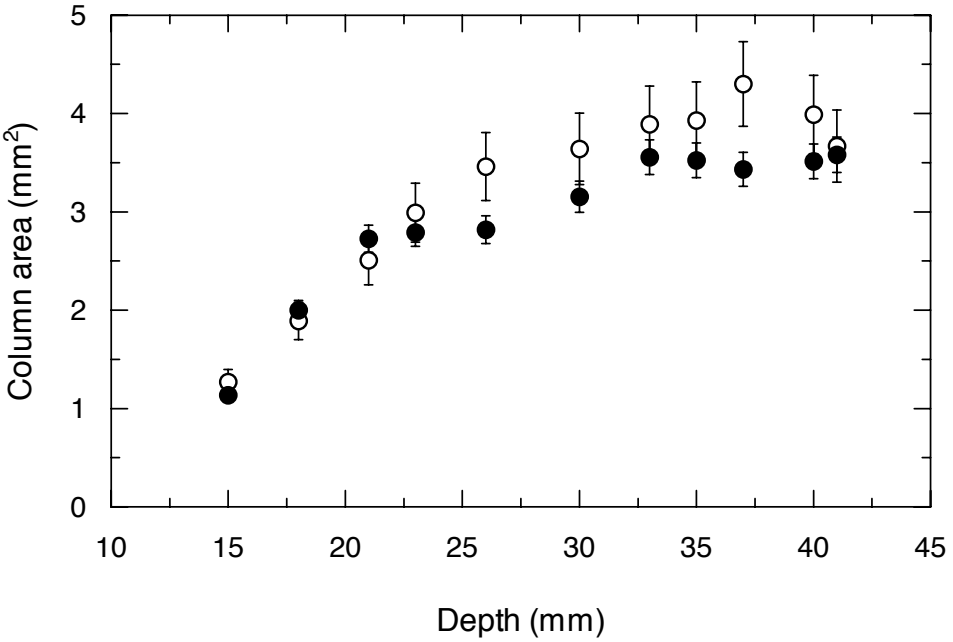

Figure 2.18: A comparison of the average cross-sectional area of columns using auto-correlation (filled circles) and direct tracing by hand (open circles) for a controlled starch experiment

is loaded into Matlab, averaged across all three color channels, and the mean value is subtracted. To avoid boundary effects in the fourier transform the image is then windowed with a cosine bell window,

$$g'(\mathbf{x}) = \frac{1}{4} g(\mathbf{x})(1 - \cos\frac{2\pi x}{x_{max}})(1 - \cos\frac{2\pi y}{y_{max}}), \tag{2.13}$$

where $x \in (0, x_{max})$ and $y \in (0, y_{max})$ are the orthogonal components of $\mathbf{x}$, and cover the entire image. The auto-correlation function is then computed as the inverse fourier transform of the power spectrum (the absolute value of the fourier transform squared) of the windowed data. Finally, the results are averaged over the azimuthal direction to obtain the radial auto-correlation function $a(r)$. The first non-trivial peak of $a(r)$ corresponds to the average distance between parallel cracks. Matlab code which implements this method is included in Appendix A.1.

Auto-correlation methods were tested on an artificial regular hexagonal network, as shown in Figure 2.16. The distance between the parallel edges of length $w = 40$ pixels is $2w\cos(30°) \simeq 69.34$ pixels in the test image. In order to test non-periodic data, the boundaries of this image are purposefully aperiodic. The calculated $a(r)$ has peaks at radius r=70, 140, 209, and 278 pixels, in excellent agreement with the expected peak

position and its harmonics.

Real data do not have peaks as sharp as those in Figure 2.16. In practice the crack spacing was found by calculating the numerical derivative of $a(r)$ and locating the first positive to negative zero-crossing, using Matlab's curve-fitting toolbox, as shown in Figure 2.17. If the first zero crossing is obscured by noise, the second or third positive to negative zero-crossing can also be used. To convert the average distance between parallel cracks, l_c, into an average column cross-sectional area A, it is assumed that

$$A = \frac{5(l_c)^2}{4\sqrt{3}}, \tag{2.14}$$

which holds exactly for regular hexagons. This assumption is validated in Figure 2.18, which compares the cross-sectional areas found by manual tracing of cracks, and by auto-correlation methods.

2.3.2 From evaporation rate to fracture position and velocity

The results from Section 2.2 can be used to extract information about the location and velocity of the fracture front from measurements of the mass of a drying starch-cake. Measurements of the moisture concentration $C(z,t)$ showed that, during the formation of columnar joints, C took a constant value below the fracture front. In addition, above the fracture front, C is close to being self-similar, when it is scaled by the fracture depth, as shown in Figure 2.19(a,b). These two features of the moisture distribution can be captured by a simple model, with no free parameters, that accurately predicts the fracture position at any point in time, given only the sample mass at that time.

A Matlab function was written (see Appendix A.2) which accepts the mass record $m(t)$ of a drying starch-water mixture, and outputs the position χ of the fracture front at all times, and the velocity v of the fracture front at all positions. This method relies on knowing $C(z/\chi)$, the moisture concentration field that has been normalized to the depth of the fracture front, as shown in Figure 2.19(a). The normalized moisture concentration is integrated, and used to construct a lookup table that estimates χ for all measured $m(t)$, given the initial moisture concentration, sample thickness and dish diameter. The fracture front velocity $v(t) = \mathrm{d}\chi/\mathrm{dt}$ is then found by estimating the slope of half-hour records of $\chi(t)$ through a linear least squares fit. These measurements are then combined to solve for $v(z)$.

To test this function, measurements of C from the controlled experiment shown in Figure 2.9(b) were used to produce a lookup table for the mass record of the uncontrolled

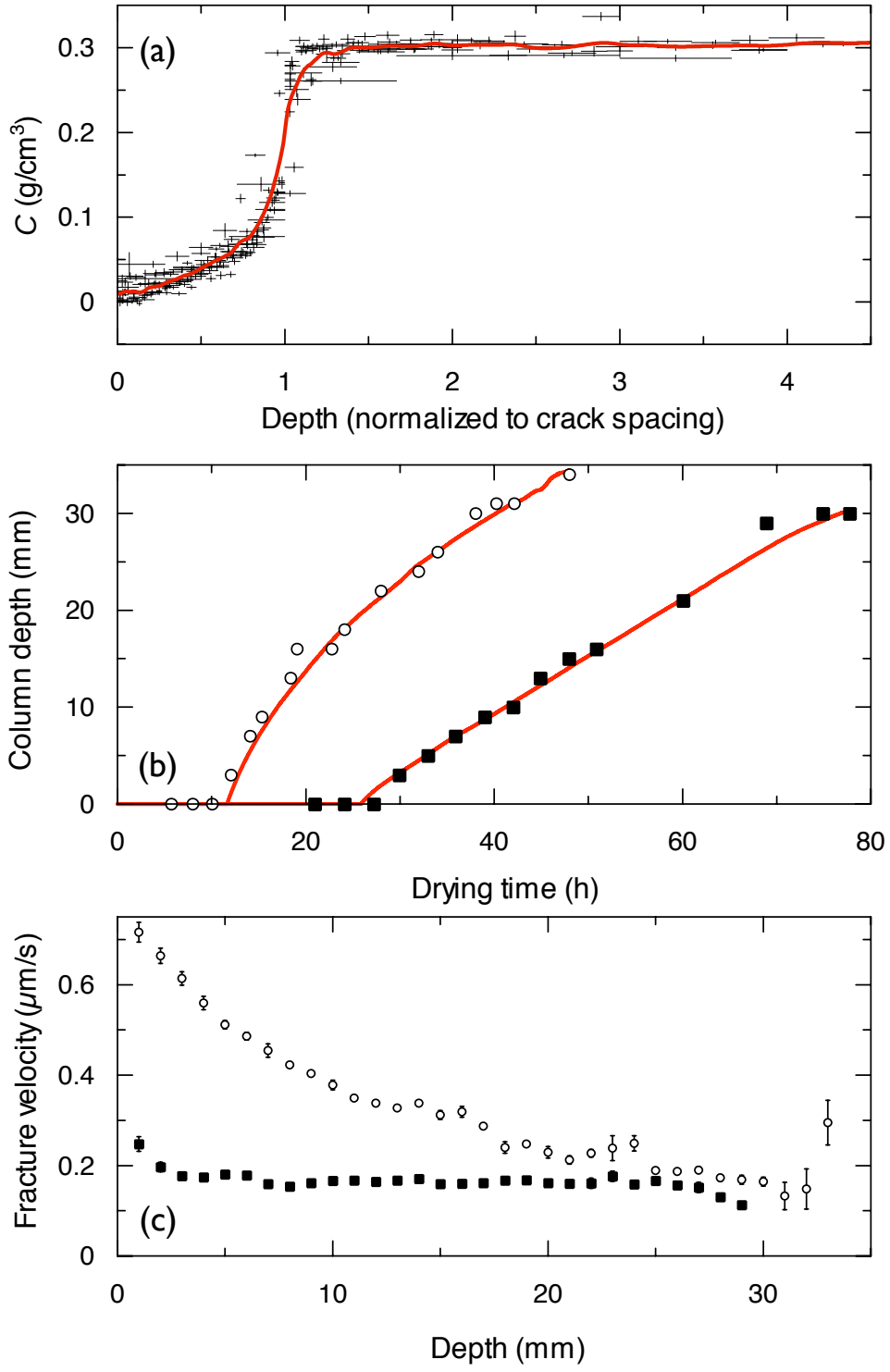

Figure 2.19: (a) water concentration data for uncontrolled experiments are shown, with the depth z normalized to the fracture front position χ. The red curve shows the same data set smoothed with a gaussian filter. (b) compares the measured fracture front position and the estimated fracture front position (red curves) for (open circles) uncontrolled and (filled squares) controlled experiments. (c) From these results the fracture front velocity $v(z)$ can be estimated.

evaporation experiment shown in Figure 2.8(a), and *vice versa*. The results are shown in Figure 2.19(b), and show good agreement between the measured and estimated fracture front position in both cases. The estimate of v in Figure 2.19(c) shows that for the uncontrolled experiment the fracture front slowed down uniformly through most of the experiment. For controlled evaporation, the estimated v agrees with the measured $v = 0.18$ μm/s through the middle three-quarters of the experiment.

In the following section χ and v will be calculated from an average $C(z/\chi)$ of the data from both controlled and uncontrolled experiments.

2.4 Scale selection of joints in corn starch

This section describes experiments which study how the scale of columnar joints is selected in desiccating starch slurries. This work is contained in References [29, 30, 31], save only for the results presented in Section 2.4.4. The first two experiments discussed in Section 2.4.1 (changing incident power, and adding gelatin) were conducted in collaboration with a visiting scientist, Zhenquan Lin.

2.4.1 Uncontrolled experiments

Changing incident light power

Several identical dishes of starch slurries were dried individually under one 250 W heat lamp without the use of feedback control. The lamp height was varied between experiments, and a photometer was used to measure the light intensity incident on the drying surface. This power is assumed to be proportional to the incident heat flux, and hence to the incident drying power. Samples 6.5 and 13 mm thick were studied, and the mean cross-sectional area of the columns was measured at the base of the dried slurry. Figure 2.20 shows the mean cross-sectional area of these samples as the lamp height was increased from 12 to 80 cm. Fast drying generally gave rise to smaller columns than slow drying. For shallow samples, an approximately inverse relationship between column area and lamp height was found. This is in agreement with Toramaru and Matsumoto [106], who observed, in similar experiments with potato starch, that the final cross-sectional area and the initial evaporation rate were inversely related. However, a strict inverse proportionality is only found for some of the data in the 6.5 mm thick samples. Otherwise, there is a weaker dependence of the cross-sectional area on the incident power.

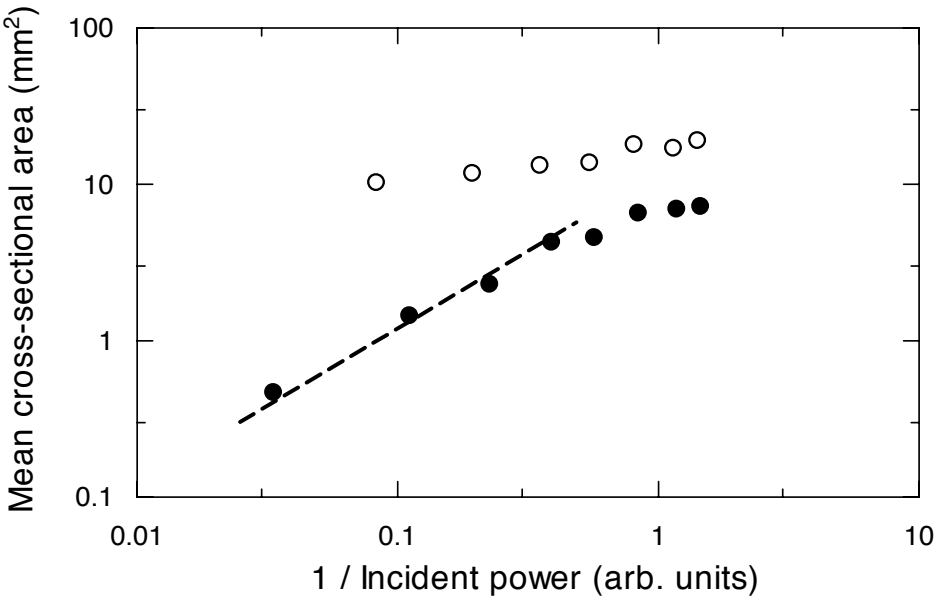

Figure 2.20: Average column cross-sectional area at the base of the colonnade for 13 mm (open circles) and 6.5 mm (filled circles) thick samples, dried under different lamp heights. The dashed line represents an inverse relationship between drying power and cross-sectional area.

Adding gelatin, and changing sample stiffness

The effects of adding gelatin to the initial slurry were investigated. Small amounts of gelatin (Knox brand) were first dissolved in boiling water, mixed with cold water, and then added to the slurry, which was allowed to set before the experiment began. The initial weights of water and starch were kept equal in these mixtures, but no bleach was added, as it tended to react with the gelatin.

These experiments were done in order to place some qualitative experimental constraints on ball-and-spring type models of columnar joint formation. Such discontinuum fracture models [51, 74, 101] are based on networks of linear springs with finite breaking strengths. Figure 2.21 shows that as gelatin is added, the average column cross-sectional area at the base of the starch-cake increases, all else being equal. This is what would be expected from discontinuum models, since the added gelatin enhances the effective Young's modulus and fracture toughness of the sample.

Drying samples do not age

To eliminate the possibility that exposure to modest heat changes the physical properties of starch over the course of a week-long experiment, six identical dishes of slurry were prepared and placed simultaneously under one heat lamp, and all but one were covered

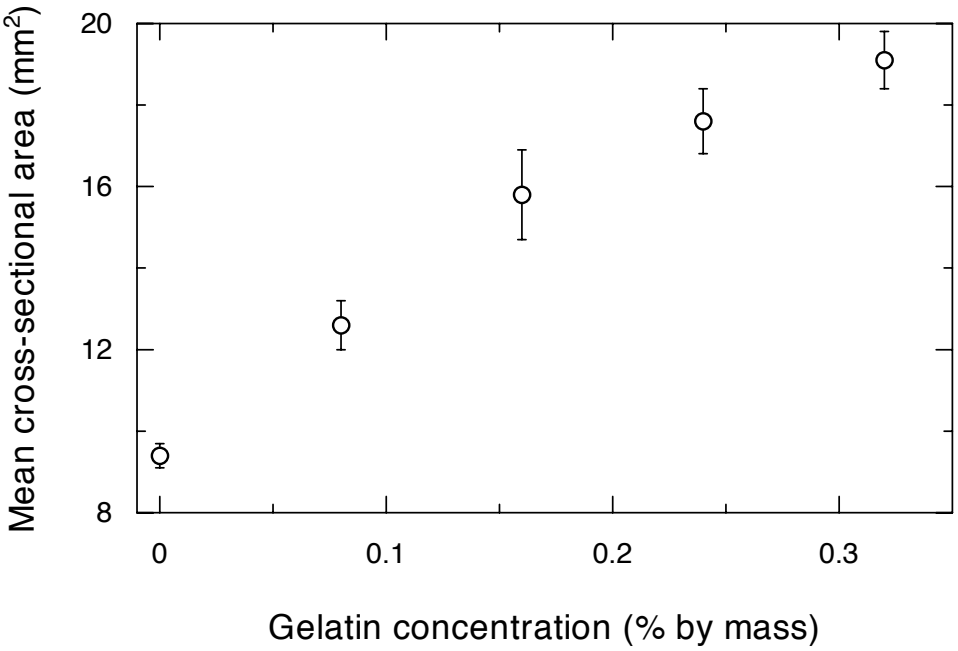

Figure 2.21: The average column cross-sectional area at the base of five 17 mm deep samples, dried slowly with a heat lamp 75 cm above. Gelatin concentrations are given relative to the initial mass of the slurry.

with Pyrex lids. The lid from one additional sample was removed each subsequent day. If there was any drift in starch properties, such as the long-term disassociation or polymerization of starch molecules, changes in the packing arrangement of the settled starch grains, or changes due to unanticipated biological activity, this experiment was designed to detect any changes that could affect the cross-sectional area of the resulting columnar joints. The cross-sectional areas at the base of all six samples were identical within error, and thus drying starch samples do not show aging effects.

This result is further supported by the rheological results presented in Section 2.2.6, and the permeability results presented in Section 2.2.7, both of which showed an absence of any drift in starch-water properties at reasonable experimental temperatures.

Coarsening of the column scale

During the course of uncontrolled experiments, the evaporation rate slows down and the fracture front velocity decreases, as the experiment progresses. In response, the column cross-sectional area is found to depend strongly on the depth at which it is measured, as shown in Figure 2.22(a). This 'coarsening' is achieved by discrete events: the merging of two or three adjacent columns into a larger column through the failure of a joint or vertex to propagate (further details of this process are given in Section 2.5). To study

coarsening an X-ray tomogram was made of a 2.5 cm thick uncontrolled experiment. A movie depiction of this image is available as an online supplement to Reference [29]. The volume-filling image was sampled in cross-section every 0.3 mm, and the cross-sectional images were analyzed by hand. This allowed precise measurements to be collected right up to the exposed drying surface. Further uncontrolled experiments were done in deeper samples and were studied through destructive sampling.

An additional data set was gathered by measuring the average cross-sectional area reached at the base of 17 identically prepared slurries dried under the same, relatively slow conditions, but with different initial thicknesses. These results show that the scale selection process in columnar jointing is highly repeatable, and that the errors in experimental repeatability are approximately $\pm 8\%$. The statistical uncertainty in each measurement is smaller than this, approximately $\pm 4\%$.

Figure 2.22(a) shows the evolution of the average column cross-sectional area as a function of the depth z, in the uncontrolled experiments just described. There is an approximate power-law coarsening of the average column area with z, with exponents in the range of 1.6 to 2.2, but this limited power law was never found to hold for more than about one decade of depth data. The fracture scale is limited by a fine surface crack pattern, which is well fit by adding a small constant term to a power law fit. The significance of this is unclear.

It is more insightful to consider the dependence of the fracture scale on the fracture front velocity. For several deep samples, the fracture spacing, here defined as the square root of the average column cross-sectional area, is inversely related to the average fracture velocity, as shown in Figure 2.22(b). However, this inverse relationship is not strict, as will be seen presently.

Scale jumps

One very suggestive way in which columns can coarsen is through sudden transitions in scale, which were only observed in deep (> 5 cm thick) starch-cakes dried in uncontrolled experiments. These transitions are relatively sharp discontinuities in the fracture pattern scale, and separate colonnades of very different scales, as shown in Figure 2.23(a). Interestingly, these jumps occur despite the fact that the evaporation rate is smoothly decreasing in these experiments. Within the transition region, the fracture pattern shows increased disorder, as shown in Figure 2.23(b), by a jump in the variance (standard deviation divided by the mean) of the column cross-sectional area. The transition regions are zones with a greatly enhanced column merger rate, an effect which would naturally

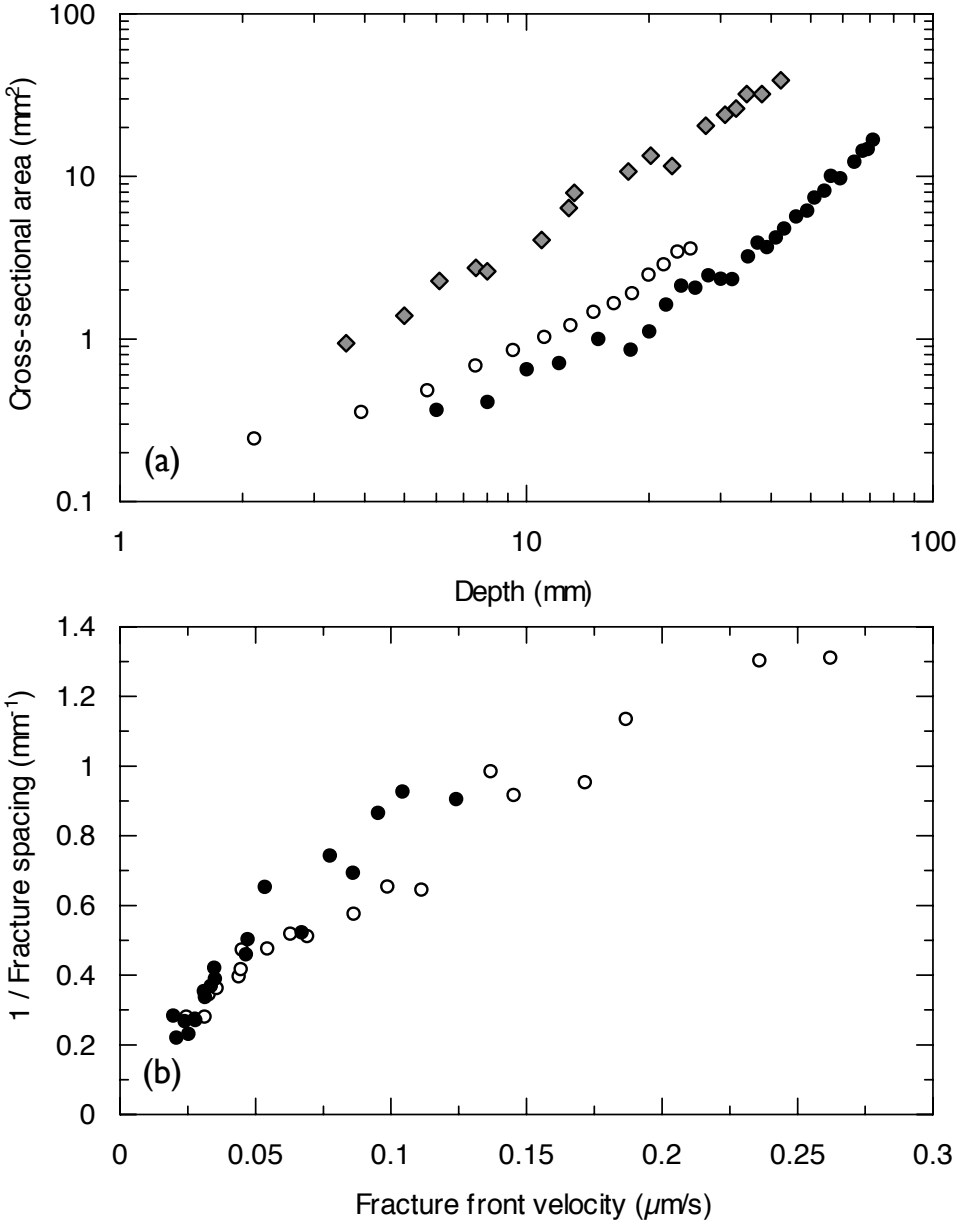

Figure 2.22: Scale selection and coarsening in uncontrolled drying experiments. (a) The average cross-sectional area evolves with depth, increasing in a power-law-like way. Grey diamonds show the area reached at the base of a series of identically prepared starch-cakes, dried slowly, with a variety of different initial thicknesses. Micro-CT X-ray observations on a more quickly dried sample (open circles) coarsen from a limiting column area near the drying surface. The filled circles show coarsening in a thick, rapidly dried sample. (b) shows how the fracture spacing evolves with the fracture front velocity for two (6 and 8 cm) thick samples.

increase the width of the distribution of the average column area during the transition. However, some strong ordering process acts to efficiently return the value of relative variation in area to its pre-transition value within one data point (2 mm) of the end of the transition. This ordering behavior will be discussed in more detail in Section 2.5.

Jumps in scale were found to be highly repeatable, and not dependent on the absolute depth of the sample. For example, two otherwise identical experiments on 7.5 and 5.5 cm thick slurries were performed, and it was found that the position of a jump in columnar scales, as shown in Figure 2.23 for the thicker experiment, occurred at the same depth in both cases.

Transitions in pattern scale appear to be a the result of a natural instability of columnar jointing. This may be related to a similar period-doubling instability that has been proposed to act on the spacing of crack tips in 2D directional drying [7].

2.4.2 Partially controlled experiments

The experiments just described show that even the simplest level of control – that of changing the lamp position or the sample rheology – has some reproducible effect on the average column size. The columnar length scale continues to increase in the interior of the starch-cakes, however. This coarsening is linked to the slowing down of the fracture front during uncontrolled desiccation, as was shown in Figure 2.22.

To study the scaling behavior of starch columns under steady-state conditions, a simple form of automated feedback was developed which fixed the final evaporation rate to a desired value Q_0. In this partially controlled scenario, the overhead lamps were given an initial duty cycle of 0.5, and a feedback loop was switched on when Q dropped naturally to Q_0. The feedback loop then maintained $Q = Q_0$ through the rest of the experiment, as was shown in Figure 2.3(c-d). In all cases, after an initial transient, the drying front moves at a constant speed, and the coarsening of the pattern is almost entirely halted. The transient coarsening is indistinguishable from that observed with uncontrolled experimental conditions.

Figure 2.24(a) shows the results of varying Q_0 from 0.9 to 1.5 g/h in 60 mm radius dishes. It also includes one experiment where $Q_0 = 0.7$ g/h, but which was accidently given an initial duty cycle of 0.25, instead of 0.5. The results of these experiments are rather surprising. All four samples dried under the same initial conditions, but with four different final desiccation rates, had average column areas that were indistinguishable within errors. The sample that was initiated differently, but subject to the same type of feedback control, selected a column cross-sectional area that was considerably larger.

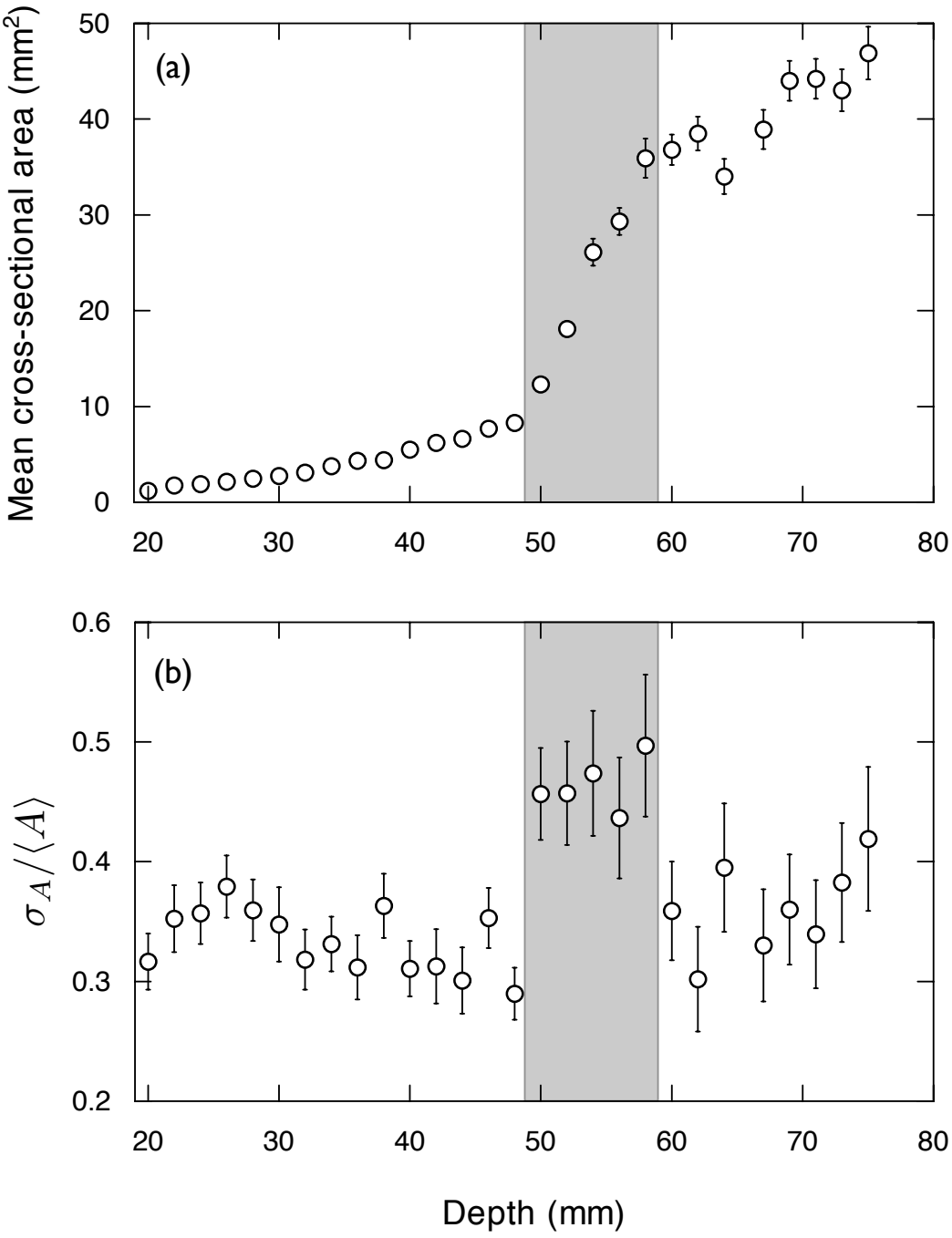

Figure 2.23: An abrupt change in the column scale observed in a deep uncontrolled sample. (a) This transition (shaded region) is a sharp discontinuity in the cross-sectional area, and is associated with (b) an increase in pattern disorder, as measured by the variance (standard deviation divided by the mean) of the cross-sectional area.

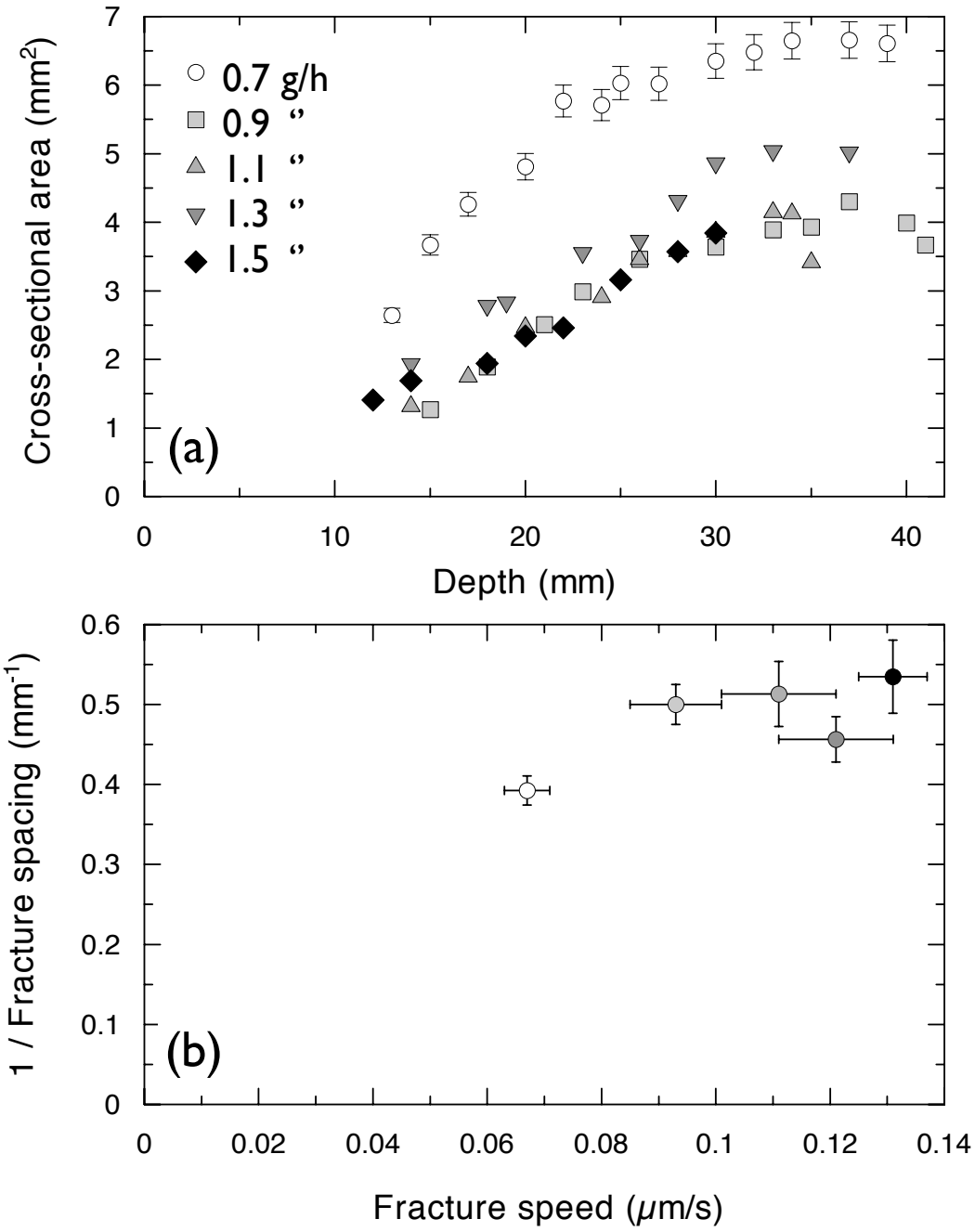

Figure 2.24: Coarsening halts when the evaporation rate is held constant. (a) shows the average column cross-sectional area measured at different depths in a series of partially controlled experiments, where the final evaporation rate is given in the legend. The initial duty cycle of the 0.7 g/h sample is half that of the other samples. Representative statistical errors are shown on one data set. (b) shows how most of the data cluster loosely, with one exception.

Figure 2.24(b) shows these data where the fracture speed has been extracted from mass data, as described in Section 2.3.2. The slowest drying sample ($Q_0 = 0.7$ g/h) is an outlier from the remaining data.

These puzzling observations suggest that the final evaporation rate Q_0 is not the only important parameter in selecting a scale, but that the path that the evaporation rate takes to Q_0 is also important in selecting that scale. In other words, the pattern selection process is hysteretic, and dependent on the early stages of drying.

2.4.3 Fully controlled experiments

Since hysteresis effects became apparent in the scale selection process of columnar jointing, a more rigorous control cycle was developed, as was described in Section 2.1.3, and Figure 2.3(e-f). In these fully controlled experiments, the evaporation rate was prescribed throughout the entire desiccation. A test of this method of drying was made by varying the control parameters Q_1, Q_2, and $\dot{Q}$ individually, as shown in Figure 2.25. For two of these data sets (shown as open triangles), coarsening is eventually halted and a final scale is selected. In these two cases the experiments both have the same final evaporation rate, Q_2, but differ in the selected average cross-sectional area by about a factor of 2. This demonstrates that even given the same evaporation rate, columnar jointing can choose scales that vary considerably, depending on the drying history. In the other two experiments, the samples are too thin to allow the cross-sectional area to stabilize.

By systematically varying Q_2, with all other parameters remaining fixed, the response of the average column cross-sectional area A to a family of constant evaporation rates was measured. All these experiments were performed in 60 mm radius pyrex dishes, with an initial starch slurry mass of 600 g. Tests were done for $Q_1 = 8$ g/h, $\dot{Q} = 0.36$ g/h^2 and 0.5 g/h $< Q_2 <$ 1.70 g/h and for $Q_1 = 6$ g/h, $\dot{Q} = 0.5$ g/h^2 and 0.5 g/h $< Q_2 <$ 1.75 g/h. The $Q_1 = 8$ g/h experiments had an initial fracture front velocity v that was significantly faster than in the $Q_1 = 6$ g/h experiments, as shown in Figure 2.26. Furthermore, the $Q_1 = 8$ g/h experiments maintained a high v for longer than the $Q_1 = 6$ g/h experiments did. These two experimental conditions will therefore be referred to as 'fast' and 'slow' initiation, respectively. In all experiments, a constant value of A is typically selected by about the mid-depth of the starch-cake, as is shown in Figure 2.25(b).

An additional series of tests was done using $Q_2 = 1$ g/h, where Q_1 and $\dot{Q}$ were varied, in order to study the range of final pattern scales that could be achieved through hysteretic effects.

Figure 2.27 shows the average A that is selected in the lower depths of both the 'fast'

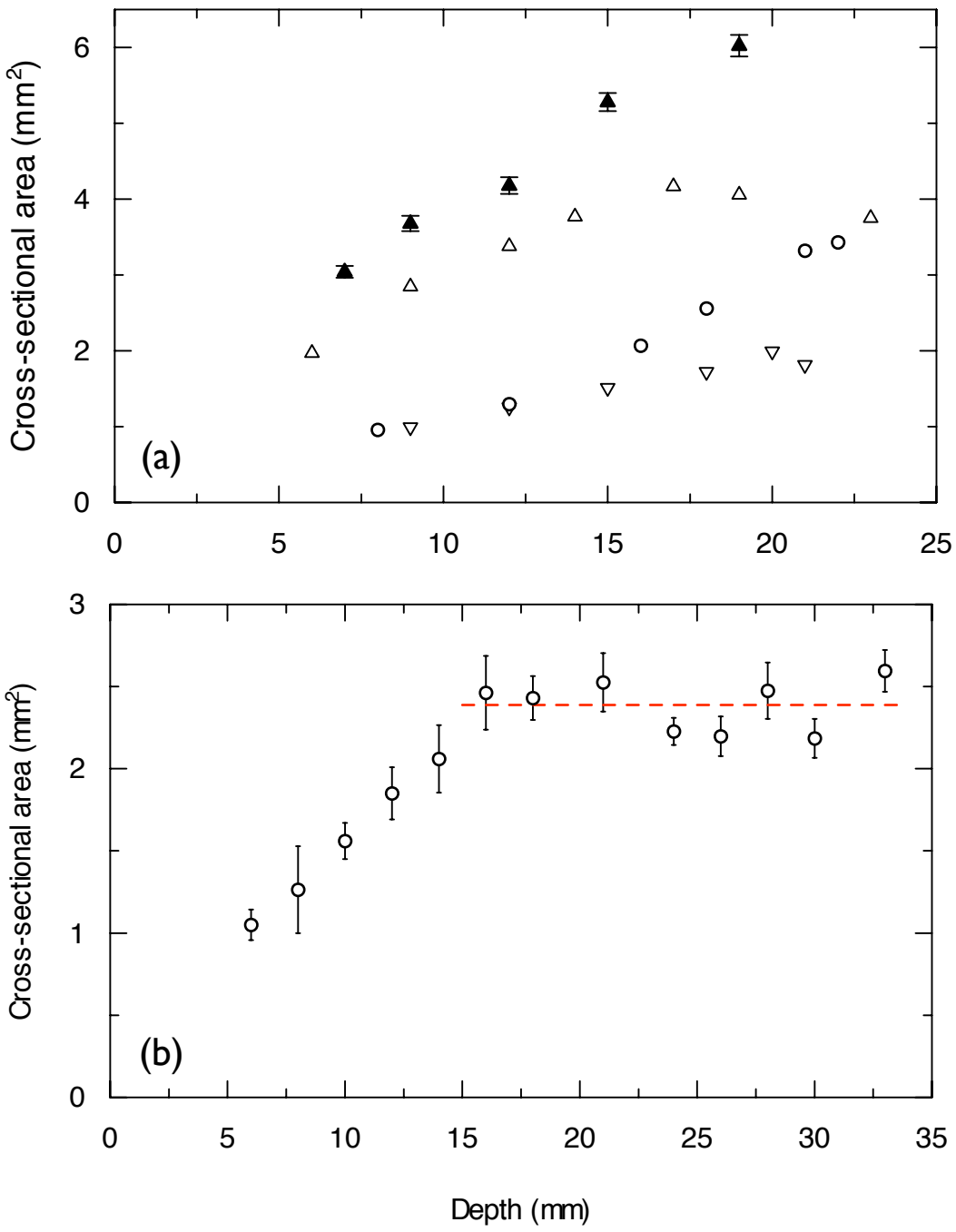

Figure 2.25: Coarsening is halted in controlled drying experiments. (a) The open triangles show the area A for a trial where $Q_1 = 6$ g/h, $Q_2 = 1$ g/h, and $\dot{Q} = 0.5$ g/h^2. Other runs are identical but instead use $Q_1 = 9$ g/h (inverted triangles), $Q_2 = 0.75$ g/h (filled triangles), or $\dot{Q} = 0.25$ (open circles). Representative errors are shown on one data set. (b) shows how A reaches a constant value by the center of a typical starch-cake dried under controlled conditions. An average of the final few data points is used to estimate the fracture scale that is selected, as shown by a dashed line.

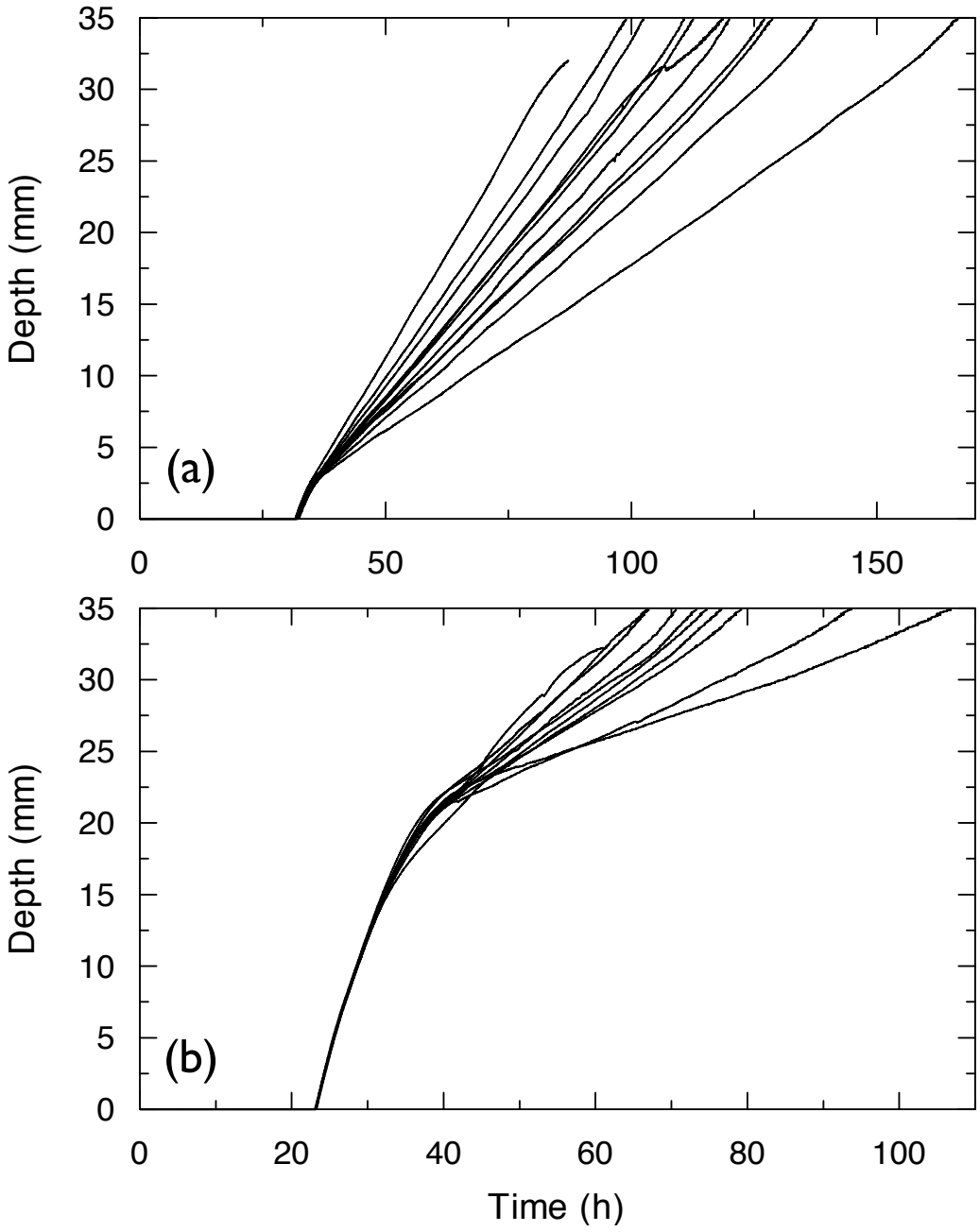

Figure 2.26: The fracture front position χ is shown for two series of fully controlled experiments: (a) the 'slow' initial conditions of $Q_1 = 6$ g/h, $\dot{Q} = 0.5$ g/h^2 and (b) the 'fast' initial conditions of $Q_1 = 8$ g/h, $\dot{Q} = 0.36$ g/h^2. Individual curves indicate separate experiments performed in range of $Q_2 = 0.5$ to 1.75 g/h.

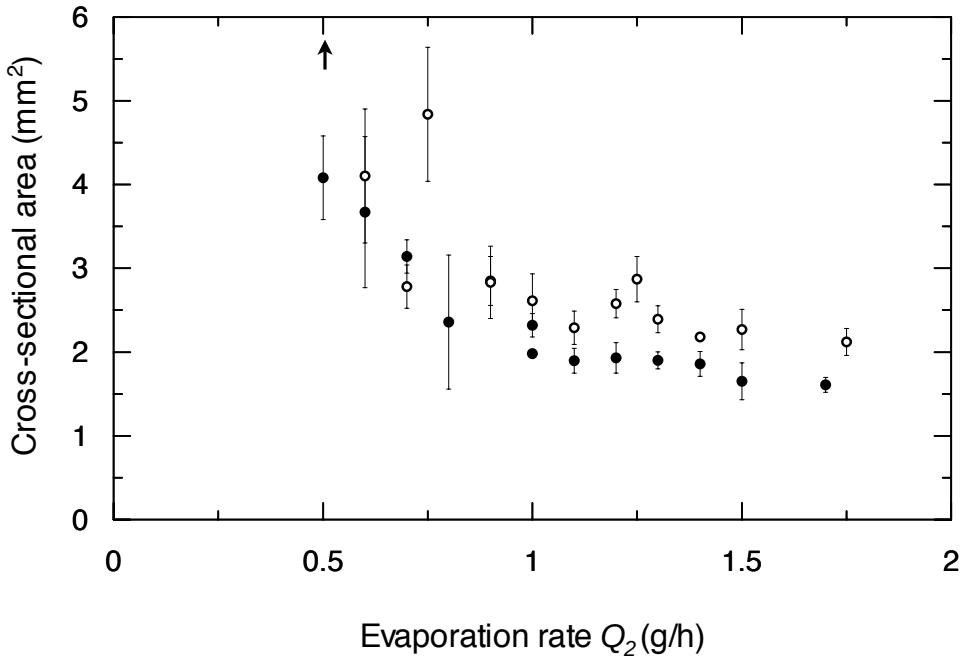

Figure 2.27: The average cross-sectional areas A attained by columnar joints in both the (open circles) 'slow' and (closed circles) 'fast' initiation type of fully controlled experiments are shown. An additional open circle data point at $Q_2 = 0.5$ and $A = 13.6 \pm 0.8$ mm^2 is indicated by an arrow.

and 'slow' initiation type experiments. As with the uncontrolled experiments, there is evidence here that slower moving fracture fronts display larger columns. Since the range of evaporation rates that can be explored by these experiments is much smaller than can be achieved in uncontrolled experiments, this correlation is not as dramatic as was shown in Figure 2.22. However, here this effect is noticeably enhanced by hysteresis: in general, for the same Q_2, the 'slow' experiment resulted in a pattern scale that was slightly larger than in the equivalent 'fast' experiment.

As shown in Figure 2.28, by comparing the measured v to the controlled volumetric water flux $J = q_2/\rho_w$, it can be confirmed that experimental control does in fact fix the velocity of the fracture front reliably. The ratio of J to v should correspond to the porosity of the sample that is opened up during the inhomogeneous drying phase (*i.e.* the difference between the limiting volumetric water concentrations below and above the drying front). It was suggested in Section 2.2.3 that this porosity is almost entirely due to pores within individual starch grains, and should correspond to ϕ_g. A best fit line included in Figure 2.28 gives $\phi_g = 26 \pm 1\%$.

Figure 2.29 shows a summary of all controlled experiments, expressed in terms of the inverse fracture spacing $(1/\sqrt{A})$ and the fracture front velocity v. The results are

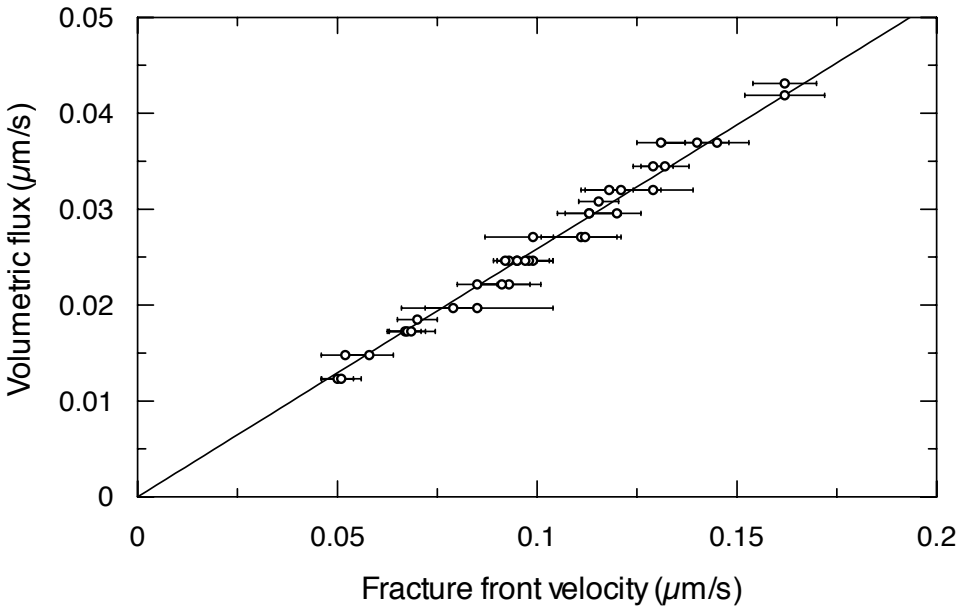

Figure 2.28: A comparison of controlled volumetric water flux $J = q_2/\rho_w$ to the observed final fracture front velocity v, in controlled experiments. The best fit line shown gives the ratio $J/v = 0.26 \pm 0.01$.

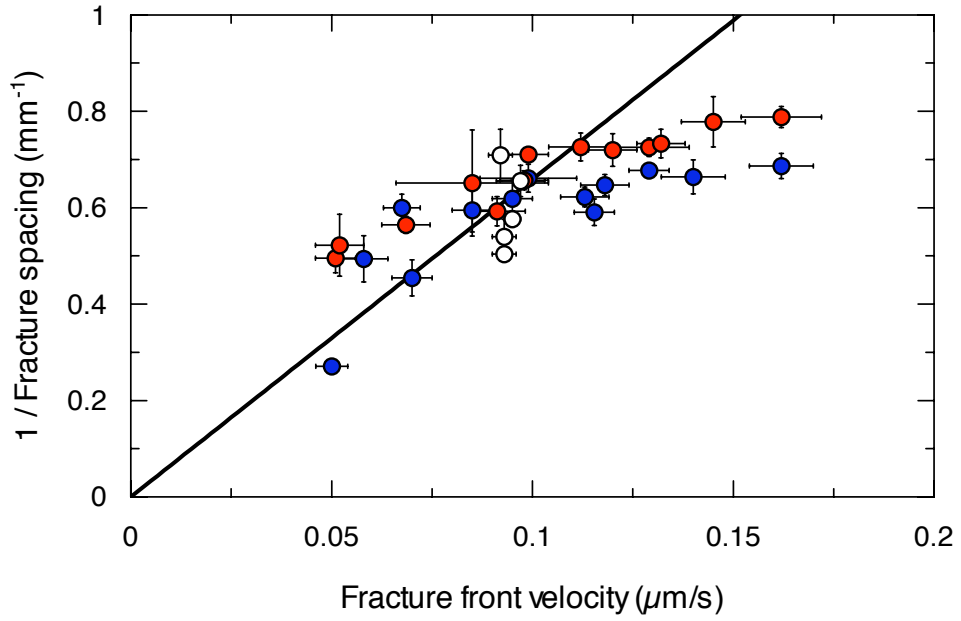

Figure 2.29: Selection of a final fracture scale $L = 1/\sqrt{A}$ occurs during controlled experiments. Red circles correspond to a 'fast' initiation, whereas blue circles correspond to a 'slow' initiation. Open circles show experiments with a desired $Q_2 = 1$ g/h. All points represent a fit to several observed cross-sections in the lower part of a colonnade, as demonstrated in Figure 2.25. A solid line marks the best-fit linear relationship found for uncontrolled experiments, from the data presented in Figure 2.22(b).

generally consistent with a fracture length scale $L = \sqrt{A}$ that is inversely related to v, as was suggested in Section 2.4.1. However, the 'slow' initiation experiments are, in 11 out of 12 comparable cases, about 25% larger in final cross-sectional area than the equivalent 'fast' initiation experiments, confirming that there is some hysteresis in the scale selection process. Further, the data flatten out for fracture front velocities greater than approximately 0.1 μm. This behavior is also likely the result of hysteresis in the scale selection mechanism, and shows that some fracture spacings are stable over a wide range of fracture front velocities. Conversely, the range of tests done at $Q_2 = 1$ g/h show that any scale within a range of 1.25 to 2 mm can be selected at this particular evaporation rate.

2.4.4 Stepped controlled experiments

A small number of exploratory experiments with evaporation profiles that were similar to the fully controlled type of experiment just discussed, but with a step in evaporation rate introduced into the Q_2 phase of drying, were performed. These were done in analogy with directional drying experiments done on a substrate that induced a step-like change in film thickness partway through the experiment [97].

The results of three stepped experiments are shown in Figure 2.30. One case (Figure 2.30(a)) shows the results of a sudden increase in Q_2. After this occurs the pattern responds by adding new cells to the developing fracture network, decreasing the length scale of the pattern. Two other cases show the results of decreasing steps in the evaporation rate. In one case there is no change in A, while in the other there is an increase in the average column area. This demonstrates that once a pattern scale is selected, it is robust to small changes in the evaporation rate, but not to large ones. Put another way, this shows explicitly that a particular length scale can be stable over a finite window of conditions.

2.5 Pattern selection

Three ways have been discussed in which the average column area, A, can evolve: A can smoothly increase with depth (*i.e.* coarsen), smoothly decrease with depth, or can change scale catastrophically. Alternatively, A can settle to some constant 'selected' value. However, this list only describes the behavior of the *average* column cross-sectional area. To study the dynamics underlying all these processes, the evolution of single columns in 3D X-ray Micro-CT images of dried starch-cakes was examined. This method

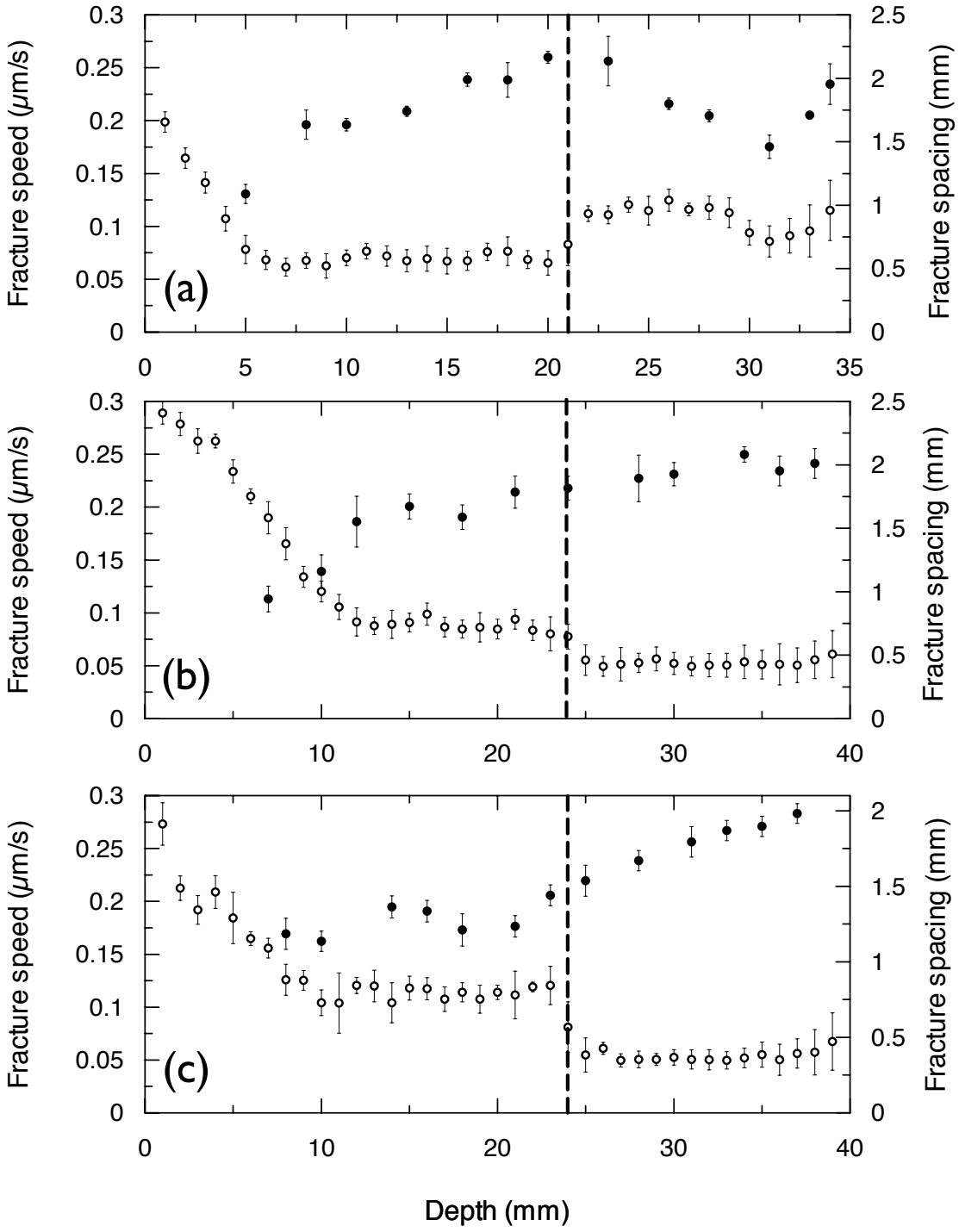

Figure 2.30: Scale selection in stepped evaporation experiments. The fracture front speed (open circles, left axis) and the fracture spacing (filled circles, right axis) are shown in three step experiments. During the final drying phase the evaporation rate is stepped from (a) 0.75 to 1.25 g/h, (b) 1 to 0.5 g/h and (c) 1.25 to 0.5 g/h, at the depth indicated by the dashed lines.

was described in Section 2.1.4, and a cross-sectional image of one tomogram image is given in Figure 2.4. Movies showing the evolution of the columnar crack pattern in these 3D images are published as online supplements (EPAPS Document No. E-PLEEE8-74-115609) to Reference [29]. A series of sequential cross-sections are also shown in Figure 2.31(b).

Viewed in detail by X-ray tomography, the upper drying surface of a starch-cake is covered with a fine network of disordered fractures. As they intrude into the sample these cracks are highly mobile, and develop in a manner somewhat suggestive of the evolution of a dry 2D foam. Crack edges move around with motion that seems almost random, but which tends to equalize the cross-sectional areas of neighboring columns. Adjacent columns often merge together when a common edge or vertex fails to propagate, which can lead to a gradual increase in the average cross-sectional area of the pattern. New columns are also occasionally created at existing vertices, but no columns were ever seen to vanish by constricting into a vertex.

Figure 2.32 shows the individual cross-sectional areas of a few representative columns. As was previously noticed, coarsening occurs through the termination of joints as they intrude into a sample, resulting in the merger of two or three columns. When columns merged, occurrences marked by solid arrows in Figure 2.32, the combined offspring column was tracked deeper into the starch-cake. Immediately after a merger event the offspring column rapidly shrinks, giving up area to its now smaller neighbors. A column that is spawned from a vertex also influences its neighbors, growing at their expense. In most cases, such a new column quickly merges with one if its neighbors. In Figure 2.32(c) the dashed arrow indicates the creation of a new column at a vertex adjacent to the one studied. When this occurs, the observed column shrinks as its new neighbor grows, until the two columns merge at the next solid arrow. In some cases, however, a new column survives and grows to average size. An example of this is also shown in Figure 2.32(c). In general, changes in an individual column's area appear to involve purely local processes, affected by and affecting its immediate neighbors only.

These dynamics again suggest a connection to a 2D dry foam. The pressure in a bubble confined to a 2D plane is inversely related to its cross-sectional area – small bubbles will push with a high osmotic pressure on the walls of neighboring larger bubbles [111]. This asymmetry leads to an enhanced migration of gas from small bubbles to large ones *via* diffusion. As large bubbles grow at the expense of their smaller neighbors, the system coarsens.

The case is exactly the reverse in columnar joints. Existing cracks release stress in their vicinity, and active cracks advance in the direction that maximizes this stress

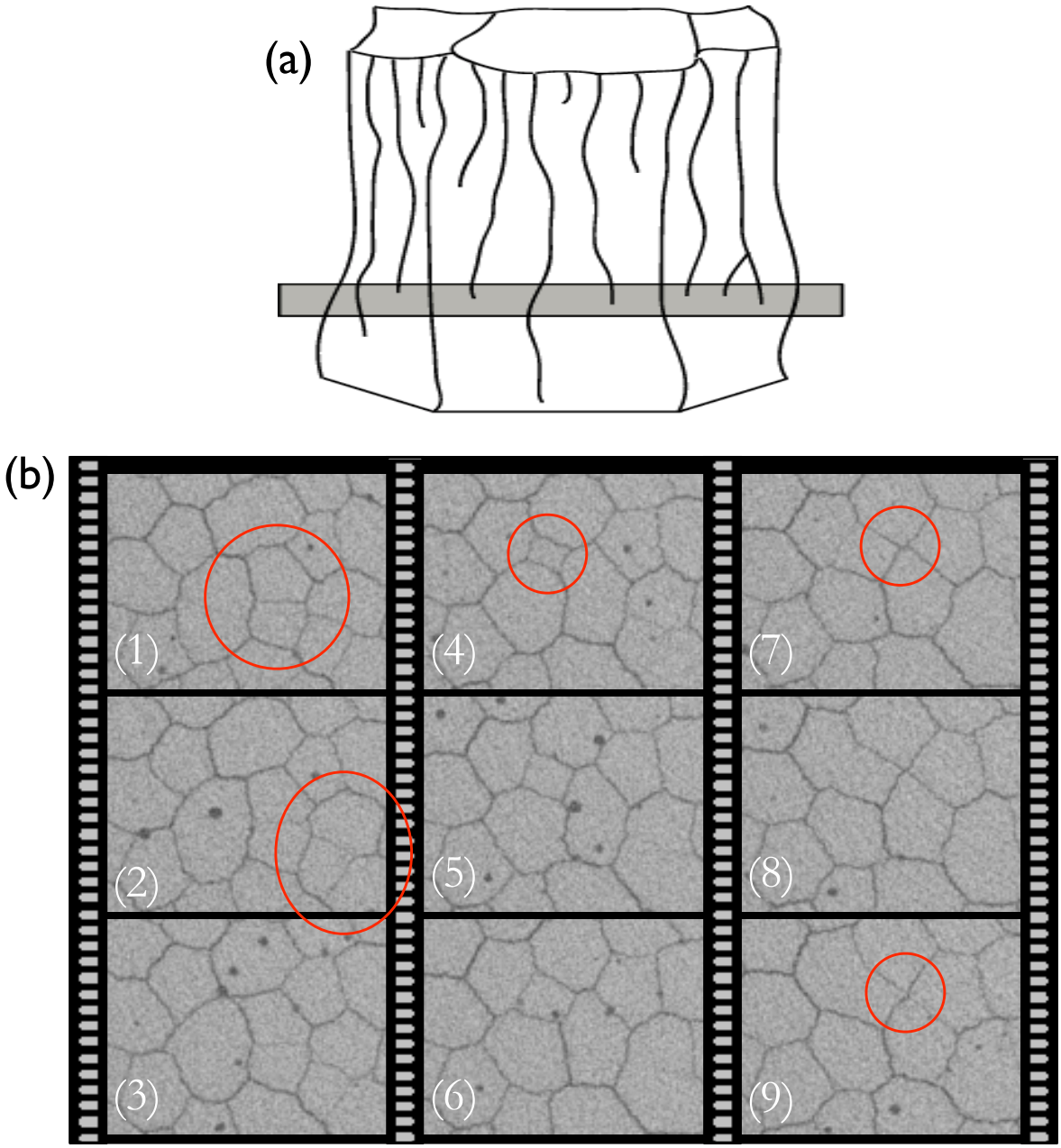

Figure 2.31: Coarsening processes observed in an uncontrolled sample. (a) sketches the essential features of coarsening: fracture termination, the motility of crack edges, and the creation of new columns from existing vertices. The grey region shows how cross-sections are sampled from a 3D image. (b) shows 4.5×3.5 mm^2 panels taken from a 3D image, at depths increasing by 360 μm per panel, beginning at $z = 10.0$ mm. Column mergers occur between the two columns near the center of panel 1, and between the three columns in the lower right corner of panel 2. Column initiation occurs at a vertex near the center of the images, between panels 3 and 4. A T1 event occurs between panels 7 and 9. All these features are indicated by red circles.

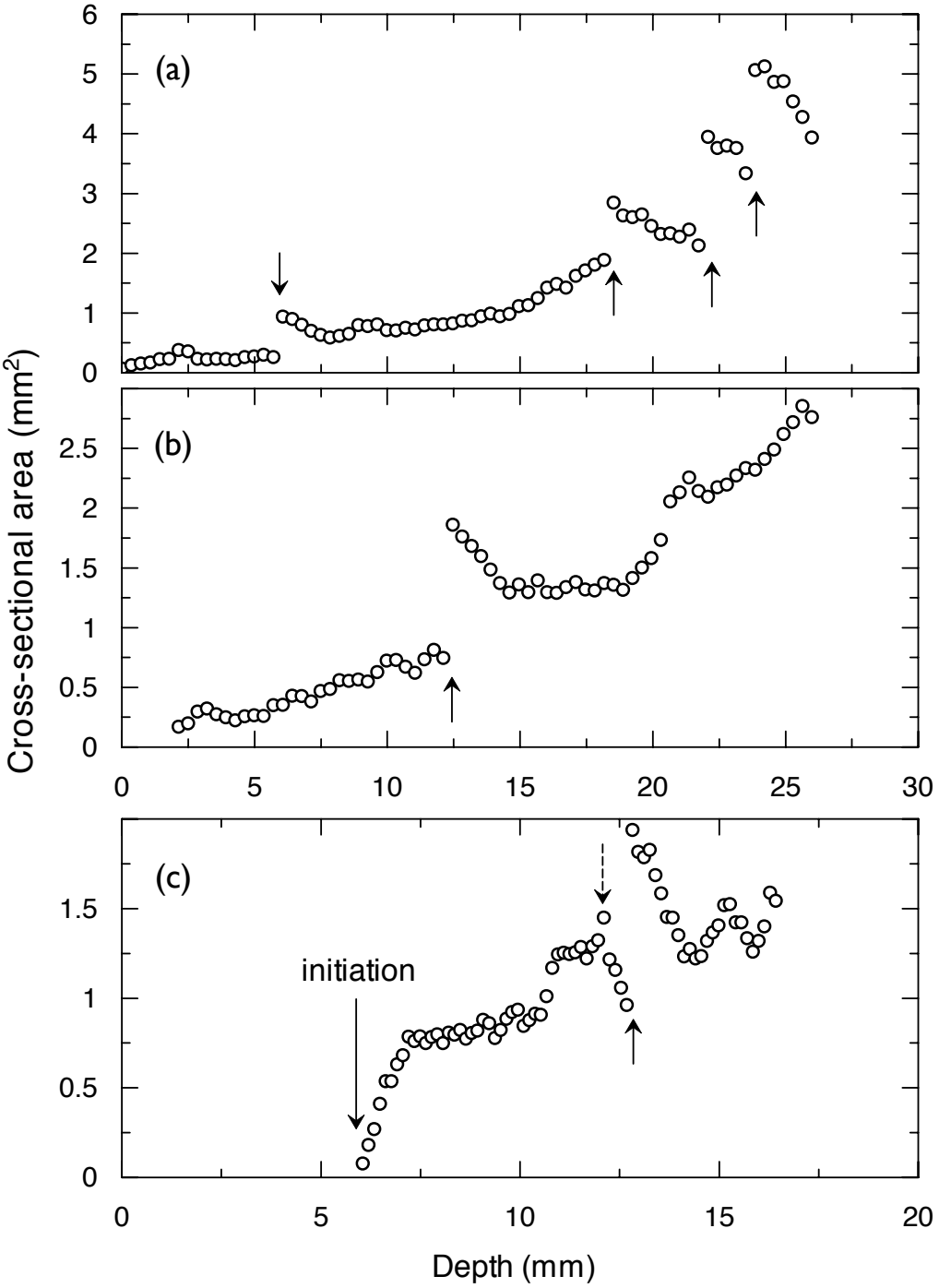

Figure 2.32: The individual cross-sectional area of a column evolves during (a) and (b) an uncontrolled drying experiment and (c) a controlled drying experiment. Column merger events are marked by a solid arrow pointing to discontinuities in the cross-sectional area. In (c), a dashed arrow points to the creation of a new column, which grew in from an adjacent vertex. The column studied in (c) also initiated from a vertex, at the depth marked.

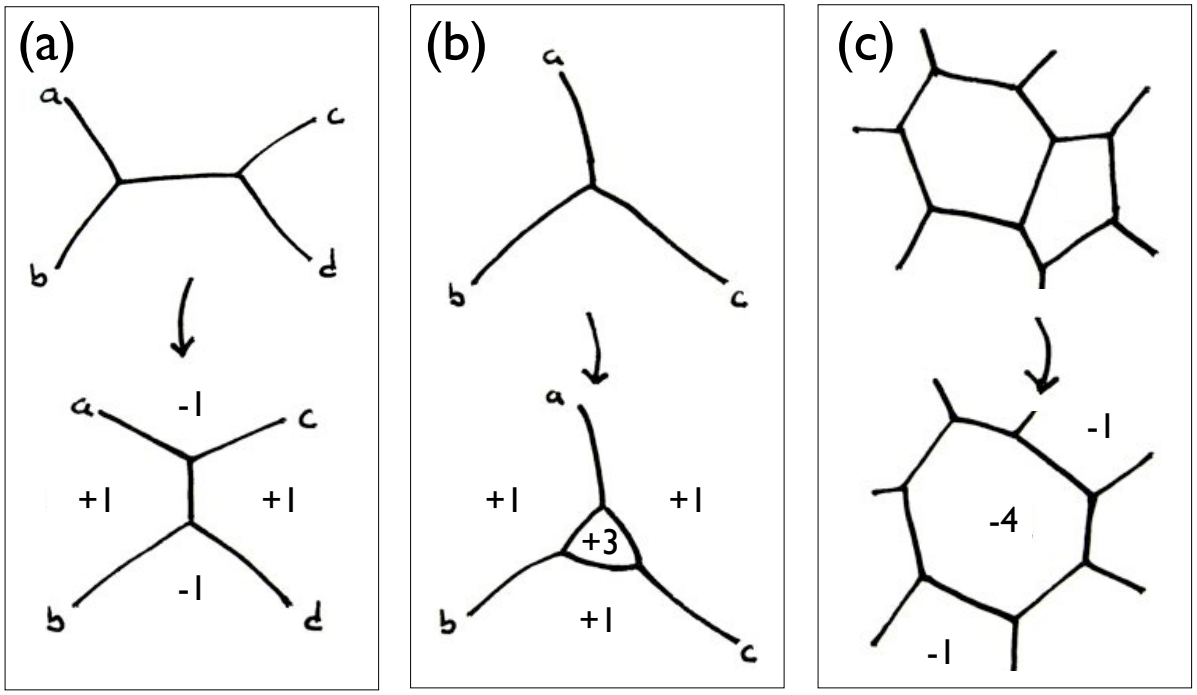

Figure 2.33: Topological changes observed in evolving starch colonnades: (a) a T1 exchange of edges, (b) a reverse-T2 extinction of a column at a vertex, and (c) a reverse-mitosis process of two columns merging. Numbers indicate the changes in the number of neighbors of individual columns.

release, according to the Cotterell-Rice principle [17]. Since a small column has a large perimeter per unit of cross-sectional area, its volume will be less stressed than a larger column. When a crack forming the interface between a small and large column advances, the direction releasing the greatest stress will not be in the vertical direction, but rather biased slightly towards the larger column. Thus, when the crack advances, it will do so in a way which will tend to equalize the areas of the adjacent columns.

The topology of columnar joints in cross-section can only change in three discrete ways, each with its own rules. First, as is shown in Figure 2.33(a), columnar evolution allows so-called T1 processes [111] to occur, whereby two adjacent pairs of columns change their shapes by exchanging an edge. Second, columns can be initiated at, and grow out of, a vertex, as shown in Figure 2.33(b). This is the time-reversal of a T2 process (the extinction of a cell into a vertex [111]) that occurs in coarsening foams. Finally, adjacent columns can merge together, the time-reversal of the mitosis, or splitting, of cells, as demonstrated in Figure 2.33(c).

In these three ways topological defects can be created or destroyed, as are indicated in Figure 2.33. For example, a T1 event will create 2 pairs of pentagons and heptagons in a

perfect hexagonal lattice. It is important to note, however, that Euler's formula relating sides, vertices and faces will require that, on average, each column has 6 neighbors, a property which is respected in all three types of topological changes discussed [111]. Since all three types of changes are generic to many 2D networks, they have been studied in great detail (see *e.g.* [111, 112] for reviews).

In a 2D dry foam, the process of coarsening leads to a pattern that is hexagonal on average, but which remains highly disordered, no matter how long it is left to develop [111, 112]. Furthermore, the disorder in this pattern can be precisely measured, and is highly repeatable. Although it has been long assumed that columnar jointing is a phenomenon that leads to perfect hexagonal order, it too gives rise to a pattern that has significant inherent disorder.

The evolution of an initially disordered surface fracture pattern into a well-ordered colonnade can be observed by panning through a tomogram volume-filling image. Movies of this process are available online [29]. To quantify ordering, the depth-dependence of four statistics of columnar jointing in cross-section were measured: the variance (the standard deviation divided by the mean) of the cross-sectional area distribution; the standard deviation of the joint angle distribution; the standard deviation of the distribution of the number of neighbors of a column; and the percentage of Y-junctions (here defined as a joint angle within 15° of 120°). These statistics are shown in Figure 2.34.

All four statistics reach a statistically steady state after only $\sim$ 1 cm of evolution, maintaining fixed, but large, values thereafter. This indicates that considerable disorder remains in the pattern. The pattern is still, however, slightly more well ordered than a dry foam. The variance in the number of neighbors for a mature starch colonnade is 0.86 ± 0.05. The corresponding limiting value in a coarsening dry foam is 1.18 [112].

As was shown in Section 2.4.1, the pattern of columnar joints can become significantly more disordered during a sudden scale transition. Some strong ordering process acts efficiently to return the value of the relative variation in area to its pre-transition value of 0.35 within one data point (2 mm) of the end of such a transition.

In all four cases the mature values of the starch statistics match the values of the same statistics calculated for the Giant's Causeway, a mature well-ordered basalt pattern [13, 75], and (as will be demonstrated in the following chapter) values from basaltic colonnades across the Columbia Plateau. In some of the experiments presented here it could be argued that the residual disorder is dictated by the continued coarsening of an uncontrolled desiccation. However statistically similar descriptions of the limiting pattern have been measured in controlled experiments, for which coarsening is effectively halted.

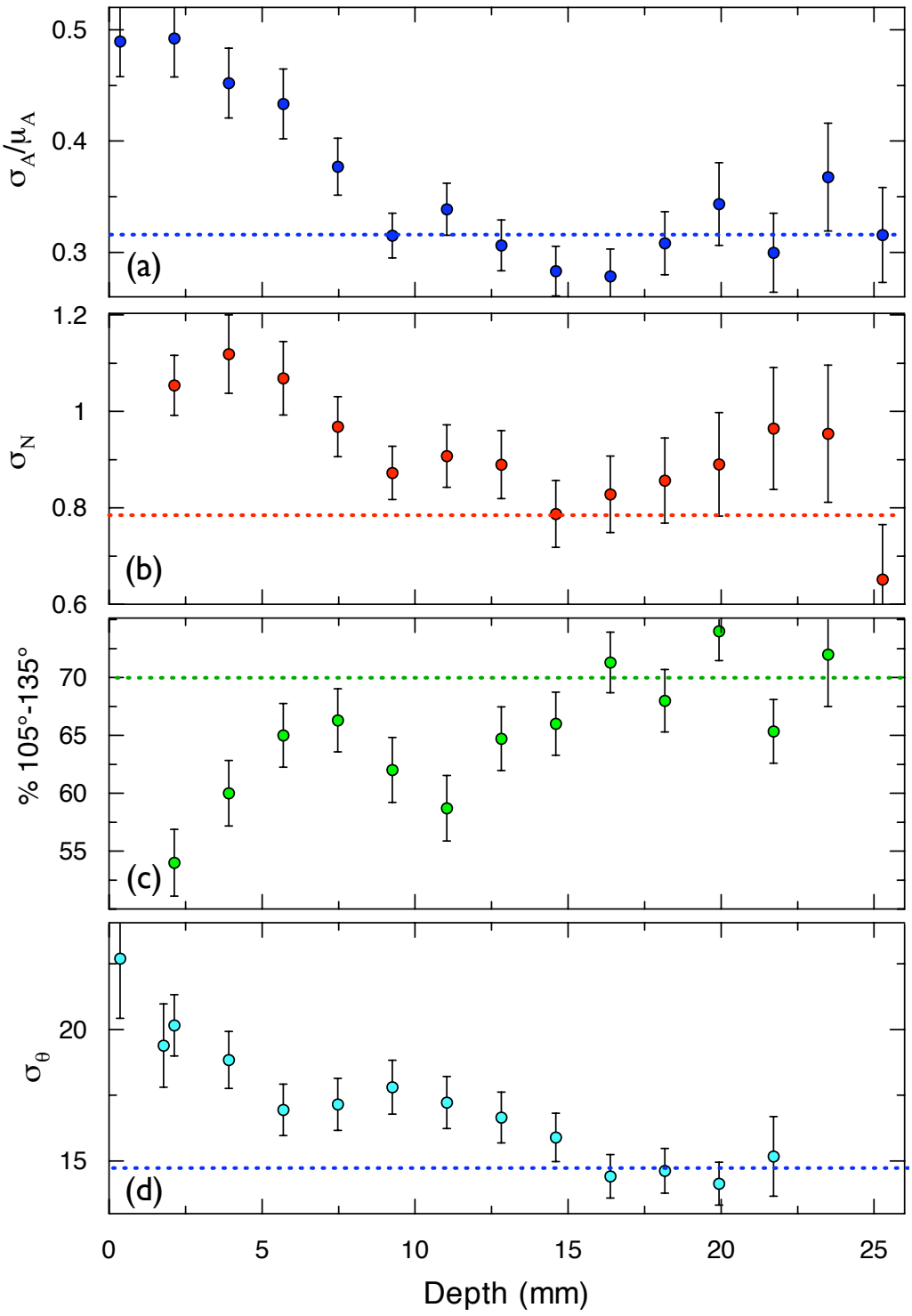

Figure 2.34: A statistical comparison of a 28 mm deep corn starch sample dried in uncontrolled conditions (data points), and O'Reilly's 1879 survey of the Giant's Causeway (dashed lines) [75]. Panels show (a) the relative variation in column cross-sectional area (σ_A/μ_A), (b) the standard deviation of the distribution of the number of neighbors, σ_N, (c) the % of Y-joints, here defined as joint angles within 15° of 120°, and (d) the standard deviation in the distribution of joint angles, σ_θ.

The similarity in the statistical description of the pattern of columnar joints in two very different systems, desiccated starch and cooled basalt, combined with evidence of a strong ordering process away from the disordered limiting pattern, suggests that residual disorder is *intrinsic* to columnar jointing. This is contrary to the assumption that columnar jointing tends towards a perfect hexagonal lattice in cross-section. However, such an assumption is based on the argument that hexagonal fracture maximizes the release of elastic energy [62]. In strongly non-equilibrium situations, such as this one, energy arguments are not necessarily valid. An alternate explanation of residual disorder is that the system geometry gets stuck in a local minimum of the free energy [51]. This scenario seems unlikely, given the observed persistent mobility of the joints, which do not seem to fluctuate around equilibrium positions. Several new dynamical models of columnar jointing have recently been proposed by Jagla [49, 50] and Jagla and Rojo [51], which seem to capture some aspects of this inherent disorder. However, none has done so in a quantitative way.

2.6 Conclusions of experimental work

In this chapter, the physics of a drying starch-cake has been described, and the scaling and ordering behavior of columnar joints in starch have been discussed in detail. Experimental techniques were presented which allowed a variety of drying protocols to be performed. These included uncontrolled experiments, where the evaporation rate continuously decreased throughout the experiments, partially controlled experiments, where the evaporation rate was held constant during the late stages of drying, and fully controlled experiments, where the evaporation rate was controlled throughout the entire desiccation. The colonnades resulting from these experiments were observed in 3D by the use of X-ray tomography, and destructive sampling. The use of feedback control and 3D visualization techniques to study columnar jointing are novel to this thesis.

Corn starch itself is a dry, hydrophilic powder of rounded grains, with an average radius of 8 μm. The surface of the grains is somewhat rough, and the grains appear to contain large voids or pores, when viewed under an electron microscope. These pores play an important role in the drying of a starch-cake.

It is apparent that the drying of a starch slurry occurs in several phases, and that each phase is controlled by a different physical mechanism. As drying progresses, surface evaporation, capillary transport and diffusive vapor transport successively take their place in dominating the transport of moisture. These mechanisms are, in turn, dictated by the depletion of the water reservoirs between starch grains, and within starch grains. Ini-

tially, a very wet starch-water slurry can be considered as a two-phase mixture of starch grains and water. Once the grains have settled, and the excess water has evaporated, air intrudes into the starch-cake, leading to a three-phase flow problem involving air, water, and solid starch. As long as the capillary bridges between grains form a connected network, capillary flow efficiently smoothes out the moisture concentration profile. However, around a critical moisture concentration of 0.3 g/cm^3, the capillary bridges become disconnected, and further drying can only occur by the diffusion of water vapor.

During this final phase of drying, which leads to columnar jointing, a drying front develops which slowly intrudes into the starch-cake. The strain which is associated with this drying front is large, but just sufficient to break the capillary bridges between grains. As the capillary bridges break, they lead to a fracture front which trails behind the drying front, following a surface of constant moisture concentration. This scenario is very similar to the dynamics of columnar joint formation in a cooling lava, as presented in Section 1.3. In the following chapter, the results of field work in regions with igneous columnar joints will be described, which will further illuminate the similarity between these two systems.

Experimental methods were developed to use these observations of drying to determine the velocity of the fracture front, based on measurements of sample mass. In uncontrolled experiments, the fracture front slowed down diffusively, while in controlled experiments, the fracture front maintained a constant velocity.

The scaling of columnar joints in starch was discussed in relation to a wide range of experiments. The relationship between the evaporation rate and the column scale was found to be somewhat complex. Experiments using uncontrolled drying procedures showed that the slower that a starch-cake dried, the larger the columns at the base of the sample would be. However, these same experiments showed that the columns coarsened, or increased in scale, throughout the sample. In general, but not always, the fracture spacing was inversely dependent on the fracture front velocity. A significant exception to this rule was observed in the form of sudden jumps in column scale, which may indicate some sort of period-doubling instability in the scale selection process.

Experiments using various degrees of feedback control showed that, if the fracture front velocity is held constant, the coarsening of columnar joints eventually halts, and a single length scale is selected in each colonnade. This length scale is typically inversely dependent on the fracture front velocity, but also clearly displays evidence of hysteresis. These observations will be further discussed in Chapter 4, where a model of scale selection based on the advection-diffusion of moisture will be presented.

The pattern of columnar joints in corn starch was studied through the inspection

of 3D X-ray tomograms. It was shown that individual columns respond to changes in their immediate neighborhood, and evolve to match the average column area relatively quickly. Three types of topological changes are supported by the pattern, which involve T1 processes (the exchange of an edge between columns), the creation of a new column at a vertex, and the merging of two or three columns as an edge or vertex fails to propagate. These changes take place in a pattern that continues to evolve throughout the entire depth of the starch-cake, and lead to a pattern that has a significant level of residual disorder. Further discussion on the pattern of columnar joints, in the context of igneous columnar joints, is given in Section 3.5.

Chapter 3

Field Work

3.1 Overview

To complement the experimental results on the scaling and ordering of columnar joints presented in the previous chapter, field work was performed in several locations, during the course of three summers. This work was focussed on determining the scaling behavior of igneous columnar joints through the insights provided by stria features on column faces (see Section 1.3 for a detailed description of striae and plumose patterns). Measurements were also made in order to determine how these columns become ordered. Furthermore, a novel length scale was discovered during the course of this work – that of an oscillatory instability which can lead to wavy columns.

A field expedition to the Columbia Plateau was made to observe the Columbia River Basalt Group (CRBG). The aim of study in this area was to establish rigorous results based on as repeatable and simple a system as possible. All material from the Columbia River Basalt Group (Section 3.2) has been submitted for publication in Reference [33]. Expeditions to British Columbia and Staffa, Scotland, were subsequently made to confirm data from the CRBG, and to demonstrate that these results are applicable to diverse lava types. Results from these trips will be prepared for a follow-up publication, and some preliminary results which are relevant to the analysis of igneous columnar joints are presented here in Section 3.3.

3.2 The Columbia River Basalt Group

The Columbia River Basalt Group (CRBG) was chosen as an ideal site for the field study of columnar jointing. Recent geological and human activities have exposed fresh basalt

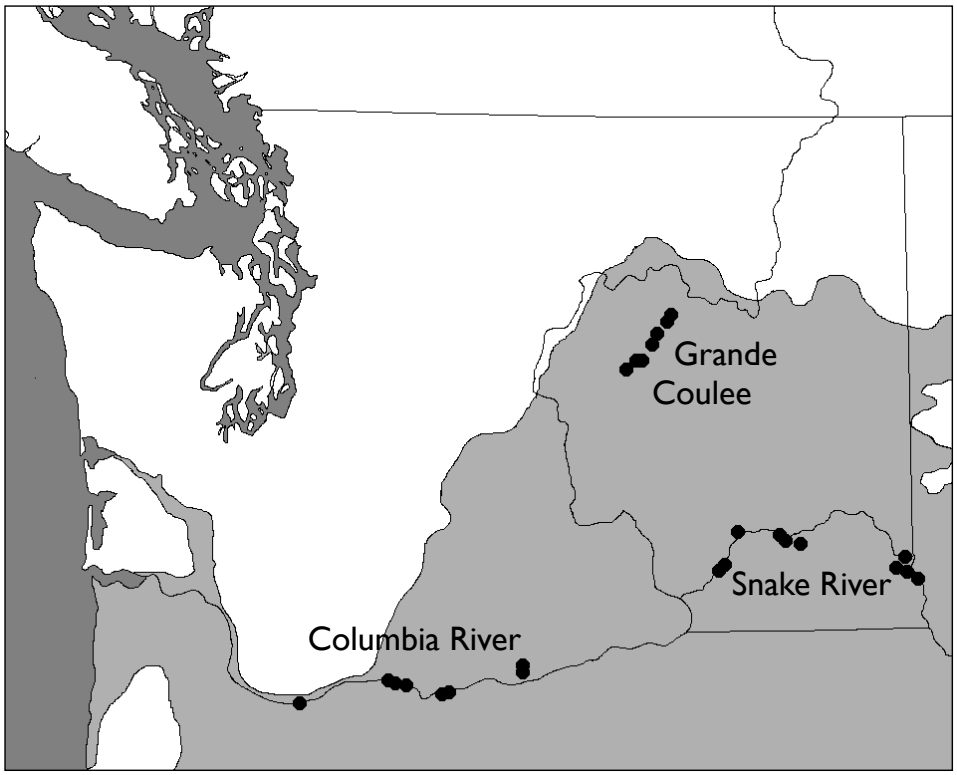

Figure 3.1: Location of field sites (black circles) and the Columbia River Basalt Group (shaded region, adapted from [44]) in and around Washington state. Further information, including GPS locations of each site, is given in Appendix B.1.

surfaces. The dry climate has helped to preserve delicate striae and plumose structures on the column faces. The homogeneity and extent of the CRBG allows access to a large number of study sites that are compositionally identical. Differences in jointing between sites, therefore, can be primarily attributed to differences in cooling dynamics, and not to differences in material properties.

3.2.1 Geology of the Columbia River Basalt Group

The CRBG is a large igneous province that formed when the Yellowstone hotspot impinged on the continental crust around 17.5 Ma [16, 44]. Several hundred massive basalt flows were released over approximately the next ten million years, which collectively covered a significant part of Washington and Oregon states over a kilometer deep in lava. The majority (>85%) of activity was confined to the Grande Ronde Basalt Formation (16.5-15.6 Ma), whose feeder dykes lie near the Washington-Oregon-Idaho border [104]. These flows are all compositionally very similar, typically ∼54% SiO_2, and are classified as low-Al tholeiitic basalt [44, 84].

Petrographic evidence shows that individual flows, some of which contained thousands of km^3 of lava, were emplaced relatively rapidly [82, 83]. Studies of chemical differentiation imply that each flow was laid down through laminar flow beneath a thin solidified crust [43, 96]. This, in turn, implies that not only was the source lava relatively homogeneous in time, but that it produced undifferentiated, isothermal lava flows across the Columbia Plateau. Emplacement temperatures are tightly constrained by these data, and are estimated to be 1085-1095°C in the Ginko flow of the CRBG [43].

Much more recently, during the last ice age, the scablands of the Columbia Plateau were created through a series of catastrophic floods caused by the periodic breakdown of an ice dam on glacial Lake Missoula [11, 109]. These floods, along with the erosive action of the Columbia and Snake rivers, have produced a large number of accessible and relatively recently exposed flow units. 28 sites in the CRBG were studied, all in three large areas - the Grand Coulee between Electric City and Soap Lake, the Snake River from near Clarkston to the Tri-Cities, and the Columbia River between Portland and Rock River Road - as shown in Figure 3.1. 21 of these sites yielded quantitative data which was used in the following analysis. This study covered a wide range of the Grande Ronde and Wanapum basaltic units of the CRBG, but is not thought to extend beyond these formations. Details of each site, including access directions, are given in Appendix B.1.

3.2.2 Observational methods

At each field site, several geometric features of an exposed colonnade were measured, with care taken to obtain enough measurements to give good statistics. The widths of column faces, the angles between joints meeting at a vertex, the heights of individual striae, and the positions of the upper and lower flow surfaces were measured, when possible, and the direction of cooling was inferred. The data collected were limited in many cases by erosion or other damage to the colonnades. Column face widths were measured to $\pm$ 1 cm, which reflects the difficulty of measuring a dimension that is often not constant over the extent of a column's height. Three measurements were usually made of the height of each stria (at the middle, and near the edge of each column face), each measurement accurate to $\pm$0.25 cm. In a few cases where the state of preservation was exceptional, it was possible to measure stria heights to $\pm$0.1 cm precision. When erosion had not rounded off the column vertices, the vertex angles were measured with an estimated error of $\pm$5%. These angles were usually easiest to measure in columnar rubble at the base of a colonnade. The lava flow margins were often irregular, which presented measurement difficulties.

In cases where striae were observed near a flow margin, the distance between the flow margin and the start of the recorded sequence of striae was measured for each column. There is an estimated 10 to 25 cm error in such measurements. The direction of cooling was determined by observations of plumose structure, as described in [19] and in Section 1.3.

The number of lower colonnades in this study – those that cooled from the base up – represent 15 of the 18 sites where a conclusive determination of the direction of crack propagation was made. This reflects the fact that although basalt is a hard, weather-resistant rock, the columns themselves are easily dislodged, and can be removed individually. This mode of erosion tends to leave the lower surface of a flow unit much more accessible than the upper limits.

3.2.3 Stria height *vs.* column width

To investigate the scaling behavior of columnar jointing in lava, stria heights were measured at 18 different sites. The size of striae varied from 36 cm near the Dalles Dam to only 3.5 cm near Clarkston; the stria heights tended to scale in direct proportion with the average size of the columns. Across all sites it was found that the ratio of the average stria height $\langle s \rangle$, to the average column width $\langle w \rangle$, $\eta = \langle s \rangle / \langle w \rangle$, has a mean value of $\eta = 0.14 \pm 0.02$ with a standard deviation of 0.06 ± 0.02, as shown in Figure 3.2(a). Although there are significant fluctuations, these results agree well with those of DeGraff and Aydin [20], who collected data across eight sites throughout the Western United States, and with Grossenbacher and McDuffie [38], who suggested that η ranged between 5% and 20%. When all the stria measurements are considered individually, however, it becomes apparent that there are several sites which display a very wide scatter in stria heights, while others show a very tightly defined stria height distribution. These data are shown in Figure 3.2(b). Their scatter has two sources – an increase in stria height as one moves away from the flow margin, and random variations between individual stria heights. The wide spread of the data also suggests that there is no uniquely defined relationship between $\langle s \rangle$ and $\langle w \rangle$, but rather that there may exist a modest range of allowed ratios η which are stable under the evolution of the fracture network.

3.2.4 Stria height *vs.* position relative to the flow margin

At six sites conditions were favorable to measure the spatial evolution of stria heights, as shown in Figures 3.3 and 3.4. In general the height s of a stria depends on its position z away from a cooling flow margin. At three locations, shown in Figures 3.3, measurements

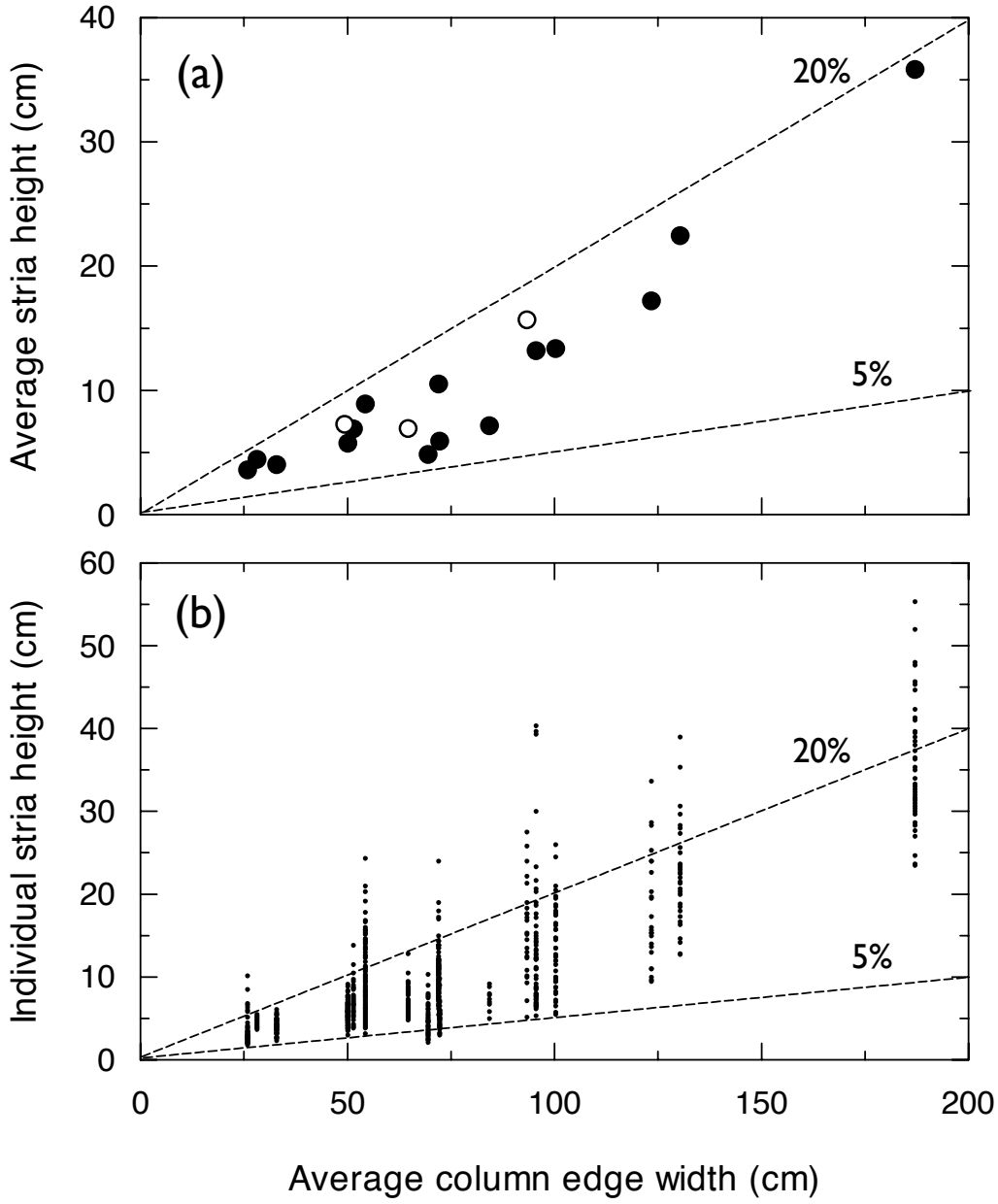

Figure 3.2: The distribution of stria heights and column widths. (a) shows the average stria height $\langle s \rangle$ and column edge width $\langle w \rangle$ at each site, while (b) shows all the individual stria measurements made at each site. In (a), black circles represent lower colonnades, or sites with an uncertain direction of cooling, while white circles represent upper colonnades.

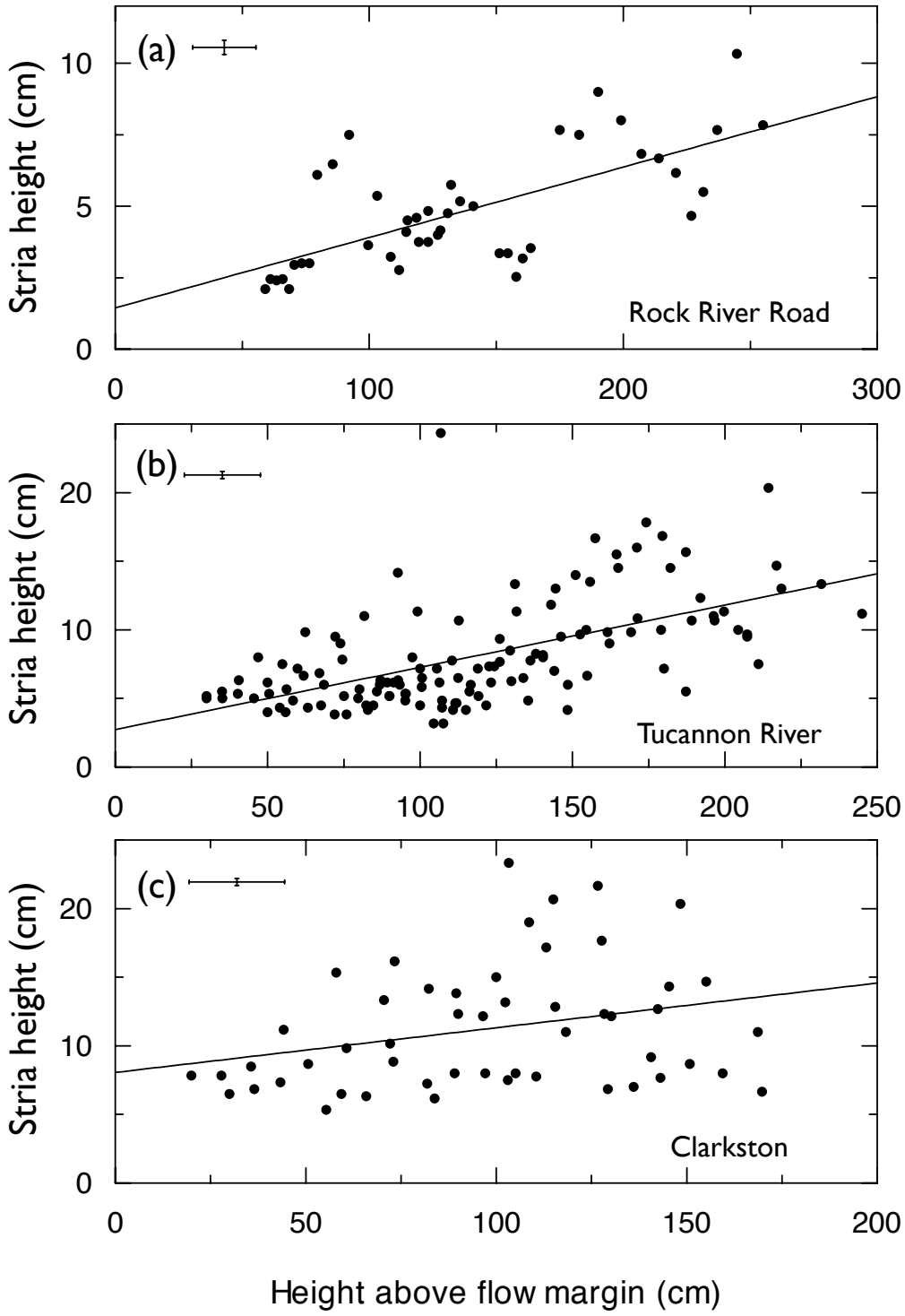

Figure 3.3: Growth of the stria height s as a function of the distance z from a flow margin, at three field sites. In each panel a best-fit line is drawn to indicate approximately the rate of increase of the stria height. Error bars in the upper left of each panel show the typical errors of ± 2.5 mm for stria height, and ± 12.5 cm for stria position.

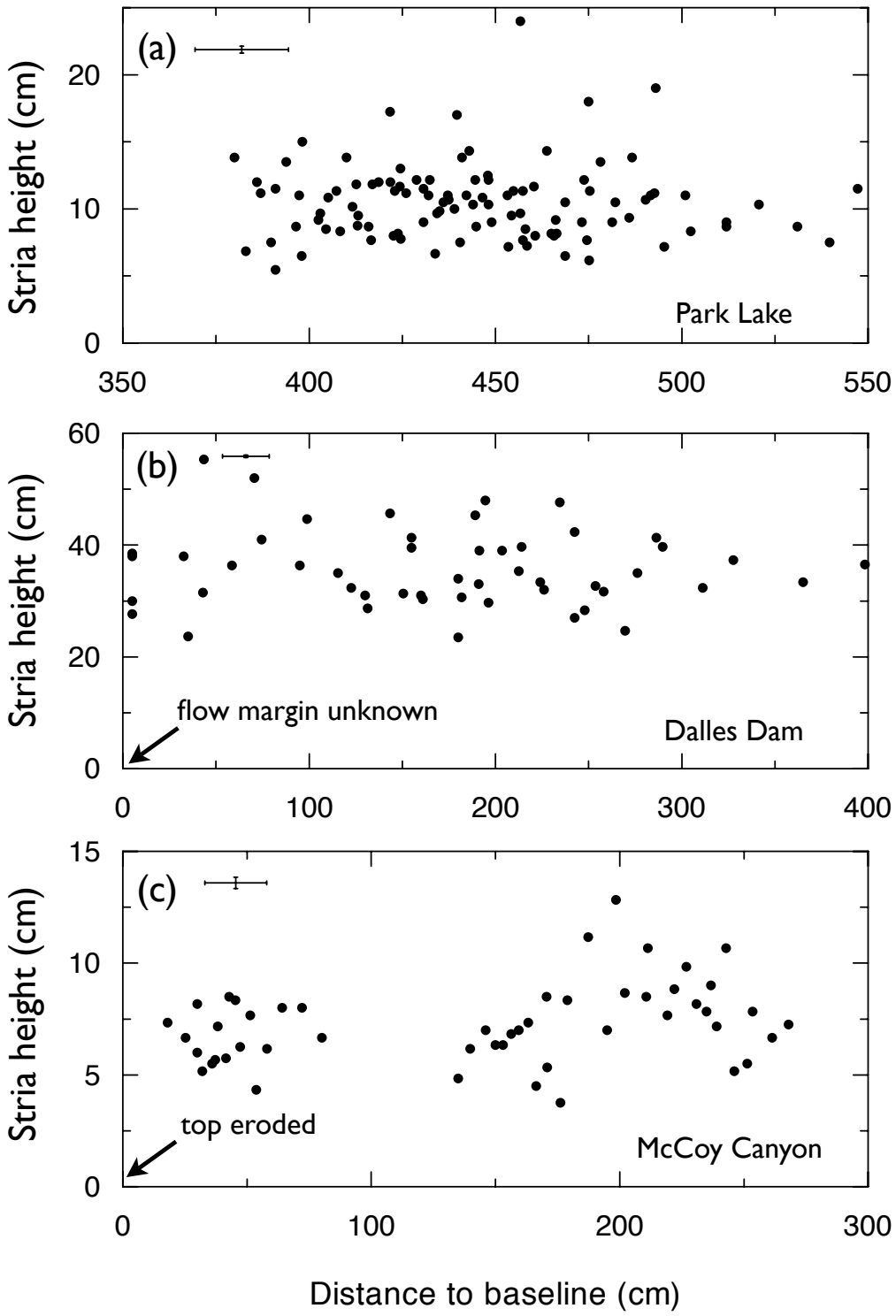

Figure 3.4: The stria height more than a few meters away from a flow margin is a constant at any field site. (a) and (b) show lower colonnades, while (c) shows striae in a partially eroded upper colonnade. Linear regressions of the data presented in each panel are consistent with zero slope in all cases. Error bars in the upper left of all panels show the typical errors of ±2.5 mm for stria height, and ±12.5 cm for stria position.

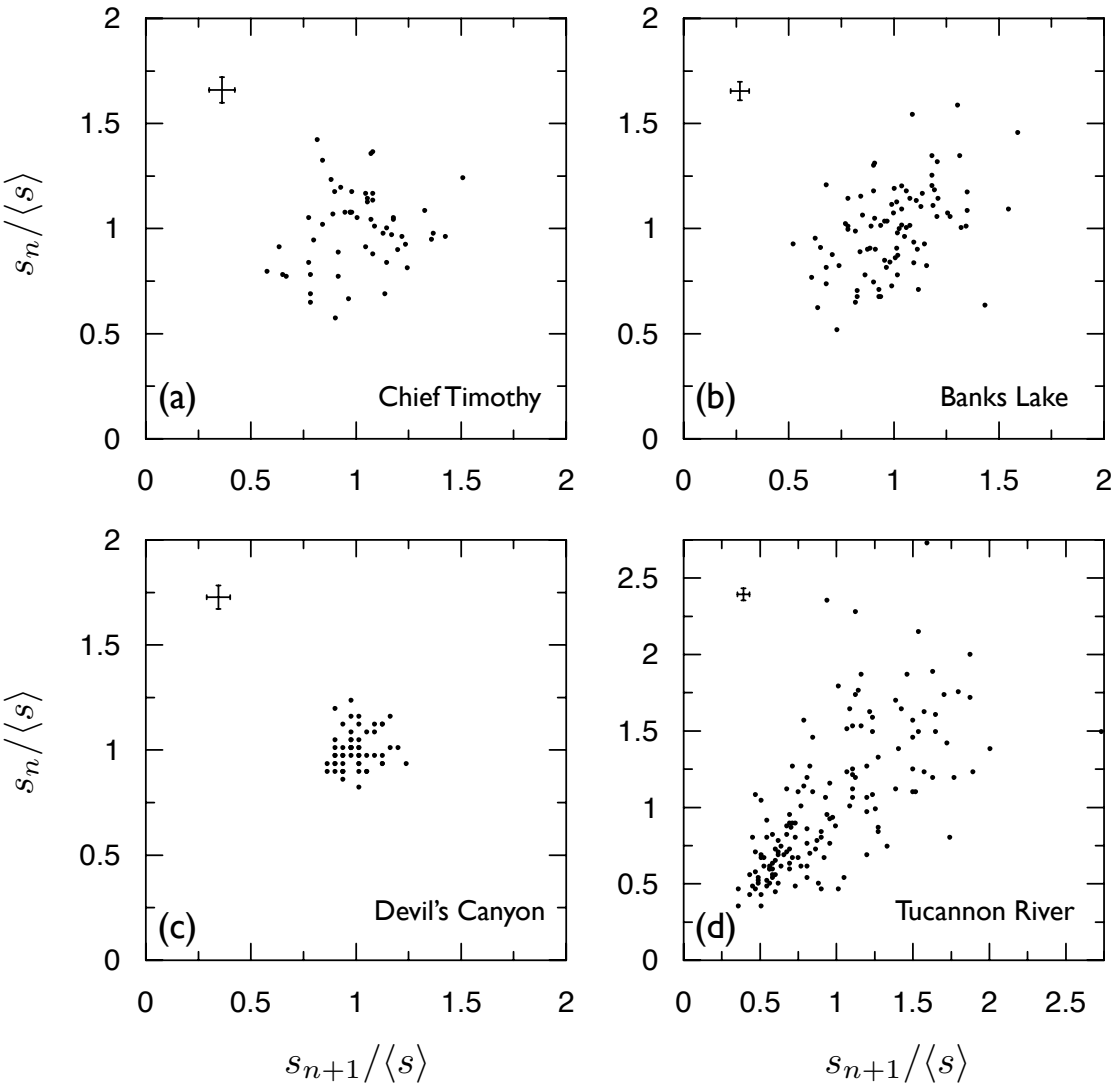

Figure 3.5: A statistical analysis of the correlations between subsequent stria heights. In (a-d), each relative stria height $s_n/\langle s\rangle$ is plotted against the relative height of the subsequent stria, $s_{n+1}/\langle s\rangle$. Error bars displayed in the upper left of these figures show the typical observational error of ± 2.5 mm. (a) and (b) are typical of most data sets, with a large scatter of data. The site shown in (c) is singularly unusual, in that successive stria heights are much more constant here than at any other site. The correlation apparent in (d) is due to a gradual increase in the stria height as a function of the position away from a flow margin.

were made near the basal flow margin. At a fourth location, shown in Figure 3.4(a), a convenient scree pile allowed an accurate estimate of the distance from the measurements to the base of the flow to be made. In a fifth case, shown in Figure 3.4(b), observations of the surroundings of the flow implied that measurements were made at least several meters above the flow margin, although the exact distance was unknown. The final location, shown in Figure 3.4(c), was the only case where the spatial dependence of stria height in an upper colonnade was measured. In this case, unfortunately, erosion prevented any reliable estimate of the position of the top of the flow unit.

These data suggest that near a flow margin, the average stria height in a colonnade increases with the distance away from the flow margin. This may be seen visually in Figure 3.10. Beyond about 3-4 meters from the basal flow margin, the stria height stops increasing and there was no observable trend in the height of the striae with position. Within the bulk of the colonnade, the stria heights are randomly distributed around an average. This lack of a trend can also be seen in Figure 3.5, which shows the relative height of the nth stria, $s_n/\langle s\rangle$, plotted against the relative height of the subsequent stria, $s_{n+1}/\langle s\rangle$. Most cases, such as those shown in Figure 3.5(a)-(c), are scatter plots with no correlation. Several cases of apparent correlation, such as that shown in Figure 3.5(d), can all be interpreted as arising from changes in the average stria height near a flow margin. Interestingly, in no case was an anti-correlation between consecutive stria heights observed. Such an anti-correlation might have been expected if a larger than average crack advance was in some way compensated for by a shorter advance during the formation of the next stria. No such interaction between successive stria was observed. As will be show in Section 3.3.5, however, there *may* be some interaction between horizontally adjacent striae.

Although the cross-sectional areas of the columns are well known to be remarkably uniform within the bulk of a colonnade, it has been shown that within about 1-3 m of a flow margin the column size can coarsen somewhat [20, 60, 79]. Furthermore, the analog experiments in corn starch presented in Section 2.4.3 showed that this type of coarsening is halted in a starch-cake when a constant front velocity is reached. It is likely that something similar happens in lava, and that both the column size and stria height evolve together, reaching some stable values a few meters away from the flow margin.

3.2.5 Statistical distribution of stria heights

The data presented in Figure 3.6(a) show that the ratios of adjacent stria heights all have a similar distribution of values, for observations from both upper and lower colonnades,

and from striae near to and far away from a flow margin. The one exception to this rule, at Devil's Canyon, has a somewhat tighter distribution of stria heights. In general the data suggest that each stria advance is well described as a statistically independent event. If this is the case, then it follows from basic statistical theory that the standard deviations of the probability distribution functions of $s_n/\langle s\rangle$ and $(s_n - s_{n+1})/\langle s\rangle$ should differ by a factor of $\sqrt{2} \simeq 1.4$. Here s_n and s_{n+1} are, again, the heights of any two subsequent striae as defined by the direction of cooling, on any column. Respectively, these standard deviations were found to be 21±1% and 31±1%, and hence their ratio is 1.45±0.08, in reasonable agreement with the expectation for independent events.

The covariance between s_n and s_{n+1} can also be used as a test of their statistical independence, where the covariance $\mathrm{Cov}(s_n, s_{n+1}) = \langle s_n s_{n+1}\rangle - \langle s_n\rangle\langle s_{n+1}\rangle$. If s_n and s_{n+1} are independent random variables, then it is a basic mathematical result that $\mathrm{Cov}(s_n, s_{n+1}) = 0$. This covariance was calculated for data from eight sites where large numbers of stria measurements were made, and where there was no obvious correlation between s_n and s_{n+1} due to the proximity of a flow margin. In all cases, the calculated covariance was consistent with zero.

The distribution of individual stria heights is presented in Figure 3.6(b). Only data obtained well away from a flow margin was used to prepare this distribution. A fit of a gaussian distribution to this data is suggestive, but cannot explain either the asymmetry of the data around the mean, or the slower-than-exponential decrease in the tails of the distribution. A Weibull probability distribution function

$$p_w(s) = \frac{k}{b}\left(\frac{s - s_0}{b}\right)^{k-1} e^{-((s-s_0)/b)^k} \tag{3.1}$$

better captures both these unusual features of the data, and is commonly used to model failure or fracture phenomena [25, 114]. This function gives the probability distribution function of the minimum value of a set of independent variables [25]. A fit of the shape parameter $k = 2.7\pm0.2$, the scale parameter $b = 0.56\pm0.03$, and an offset $s_0 = -0.51\pm0.03$ in Equation 3.1 to the probability distribution of the relative striae heights is shown in Figure 3.6(b). This type of distribution would naturally arise in a material where the local tensile strength at the crack tip is a random variable with a fixed variance, and where a fracture, once active, runs until the fracture tip reaches some lower, constant, termination stress. If the termination stress were not constant, subsequent striae would be slightly anti-correlated, which is not the case. Weibull statistics can follow from the observations that a fracture can initiate at any position along the column edge (although the vertices are preferred initiation sites), and that failure of the weakest point causes

the failure of the entire crack edge. This distribution could also arise if crack advances on different columns are coupled in some way – if the arrival of an advancing crack at a vertex triggers crack advances on other edges sharing that vertex, as was suggested by Aydin and DeGraff [2], based on a study of plumose structure.

3.3 British Columbia, Staffa, and the Giant's Causeway

Additional field work was performed in the Cascade volcanic arc and Intermontane Belt of British Columbia, Canada, and on the island of Staffa, Scotland, in order to test the relevance of the observations made within the Columbia River Basalt Group to a more broad range of igneous columnar jointing. Also included in this section, for the sake of completeness, is a brief discussion of the geology of the Giant's Causeway.

The methods used in this section are similar to those described in Section 3.2.2. Column widths and stria heights were measured at a number of sites, however only one measurement of each stria height was made, rather than three, in order to focus on obtaining large data sets. All colonnades, save one, presented in this section are lower colonnades.

3.3.1 The geology of South-Western British Columbia

Most of the field work performed in British Columbia was conducted in the Garibaldi volcanic belt (situated around the Vancouver-Whistler-Pemberton corridor), and on the plateau basalts of the Intermontane Belt of that province. The locations of the field sites that were studied are shown in Figure 3.7, and described individually in Appendix B.2.

The Garibaldi volcanic belt is part of the Cascade magmatic arc that has formed due to the subduction of the Juan de Fuca plate under the North America plate [34]. It includes Mount Garibaldi, Mount Caley, and Mount Meager, in addition to other minor volcanoes, and is still active (the last eruption being 2350 years B.P. at Mount Meager [42]). Much of the volcanism in this area occurred during glaciations, and many lava flows show signs of interactions with ice during cooling [88]. The lava types present in the Garibaldi volcanic belt are highly varied, and include dacite flows at Watt's Point quarry, and in the Tricouni area [88], alkali olivine basalts in the Chekamus valley [34], and the recent eruption products of Mount Meager which border between dacite and trachydacite [42].

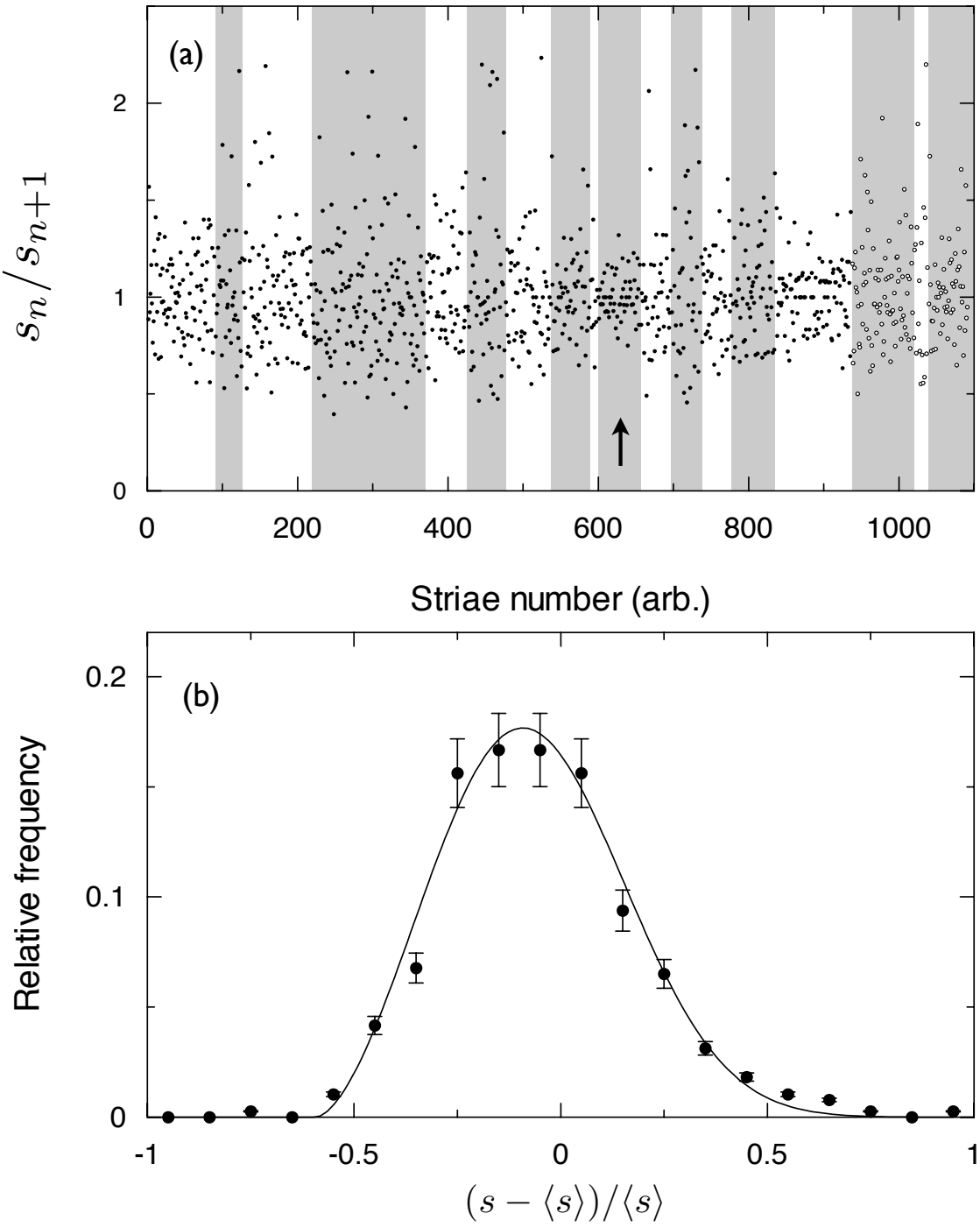

Figure 3.6: A statistical analysis of the distribution of stria heights. (a) shows that the ratio s_n/s_{n+1} is not generally dependent on the site, or on the position in the flow. Alternations between white and grey backgrounds distinguish between data from different sites. An arrow points to the exceptionally constant Devil's Canyon data. White circles show data from upper colonnades, while dark circles show data from lower colonnades, or from sites where the direction of cooling was uncertain. (b) shows that the probability distribution function of the stria height s, for data sampled from the interior of colonnades, is well described by a Weibull distribution.

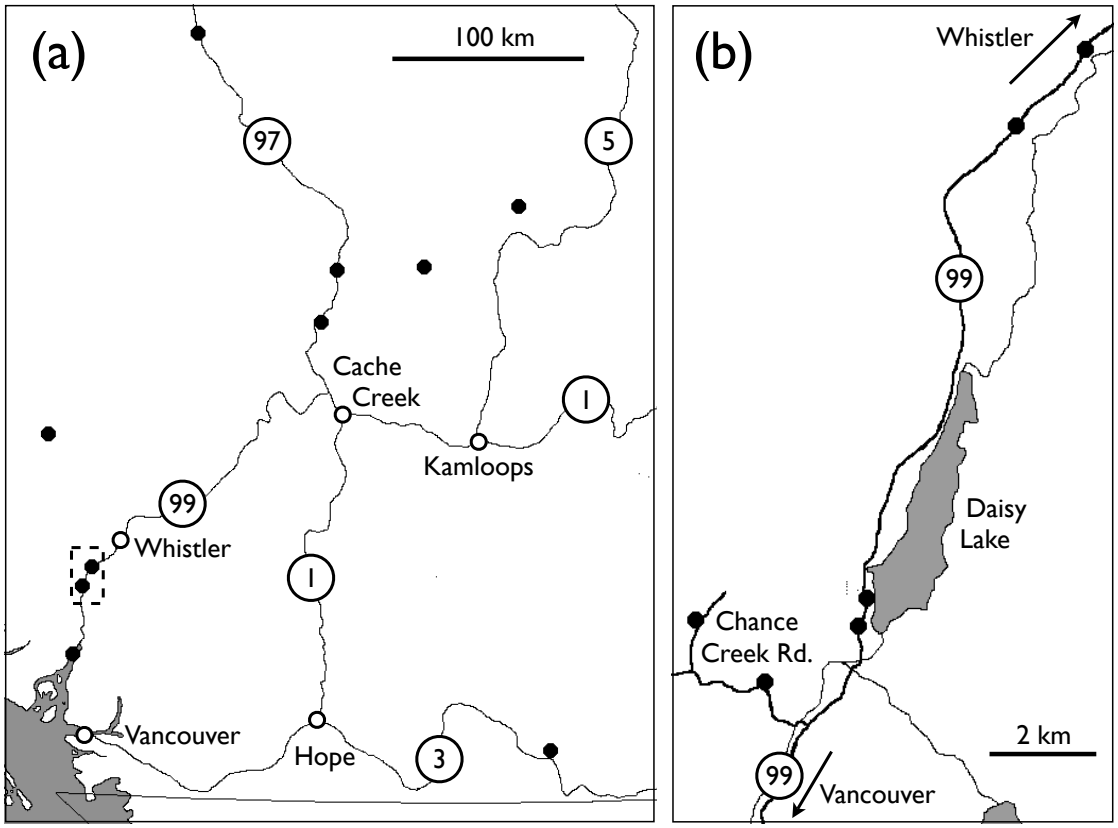

Figure 3.7: Locations of field sites studied in British Columbia. (a) shows the field sites (black circles) visited throughout this region. The area indicated by a dashed rectangle near Whistler is shown enlarged in (b). Major highways are indicated, along with their numbers, in both panels. Further information on these sites, including GPS locations, can be found in Appendix B.2.

The Intermontane Belt (also known as the interior plateau) of British Columbia sits between the mountain ranges of the Coast and Omineca Belts. Since British Columbia is an accreted terrane province, this region is host to a highly complex and heterogeneous geology. Any comprehensive discussion of this region is therefore best left to detailed field guides (*e.g.* [63]). The field sites studied in this belt were mainly Miocene plateau basalts.

3.3.2 The geology of Staffa and the Giant's Causeway

The lava flows in the Scottish Hebrides are part of the North Atlantic Tertiary Igneous Province, and are associated with the North Atlantic (*aka* Icelandic) mantle plume [53, 115]. The Staffa sub-type of the Mull Plateau group is one of the earliest igneous members in that area, and was emplaced at 63-65 Ma [54, 53]. Chemically, the Staffa sub-type is

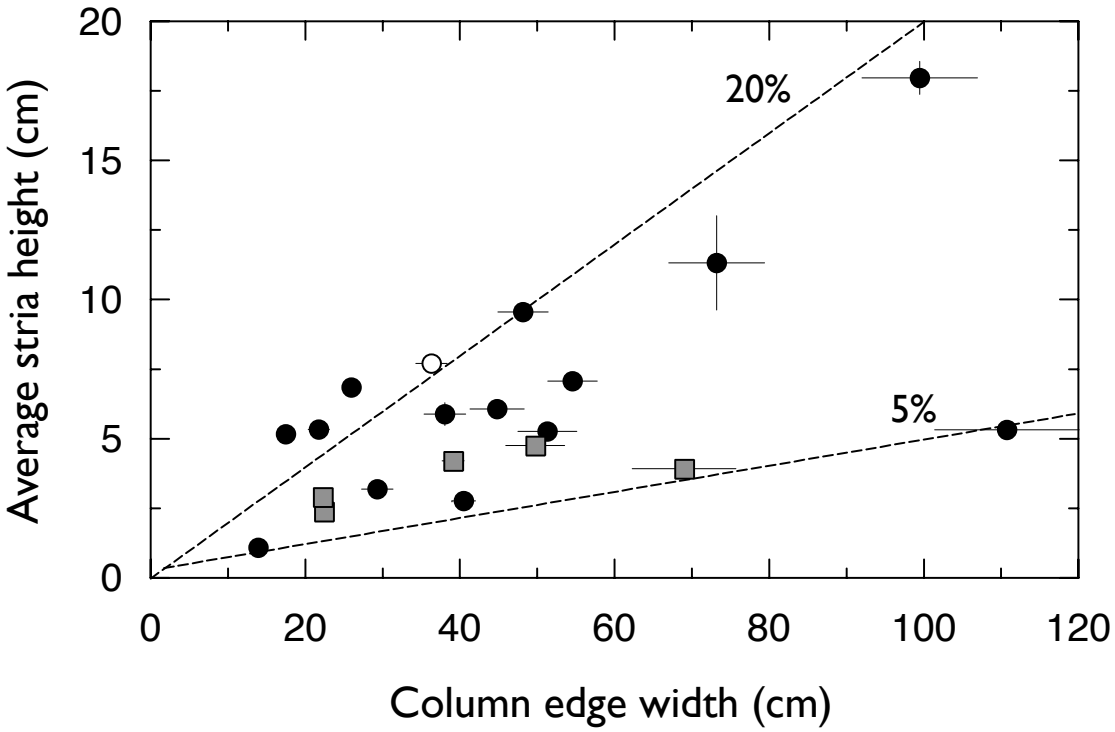

Figure 3.8: The distribution of stria heights and column widths in BC (circles) and Staffa (grey squares) agree with the results observed in the Columbia Plateau. The single upper colonnade measured is shown as an open circle; all other data depict lower colonnades.

a tholeiitic basalt with an average SiO_2 concentration of 49±2% [54, 103]. On the island of Staffa, the lowest flow unit of this sub-type overlies a thick ash layer, as can be seen in Figure 1.1. This unit will be referred to as the Fingal's lava unit, as it is within this flow unit that Fingal's Cave is carved. In this study, geometric properties of the Fingal's lava were measured at a number of sites along the SW coast of Staffa, from the region near Clamshell Cave and Fingal's Cave to near Float Cave, as is described in Appendix B.3

The Giant's Causeway is similarly part of the North Atlantic Tertiary Igneous Province. A detailed study of the geology in the area was done by Tomkeieff [105], who identified several flow units of tholeiitic basalt belonging to what is now referred to as the Causeway Tholeiite member of the Antrim Lava Group's Interbasaltic Formation [61]. The columns of the Giant's Causeway were well surveyed in the 19th Century [75], as was shown in Figure 1.2.

Both the Fingal's lava unit and the Causeway member are similar in composition and mantle plume origin to the plateau basalts of the Columbia River Basalt Group, although in general they are slightly more basic in composition.

3.3.3 Stria height *vs.* column width

The heights of striae and the widths of columns were measured at 15 sites throughout BC, and at 5 sites within the Fingal's lava unit. As shown in Figure 3.3.3, most of the data from these regions agree with the estimate, established in relation to the Columbia River Basalt Group, that $\eta = \langle s \rangle / \langle w \rangle$ is usually between 5% and 20%. There is significantly more scatter, however, in the data from BC than from either the CRBG or Staffa. Some of this scatter could be attributed to variations in composition throughout the lavas studied in BC. On the other hand, much of this scatter must be due to variations in emplacement history and local cooling effects. As one example, consider the two flows studied in the Tricouni Southeast unit, which differ in scale by a factor of over five, but which have striae that are almost identical in size at both sites. In one of these cases, where small columns have larger than expected striae, it is known that the site formed as lava was impounded against an ice-wall [88]. These columns form a fan where column diameters are largest near the flow margins, and smaller at the measurement location. This geometry would have lead to enhanced cooling near the center of the flow. The other Tricouni site, further up the mountain, features ordinary large blocky horizontal pillars.

3.3.4 Striae *vs.* position in the Cheakamus basalts

The Cheakamus basalts lie near Daisy Lake and the Cheakamus River. Ongoing highway upgrade work in the area has exposed fresh column surfaces, and several well formed lower colonnades were measured there. As shown in Figure 3.9, there is an increase in the average stria height as the distance to the lower flow margin grows. These results are very similar to those obtained in the CRBG, and the rates of increase of the stria height measured here are also comparable to the rates presented in Figure 3.3. More than a couple meters into the flow unit the striae cease to increase in size. These features are also displayed in Figure 3.10, which shows a photo of striae in the Cheakamus basalts, near a lower flow margin.

3.3.5 Correlations between horizontally adjacent striae

At the Bridge Lake site, a Miocene plateau basalt, excellent records of both striae and plumose were visible. Column widths, stria heights, and stria propagation directions were measured at this site. As shown in Figure 3.11(a), it was observed that, in most cases, horizontally adjacent striae on two sides of a column begin and end at the same vertical

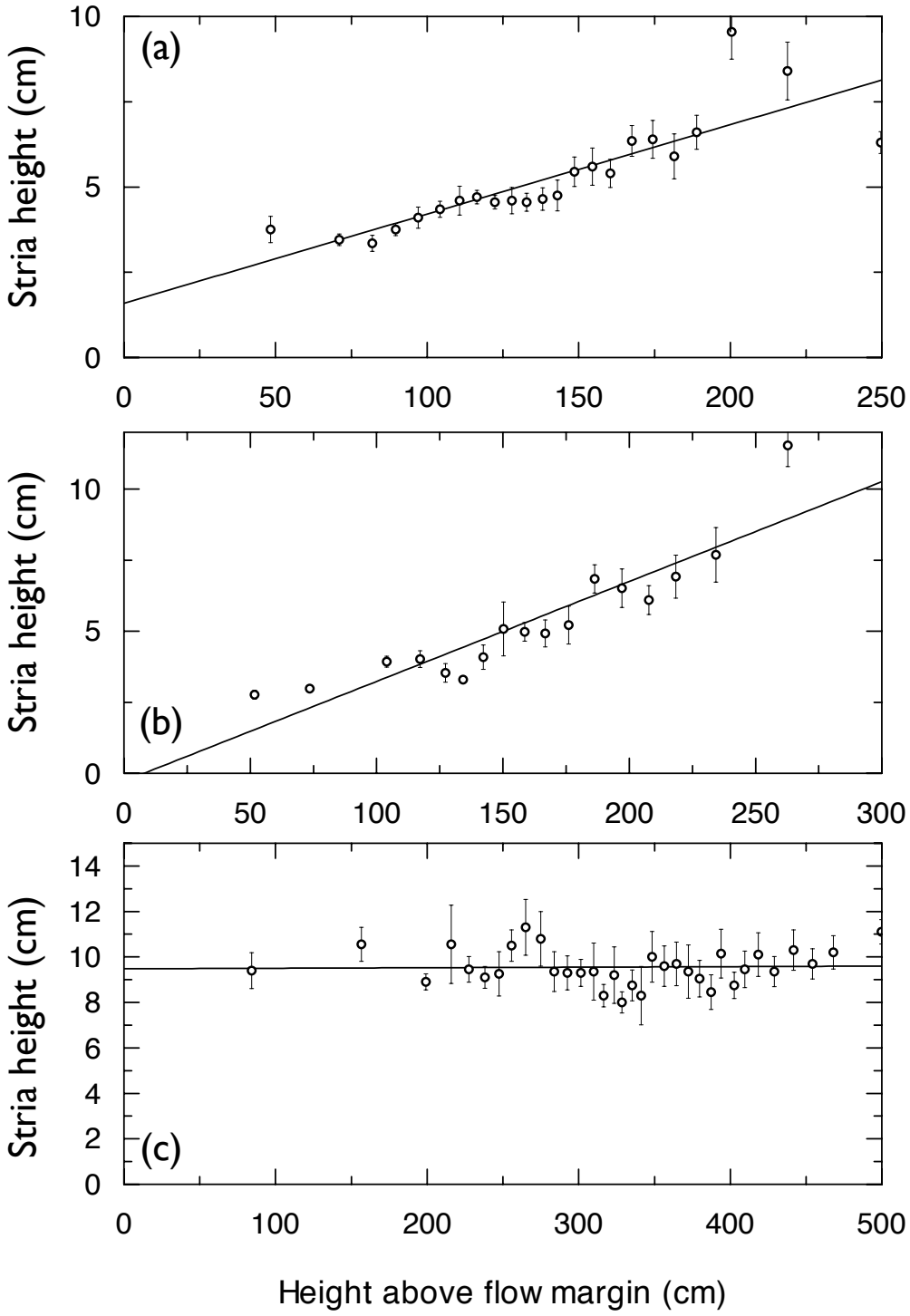

Figure 3.9: Striae height *vs.* position within the flow unit, in the Cheakamus basalts. In (a) and (b) measurements are made near a lower flow margin, and stria heights depend on their position within the flow. In (c), striae are sampled from slightly further into a flow unit, and show no variations in height. In all cases the displayed data points are averaged over 10 striae measurements, in order to reduce scatter. Best-fit linear regressions are shown for all panels.

Figure 3.10: An example of the increase in stria height s with respect to position above the flow margin, at the Whistler Train Tracks site. The dark rough strip of rock exposed at the bottom of this figure is the lower flow margin, which overlies a friable soil layer. Measurements of the height of striae seen in this figure are presented in Figure 3.9(b).

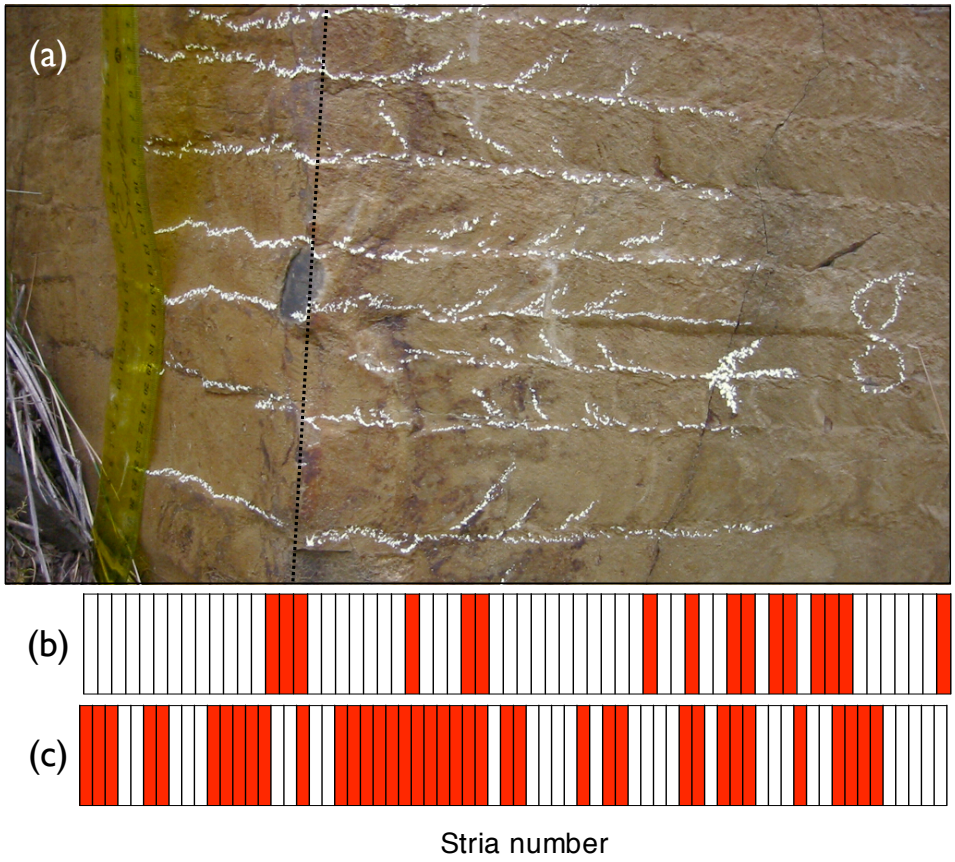

Figure 3.11: Correlations in the plumose direction. (a) shows a column from the Bridge Lake site where striae have been highlighted by lines of white chalk. The plumose on one face have been indicated by three short lines on each striae; the top of each plumose line is inclined in the direction of crack propagation for that stria. The dotted black line indicates a vertex, across which all adjacent striae, but one, cleanly meet. (b) and (c) show the direction of propagation of striae on two columns. Each striae is depicted as a vertical bar colored white if the stria formed from the left to the right, or red if from the right to the left.

position – striae can be matched up across a vertex. Furthermore, in almost all cases, the plumose lines on striae can be traced back to a column vertex, showing that most striae are initiated at one of their vertices. Both these observations have previously been made by Aydin and DeGraff [2], who suggested the interpretation that, when a crack advances across a column face and reaches a vertex, it can either halt, continue running onto another column face, or split into two continuing cracks.

When the stria propagation directions were measured, it was obvious that there was a bias to these directions on most columns. For long stretches, of at least a few meters, the plumose on some columns were preferentially pointed to the left, while the plumose on other columns tended to point right. Two examples of this are shown in Figure

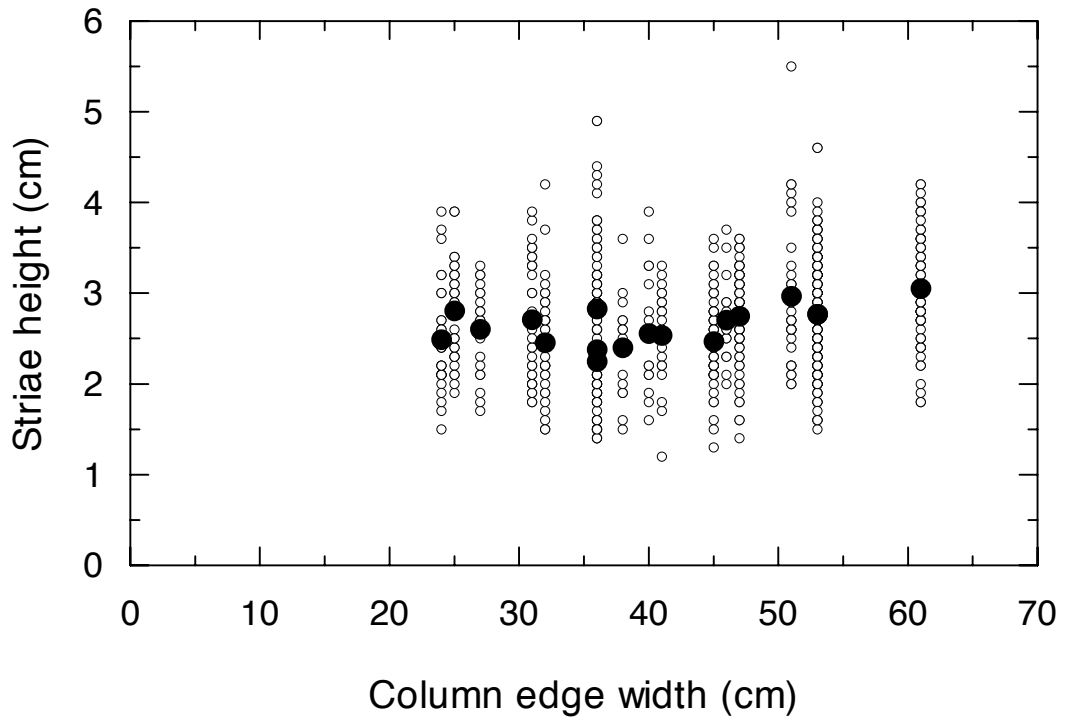

Figure 3.12: A comparison of stria heights on different column faces. Open circles show all stria measurements made, while the larger black circles show the average striae height on a particular column face, plotted against the width of that face.

3.11(b,c). In order to quantify the observed bias, the number of pairs of sequential striae that pointed in the same direction (left-left or right-right) was compared to the number of pairs of sequential striae that pointed in the opposite direction (left-right or right-left). If the direction of each plumose feature was determined at random, subsequent striae should be aligned exactly half of the time, on average. More precisely, since 835 such pairs were measured, statistical fluctuations would predict that a random distribution of this size would show aligned striae 50±3.5% of the time. In the case of the Bridge Lake site, plumose were found to be aligned much more often, 64±2% of the time.

Since the striae on adjacent faces in a colonnade appear to be correlated, it would be expected that the average stria size on any particular column face would not depend on the width w of that particular face, but only on the average $\langle w \rangle$. This expectation was tested at Bridge Lake, as shown in Figure 3.12, and no such dependence was found.

These results suggest that there may be some preferred directions, or pathways across the columnar fracture network, that are followed when striae advance, and confirm the suggestion that crack advances often continue to propagate through individual vertices.

3.3.6 Striae on Staffa

In the vicinity of Fingal's Cave, the Fingal's lava unit is at least 40 meters thick. The lower ∼15 meters of this unit is a remarkably well formed lower colonnade, and is topped by a thick entablature layer consisting of a much finer joint network. A lightweight extendable ladder was used to access large portions of the lower colonnade near Fingal's Cave, and stria heights were measured across most of the Fingal's unit. The resulting stria height measurements are shown in Figure 3.13.

The records of striae previously presented in Figure 3.4 might be considered somewhat sparse. In order to prove that the striae within the bulk of a lower colonnade have a constant average size that does not depend on position, a long, continuous set of stria measurements was gathered on both sides of the mouth of Fingal's Cave. More than a thousand striae were measured (more than across all CRBG sites combined), over the upper two thirds of colonnade height, as are summarized in Figure 3.13(a). Apart from a possible slight downward drift in the stria height over ten meters, there is no apparent dependence of the height of a stria on its position above the ash layer. The probability distribution function of the relative heights of these striae is identical, within error, to the probability distribution shown in Figure 3.6. A fit of the Weibull distribution to the observations gives the shape parameter $k = 2.6\pm0.2$, the scale parameter $b = 0.60\pm0.04$, and the offset s_0 = -0.59±0.05.

A further data set was collected near Horses Cave, 30 m west of Fingal's Cave, from near the base of the Fingal's lava, as shown in Figure 3.4. Unfortunately this area of the Fingal's lava did not have any safe spot to anchor a ladder, and this data does not fully connect to the data gathered around the mouth of Fingal's Cave. There is a slight increase in striae height with respect to distance above the ash layer, however this increase is less pronounced here than in either the CRBG or Cheakamus basalts.

As was shown in Figure 3.3.3, the average stria heights and column widths were measured at five sites within the Fingal's lava. These sites were all laid down at the same time, and are less than a kilometer apart - yet they differ in column scale by up to a factor of three. This could only be due to local cooling effects, and clearly indicates that the column scale is selected by local cooling behavior.

3.4 Undulations of the column width

The column size and stria height do not exhaust the length scales exhibited by columnar joints. An additional length scale inherent to columnar jointing was discovered during

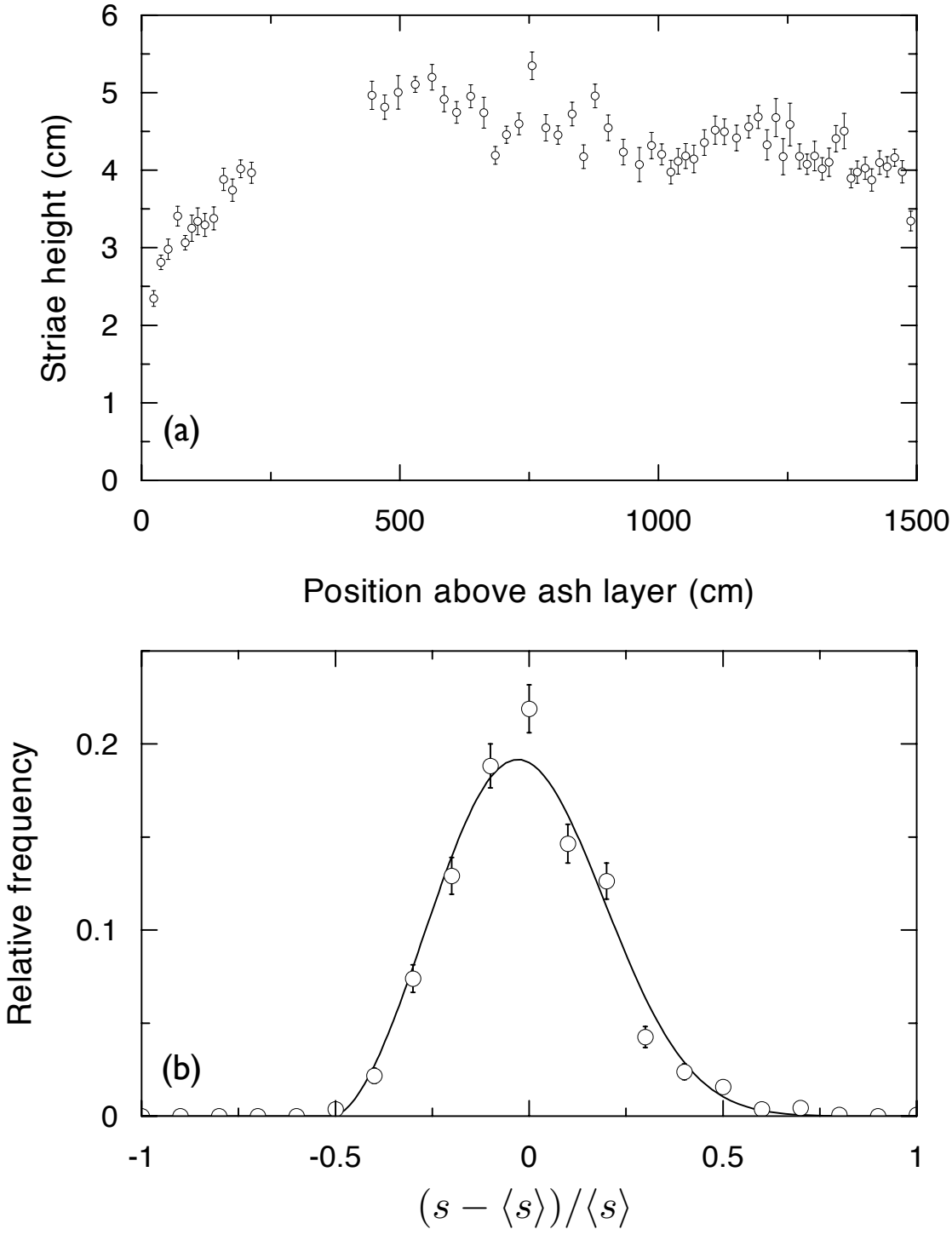

Figure 3.13: Stria height data from Staffa. (a) shows the stria height through most of the lower colonnade of the Fingal's lava unit, which meets the entablature at a height of 15 m. The displayed data are averaged over 25 measurements, to reduce scatter. (b) shows the probability distribution for the relative stria width, in data collected from more than 4 meters above the ash layer, with a fit to a Weibull distribution.

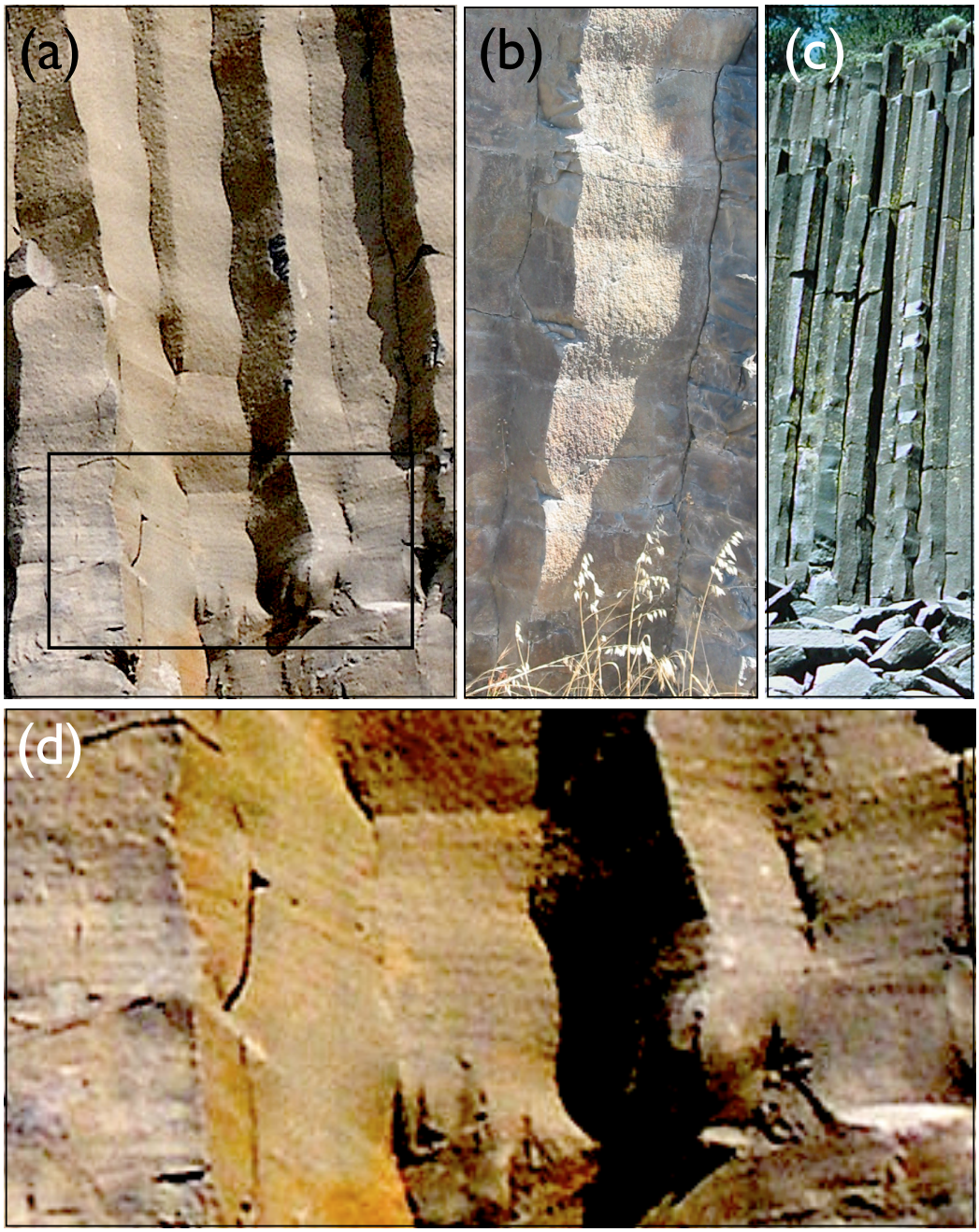

Figure 3.14: Examples of wavy columns near (a) Banks Lake, and (b) Bingen. Undulations of column faces can also be observed at the Devil's Postpile (c) in California. The rectangle in (a) is shown enlarged, and with increased contrast, in panel (d), so that the striae visible at this site can be more clearly seen. The wavelength of the undulations is much larger than the height of the striae.

Site Description	$\langle s \rangle$ (cm)	$\langle w \rangle$ (cm)	$\langle \lambda_z \rangle$ (cm)	$\langle \theta_k \rangle$
Chief Timothy	4±0.2	32±2	44±3	164±2°
Rock Creek	-	17±2	16±2	163±2°
Shepherd's Dell	-	35±3	36±4	158±2°
Bingen	-	31±2	39±2	164±2°
Banks Lake	6±1	55±3	68±10	-

Table 3.1: Observations of wavy columns: s is the stria height, w is the column face width, λ_z is the crest separation of each undulation (*i.e.* its full wavelength), and θ_k is the angle defined by the intersection of planes tangent to the flat faces of the column on either side of a crest. The oscillation wavelength λ_z is approximately equal to the column face width w.

the course of this field work – the scale associated with a periodic undulation of the column faces. This undulation takes the form of alternating regions where the cracks defining individual column faces advance and retire radially. This gives rise to a regular oscillation of the faces of columns, as shown in Figure 3.14. These "wavy columns" are uncommon, and only occurred at a small number of the sites visited in the CRBG. In BC, and on Staffa, no cases of wavy columns were measured, although the upper reaches of the Keremeos Columns did appear to be wavy. Wavy columns have not been observed in the laboratory, in starch colonnades.

The half-wavelength of the undulations of wavy columns is significantly larger than the stria height (see Table 3.1), and these undulations must, therefore, be the result of collective behavior occurring over several crack advances. On the other hand, the full wavelength of the undulations is approximately equal to the column edge width, or the column radius. The relative phase of these waves on adjacent columns, or adjacent faces on the same column, is unknown. Further, it is unclear if these undulations have sharp peaks, which have been subsequently smoothed by weathering, or if they form as smooth, roughly sinusoidal, curves. In either case, much of the surface of a wavy column consists of alternating flat sections, from which a kink angle between subsequent sections can be defined. This kink angle was observed to be reasonably consistent with about 160° at all sites where undulations were observed, as shown in Table 3.1. Assuming that the undulations have a single scalable shape, this result would imply that the amplitude of the undulations scales linearly with the column diameter.

Wavy columns bear a striking resemblance to sinusoidal cracks that appear in thin, thermally stressed strips. Yuse and Sano [117] showed that a slowly advancing crack tip intruding into a cooling glass strip can advance in an oscillatory manner. Ronsin and Perrin [87] studied the transition between straight and wavy cracks in a periodic

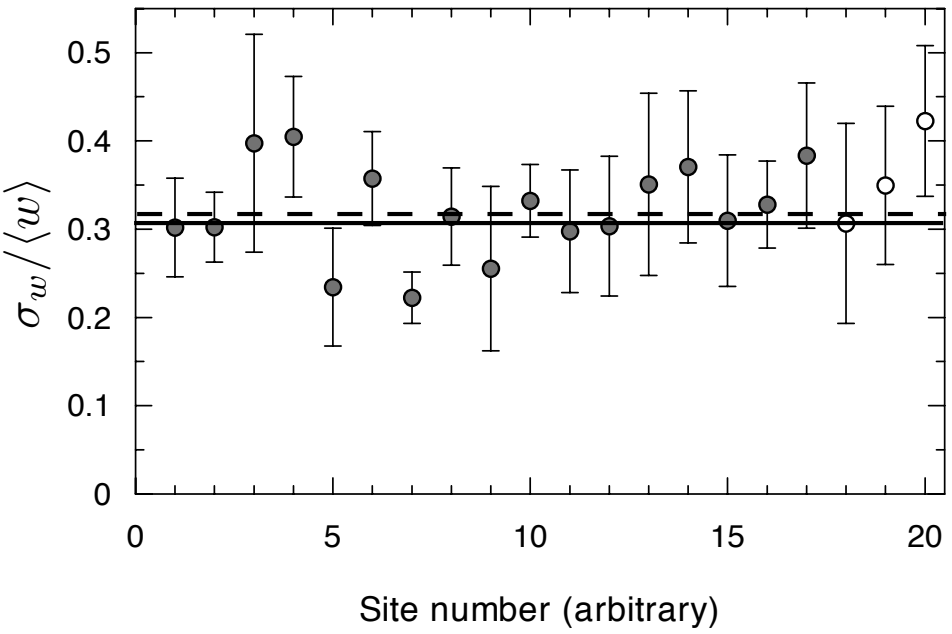

Figure 3.15: A relative measure of the disorder observed in the column edge widths for 20 sites in the CRBG. Plotted is the standard deviation, σ_w, divided by the mean, $\langle w \rangle$, of the column edge width distribution. This dimensionless ratio would be zero for perfect hexagonal columns. Sites with black circles (No. 1-17) represent lower colonnades, or sites with an uncertain direction of cooling, while those with white circles (No. 18-20) represent upper colonnades. The solid line is an error-weighted mean of all measurements. The dashed line shows the equivalent statistic for desiccated starches reported in Section 2.5.

array, and showed that an oscillatory instability develops when cracks get too far apart from each other. Although these experiments were done in 2D analog systems, it seems entirely plausible that a similar instability could generate wavy columns in 3D columnar joints. This would suggest that wavy columns might also occur when the average column diameter is larger than some critical size, given any particular cooling rate. This interpretation is problematic, however, in that the stria heights on wavy columns do not seem unusually small (or large) for the given column diameter. It remains reasonable, however, to conjecture that these undulations are the result of an oscillatory instability of the fracture tips, as they advance to form the column faces.

3.5 Column ordering in lavas

As demonstrated in Section 2.5, the patterns of columnar jointing in starch are not perfectly hexagonal, but retain a certain residual level of disorder. Even mature arrays of

Description	$\sigma_A/\langle A\rangle$	$\sigma_w/\langle w\rangle$	σ_N	σ_θ	% 105°-135°
Desiccated starch	0.32±0.01	0.313±0.015	0.86±0.05	14.6±0.3°	70.1±1.7%
Giant's Causeway	0.32±0.02	0.342±0.02	0.75±0.06	14.3±0.6°	69.7±1.4%
CRBG	-	0.305±0.014	-	15.6±1.2°	67±3%

Table 3.2: Statistical measures of disorder in columnar jointing. From left to right: the relative variation (standard deviation divided by the mean) in column cross-sectional area A; the relative variation in edge width w; the standard deviation in the number of neighbors N; the standard deviation in the joint angle θ; the fraction of Y-junctions.

columns exhibit significant disorder, which is not eliminated by the further evolution of the crack network. It is interesting to compare the degree of disorder found in experimental systems to that found in the CRBG. The distributions of the column edge widths w and column joint angles θ were measured at a range of sites, in different flow units. Figure 3.15 shows a representative dimensionless statistic of the degree of disorder in the column width distribution for 20 distinct sites. The width of the distribution of column edge widths is remarkably consistent for widely separated sites in the CRBG, and agrees within error with the same statistic measured in mature starch colonnades.

The joint angle distribution was also measured at three sites. It was difficult to make accurate measurements of joint angles on standing columns, due to the constrained geometry. Instead, most joint angle data were taken from nearby columnar rubble. The distribution of joint angles was similar at all sites, and, as expected, clustered around 120°. The standard deviation of the joint angle distribution averaged over all sites was 15.6±1.2°, which is in excellent agreement with the standard deviation of this distribution that was found for starch columns in Section 2.5.

A summary of these results is given in Table 3.2. The statistics of both the joint angle distribution and the column edge width distribution agree with the corresponding measures of disorder in the survey of O'Reilly [75], and in the starch experiments described in Section 2.5. This implies that the crack network of columnar jointing in lava does not evolve toward perfect hexagonal symmetry, but rather to an dynamic pattern whose statistics deviate from those of a perfect hexagonal network by an amount which is similar in all well-developed patterns, as was discussed in Section 2.5.

Aydin and DeGraff [2] showed that the stick-slip growth of striae can allow sequential striae to be slightly misaligned, giving rise to a fracture network that can change as it advances. They proposed that this adjustment mechanism explains why the surface of a lava flow shows rectilinear cracks, while the interior shows hexagonal cracks [2]. This ordering behavior is evident both in igneous columnar joints, and in their laboratory

analogs. But Aydin and DeGraff's mechanism also works equally well to explain the continued evolution of the fracture network, even after it has reached a roughly hexagonal state. This continued evolution can act to maintain the measured residual level of disorder, as happens in starch colonnades. Additionally, the presence of the oscillatory instability shows that igneous columnar jointing can also have coherent, and not merely random, joint motion in the mature state.

3.6 Conclusions of field work

In this chapter, observations from several field expeditions were presented. The basalts of the Columbia Plateau were visited, as an example of a spatially uniform, chemically homogeneous group of basalts that all share similar emplacement histories. The more varied igneous rocks of southwestern British Columbia were also studied, in order to confirm the findings made in the Columbia Plateau in a wider range of lava types and emplacement conditions. Finally, a detailed case study of the Fingal's lava unit on Staffa, Scotland, was made.

Data collection at these field sites focussed on the details of striae, small markings on the faces of columns, which offer insight into the cooling histories of their host columns. When site conditions permitted it, measurements were made of the height of striae, their position with respect to the cooling flow margins, and their direction of propagation. The average stria height was found to be typically 5%-20% of the average column side width at any site. This height only seems to depend on this average width, and not on the width of the particular column observations are made on. Unusual cooling conditions, such as the impoundment of a flow against an ice wall described in Section 3.3.3, can lead to stria heights that lie outside this range. The relationship between column diameter and stria height will be used in the following chapter to show that the fracture spacing of a colonnade is inversely related to the cooling rate of the lava flow in which it forms.

Near the lower flow margin, striae increase in height as the distance to the cooling surface increases. This will be shown, in Section 4.2.2, to agree with the predictions of diffusive cooling across the flow margin. More than a few meters away from a flow margin, stria heights cluster around a single average size at each site that was studied. Although no striae were observed near an upper flow margin during the course of this research, Hardee has previously observed how conductive cooling near the upper surface of the Kilauea Iki lava lake is enhanced by crack-aided cooling within the bulk of the lava lake [41]. The data presented in this chapter show no distinction between upper and lower colonnades, indicating that cooling likely proceeds in the same manner in both

type of feature. A simple cooling model which describes, and quantifies, the crack-aided cooling process, independently of gravity, is developed in Section 4.2.3.

The statistical distribution of stria heights was studied in this chapter. There is no dependence of the relative height of one striae on the height of its predecessor, or on the width of the specific column on which it is observed. Instead, each stria height appears to be an independent random variable selected from a probability distribution that is well fitted by a Weibull function. These results agree with a simple fracture formation model, which is described in Section 4.2.4.

Although each stria advance seems to be independent from its predecessor, individual striae *are* related to their horizontal neighbors - on adjacent faces or columns. Aydin and DeGraff have suggested that this is due to cracks propagating across several column faces sequentially, before they terminate [2]. The data presented here validate that hypothesis, but also show that the crack propagation pathways may be persistent, at least statistically, over many individual stria advances.

While measuring the column edge widths and striae heights, an additional length scale was discovered to occur in the pattern of igneous columnar joints - that of wavy columns. This undulatory instability of the column crack tips, as they grow into the cooling lava flow, is reminiscent of a similar type of wavy cracks that can form in cooling glass plates. Although wavy columns were only observed at a handful of sites, they appear to have a wavelength comparable to the column radius, and which is too large to be formed by the action of individual stria advances.

The ordering of igneous columnar joints was considered, in light of experimental observations reported in the previous chapter. The distribution of column edge widths was found to be constant across twenty field sites, and found to agree with the level of disorder inherent in a well-developed starch colonnade. This suggests that the pattern of columnar jointing is independent of material properties, and material defects such as bubbles or inhomogeneities.

In the following chapter, the field results presented here will be analyzed with respect to a simple advection-diffusion model, which will allow a direct comparison to be made between these results, and the experimental results presented in the previous chapter.

Chapter 4

Modeling and analysis

In this chapter the formation of columnar joints is considered in relation to an advection-diffusion transport model. The origin of columnar joints lies in the tensile stresses caused by the shrinkage of their host material. For starch, evaporation causes shrinkage, while for lava, cooling causes shrinkage. In both cases, the stress field is slaved to a transport problem, and thus any length scale natural to fracture formation will be linked to the length scales associated with the transport of either heat or moisture.

In Section 4.1 the details of crack formation in a desiccating starch-cake are described, while Section 4.2 considers the case of a cooling lava. Section 4.3 summarizes the main features of the advection-diffusion model, and presents a simple dimensional analysis of the problem. The existence of hysteresis in the scaling of columnar joints is discussed in Section 4.4. A brief chapter summary is given in Section 4.5.

The material in this chapter is largely developed in References [29, 30, 33].

4.1 Advection-diffusion in starch

The range of experiments that have been presented in Chapter 2, in addition to the additional experiments performed by Müller [70, 71, 72], Toramaru and Matsumoto [106], and Mizuguchi *et. al.* [67], present a rather complex picture and require careful interpretation. Even restricted to the question of how the average column cross-sectional area scales with the desiccation rate, it is still difficult to extract a single, simple answer from the data. Taken together, however, the experiments make it possible to draw some important general conclusions about the mechanism of scale selection in columnar joints.

4.1.1 Nonlinear diffusion in starch

The dynamics of columnar jointing in starch can only be understood in conjunction with the dynamics of the moisture content within the sample. Given the observations described in Section 2.2.4, a nonlinear diffusion equation such as

$$\frac{\partial C}{\partial t} = \nabla \cdot [D(C)\nabla C], \tag{4.1}$$

where the hydraulic diffusivity D depends on the moisture concentration C, is appropriate to model the moisture transport in the bulk of the starch.

In the case of a drying half-space on $z > 0$, moisture transport in the horizontal x and y directions can be neglected. By applying the chain rule to Equation 4.1, and considering only the vertical z direction, it is easily shown that

$$\frac{\partial C}{\partial t} - D(C)\frac{\partial^2 C}{\partial z^2} = \left(\frac{\partial C}{\partial z}\right)^2 \frac{dD}{dC}. \tag{4.2}$$

The moisture concentration C is continuously decreasing in time as the starch-cake dries, and, as was shown in Section 2.2.4, the curvature $\partial^2 C/\partial z^2$ is positive once the starch is drier than a critical moisture concentration of $C = 0.25 \pm 0.05$ g/cm^3. Equation 4.2 therefore implies that, below this critical value, $D(C)$ is a strictly decreasing function. It was further shown in Section 2.2.4 that, for wet enough starches, a 4 cm thick sample dries uniformly. This implies that the effective diffusivity must be comparatively large for a large enough C. Somewhere between these two regimes, near the transition in drying behaviors observed at $C = 0.3$ g/cm^3, there must be a minimum in $D(C)$.

The Taylor expansion

$$D(C) = D_0 + D_2(C - C_0)^2 + ... \tag{4.3}$$

can be made around the minimum value of $D(C)$. Since the position of the fracture front χ is in the vicinity of this minimum, tracking the particular concentration $C_f = 0.20 \pm 0.005$ g/cm^3 (see Section 2.2.5), it will likely be subject to an effective diffusivity close to D_0. An initial estimate of D_0 can therefore be made by considering the ordinary diffusion equation

$$\partial_t C = D_0 \nabla^2 C. \tag{4.4}$$

If the position χ follows the depth of constant $C = C_f$, then the solution

$$\chi(t) = \sqrt{4D_0 t}\ \mathrm{erf}^{-1}(C_f/C_{init}) \tag{4.5}$$

arises from Equation 4.4 applied to an initially uniformly wet half-space, with a dry dirichlet boundary condition at $z = 0$. This boundary condition would represent the maximum drying efficiency possible at the upper drying surface. As any real experimental conditions will not be this effective, Equation 4.5 will lead to an estimate of the upper bound on D_0. Given the data presented in Section 2.2.4, which was dried nearly as quickly as was experimentally possible, and $C_{init} = 0.3$ g/cm^3, this estimate is $D_0 = (3\pm2)\times10^{-9}$ m^2/s. This is somewhat lower than the diffusivity measured by Müller, who suggested that D was $(1.7\pm1.0)\times10^{-8}$ m^2/s [71]. However, Müller's value was based on measurements of mass changes during only the first 5 hours of evaporation, which means he was probably sampling the large effective diffusivity of wet starch, rather than the diffusivity relevant to the formation of the drying front.

A more accurate estimate of $D(C)$ can be obtained by integrating Equation 4.1 to give the concentration dependent diffusivity

$$D(C) = \frac{\int_{z_0}^{z} (\partial C/\partial t) dz'}{\partial C/\partial z}, \tag{4.6}$$

where it has been assumed that moisture is only transported along the z axis, that the sample lies within $0 \leq z \leq z_0$, and that a no-flux boundary condition exists at the lower boundary $z{=}z_0$. Figure 4.1 shows $D(C)$ as calculated from Equation 4.6, and the water concentration data presented in Section 2.2.4. There is a broad minimum in $D(C)$, reaching $D_0 = 1.1 \times 10^{-9}$ m^2/s between approximately $C = 0.1$ g/cm^3 and 0.3 g/cm^3. Above a concentration of 0.3 g/cm^3, the diffusivity must strongly increase with C, as the starch-cake dries almost uniformly from saturation down to this moisture concentration. However, under these wet conditions $\partial C/\partial z$ is very small, and these data cannot be reliably used to find $D(C)$.

A simple empirical model of water transport in a drying medium can be expressed by a pair of exponential terms,

$$D(C) = D_l e^{k_l C} + D_v e^{-k_v C}, \tag{4.7}$$

where the constants D_l and k_l in the first term describe liquid water transport, and the constants D_v and k_v in the second term describe vapor water transport. This is similar to a model developed by Pel *et al.* [80], who proposed the slightly different form

$$D(C) = \begin{cases} D_l e^{k_l C} & C \geq C_0 \\ D_v e^{-k_v C} & C \leq C_0 \end{cases} \tag{4.8}$$

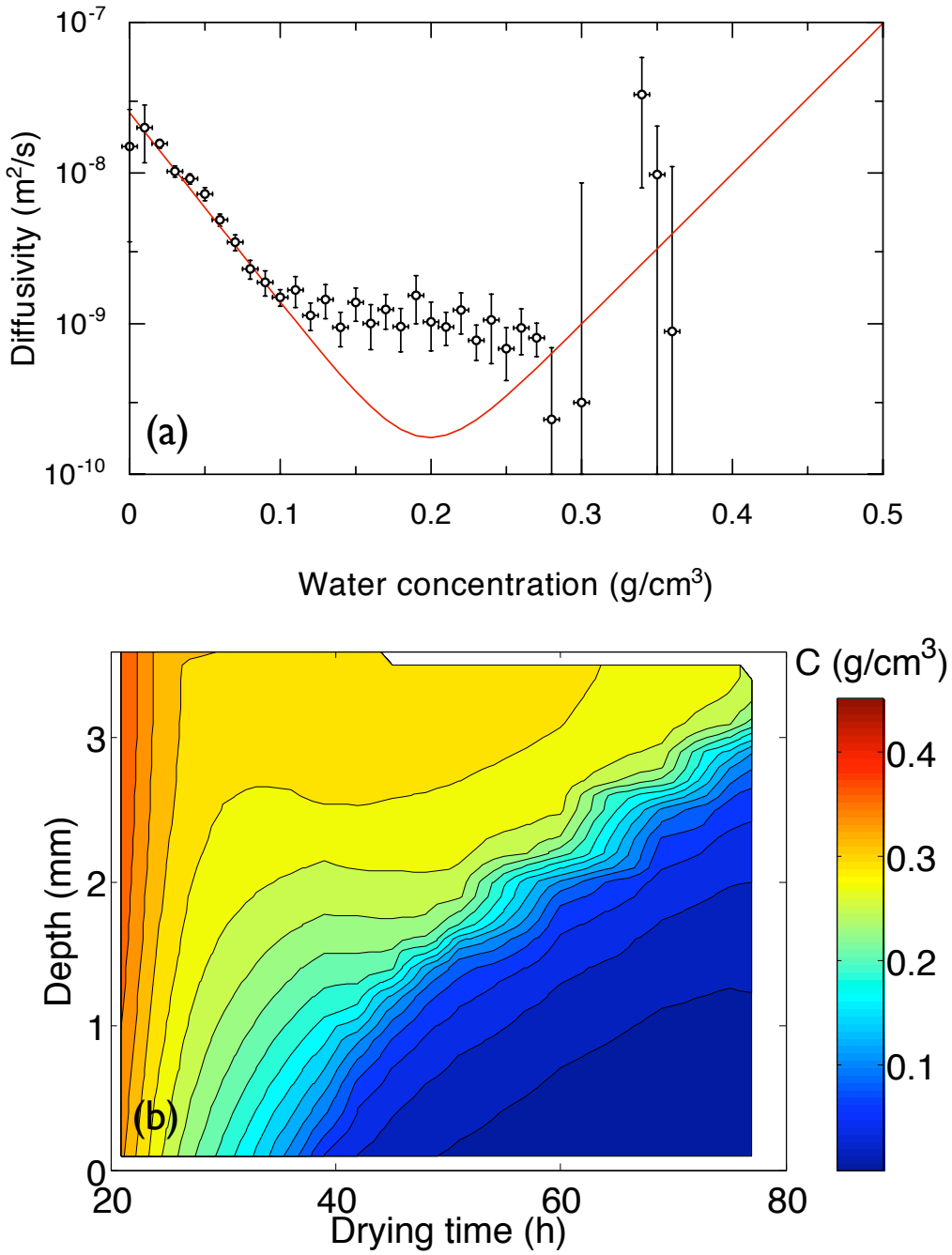

Figure 4.1: The data points in (a) show the hydraulic diffusivity $D(C)$, averaged over 0.01 g/cm^3 bins, as calculated from Equation 4.6. For low concentrations the diffusion of water vapor dominates, while at high concentrations liquid water moves through capillary bridges between the grains. A simple model of these two types of water transport (red line), given in Equation 4.7, captures the most essential details of this behavior, and (b) predicts a moisture concentration field for a controlled experiment that closely matches the observed one shown in Figure 2.9(b).

in order to compute an analytic solution of the nonlinear diffusion equation. However, the sharp minimum predicted by the discontinuous derivative of $D(C)$ in Equation 4.8 is not observed in either the data of Pel *et al.* [80], or in the data presented in Figure 4.1(a).

A numerical least-squares fit of the constants in Equation 4.7 to the nonlinear diffusion equation was performed. The measured evaporative flux $q_m(t)$ from the controlled experiments described in Section 2.2.4 was used as an upper boundary condition, and a no-flux boundary condition was assumed at the lower boundary $z = z_0$. This fit attempted to match the measured moisture profile given in Figure 2.9(b) by minimizing the sum of the squares of the differences between this data and the fit output. The resulting nonlinear diffusion model, using $D(C)$ as given by Equation 4.7 and its best fit parameters, closely matches the measured concentration dependence of D, as shown in Figure 4.1(a). Further, when driven by the measured surface evaporation rate, this model predicts a water distribution, shown in Figure 4.1(b), that is close to that observed in the experiments (see Figure 2.9(b)). This accuracy is reasonable, especially considering the simplicity of the model.

The empirical models described above can be, to a certain extent, derived from the continuity equation for moisture in a starch-cake:

$$\frac{\partial C}{\partial t} = -\nabla \cdot (\mathbf{J}\rho_w), \tag{4.9}$$

where the mass flux $\mathbf{J}\rho_w$ consists of both a liquid component $\mathbf{q}_l$ and a vapor component $\mathbf{q}_v$ [74]. During drying, as the water concentration decreases, liquid water becomes confined to smaller and smaller water bridges between grains, decreasing transport efficiency. When water bridges form a connected network, the liquid flux $\mathbf{q}_l$ is driven by the capillary pressure $P_c = -2\gamma/R_w$, and obeys D'Arcy's law,

$$\mathbf{q}_l = -\frac{\kappa_w(C)\rho_w}{\mu}\nabla P_c, \tag{4.10}$$

where the unsaturated permeability $\kappa_w(C)$ depends on the water concentration, and where ρ_w and μ are the density and viscosity of water, respectively. When the water concentration is lower than 0.30 ± 0.01 g/cm^3, as was suggested in Section 2.2.8, the capillary network will enter the pendular regime and will lose connectivity, causing capillary transport to cease.

On the other hand, the opening of pore space allows more connected volume to be accessible to vapor transport, and thus the effective diffusivity (with respect to the total

sample volume) of vapor increases as C decreases. The vapor flux component of the right hand side of Equation 4.9 is purely diffusive, and obeys Fick's first law,

$$\mathbf{q_v} = -\epsilon_0 D_v(\phi - C/\rho_w)\nabla C_v, \tag{4.11}$$

where D_v is the diffusivity of water vapor in air, ϵ_0 is the tortuosity of the pore network through which the vapor must move, and C_v is the concentration of water in the vapor phase [74].

Finally, as water evaporates, the radius of curvature of the capillary water bridges increases, thereby increasing the vapor pressure of water in equilibrium with the bridges [74]. If this equilibrium holds, then C_v will be related to the capillary pressure P_c by the Kelvin equation,

$$C_v = C_{sat} e^{P_c V_m/RT}, \tag{4.12}$$

where C_{sat} is the saturated moisture concentration, V_m is the molar volume of water vapor, and R is the universal gas constant. Since the capillary pressure in the water bridges between the starch grains will depend only on their radius of curvature, which in turn depends only on C (albeit in some complex way) then Equations 4.9 - 4.12 can in principle be combined to yield Equation 4.1. The simplified model given in Equation 4.7 captures the essentials of both the liquid and vapor transport mechanisms, and the cross-over dynamics between them [80].

4.1.2 The scaling of starch columns

It was shown in Chapter 2 that the scale of columnar joints in a dried starch cake is inversely dependent on the fracture front velocity. In this section it will be shown how this scaling arises from the consideration of moisture transport.

The porous medium equation that can be obtained from Equation 4.1 by setting $D(C) \sim C$ is known to give rise to propagating self-similar solutions with parabolic shape [4]. Analogously, as has just been shown, the shape of the moisture concentration front shown in Figure 2.10 can be explained by the presence of a minimum in $D(C)$ at a moisture concentration of around 0.30 g/cm^3. Such a sharp front indicates a shift from flow-limited to evaporation-limited dynamics [23, 74], and is typical in drying slurries [1, 23, 78, 91].

Now consider a starch-cake in which the fracture front and the drying front are both moving at a constant speed v in the (inwards) z direction, as in the fully controlled experiments described in Section 2.4.3. A change of coordinates into the co-moving

reference frame introduces an advective term into Equation 4.1,

$$\partial_t C = v\partial_z C + \nabla \cdot [D(C)\nabla C]. \tag{4.13}$$

Since the position of the fracture front follows closely behind the desiccation front, it is subject to an effective diffusivity close to the bottleneck diffusivity D_0, the linear term in the Taylor expansion around the minimum in $D(C)$. Under these conditions a constant moisture content boundary condition leading the front, and a constant flux boundary condition trailing the front, are appropriate. These will quickly lead to a time-independent version of Equation 4.1 which assumes the non-dimensional form

$$\nabla^2 C + \mathrm{Pe}\ \partial_{z'} C = \text{nonlinear terms}, \tag{4.14}$$

where $z' = z/L$, and the Péclet number $\mathrm{Pe} = vL/D_0$ measures the ratio of advective to diffusive effects. Here, the nonlinear terms are small near $C = 0.3$ g/cm^3, and at least second order in C, so can be largely neglected. The characteristic length scale L of this problem is taken to be the square root of the column cross-sectional area, for convenience.

Since the Péclet number is the only dimensionless parameter that determines the scaling of the advective-diffusive drying front, and since it is this drying front that generates tensile stresses, the scaling of columnar joints can be expected to depend chiefly upon Pe. As will be explained in Section 4.3, the Péclet number associated with columnar joints should be of order one.

The constants composing the Péclet number in starch have been measured directly in a range of experimental conditions. The minimum diffusivity $D_0 = 1.1\times10^{-9}$ m^2/s was measured in the previous section. In Section 2.4.1 thick starch-cakes were described that had directionally dried under fixed heat lamps, along with measurements of how the fracture spacing evolved within those samples. By continuously monitoring the mass of these cakes during drying, the position of the crack front was determined at all times, along with the fracture front velocity, v, using the methods described in Section 2.3.2. As summarized in Figure 4.2, the fracture spacing continuously increases throughout the depth of the sample, but remains inversely proportional to the front velocity, which continuously decreases.

The fracture spacing was also measured in experiments that fixed the average fracture speed through feedback control, as described in Section 2.4.3. Under these conditions, which are analogous to the way columns form in cooling lava, a column scale within some relatively narrow range was selected. Figure 4.2 shows how the fracture spacing in

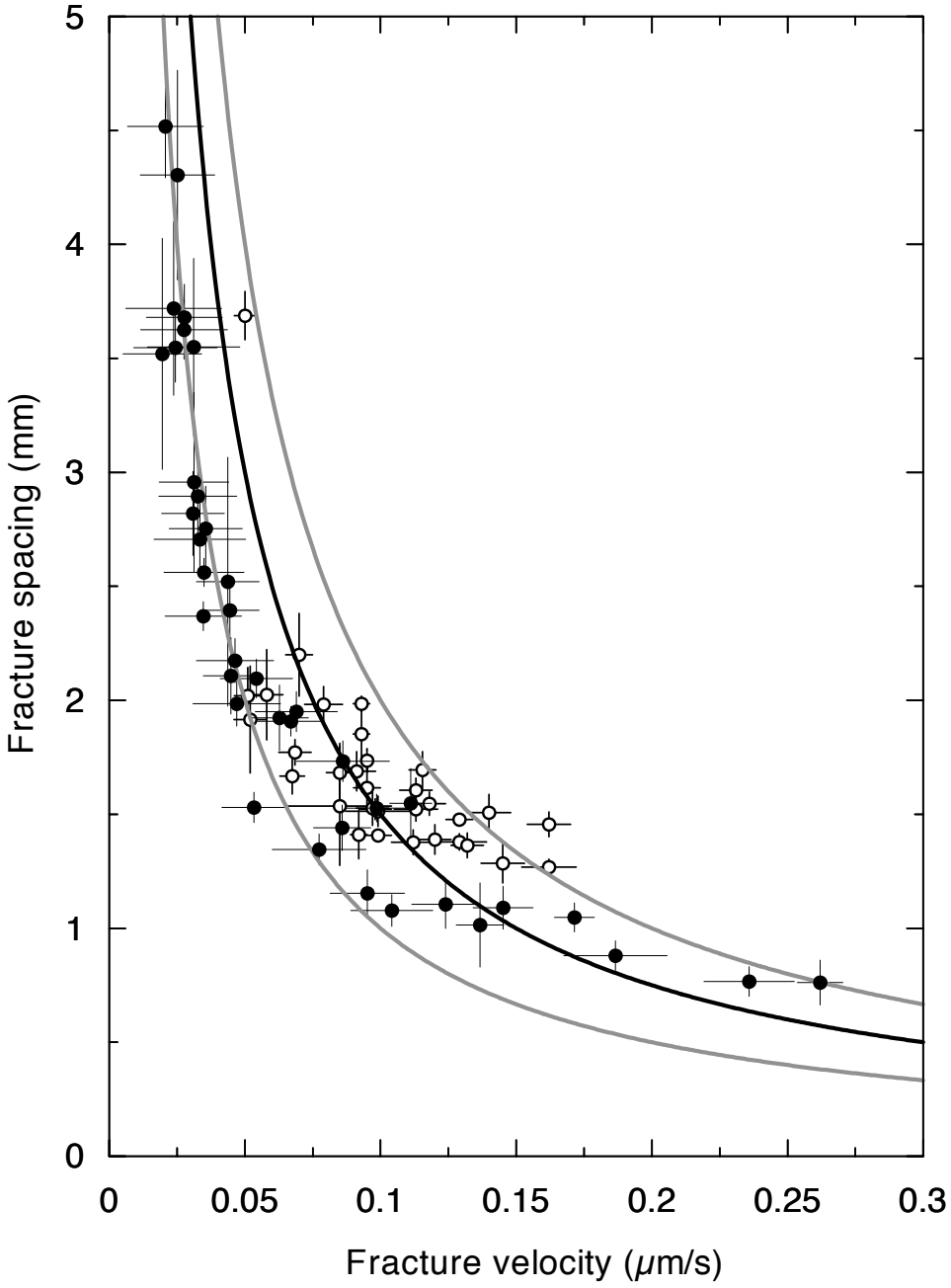

Figure 4.2: The average fracture front velocity v, and the fracture spacing χ in starch colonnades are inversely related. Closed circles show the fracture spacing in two deep samples as they coarsen in response to gradually slowing drying fronts. Open circles show the final fracture spacing that was selected in individual experiments in which the evaporation rate was kept constant. Solid lines indicate curves of constant Péclet number $\mathrm{Pe} = 0.1$, 0.15, and 0.2.

these experiments also indicates that the average fracture advance speed and the fracture spacing are inversely related. In almost all cases the measured columnar fracture spacings correspond to a range of Péclet numbers from 0.1 to 0.2. This result will be discussed further in Section 4.3. The fact that all data do not fit on a single line, even accounting for experimental error, will be discussed in Section 4.4, which deals with hysteresis.

4.2 Advection-diffusion in lava

The advection-diffusion model developed in the previous section requires only slight modification to apply to the columnar jointing of lavas. The thermal formulation of Equation 4.14 is simply

$$\nabla^2 T + \mathrm{Pe}\ \partial_{z'} T = 0, \tag{4.15}$$

where T is the temperature field, and $\mathrm{Pe} = vL/\kappa$. The thermal diffusivity κ of basalt does not vary by more than a factor of two or so over the temperature range $0 \leq T \leq 1500°\mathrm{C}$ [69, 73, 107], so the nonlinear terms in Equation 4.14 have been neglected.

In the case of lava, it is known that heat flow through cracks provides an important, indeed dominant, contribution to the total heat transport budget [13, 41]. The crack surfaces can be treated as boundary conditions on Equation 4.15. If the surface of a crack at a point is actively cooled to some constant temperature T_c, then the heat flux into that crack from the lava is given in dimensionless terms by Newton's law of cooling

$$\partial_{y'} T = \mathrm{Bi}(T - T_c), \tag{4.16}$$

where the Biot number $\mathrm{Bi} = hL/\lambda$. Here, λ is the thermal conductivity, h is a phenomenological heat transfer coefficient, and the coordinate $y'{=}y/L$ is perpendicular to the crack surface. Cooling in the fractured lava is greatly enhanced by the boiling and reflux of groundwater in the cracks [13, 41]. The high efficiency of this convective heat transfer process, compared to that of thermal conduction, suggests that the Biot number is large in cooling lava. However, although fracture-aided cooling is driven by the boiling of water, the fracture front in lava is located in a region at a much higher temperature. The fracture tips are therefore in a region where ordinary thermal conductivity dominates, and up to several meters distant from the cooler convective zone [41].

It should be noted that if, as was previously assumed, cracks in starch do not significantly enhance the water transport, then the corresponding "hydraulic Biot number" is effectively zero.

25 years of observations of the gradual solidification of the Kilauea Iki lava lake,

formed in 1959, show that Equation 4.15 accurately describes both the isotherms that are measured in bore-holes, and the position of the solidification front [41]. These data yield values of $\kappa = 5.0 \times 10^{-7}$ m^2/s, and $v = 6.7 \times 10^{-8}$ m/s for that site. Observations of columnar jointing near the Kilauea caldera of Mauna Loa (although not at Kilauea Iki) suggest that recent columnar jointing in the vicinity is typically rather large, with diameters in the range 1.5-3 m [79]. From these data, the Péclet number associated with the formation of columnar joints at the Kilauea crater can be seen to be 0.15, to within a factor of two or so. This is in remarkable agreement with the value of Pe just found to describe the scaling of columnar joints in starch. This estimate will be confirmed, and expanded upon greatly, in Sections 4.2.2 and 4.2.3, which will describe the application of a simple thermal model to the measurements reported in Chapter 3. First, however, a brief summary of the physical properties of basalt is necessary.

4.2.1 The physical properties of the CRBG

The important physical properties of basalt from the Columbia River Basalt Group and their estimated values are given in Table 4.1. The density ρ_b was measured directly from rock samples collected in the field, at room temperature. The thermal conductivity λ has been measured in the Picture Gorge member of the CRBG by Murase and McBirney [73], and does not depend strongly on temperature. The glass transition temperature T_g is taken to be 750°C to be consistent with the observations of Ryan and Sammis [90], although the implications of a higher T_g will be considered. Most of the remainder of the values in Table 4.1 are compiled from sources cited in Touloukian *et al.* [107]. Although the CRBG has been well characterized chemically, most of its physical properties have to be estimated from other tholeiitic basalts (typically from recent Hawaiian eruptions). When any temperature dependence of a property is known, the value close to, but below, the value relevant to the glass transition temperature is chosen.

4.2.2 The conductive cooling regime in the CRBG

Within the bulk of a cooling lava flow, heat moves diffusively, and

$$\partial_t T = \kappa \nabla^2 T, \tag{4.17}$$

where T is the temperature field. In addition to the diffusive motion of heat described by this equation, the presence of water within cracks can lead to convective heat transport which will enhance cooling under certain conditions [13, 41]. However, close enough to

Property	Symbol	Value	References
Density	ρ_b	2 850 kg/m^3	measured
Thermal diffusivity	κ	6.5×10^{-7} m^2/s	$\lambda/\rho_b c_p$
Thermal conductivity	λ	1.7 W/(m °C)	[73, 81, 107]
Poisson's ratio	ν	0.2	[79, 107]
Young's modulus	E	50 GPa	[3, 107]
Specific heat	c_p	900 J/(kg °C)	[41, 69, 81, 107]
Latent heat	$\mathscr{L}$	400 kJ/kg	[41]
Linear coefficient of thermal expansion	α	7×10^{-6} °C^{-1}	[90, 107]
Glass transition temp.	T_g	750	[60, 90]
Tensile strength	σ_{max}	8.5 MPa	[3, 79]

Table 4.1: Estimated physical properties of basalts from the CRBG.

a flow margin, diffusion through the flow surface will be the more efficient of these two mechanisms. Therefore, diffusive effects will be discussed alone here, while convective effects will be treated in the next section.

In considering the formation of a lower colonnade, the initial state of the lower part of a flow unit can be modeled as a half-space, $z \geq 0$, which is initially at a high temperature T_1 at time t=0. This assumption is particularly appropriate in the CRBG, the massive flow units of which Ho and Cashman showed were emplaced isothermally [43].

Two types of boundary condition are here considered on the cooling surface $z = 0$. This basal surface could be held at a constant (cooler) temperature T_0, corresponding to a dirichlet boundary condition on T, or could be thermally coupled to a second half-space $z < 0$, initially at T_0. These two boundary conditions represent the limiting cases of emplacement on a wet, porous substrate where water can efficiently extract heat from the basal lava surface, or emplacement on a dry thermally conductive substrate, respectively. In reality, cooling can be expected to proceed somewhere between these two extremes. The solution to Equation 4.17 for $t > 0$, under either of these boundary conditions, is

$$U(z,t) = \operatorname{erf}\left[\frac{z}{\sqrt{4\kappa t}}\right], \tag{4.18}$$

where the reduced temperature $U = (T - T_0)/(T_1 - T_0)$ for the dirichlet boundary condition, or $U = (2T - (T_0 + T_1))/(T_1 - T_0)$ for the coupled half-space boundary condition.

It will be assumed that stria marks are produced by cracks which propagate between an average initiation stress σ_{init} and a (lower) termination stress σ_{term}, and that these stresses are directly related to corresponding material temperatures T_{init} and T_{term}. The validity of these assumptions will be discussed in Section 4.2.4. Under these assumptions,

the average stria height $\langle s \rangle$, at a particular vertical position z, represents the distance between the two fixed isotherms $T = T_{init}$ and $T = T_{term}$, when those striae were formed. Thus, the stria heights can be used as a proxy to track the evolution of the temperature field during the cooling process. Conversely, models of the evolution of the temperature field have been used to predict features of the stria height, at least on average [20, 38, 85], but these models have not been previously well tested or calibrated.

In dimensionless form, the average crack initiation temperature is $U_{init} = U(T_{init})$ and the crack termination temperature is $U_{term} = U(T_{term})$. The above assumptions, along with Equation 4.18, imply that

$$\langle s \rangle = \left[\frac{\mathrm{erf}^{-1}(U_{term})}{\mathrm{erf}^{-1}(U_{init})} - 1 \right] z, \tag{4.19}$$

which predicts a linear increase in the horizontally averaged stria height with respect to the distance moved away from a flow margin along the normal direction z. This linear increase was observed in the CRBG, as shown in Figure 3.3, and also in the Cheakamus basalts, as shown in Figure 3.9. Table 4.2 shows the results of solving Equation 4.19 for the temperature change across a stria, $\Delta T = T_{init} - T_{term}$, using the data presented in Figure 3.3. Calculations for both dirichlet and coupled half-space boundary conditions are shown. In evaluating Equation 4.19 an emplacement temperature $T_1 = 1090°\mathrm{C}$, an initial substrate temperature of $T_0 = 20°\mathrm{C}$, and a fracture initiation temperature at the glass transition temperature, $T_{init} = T_g$, were assumed.

The data presented in Table 4.2 suggest that the temperature difference across a stria, during its formation, is in the range of 7 - 15°C. The fracture initiation temperature T_{init} is not well constrained, and may be as high as 900° [79]. Fortunately, the gradients in the temperature field do not strongly depend on the particular isotherm chosen as T_{init}; in general, as T_{init} increases to 900°C, the estimates of ΔT from the two boundary conditions converge to the range 9-13°C. As there are no other adjustable parameters in Equation 4.19, it can thus be confidently stated that $\Delta T = 11 \pm 4°\mathrm{C}$.

In a thermally inhomogeneous layer with no viscous relaxation, assuming that the layer is constrained horizontally but free to contract vertically, the horizontal stress can be estimated,

$$\sigma = \frac{\alpha E \Delta T}{(1 - \nu)}, \tag{4.20}$$

where the linear coefficient of thermal expansion α, the Young's modulus E, and Poisson's ratio ν are given in Table 4.1. The temperature difference $\Delta T = 11 \pm 4°\mathrm{C}$, estimated above, corresponds to a tensile strength, in the presence of an existing crack tip, of 5±2

Site Description	slope ($\langle s \rangle / z$)	$\Delta T_{Dirichlet}$	$\Delta T_{1/2space}$
Rock River Road	2.5±0.5%	13±2°C	5±1°C
Tucannon River	4.5±0.6%	23±3°C	8±1°C
Clarkston	3.2±1.3%	16±6°C	6±2°C
Cheakamus basalt I	2.6±0.2%	-	-
Cheakamus basalt II	3.5±0.3%	-	-

Table 4.2: Rates of stria height increase as a function of distance away from the lower flow margin, taken from Figures 3.3 and 3.9, and the estimated temperature differences across the stria height ΔT, for two different boundary conditions. Results from the Cheakamus basalts are included for comparative purposes, but are not analyzed.

MPa. This is quite reasonable, considering the brittle nature of basalt, which has a measured tensile strength of between 8 and 10 MPa at room temperature [79, 107]. Even allowing for some uncertainty in the physical properties of basalt, and for some viscous relaxation near the solidus, it would be hard to rectify any ΔT of more than ~ 20°C with the known strength of basalt.

It is interesting to calculate the heat flux through the lower surface of a flow using this model. This heat flux will later be compared with that caused by crack-aided cooling, and used to put limits on the physical processes responsible for columnar jointing. The flux q_h, here interpreted as the the heat flow per unit area across the plane $z = 0$, can be found by integrating $1 - U(z,t)$ throughout the flow, and then differentiating with respect to time, yielding

$$q_h = c_p \rho_b (T_1 - T_0) \sqrt{\frac{\kappa}{\pi t}}, \tag{4.21}$$

for the case of a dirichlet boundary condition. With the coupled half-space boundary condition, the heat flux is exactly half the value given by Equation 4.21.

Thus far, this model does not take into account the release of latent heat by the solidifying basalt. Including the latent heat $\mathscr{L}$ converts the calculation into a moving boundary problem of the Stefan type, where the speed of the solidification front is limited by the rate of extraction of the latent heat. In this case, the heat flux in Equation 4.21 needs to be corrected by the factor $1/\mathrm{erf}(\lambda_1)$, where λ_1 is given by

$$\frac{\mathscr{L}\sqrt{\pi}}{c_p(T_1 - T_0)} = \frac{e^{-\lambda_1^2}}{\lambda_1 \mathrm{erf}(\lambda_1)}, \tag{4.22}$$

(See Turcotte and Shubert section 4-18 for more detail [108]). Using the thermal properties of the CRBG given in Table 4.1, $\mathrm{erf}(\lambda_1) = 0.77$.

This section has shown how, near a flow margin, the increase in the stria heights that

was measured in Sections 3.3 and 3.9 can be interpreted to arise from the slowing down of diffusive heat transport through the flow margin. The rate of increase in stria height implies that the temperature drop across an individual stria advance is only 11±4°C, which agrees with the known tensile strength of basalt. Farther than a few meters from a flow margin, convective processes in the cracks begin to control the cooling of the lava flow [13, 41]; these will be discussed in the following section.

4.2.3 The convective cooling regime in the CRBG

Approximately three to four meters above the lower flow margin, striae cease to increase in size. The average column size also becomes constant by the same position [20]. Beyond this point the cooling rate has likely been stabilized by the intrusion of water into the cracks. It is well-established that two-phase convection occurs in the upper colonnade as water in the cracks boils at the 100°C isotherm and recondenses nearer to the flow margin [13, 41, 90]. This reflux of water and steam efficiently transports heat up the cracks, and maintains a constant solidification front speed [41]. There is at present no direct evidence that this mode of cooling is also active in lower colonnades. It shall be argued here, and in Section 4.2.5, that a similar (and probably identical) crack-mediated cooling mechanism must also operate within lower colonnades.

In order to study the temperature field far from the lower flow margin, where the cooling front is moving at a constant speed, Equation 4.17 must be shifted into the reference frame moving with the cooling (or fracture) front. The resulting advection-diffusion equation is

$$\partial_t T = \kappa \nabla^2 T + v \partial_z T, \tag{4.23}$$

where v is in this case the fracture front velocity in the *upward* z direction. In this co-moving reference frame the cracks are stationary, neglecting the intermittent crack advance part of their motion. The convective cooling must be accounted for in the boundary conditions on T at the crack surfaces.

The lack of variations in the stria height in the interior of a lava flow suggests a time independent solution to Equation 4.23, where the positions of the temperature isotherms remain fixed in the moving reference frame. This simplification yields Equation 4.15 directly, and is also consistent with deep bore-hole measurements from Kileui Iki [41], whose temperature profiles are well fit by a time-independent advection-diffusion model.

A normalized form of Equation 4.15,

$$\nabla'^2 U + \mathrm{Pe}\ \partial_{z'} U = 0, \tag{4.24}$$

is obtained by the introduction of the reduced temperature field $U = (T - T_0)/(T_1 - T_0)$, where $z' = z/L$ and $\mathrm{Pe} = vL/\kappa$. To simplify the geometry, it is again sensible to choose the length scale L to be the square root of the average cross-sectional area of the column cross-sections. Assuming each column to be a regular hexagon with equal sides of length $\langle w \rangle$ this implies that $L = \sqrt{3\sqrt{3}/2}\langle w \rangle \simeq 1.61\langle w \rangle$.

The temperature of the lava near the crack tips is approximately T_g, so based on the conductive solution discussed in the previous section, the 100°C isotherm must be several column diameters removed from the crack tips. The measurements of Hardee [41] suggest that in this intermediate zone the cracks are filled with steam, and are therefore poor conductors. As a first approximation to the convective cooling effect, therefore, a lower colonnade model where $T = T_0 = 100°\mathrm{C}$ below some plane $z' = 0$ is considered. This would be the situation if the region below this plane is uniformly and efficiently cooled by two-phase convection, while the region above is maintained with no net heat flux into the steam-filled cracks. The solution to Equation 4.24 with this boundary condition is

$$U(z') = 1 - \exp(-z'\mathrm{Pe}). \tag{4.25}$$

When this solution is inverted,

$$z' = \frac{z}{L} = -\frac{1}{\mathrm{Pe}} \log(1 - U), \tag{4.26}$$

an estimate of the Péclet number

$$\mathrm{Pe} = \frac{L}{\langle s \rangle} \log \left[\frac{1 - U_{init}}{1 - U_{term}} \right] \tag{4.27}$$

is obtained by the application of the previous assumption that $\langle s \rangle = z(U_{term}) - z(U_{init})$.

The main uncertainty in evaluating Equation 4.27 is the range that exists in the ratio of the stria height to column width, $\eta = \langle s \rangle / \langle w \rangle$, as was shown in Figure 3.2. Using the measured average $\eta = 0.14$ and $\sigma_\eta = 0.06$, from the CRBG, $\mathrm{Pe} = 0.4 \pm 0.2$. As in the case of starch, it should be emphasized that there exist examples of colonnades which have values of Pe throughout this range. Further details of this scaling, including data from BC and Staffa, are presented in Section 4.2.6.

A number of estimates of the heat flux that must be carried through the cracks can be made with this model. This will lead to considerations of the efficiency of crack-aided cooling, which can be compared to published thermal measurements from near the *upper* flow surface of Kileui Iki [41]. A simple order-of-magnitude estimate of the heat flux q_h can be obtained by assuming that the convective heat flux matches the diffusive heat

flux at a height of 3 to 4 meters, where the stabilization of the stria heights indicate that these two transport mechanisms cross over. Using Equation 4.18 to determine when the T_g isotherm reaches this height, the heat flux given in Equation 4.21 can be solved for, incorporating the $1/\mathrm{erf}(\lambda_1)$ correction due to latent heat. Given the large uncertainties in the underlying assumptions, this gives a broad heat flux estimate of $q_h = 400\pm300$ W/m^2 through the basal flow surface.

A more rigorous estimate of heat flux can be made by noting that, for a cooling front which is steadily advancing at a speed v, energy balance requires that the heat flux

$$q_h = \rho_b v(c_p(T_1 - T_0) + \mathscr{L}). \tag{4.28}$$

By using this equation, Equation 4.27 and the definition of the Péclet number to eliminate v, the estimate

$$q_h = \frac{\rho_b \kappa}{\langle s \rangle}(c_p(T_1 - T_0) + \mathscr{L}) \log\left[\frac{1 - U_{init}}{1 - U_{term}}\right] \tag{4.29}$$

is obtained. Using the values measured previously, this gives the product $q_h\langle s\rangle = 80\pm30$ W/m. In the CRBG $\langle s\rangle$ ranges from 3.5 to 36 cm, hence the total heat flux through the base of the flow, due to convective cooling, is in the range 200-2000 W/m^2. In this prediction q_h and $\langle s\rangle$ are inversely related, and therefore so are q_h and $\langle w\rangle$; the smallest columns have the largest heat flux and vice versa.

It is insightful to consider this problem in terms of the heat flux per unit crack length. ρ_{c_A}, the linear crack density per unit area, can be estimated to be the ratio of half the perimeter of a hexagonal column with side length $\langle w\rangle$ to its area. The factor of one half arises because each crack is shared between two columns. Thus,

$$\rho_{c_A} = \frac{[\frac{1}{2} \times 6\langle w\rangle]}{[(3/2)\sqrt{3}\ \langle w\rangle^2]} = \frac{2}{\sqrt{3}}\left[\frac{1}{\langle w\rangle}\right], \tag{4.30}$$

and the heat flux per unit crack length is

$$J_c = q_h/\rho_{c_A} = \left(\frac{\sqrt{3}}{2}\right) q_h\langle w\rangle = \left(\frac{\sqrt{3}}{2}\right)\frac{q_h\langle s\rangle}{\eta}, \tag{4.31}$$

where the definition $\eta = \langle s\rangle/\langle w\rangle$ has been used. Therefore J_c can be expressed as the ratio of two rather well measured quantities, $q_h\langle s\rangle$ and η, which themselves consist only of known material parameters and statistical data from many sites. Using the value of $q_h\langle s\rangle$ discussed above, and $\eta = 0.14\pm0.02$, then $J_c = 500\pm200$ W/m. This level of cooling could be maintained by boiling and condensing 0.2 ml/s of water per meter of

crack cross-sectional length. This is not an unreasonable volume of water to reflux. It is interesting to note that the estimated heat flux per unit crack length does not vary by more than a factor of 2 or so between all the colonnades that have been studied in the CRBG. This result will be discussed further in Section 4.2.5

An independent estimate of heat flux can be obtained from the measurements of Hardee [41]. He measured the depth of the solidus at the Kileui Iki lava lake, recording a steady advance rate of $v = 6.7 \times 10^{-8}$ m/s. In this case the heat flux given by Equation 4.28 evaluates to 270 W/m^2 using the properties Hardee estimates for Kileui Iki lava [41] or to 250 W/m^2 using the properties listed in Table 3. Given the large columns of Kileui, this is in agreement with the heat flux estimates presented above.

This section has used copious striae and column measurements from the Columbia River Basalt Group, described in Chapter 3, to estimate the heat flux and Péclet number of an advancing cooling front that leads to columnar joints in lava. Throughout the flow unit, values of the heat flux q_h were found which are consistent with previous measurements in the upper colonnade, and which are attainable with reasonable groundwater reflux rates. Many of these results are summarized in Section 4.2.6, which considers the overall scaling of igneous columnar joints. First, however, discussion must turn to the consideration of the formation of striae, and convection within cracks, the details of which underlie key assumptions made in both this section, and Section 4.2.2.

4.2.4 Stria formation

The results of the heat-flow modeling described above suggest that there exists an efficient means of extracting heat through the cracks of the lower colonnade. The size of the striae near the lower flow margin increases linearly with the distance from the cooling boundary, as would be expected if $\langle s \rangle$ represents the distance between two fixed isotherms. Further into the lower colonnade the striae cease to increase in size, implying a nearly constant heat flux through the lower flow margin throughout the rest of the joint forming process. Sparse data from upper colonnades suggest the same trend exists near the upper flow margin. A consistent picture of striae formation is here developed, which requires that some crack-aided cooling mechanism to be present in the cooling of a lower colonnade. Several alternative explanations for the striae scaling results are also considered, and rejected, in this section.

During early cooling, when thermal diffusion through the flow margin dominates, there must be a $1/\sqrt{t}$ slowing down of the cooling rate. This decrease in cooling rate can be expected to alter T_g – the viscous response depends exponentially on temperature,

and slower cooling would require a lower cutoff T_g [60, 90]. However, this change in T_g will have little effect on the observed stria heights, and cannot explain any significant variations in the stria height. According to Equation 4.19, the average stria height $\langle s \rangle$ depends strongly on ΔT, but only weakly on T_{init}. A decrease in T_{init} from 900°C near the flow margin (as suggested by the fracture initiation temperature recorded at the surface of a Kilauean lava lake by Peck and Minakami [79]) to 750°C (the glass transition temperature in bulk lava, as estimated by Ryan and Sammis [90]) in the bulk of the flow would change $\langle s \rangle$ by only 15%, whereas the observed change in $\langle s \rangle$ is greater than 100%, as shown in Figures 3.3 and 3.9.

Similarly, the effects of the confining pressure of the lava above the growing lower colonnade cannot account for the observed growth of striae near the lower flow margin. Such pressure would not be expected to affect ΔT, and could only cause a slight depth dependence in T_{init} by imposing a compressive pressure gradient.

The vicinity of the crack tips themselves will necessarily be dry at all times, by virtue of its existence near T_g. For example, in an advective-diffusive cooling scenario with Pe = 0.4, the crack tips are about 3 column diameters away from the crack surfaces where active convective cooling is taking place. Thus, the fracture behavior near the crack tips is probably insensitive to whether the cooling is diffusive or aided by convection in the cracks. The cooling mechanism merely serves to sustain the heat flux q_h, as will be discussed in the following section.

The observed independence of individual stria advances, described in Sections 3.2.5 and 3.3.6, agrees with a simple mechanical model of fracture. Hot, solid basalt may be expected to have an average tensile strength of between 8 and 10 MPa, based on measurements made at lower temperatures [3, 79, 107]. Various defects, inhomogeneities and imperfections imply that there will be variation in the tensile strength of individual samples. For example, Bacon [3] found that samples of basalt had an average tensile strength of 8.5 MPa, with a standard deviation of 1.6 MPa. This will translate into a spread in the thermal strains at which a crack tip will be activated. The observed 21% standard deviation in stria heights agrees approximately with this variation in strength. Once a crack begins to advance, it will run until it ceases to be able to release elastic energy at a rate sufficient to create new crack surfaces [35]. This can be interpreted to mean that the cracks have some fixed, though not necessarily zero, termination stress. When the crack stops, it blunts, an effect which accounts for the ∼5 MPa difference between the crack initiation and crack termination stresses [20, 24]. This type of sequential crack advance is summarized in Figure 4.3, and appears to be common to many fracturing systems [24].

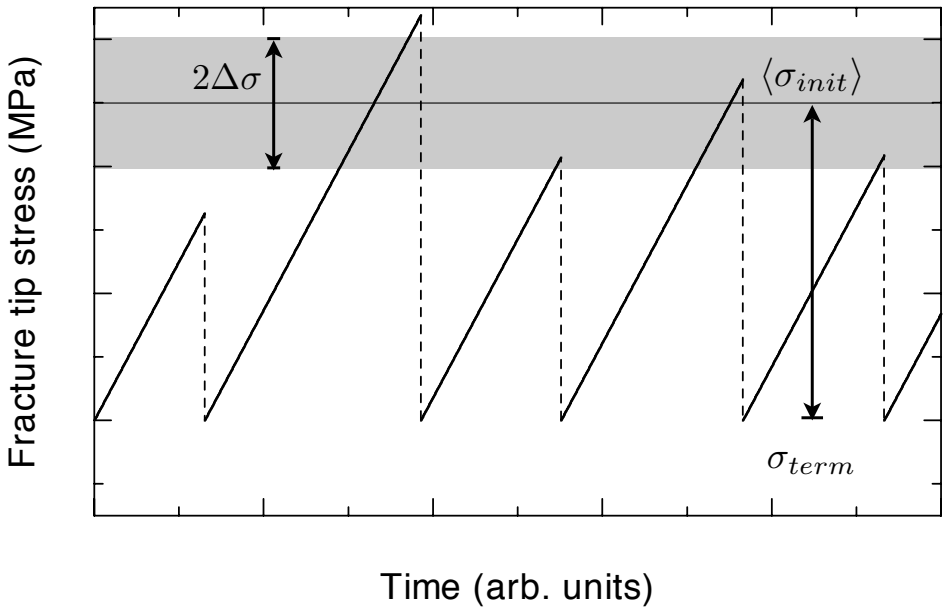

Figure 4.3: A sketch of stria formation and sequential advance crack motion. Thermal stresses slowly build up until they are near the average crack initiation stress $\langle\sigma_{init}\rangle$. Variations in local material strength cause a spread, $\Delta\sigma$, in the individual crack initiation stress. The crack then advances rapidly until it reaches a fixed termination stress σ_{term}. Each step leaves behind a single stria.

4.2.5 Convection within cracks

As has been argued in the preceding sections, the role of water in removing heat from the interior of a flow is crucial to understanding the formation of columnar joints in lava. Near the flow margin of a colonnade, in both the upper and lower colonnades, there is a region of coarsening in which the column scale increases, and in which the columns become more ordered [20, 60, 79]. Similar coarsening occurs in desiccated starch colonnades when the fracture front is decelerating [31]. In the starch case, although there is no crack-enhanced evaporation, this coarsening halts when the front is forced to maintain a constant velocity. It is natural to suppose that the stabilization of the column diameter in lava occurs in a similar way, *i.e.* when the fracture front settles down to a fixed velocity.

The constancy of the stria heights in the interior of lower colonnades indicates that a constant heat flux through the lower flow surface is necessary during much of the cooling of a lava flow. Furthermore, the proportionality of the stria height to the column diameter implies that the heat flux per unit cross-sectional crack length, J_c, is also nearly constant in all cases. When a well-formed upper colonnade is present, it appears to have striae that are indistinguishable (other than their direction) from those in the lower colonnade, and in both cases the average stria and column sizes settle down to fixed values within

at most a few meters of the flow margins. Also, the Péclet number calculated from stria measurements, made in lower colonnades, matches that value inferred from bore-hole measurements in an upper colonnade [41]. All these observations strongly suggest that the same convective cooling mechanism operates whether the colonnade is cooling upward or downward.

It has previously been established that groundwater boil off and reflux is important in upper colonnades, although the exact mechanism of water transport is somewhat unclear [13, 41, 90]. While it may seem intuitive that water, in upper colonnades, is carried by gravity to the bottom of the cracks, and then that buoyancy-driven convection is in the right direction to effect its transport back up as steam, the reality is quite different. In fact, the narrowness of the cracks almost certainly means that capillary forces dominate over gravity. Also, the two-phase (water and steam) nature of the reflux means that the flow is more complex than what might be expected from considerations of single-phase (water *or* steam) convection.

Even if water flooded all its cracks, an upper colonnade, considered as a porous medium, will have an extremely low permeability [41]. Consequently, buoyancy-driven D'Arcy law convection would be an extremely slow process, unable to sustain the observed heat flux rates [5, 41]. Such a mechanism would not operate at all in the lower colonnade, where the buoyancy force has the wrong sign. If, as is instead likely, the direction of gravity is irrelevant to the cooling process, then the similarity between upper and lower colonnades is less difficult to understand. The most plausible hypothesis, that does not impose a preferred direction, is that heat is transported by closed two-phase convection in unsaturated joints. According to the estimate of J_c, discussed in Section 4.2.3, only a small amount of water needs to be present to maintain an effective cooling cycle.

Capillary forces and surface adsorption will ensure that there is at least a thin film of water spread over all the rough, porous crack surfaces. As this water film absorbs heat near the cooling front it will change to steam. This phase change results in a pressure drop in the water phase, causing suction on the rest of the water column and drawing water toward the cooling front. In equilibrium with water at 100°C, the steam that is produced will not condense until it is forced to a cooler region near the flow margin. The pressures arising from the generation and condensation of steam will drive the flow of the steam phase that completes the reflux loop. This convection cycle is equivalent to the action of a heat pipe [37, 39]. Marangoni (surface tension driven) convection could also be present as a secondary effect, as surface tension gradients between the hot interior of the crack, and the cooler flow margin act in the right direction to assist the flow of water toward the cooling front.

Unfortunately, the tortuous, fractal geometry of the crack surfaces [12, 93] complicates any simple predictions of water/steam flow rates, and hence J_c, from heat pipe theories [37, 39]. While some steam might escape from upper colonnades, the large-scale horizontal extent of the layers of lava in the CRBG means that steam generated in the lower colonnade could not, in most cases, escape to the upper surface. It would be blocked by the melt layer between the upper and lower colonnades. However, the closed reflux of water makes the escape of steam inessential to the cooling process.

4.2.6 The scaling of igneous columnar joints

In Section 4.2.2, it was shown how the increase in stria height near a flow margin puts quantitative constrains on the fracture mechanics of stria formation. Following this, it was shown in Section 4.2.3 that for striae measured within the interior of colonnades in the Columbia River Basalt Group, jointing proceeded according to a roughly constant Péclet number.

Although most of these observations have been made in relation to the CRBG, they are supported by data gathered from BC and Staffa. In particular, measurements of the stria height near the flow margins of basalts in the Vancouver-Whistler corridor confirm the linear rate of increase in stria height that was measured in the CRBG. Furthermore, the long sequences of stria measured at Bridge Lake, the Keremeos Columns, and near Fingal's Cave all indicate, quite clearly, that the striae height is nearly constant within the bulk of a flow unit. Together, these results imply that the thermal analysis presented in this chapter is applicable to columnar joints in a wide range of igneous lava types.

Figure 4.4 shows the crack spacing that was observed in lavas, over a wide range of inferred fracture speeds, from all three of the field regions discussed in Chapter 3. The fracture scale ($L \simeq 1.61\langle w \rangle$) is defined, as elsewhere in this thesis, as the square root of the average column cross-sectional area. Here, v is calculated using Equation 4.27 and the thermal definition of the Péclet number. The simplifying assumption that all lavas have the same initial conditions and material properties as the basalts of the CRBG was made. Although this is reasonable for the Fingal's lava of Staffa, it is less appropriate for the British Columbian lavas, which were quite varied in composition and emplacement history. As was described in Section 3.3.3, the additional scatter in the British Columbia data is likely due, in some part, to both of these types of variations. An error-weighted best fit relationship to all the data gives $\mathrm{Pe} = 0.3 \pm 0.2$, as shown in Figure 4.4. These results complement those obtained through the experimental investigation of dried starch-cakes, and imply that columnar jointing throughout all observed field sites

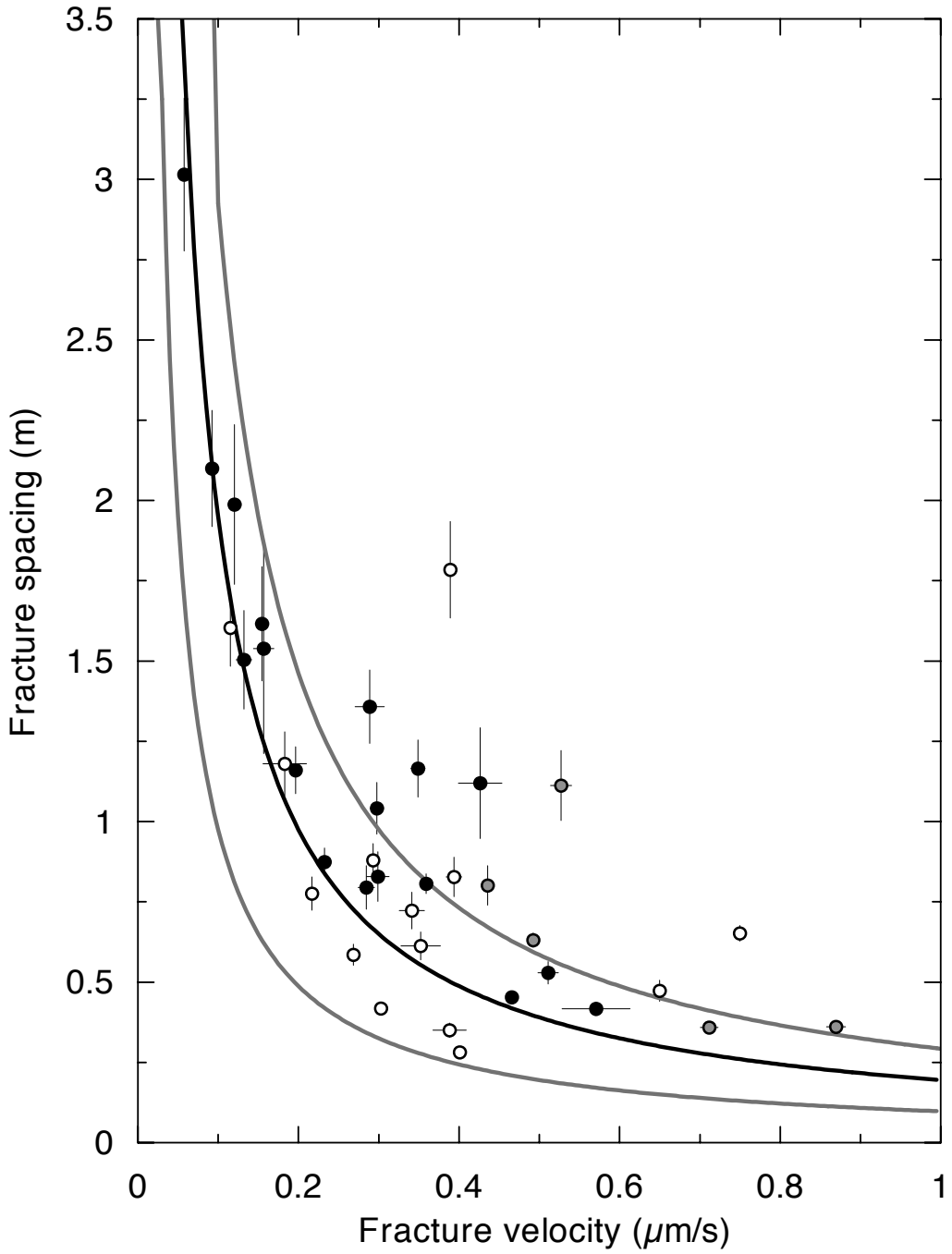

Figure 4.4: The average fracture front velocity and fracture spacing are inversely related in joints in lava. The fracture spacings from field observations in the tholeiitic basalts of the Columbia River Basalt Group (black circles), and the island of Staffa (grey circles), and from a range of columnar lavas types found in southwestern British Columbia (open circles) are shown. Solid lines indicate an inverse dependence of fracture spacing on fracture velocity, with lines of constant Péclet number Pe = 0.15, 0.3, and 0.5 shown.

occurred at a nearly constant value of Pe.

If columnar joints advance at a constant Pe, then the product of the fracture front or solidification front velocity v and the column size L is a constant, $vL = \kappa \mathrm{Pe}$. This conclusion can also be reached by considering the mechanism for heat transport by water reflux in the cracks. According to Equation 4.29, energy balance requires that the heat flux q_h is proportional to the crack advance speed v, with the constant of proportionality depending only on material parameters. The crack density per unit area ρ_{c_A} given by Equation 4.30 scales as $1/L$. Hence the heat flux per unit crack length J_c, given by Equation 4.31 scales as $J_c = q_h/\rho_{c_A} \sim q_h L \sim vL \sim \mathrm{Pe}$. Thus, the constancy of the Péclet number can also be understood as being equivalent to the constancy of J_c, the amount of heat that the cracks carry per unit of cross-sectional length. This is fixed by the scale-independent, microscopic physics of an individual crack, and only depends on the typical crack opening, surface roughness, and the properties of water such as surface tension, latent heat, *etc.* The inverse relationship between the cooling rate q_h and the column scale L can thus be explained physically.

4.3 Shrinkage fronts and scaling

The similarity between columnar crack patterns induced by drying and cooling can be traced to the fact that the transport of water in a drying slurry and the extraction of heat from a hot solid are mathematically analogous [6, 10]. As was described in Section 4.1, when drying a thick starch-cake, cracks appear at the drying surface, and slowly penetrate into the material. Similarly, as was described in Section 4.2, cracks in a lava flow appear at a cooling surface, and slowly move into the flow. In each case, the mechanisms of heat and water transport cause a sharp shrinkage front to propagate, and the cracking follows this front. Therefore, it is sufficient to consider the origin of the column scale in one of these cases, say drying, and then transpose the result to the other with an appropriate reinterpretation.

In this section a simple scaling theory, that emphasizes the physical mechanisms at play, and leads to predictions that are quantitatively consistent with both starch experiments and field observations of lava, will be outlined.

Consider a semi-infinite starch-cake, *i.e.* one whose lateral extent and depth are both large, which dries from a surface exposed to air at a constant relative humidity. After a time t following the beginning of the experiment, a surface layer of thickness L_s has shrunk because of the loss of water from it. Shrinkage is easily accommodated in the direction normal to the surface, but leads to an isotropic tensile stress in the plane

parallel to it. If the stresses induced by drying are comparable to the tensile strength of the starch-cake, then cracks can, and will, nucleate from the free surface and propagate into the bulk material. These cracks will relieve stress in a region of size $\sim L_s$, the elastic screening length perpendicular to the crack face [46]. However, unlike in static elasticity, the stresses at the crack tip vary dynamically, since the crack actually moves from the highly stressed surface into the bulk – which is not so highly stressed. This decrease in dynamic stress will cause the crack to slow down and eventually stop.

If the starch-cake were thin things would end here, and L_s would end up being proportional to the cake layer thickness. Indeed in homogeneously dried thin layers the fracture spacing is known to be proportional to the layer thickness [8, 36, 97]. In thick layers further drying leads to a repetition of this cycle, and to the intermittent advance of the fracture tip. This behavior leaves behind striae in lavas [89] and similar features, such as those shown in Figure 2.2(b), that can sometimes be seen in dried starch samples. Exactly this process has also been observed for cracks in a confined, directionally dried suspension [24]. In the problem of a diffusively drying half-space, the only natural length scale is $L_s \sim (D_0 t)^{1/2}$, where D_0 is the diffusion constant characterizing the equilibration of the moisture concentration. In order to dissipate the stresses that drying induces, the crack spacing L must be proportional to L_s. Thus, as time progresses, and the stress relaxation length increases, the crack pattern should coarsen, *i.e.* the cross-sectional area of the average column should increase with increasing distance from the exposed surface. This coarsening was demonstrated in Section 2.4.1, and has been noticed previously in both lava and starch [21, 29, 31, 67, 71].

When the rate of drying is kept constant, so that the surface volumetric flux per unit area J is invariant in time, the starch-cake enters a non-equilibrium steady state which requires that the drying power increase with time. Under these conditions the elastic screening length is also invariant and scales as D/J, so that the invariant crack spacing should in turn scale as

$$L \sim D/J. \tag{4.32}$$

Such a steady state is achieved in the controlled starch experiments, described in Section 2.4.3, which do not coarsen. Equation 4.32 is equivalent to defining the dimensionless Péclet number for a crack spacing L,

$$\mathrm{Pe} = vL/D, \tag{4.33}$$

where the velocity v is related to the volumetric flux and the porosity ϕ by $v = J/\phi$. As discussed in the previous sections, Pe is the most important parameter controlling the

scaling of columnar joints. Since Pe $\sim L/L_s$ the inverse scaling of the fracture spacing and the fracture front velocity that has been observed in both experiments and fieldwork follows if jointing proceeds at a Péclet number of order 1.

It is clear on physical grounds that Pe must not be too different from unity. Pe cannot be far from one, or the cracks would either outrun the relaxation of the stress field (Pe $\gg$ 1), or be too close to equilibrium with it (Pe $\ll$ 1). Neither extreme case could lead to an ordered crack pattern, as the cracks would not be able to interact with their neighbors' stress fields.

In order to transpose this result to the case of cooling lava, one need only exchange D with the thermal diffusivity κ, and J_0 with the heat flux q_h. As has been discussed, cracks in lava greatly enhance the rate of cooling of thick layers by supplying avenues for efficient heat transport via the boiling and reflux of water [33, 41]. This effectively short-circuits the heat flow between the cooling front and the surface, leading to a traveling cooling front that maintains a constant q_h. A Pe of order 1 is still expected. Here, as shown in cartoon in Figure 4.5, a very large Pe would imply that the cracks move independently through an essentially uniform background temperature field, and thus could not be dynamically affected by their neighbors through that field. On the other hand, a very small Pe would mean that temperature gradients near the crack tips would be smoothed out. Since the thermal diffusivity of basalt from the Columbia Plateau is approximately 6.5×10^{-7} m^2/s [33, 73, 107] (about two orders of magnitude larger than the effective hydraulic diffusivity in starch), and the fracture front velocities are comparable to starch experiments, it should be expected that columnar jointing in lava be 10-100 times larger than jointing in starch. Indeed, this is the case.

4.4 Hysteresis in the scaling of columnar joints

It has often been assumed that there exists a single one-to-one relationship between the scale of columnar joints and some externally imposed driving force. In lava it has previously been argued that the cooling rate of a lava flow determines the scale of the joints formed within it [13, 20, 38, 59, 85]. Other than the material presented in this thesis, the primary geological evidence for this relationship comes from studies of the crystal texture of the rock in colonnades separated by regions of entablature. The crystal texture of the columnar layers is coarser, implying that they cooled more slowly than the entablature [21, 59]. In starch experiments it has also been observed that faster evaporation rates generally give smaller columns [29, 31, 67, 71, 106]. While suggestive, these qualitative results are insufficient to supply any strong constraint, much less to

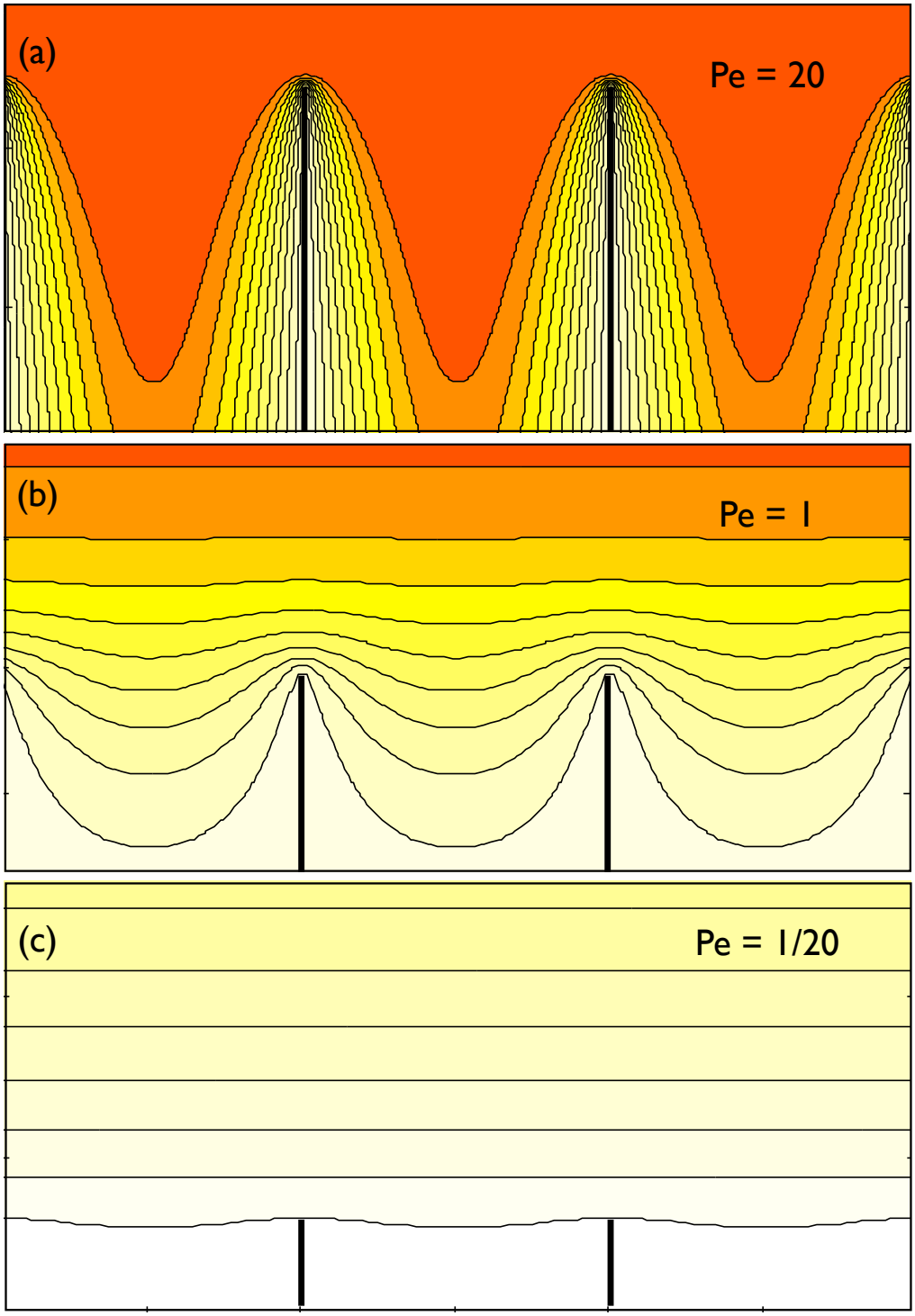

Figure 4.5: The Péclet number of an ordered fracture front must be near 1. (a) If Pe $\gg$ 1 cracks outrun the relaxation of the temperature or stress field. (b) If Pe $\sim$ 1 cracks can communicate with each other through the temperature or stress field. (c) if Pe $\ll$ 1 cracks are close to equilibrium with the field. In all panels the time-independent solution of the 2D thermal advection-diffusion equation are presented, where the temperature is held constant on crack surfaces (shown by dark lines).

imply a one-to-one relationship, between the cooling or evaporation rates and the average column area. Nonetheless, the assumption that there exists such a relationship is implicit in much of the modeling of columnar joints [38, 85, 106].

This assumption is not universally accepted. Müller, although using the one-to-one assumption in his analysis, expressed concern over the lack of experimental proof for this principle [71]. Saliba and Jagla [92] have produced a finite-element calculation of a fracture front intruding into a cooling solid, and have made the alternate prediction that the fracture scale is independent of the driving temperature gradient – except possibly during initiation.

Although the dimensional analysis presented in the previous section implies that Pe must be of order 1 to produce columnar joints, it does not require that Pe take a unique value. The results of the models described in Sections 4.1 and 4.2 are similarly ambiguous, although they did show that only a small range of Pe are actually selected, between approximately 0.1 and 0.5. On the other hand, the empirical evidence discussed in Chapters 2 and 3 suggested that hysteresis was present in the scale selection process. In this section it will be argued that, although the Péclet number sets general constraints on the scaling of columnar joints, the particular scale that is selected is, within a narrow range, history dependent.

4.4.1 The scaling predictions of traditional fracture mechanics

A quantitative approach to the energetics of fracture patterns is provided by Griffith's fracture theory [35]. In Griffith's theory fractures can only advance if the rate of increase in the surface energy of the opening fracture is less than or equal to the corresponding rate of decrease in the bulk elastic energy. The difference, if any, between these rates represents dissipation; fracture is, in general, a thermodynamically irreversible process. A simplifying assumption often made is to assume a quasi-static, or steady and slow, fracture advance. In this case the dissipation is presumed to be small, and the equality in the Griffith's criterion holds. This can be a rather restrictive and unrealistic assumption, however. In fact, both the rate of strain energy generation and dissipation are proportional to the velocity of the fracture front. Griffith's theory can, therefore, only be used to set an upper bound on the fracture density ρ_c, expressed as the crack area per unit volume, given by

$$\rho_c \leq \rho_{max} = \frac{\Delta\mathscr{E}}{\gamma_c}, \tag{4.34}$$

where $\Delta\mathscr{E}$ is the difference in the elastic energy density between wet and dry starch-cakes, or hot and cold lava, and γ_c is the energy required to open a unit area of crack surface.

Thus, energy considerations alone are insufficient to require any particular relationship between the fracture advance rate and the fracture spacing.

Irwin's modifications to Griffith's theory [48] are somewhat more useful to the problem of columnar jointing. Irwin introduced the concept of fracture toughness, and showed how the stress intensification in the vicinity of a crack implies that it is much easier to lengthen an existing crack than it is to nucleate a new one [48]. Although a quantitative calculation of the stress intensity factor would be difficult for a geometry as complex as that of columnar joints, the existence of this factor can supply the effect of memory to the columnar structure. For a wide range of stresses the downwards extension of existing cracks will be favored over the nucleation of new ones, or the termination of old ones. Thus, if a network of cracks with a given average area is advancing under changing conditions, their propagation may be stable, even if the changed conditions would not initiate a pattern of that scale.

4.4.2 Scale selection, memory, and hysteresis

Despite what has just been presented, a superficially appealing argument for a uniquely selected column length scale under given external conditions has often been sought in energy considerations. It has been asserted that the hexagonal geometry of columnar joints arises because such a form optimally releases the elastic energy per unit area, or otherwise optimally reduces the free energy of the system [51, 62]. In this view, the evolution of the columns tends toward a perfectly hexagonal lattice, or at least to a static pattern corresponding to a local free energy minimum with frozen-in disorder [13, 51]. However, this result is not supported by standard fracture treatments such as Griffith theory or Irwin's fracture mechanics. Furthermore, the experimental results described in Chapter 2 suggest a more dynamical interpretation, in which a possibly non-unique scale may be selected within some small band of stable Péclet numbers, depending on the system history. Such a pattern need not be perfectly ordered [31] or static [29].

In cooled lava, while there is certainly a rough inverse proportionality between the column diameter and the cooling rate, as reflected in the average stria height, the causal relation governing the column scale is in fact quite subtle. In the presence of a crack-enhanced heat flux the column diameter, the fracture front speed, and the rate of cooling are all interdependent, as was shown in Section 4.2.6. There is still some freedom in choosing the column scale, however. This is particularly evident in situations like that of the Tricouni flows, described in Section 3.3.3, where impoundment against an ice wall modified the ratio of striae height to column width.

Dynamic hysteresis due to the inherent rigidity of the pattern, partly guaranteed by Irwin's fracture toughness argument, probably means that there exists a finite range of stable scales near Pe ~ 0.2, as will now be demonstrated.

The freedom of scale selection, or hysteresis, was tested rigorously in experiments on scale selection in drying corn starch. The controlled experiments described in Section 2.4.3 show that when the evaporation rate is explicitly fixed, there are some conditions for which there is no strong dependence of the selected average cross-sectional area on the final evaporation rate. With some other conditions there is such a dependence. Furthermore, it was shown that there is a range of column scales that are attainable *via* different approaches to the same final evaporation rate. It was also observed, in Section 2.4.1, that smoothly changing evaporation rates can lead to sudden jumps in the column diameter, which could indicate the crossing of a stability boundary between stable crack propagation and strongly coarsening crack propagation. And finally, there are the differences in the scales that were selected under the same final drying conditions, but with 'fast' and 'slow' drying initiations, discussed in Section 2.4.3.

All these observations can be made consistent with each other if it is assumed that the columnar joint pattern exhibits a form of dynamical stability, leading to hysteresis. If the pattern has a memory there may exist a range of column scales that are stable for any given fracture advance rate. The scale observed then depends on the evolutionary history of the pattern.

By suggesting that the pattern of columnar joints exhibits memory, nothing more is claimed than that the fracture network at any given depth is, in general, similar to the fracture network at depths near to it. This is suggested by the way that column scale changes, as was shown in Section 2.5. To effect a small increase in the average column area, a number of discrete local column mergers must occur, after which the column network will slowly relax by propagating the changes through local interactions of columns with their neighbors. Small rapid changes over the whole pattern are not possible, or at least highly constrained by geometry. Thus, a given pattern scale may be marginally stable over some range of conditions. Large, sudden changes of average column scale may be possible if a stability threshold is passed where, on average, it is more favorable to have all columns more than twice as large as they currently are. Under these conditions a large scale change can be enacted by a catastrophic event consisting of many column mergers, as was shown in Section 2.4.1. This has the appearance of a global instability of the whole pattern.

The experiments reported in Section 2.4.3 imply that a range of column scales can be selected under the same final evaporation rate. Alternatively, along with the results

shown in Section 2.4.2, they also show that the same column scale can be chosen over a range of final drying rates, given the same drying initiation. This suggests a stability boundary between column scales that are stable, and those that coarsen, for any given evaporation rate. Different drying histories could lead to the selection of different scales from within this stable range. Similarly, in lava different cooling histories could lead to the selection of different scales from within this stable range. This may indeed have been the case locally in the Fingal's Lava, where columns from the same flow unit differ in size by a factor of two or so, on adjacent sides of that small island.

4.4.3 2D analogs of columnar joints

Since no comprehensive elastic theory exists for the 3D case of columnar joints, it is useful to briefly consider its better-studied 2D analogs. In one of these cases, propagating arrays of periodic, parallel cracks are observed to form behind shrinkage fronts moving through thin samples. Both thermal and desiccation experiments of this type have been performed. Crack arrays form when a thin layer of wet slurry is dried from one edge, both in samples with one free surface [78, 97], and in suspensions confined between two plates [1, 23, 45]. Thermal experiments, on the other hand, typically consist of dipping a heated strip of glass, or other material, into a cooler water bath at a fixed rate [86, 117]. These 2D fracture processes have also been studied theoretically in some detail [7, 51, 56].

Directional fracture patterns in thin layers may be regarded as the two-dimensional analogs of columnar joints. In general, for a thin layer that is either thermally stressed, or directionally dried, the average fracture spacing depends on the thickness of the layer [78, 97]. In some cases fractures advance intermittently in a manner similar to the behavior that produces striae in columnar joints, although this is not observed in all materials [23, 24].

Boeck *et al.* have proposed a theory for the scaling of the case of a thermally quenched strip [7]. Beginning with Equations 4.15 and 4.16 for the planar temperature field, and appropriate equations for the temperature-dependent stress field, they assume quasi-static fracture advance with a speed v and fracture spacing $2L$. Under these assumptions they find a one-dimensional manifold of solutions linking L and v. Thus, for a given v there *may* exist a unique spacing L which is stationary, and stable, in the co-moving reference frame, or there may not. In general what is actually observed depends on stability considerations. Some stationary solutions will be unstable to small perturbations, leading either to new stable solutions with different v and L, or possibly to no stable solution. For a restricted set of perturbations, they analyzed a period doubling instability where every

other crack falls behind the front and presumably stops. They showed that there exists a critical Péclet number Pe_c such that for $\mathrm{Pe}>\mathrm{Pe}_c$ *any* value of the crack spacing is stable against period doubling [7]. Pe_c depends only very weakly on Bi, varying only by a factor of two when Bi is varied over four orders of magnitude. While these calculations cannot be directly applied to the 3D case of columnar joints, they do suggest that all column scales within some critical range might be stable for any given conditions, and hence that some stability criteria might drive the observed coarsening towards larger column scales. The period doubling instability that Boeck *et al.* considered bears some resemblance to the sudden changes in the column scale that were observed in thick starch-cakes in Section 2.4.1.

2D experiments also suggest that a range of crack spacings can be stable for the same fixed external conditions. In these experiments, the crack spacing generally increases linearly with sample thickness [78, 97]. However, Ronsin and Perrin [86] observed a window of allowed crack spacings for a given dipping velocity in experiments with glass. Similarly, Shorlin *et al.* performed experiments using directionally dried slurries on substrates that incorporated a discontinuous step [97]. In certain cases the pattern of parallel cracks continued over these steps with the original spacing, even when the steps doubled the layer thickness. In other cases, the cracks responded by doubling their spacing. Similar effects were observed when stepping the evaporation rate up and down in Section 2.4.4. Thus, a variety of experiments and theory in 2D make it plausible that a hysteretic, non-unique column scale exists for columnar joints, within some band of scales limited by stability considerations.

4.5 Model summary

This chapter has focussed on describing the physical mechanisms at work in a drying starch-cake and a cooling lava flow. Despite the apparent differences between these two systems, the conceptual description of moisture transport is very similar to that of heat transport.

In starch, as is described in Section 4.1, the transport of moisture occurs *via* both liquid and vapor phases. Both types of transport can be described by a nonlinear diffusion problem, which follows from the continuity equation for water in a starch-cake. The effective diffusivity arising from moisture transport decreases with increasing moisture concentration, while the effective diffusivity arising from capillary transport increases with increasing moisture concentration. The cross-over between these transport mechanisms drives the generation of a sharp drying front, where the effective diffusivity is low.

The columnar fracture front is slaved to this drying front. On the moist side of this front, there is no strain, while on the dry side strain is relieved by open cracks. By performing a Taylor expansion of the nonlinear diffusion equation, in the reference frame moving with the fracture front, an advection-diffusion problem was shown to control the thickness of the drying front. This model has a single dimensionless parameter, the Péclet number, which describes the ratio of diffusive to advective effects. In both uncontrolled and controlled desiccation experiments, the Péclet number was found to be consistent with 0.15 ± 0.05.

In lava, cooling occurs by diffusion through the bulk lava, and through the two-phase convection of water and steam in the cracks, as was described in Section 4.2. Near a flow margin, bulk diffusion is the dominant heat transport mechanism. By considering heat flow in this case, it was shown that the height of striae should depend linearly on their distance away from a cooling flow margin. This agrees with field observations, which in turn show that the temperature drop across a stria advance must be $11 \pm 4^\circ$. Away from a flow margin, convection within cracks dominates the cooling of a lava flow. This efficient heat extraction mechanism leads to a cooling front that advances into the lava at a constant velocity. On the hot side of this front, strain is viscously relaxed, while on the cool side it is relieved by open cracks. In the co-moving reference frame, this cooling front is well-described by an advection-diffusion problem. By inverting the measurements of striae to obtain the fracture front velocity, it was shown here that the cooling front that forms columnar joints scales with a Péclet number of 0.3 ± 0.2. This implies that the heat flux through the surface of a cooling lava flow is approximately 500 ± 200 watts per meter of cross-sectional crack length.

The scale selection process of columnar joints in starch and lava occurs at a Péclet number near to, but slightly less than 1. In Section 4.3 this situation was studied, and a simple dimensional argument was presented, which explained this observation by invoking an elastic screening length natural to the advection-diffusion problem. This explanation is in sharp contrast with many theories given hitherto for these crack patterns [50, 51, 62, 71, 92] which are based on the approach to equilibrium in an energy minimization sense, and necessarily invoke the assumption that fracture formation is a quasi-static, near-equilibrium process.

The range of Péclet numbers observed in both laboratory experiments and field work are not only due to observational uncertainty. In Section 4.4 it was argued that a hysteretic range of column scales is possible, where the particular pattern scale that occurs at any point is dependent on the dynamics of the pattern leading up to that point. This interpretation is supported by considerations of classical fracture mechanics, as Irwin's

theory of fracture toughness implies that it is easier to propagate an array of cracks with a given spacing than it is to form that set of cracks originally. Experiments on scale selection in drying corn starch also support the existence of hysteresis, as do analog 2D theories and experiments on directional cooling.

Chapter 5

Conclusion

This thesis has presented observations and interpretations of columnar jointing in drying starch and cooling lava. These have included the first use of 3D visualization techniques to probe the structure of columnar joints, the design and construction of a unique system to fully control the drying of a starch-cake, a demonstration of the dynamics of the pattern of columnar jointing, the discovery of a new length scale in wavy columnar joints, and the development of a dimensionless scaling theory which explains the appearance of 1-10 mm wide joints in starch and 0.1-1 m wide joints in lava.

Jointing in starch is controlled by the dynamics of water transport in a drying colloidal mixture of starch, water, and air. It was imperative, therefore, that the drying of starch be studied, in order to make sense of any scaling results. In Chapter 2 the drying of starch was found to depend on the distribution of water between inert starch grains, and in pores within those grains. As water was removed, a drying front was set up, controlled by a balance between the diffusive and capillary transport mechanisms of water. As this front passed through the starch-cake, a large strain developed in a thin, moving layer, causing the directional propagation of a columnar crack network.

A relatively complex relationship between the evaporation rate and the average column area was found in experiments on the scaling behavior of starch columns. Individual columns rapidly evolved toward the average cross-sectional area, even while coarsening continued. In most cases, however, the pattern exhibited scaling behavior where the average crack spacing depended inversely on the fracture front velocity.

In order to explain several peculiar exceptions to this general scaling result, it was argued that the stress intensity factor in the vicinity of existing cracks, which produces a kind of geometric memory, can allow scale selection to be history dependent. This was demonstrated most clearly in fully controlled experiments, where in some experiments a scale was selected that was stable over a range of final evaporation rates. In other

cases, where the final evaporation rate was fixed, changes in the initiation and early development of the fracture pattern influenced the final scale that was selected. These results imply that there is a window of column scales that are allowed under any given externally applied evaporation rate. This appears to be true in igneous columnar joints as well.

Observations of columnar jointing in the lavas of the Columbia Plateau, British Columbia, and Staffa were presented in Chapter 3. These have emphasized quantitative measurements of the various length scales in columnar jointing, including the stria heights on column faces. A novel length scale was also discovered, and reported here, that of gentle oscillations of the column diameter, which produce 'wavy' columns.

In general, the stria height was found to vary in direct proportion to the column size, and was almost always between 5% and 20% of the average column edge width. There was no observable dependence of the stria height on the relative width of the individual face that it is on, only the average width. Furthermore, the height of each stria was shown to be statistically independent of the height of the previously formed stria on the same column, and to be selected from a probability distribution function well described by a Weibull function. However, horizontally adjacent striae *are* related, as the arrival of one crack advance at a vertex can trigger the advancement of an adjacent edge. The particular pathways that are followed by the advancing fracture network seemed to be somewhat consistent over several fracture advances.

Near to a flow margin, where diffusive cooling is most important, striae are smaller in size than they are further into the flow unit. In general, it was found that the stria height increases linearly with respect to position above the flow margin, for at least a few meters. More than 3-4 meters into a lava colonnade, striae have ceased to increase in size, and maintain the same average size independent of position. This implies that, regardless of the direction of cooling, a constant heat flux must be maintained by some convective mechanism acting within the cracks. Previously, a convective mechanism has only been suggested to exist in upper colonnades [13, 41].

In both Chapters 2 and 3 the ordering of columnar joints was investigated. It was shown that the mature pattern of columnar jointing is dynamic. The use of 3D tomographic imaging in starch columns allowed these dynamics to be studied. Cracks were seen to move as they intruded into the shrinking layer, and to quickly organize into a 'mature' state. This occurs over ~ 1 cm in a starch layer, and ~ 1 m in a lava layer [20]. However, this well-developed state is not perfectly ordered, nor static, and bears some similarity to other evolving planar networks such as coarsening dry foams. Interestingly, several simple statistical measures of the disorder inherent in the mature pattern were

shown to be the same in dried starch columns, and in lava columns. The cause of this is currently uncertain, but it is doubtful that the distribution of edge lengths, joint angles, and column neighbors could all be coincidentally the same in joints formed both in starch and in lava. Future investigations into columnar jointing may help to explain this dynamic pattern.

A scaling theory for columnar joints was developed in Chapter 4. This model gave a consistent physical description of the fracture processes in cooling lavas and drying starches, and reduced the transport of heat and moisture in these two systems to the same basic advection-diffusion problem.

In starch, it was shown that the transport of water could be modeled by a non-linear diffusion equation with a minimum in the diffusivity near the fracture front. By linearizing around this minimum, the transport of moisture was converted into an advection-diffusion problem, from which a hydraulic Péclet number of 0.15 ± 0.05 was extracted to describe the scaling of joints in starch. This Péclet number was consistent in both uncontrolled experiments, where columns coarsened, and controlled experiments, where a scale was selected. A slight spread of Péclet numbers was found, rather than a single unique Péclet number, reflecting hysteresis in the scale selection mechanism.

In lavas, thermal modeling was used to deduce that a convective cooling mechanism known from upper colonnades also operates in lower colonnades. This style of convection allows crack-aided cooling to set up a traveling cooling front, which is well-described as an advection-diffusion heat transport problem. By analyzing the height of striae on column edges, a thermal Péclet number of 0.3 ± 0.2 was estimated to have existed during the cooling of the host lavas in the Columbia Plateau. This made quantitative what has long been suspected, that the size of igneous columns depends on the cooling rate during their formation, and proved that these two variables are inversely related to each other.

Although much of the thermal analysis presented in Chapter 4 was confined to data collected from one very homogeneous system, the Columbia River Basalt Group, the conclusions are generally applicable to the additional igneous columnar joints that were studied in the more heterogeneous lavas of British Columbia.

Finally, it has been argued that the scale of columnar joints is probably not fully deducible from an energy balance between the elastic energy released and the energy consumed to create new fracture surfaces. Rather, the column scale and its dynamical evolution could be understood to follow from the elastic screening length in a thin elastic layer. The joint scale is therefore not selected by any sort of free energy minimization or other energy optimization considerations, but is only a function of the scaling of the non-equilibrium state of stress in that thin layer. This paradigm accounts for the

hundredfold differences in scales between joints in lava and starch; the scale of the stress state is controlled by the dimensionless Péclet number, which is, and must be, of order one in both cases.

Appendix A

Matlab code

The code included in this Appendix is described in Sections 2.3.1 and 2.3.2. The code in Appendix A.1 is used to measure the radial auto-correlation function of a cross-sectional image of a starch colonnade, in order to determine the average fracture spacing in that image. The code in Appendix A.2 is used to determine the fracture front velocity in a desiccation experiment, from measurements of the sample mass.

A.1 Autocorrelation methods

```
function z = corfft(name,name2)
% CORFFT returns the radial auto-correlation function of a bitmap
% name = input image file name (eg. 'cut01.bmp')
% name2 = output text file name (eg. 'cut01.txt')
% Copyright L. Goehring, 2007

% Load raw image into A.  Average colour channels.
A = double(imread(name,'bmp'));
A = (A(:,:,1)+A(:,:,2)+A(:,:,3))./3;
A = (A - mean(mean(A)));

% Build cosine bell filter F(x,y)
x = (1-cos(2*pi*(0:size(A,1)-1)/(size(A,1)-1)))/2;
y = (1-cos(2*pi*(0:size(A,2)-1)/(size(A,2)-1)))/2;
F = x'*y;

% Compute B = auto-covariance, C = auto-correlation
B = ifft2(abs(fft2(F.*A).^2));
C = real(B(1:round(size(B,1)/2),1:round(size(B,2)/2))/B(1,1));

% Calculate the radial auto-cor. from C.
```

```
D = zeros(ceil(sqrt(size(C,1)^2+size(C,2)^2)),1);
D1 = zeros(ceil(sqrt(size(C,1)^2+size(C,2)^2)),1);

for m = 1:size(C,1)
   for n = 1:size(C,2)
      p = ceil(sqrt(n^2+m^2));
      D(p) = D(p) + C(m,n);
      D1(p) = D1(p) + 1;
   end
end

D = D ./ D1;

%Plot radial auto-correlation function
plot(0:(length(D)-1),D);

%Write radial auto-correlation function to file
E = cat(2,(0:(length(D)-2))',D(2:end))
dlmwrite(name2,E,'\t');

z = D;

end
```

A.2 Fracture position and velocity inversion

```
function z = evap_inv(in_data)
% EVAP_INV reads mass data (text file of sample mass recorded every minute),
% and outputs a list of fracture position and fracture velocity,
% throughout the experiment.  A number of experimental conditions must
% be edited by hand.
% Copyright L. Goehring, 2007

% Variables depending on experimental setup
m0 = 317.1;  % initial mass
R = 1 % Initial ratio of water to starch, by mass
r0 = 43.1;   % radius of beaker (mm)
rho1 = 0.76;  % density of dry starch, assuming horizontal strain

w0 = m0/(1+1/R);            % initial water mass
w_max = 0.30;               % water concentration outside any given data
m_dry = m0 - w0             % mass of dry sample (g)
```

```
d0 = 1000*m_dry/(pi*r0^2*rho1)   % depth of fully dried slurry (mm)

m_crack = m_dry+w_max*pi*r0^2*d0/1000;    % mass when cracking starts (g)

mass_rec = load(in_data);     % Read input data
w_norm = load('average.txt'); % Read normalized fracture-moisture curve

% Generate a table of the crack position as a function of mass
crack = [m_crack,0]; % crack will be [mass(g),crack position(mm)]
for x_crack = 0.01:0.01:d0
    x_step = w_norm(2,1)*x_crack;   %x-direction step size
    w_norm1 = w_norm(:,1)*x_crack;  %convert normalized form to length
    if w_norm1(end) < d0            % if no data is given, add w_max.
        w_norm2 = w_norm(1:length(w_norm1),2);
        m_c = m_dry + sum(w_norm(:,2))*(pi*r0^2*x_step/1000)
              + w_max*(d0-w_norm1(end))*pi*r0^2/1000;
        crack = cat(1,crack,[m_c,x_crack]);
    else                                % otherwise crop data
        while w_norm1(end)>d0
            w_norm1 = w_norm1(1:end-1);
        end
        m_c = m_dry + sum(w_norm(1:length(w_norm1),2))
              *(pi*r0^2*x_step/1000)-w_norm(end)*(w_norm1(end)-d0)
              *(pi*r0^2/1000);
        crack = cat(1,crack,[m_c,x_crack]);
    end
end

% Change the input data into a measure of crack depth with time
depth_rec = [];
for count = 1:length(mass_rec)
   [C,I] = min(abs(crack(:,1) - mass_rec(count)));
   depth_rec = cat(1,depth_rec,crack(I,2));
end
figure(1);
plot(depth_rec);

% Take a derivative to get the velocity versus time.
k = length(depth_rec)-16;
for count = 1:k
    if depth_rec(count) == 0
        deriv_rec(count) = 0;
    elseif depth_rec(count) == d0
        deriv_rec(count) = 0;
    else
```

```
        deriv1 = polyfit((0:30)',depth_rec((count-15):(count+15)),1);
        deriv_rec(count-1) = deriv1(1);
    end
end
figure(2);
plot(1000*deriv_rec)

% Combine the previous 2 plots to get the depth versus crack speed.
figure(3);
size(depth_rec)
size(deriv_rec)
plot(depth_rec(1:k-1)',1000*deriv_rec(1:k-1));

for count = 1:1:(floor(depth_rec(end)-1))
    [C,I1] = min(abs(depth_rec - count-0.5));
    [C,I2] = min(abs(depth_rec - count+0.5));
    deriv_rec2(count) = mean(deriv_rec(I2:I1))
    deriv_rec3(count) = std(deriv_rec(I2:I1))
end
figure(4);
plot(1:1:floor(depth_rec(end)-1),1000*deriv_rec2,'r+');
z = cat(2,(1:1:floor(depth_rec(end)-1))',1000*deriv_rec2',1000*deriv_rec3')
```

Appendix B

Field site descriptions

This section contains supplementary information regarding the field sites described in Chapter 3. A brief description of each site, with GPS coordinates and directions, is followed by a summary of the measurements made at that site. Sites are identified by a nearby geographic feature, and numbered by a 4 digit code consisting of the date, and a number describing the order of sites visited in any day (*e.g.* the 2nd site visited on the 15th would be 1502). These numbers are preceded by a letter identifying the field region. Only sites where quantitative measurements were made are listed here. The terms upper and lower colonnade will refer to columns that cooled from the top down and from the bottom up, respectively.

B.1 Columbia River Basalt Group

Site A1003: Banks Lake

GPS coordinates: 47°44′33″ N, 119°14′0″ W, roadside access on Highway 155. Lower colonnade site accessed by climbing down E from roadside featured 12 columns with measured striae. Upper site ($\sim$ 20m above) showed excellent wavy columns. Rubble from upper site allowed direct measurement of column width. Striae and wavy columns were measured on the upper site through analysis of photographs. Rock samples collected from both sites.

Site A1101: Banks Lake gravel pit

GPS coordinates: 47°40′58″ N, 119°16′24″ W, roadside access on Highway 155. A long stretch of columns showing several layers of blocky colonnade. Stria heights and column widths were measured on a lower colonnade, and a rock sample was collected.

Site A1102: Dry Falls
GPS coordinates: 47°35′16″ N, 119°20′35″ W, at the end of the access road to Deep Lake. An exposed hill beneath Dry Falls shows about 20 very straight upright columns. Side lengths and joint angles were measured, and a sample collected. A similar, adjacent hill showed some evidence of wavy columns.

Site A1201: Park Lake
GPS coordinates: 47°34′57″ N, 119°24′48″ W, accessed by a short hiking trail leading into a peninsula on Park Lake, 2 km S of Sun Lakes campground. 3 tiered colonnades are visible. A lower colonnade had stria heights and column widths measured, with a reference distance measured to the lower flow margin. A rock sample was collected.

Site A1301: Tucannon River
GPS coordinates: 46°30′30″ N, 118°0′15″ W, 10 km SW of Starbuck on Highway 261. About 100 meters of well formed lower colonnade, 4-5 m high, are exposed from blasting. The column widths and stria heights were measured, relative to their position above an exposed flow base. A sample was collected.

Site A1302: Lyon Ferry Railway
GPS coordinates: 46°33′38″ N, 118°11′4″ W, near Highway 261, beside abandoned Union Pacific rail tracks, 1 km S of a rail bridge over the Snake River. At least 3 exposed flow units are visible, all blocky and large. Stria heights and column widths were measured on an upper colonnade at several points walking S from GPS point. A sample was collected.

Site A1401: Little Goose Dam Road
GPS coordinates: 46°31′55″ N, 118°8′42″ W, on Highway 261 near Little Goose Dam road turnoff. Several exposed colonnades are generally similar to site A1302. Stria heights and column widths on a road-level upper colonnade were measured.

Site A1501: Chief Timothy
GPS coordinates: 46°24′44″ N, 117°11′25″ W, just S of Chief Timothy campground, adjacent to Highway 12 in the abandoned Silcott quarry. An excellent +10 m tall lower colonnade with a very fresh exposure is present. Wavy columns, stria heights, column widths and joint angle were measured. A sample was collected.

Site A1502: Clarkston I

GPS coordinates: 46°25′10″ N, 117°6′49″ W, on Highway 12, W from Clarkston, beside Evans Road turnoff. A large lower colonnade and upper entablature are exposed overlying a soil/ash layer. Stria heights and column widths were measured, and the stria positions above the ash layer were determined.

Site A1503: Clarkston II

GPS coordinates: 46°25′19″ N, 117°7′25″ W, 500 m W of site 1502, along Highway 12, and probably in the same flow unit. The stria heights and column widths of a lower colonnade were measured.

Site A1601: Snake River Road

GPS coordinates: 46°17′6″ N, 116°59′29″ W, 10 km S of Asotin on Snake River Road. Several flow units (at least 2, probably 3) are exposed on a cliffside next to the road. Stria heights and column widths were measured on an upper colonnade.

Site A1602: Asotin Creek

GPS coordinates: 46°19′52″ N, 117°5′26″ W, next to barn along Asotin Creek Road, 6 km W of Asotin. A colonnade is visible, but with no identifiable direction of cooling. Stria heights and column widths were measured.

Site A1701: McCoy Canyon

GPS coordinates: 46°23′25″ N, 116°40′55″ W, at end of Snake River Road, S of Winddust. An access trail runs along abandoned rail lines, and the site covers 2 km N and S of GPS point. A large blocky colonnade topped by smaller colonnade runs along the tracks. Stria heights and column widths were measured at several points, and a sample was collected.

Site A1801: Devil's Canyon Pyramid

GPS coordinates: 46°35′53″ N, 118°32′53″ W, 4 km N of Lower Monumental Dam on E side of Highway 263. The site consists of a large pyramid composed of many small, complex colonnades. Columns appear in many different non-vertical directions, making for difficult interpretation. Stria heights, column widths, and joint angles were measured near the base of the pyramid, and a sample was collected.

Sites A1901 & A1902: Rock River Road I and II

GPS coordinates: 45°46′4″ N, 120°20′29″ W, and 45°48′35″ N, 120°20′42″ W, both accessed on the roadside of Rock River Road, off Highway 14, 20 km W of Roosevelt. A1901 consisted of a large blocky lower colonnade, where stria heights and column widths were measured, and a flow base established. A1902 showed small columns with no striae or indications of cooling direction, but displayed wavy columns that were measured. A sample was collected from A1901.

Site A2001: Sheppard's Dell

GPS coordinates: 45°32′48″ N, 122°11′55″ W, on a short trail to Sheppard's Dell waterfall off Highway 84. The site consists of a partially eroded colonnade, with no indication of the cooling direction, where wavy columns were measured.

Site A2101: Dell Road

GPS coordinates: 45°40′52″ N, 121°18′49″ W, at a small hill of well-formed columnar joints near the junction of Dell Road and Highway 30, off Highway 84. Stria heights and column widths were measured, and striae position was measured with respect to an arbitrary baseline.

Site A2102: The Dalles Dam

GPS coordinates: 45°38′53″ N, 121°0′31″ W, roadside on Highway 84, 15 km E of The Dalles. The site consists of a very large, regular lower colonnade along the cliff face. Another flow unit is visible above. Stria height and column width were measured, and striae position was measured with respect to an arbitrary baseline. A sample was collected.

Site A2103: Des Chutes Park

GPS coordinates: 45°39′6″ N, 120°57′14″ W, roadside on Highway 84, 5 km E of site A2102, and likely part of the the same flow. Site consists of a very large well formed lower colonnade, where stria heights and column widths were measured.

Site A2201: Bingen

GPS coordinates: 45°42′16″ N, 121°26′26″ W, small roadside site just E of Bingen on Highway 14. No striae were observed, but the well formed columns display a wavy column instability, which was measured. A sample was collected.

B.2 British Columbia

Site B0801: Watts Point Quarry
GPS coordinates: 49°39′17″ N, 123°13′6″ W, at the end of the forestry service road W off Highway 99 between Britannia Beach and Squamish. The site consists of columnar hornblende pyroxene dacite lava, with an exposed lower colonnade from a subglacial eruption [15]. Stria heights, column widths, and joint angles were measured, and a sample was collected.

Site B0902: Tricouni Flow II
GPS coordinates: 49°58′39″ N, 123°11′7″ W, accessed through the Chance Creek logging road off Highway 99, N of Squamish near Daisy Lake. The site is composed of a porphyritic plagioclase-hornblende dacite flow from the Tricouni Southeast unit [88]. Stria heights and column widths were measured in a large, vesicular lower colonnade. Stria position was measured with respect to an arbitrary baseline.

Site B0903: Tricouni Flow III
GPS coordinates: 49°58′5″ N, 123°10′2″ W, with the same access as site B0902, 500 m closer to Highway 99. These small well-formed curving columns are at the edge of the Tricouni Southeast unit, and formed when lava was impounded against ice [88]. Stria heights and column widths were measured in a lower colonnade, and several columns were surveyed in cross-section. A sample was collected.

Site B0904: Roadcut Cheakamus Basalt
GPS coordinates: 49°58′39″ N, 123°11′7″ W, roadside on both sides of Highway 99 near Daisy Lake and Brandywine Falls, and newly exposed due to current construction on Highway 99. The Cheakamus Basalts are alkali olivine basalt flows a few tens of thousands of years old [64, 88]. 3 data sets were collected at this site, which had two lower colonnades and one upper colonnade exposed. In each case stria heights and column widths were measured, and stria positions were measured with respect to a flow margin.

Site B1101: Daisy Lake
GPS coordinates: 49°58′57″ N, 123°8′33″ W, on E side of Highway 99 near Daisy Lake. About 30 large columns of a lower colonnade are exposed in a Cheakamus Basalt flow. The lower flow margin is several meters below the road level. Stria heights and column widths were measured, and a sample was collected.

Site B0902: Callaghan Creek

GPS coordinates: 50°3′37″ N, 123°6′33″ W, accessed on the Callaghan forestry service road, on route to Callaghan Lake. An exposed lower colonnade sitting on a vesicular layer was studied. Stria heights and column widths were measured, and stria positions were measured with respect to a lower flow margin. A sample was collected.

Site B1201: Pebble Creek Hotsprings

GPS coordinates: 50°40′2″ N, 123°27′32″ W, half-way down the hiking trail to Pebble Creek hot springs off of Upper Lillooet forestry service road. Part of the Pebble Creek Formation of dacite/trachydacite and related deposits erupted in 2350 B.P. is visible [42]. Stria heights and column widths were measured on a lower colonnade, and a sample was collected.

Site B1401: Chasm

GPS coordinates: 51°13′21″ N, 121°28′45″ W, in Chasm provincial park off Highway 97, and accessed by descending a rope near the parking lot, on trail N. Very large blocky columns from a lower colonnade are visible. Stria heights and column widths were measured.

Site B1402: 83 Mile House

GPS coordinates: 50°27′58″ N, 121°22′6″ W, on a roadcut exposed to the E side of Highway 97, 13 km S of the junction with Highway 24. Stria heights and column widths were measured on a lower colonnade, and a sample was collected.

Site B1601: Bridge Lake

GPS coordinates: 51°28′54″ N, 120°43′9″ W, in a roadcut exposed on both sides of Highway 24, between the two turnoffs to the town of Bridge Lake. Two sites 50 m apart were measured in one flow unit. At the E site stria heights, column widths, and plumose directions were measured in large columns from a lower colonnade. Stria positions were measure with respect to an arbitrary baseline. In the much smaller, curved columns of the W site stria heights and column widths were measured. A sample was collected at the E site.

Site B1901: First Canyon

GPS coordinates: 51°46′2″ N, 120°0′54″ W, on E side of access road to Wells Gray provin-

cial park 15 km N of Clearwater. Stria heights and column widths were measured in a lower colonnade, and a sample was collected.

Site B2101: Keremeos Columns
GPS coordinates: 49°14′45″ N, 119°47′23″ W, on private land off Highway 3A (contact nearby Clifton farm for access) adjacent to Keremeos Columns Provincial Park, and 4 km N of Keremeos. This large site consists of a very tall (+20 m) well-formed lower colonnade, the top part of which appears to display wavy columns. Stria heights and column widths were measured, and stria positions were measured with respect to an arbitrary baseline. A sample was collected.

Site B2601: Whistler Train tracks
GPS coordinates: 50°4′26″ N, 123°5′35″ W, on S side of Highway 99, across train tracks, near Callaghan Forestry Service Road. A small hill of ∼30 exposed columns of a lower colonnade is visible facing the highway. Stria heights and column widths were measured, and stria positions were measured with respect to the base of the flow. A sample was collected.

B.3 Staffa

Stria heights and column widths were measured at several sites around the coast of Staffa, as indicated in Figure B.1. All sites were in the lower colonnade of the Fingal's lava unit. Access to all sites on W coast can be made at low tide, walking and wading N from a shorefront across the island from Clamshell Cave. The sites around Fingal's Cave were measured using a large stepladder, and stria positions were measured with respect to either the base of the flow, or the contact with the upper entablature. Clinometer readings indicated that the lower colonnade was 15 m thick, allowing comparison of the two baselines. The two sites W of Fingal's Cave are accessible only at low tide, and then only by swimming across Fingal's Cave mouth.

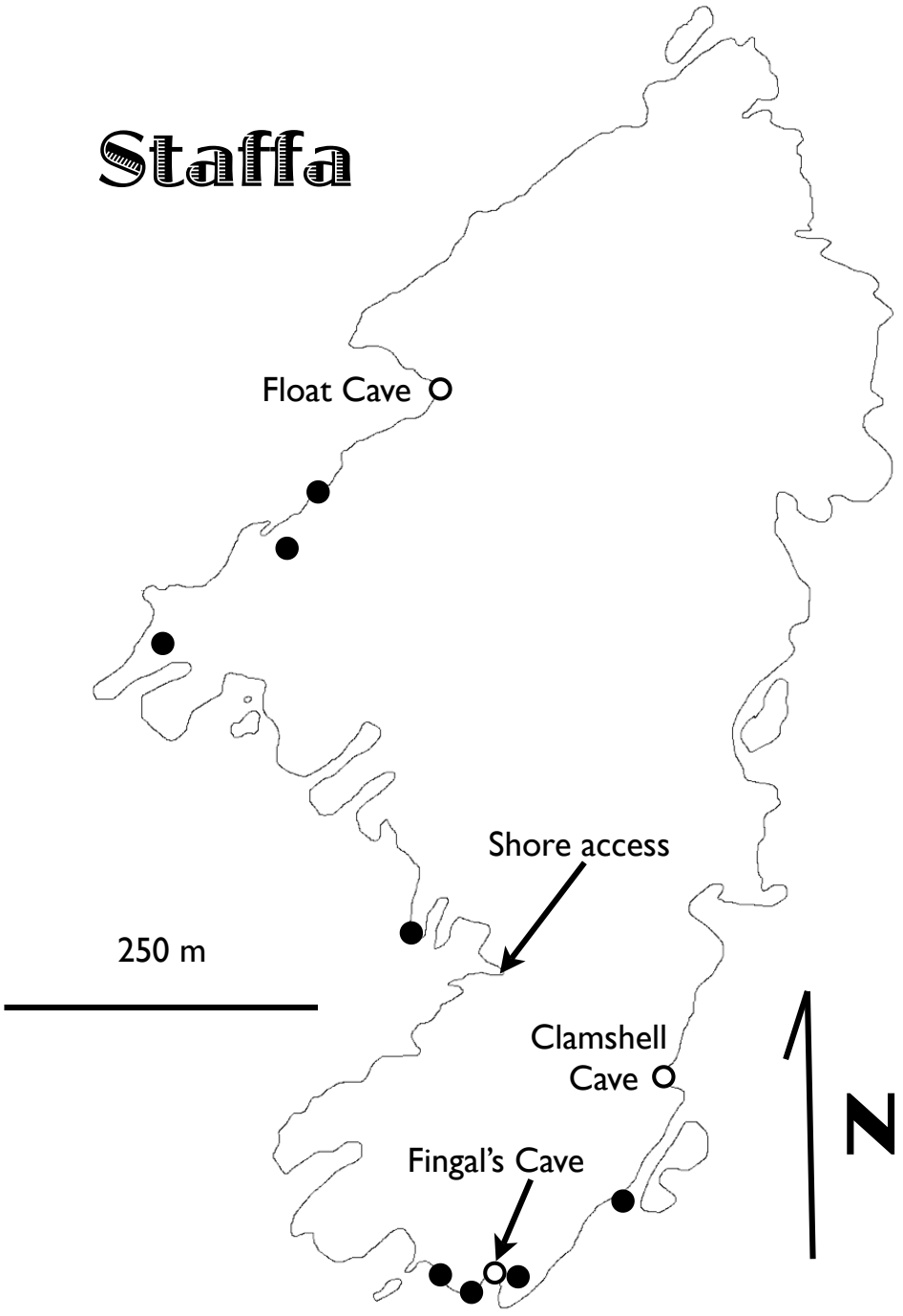

Figure B.1: A map of field sites (black circles) on Staffa, also showing several major caves (open circles).

Bibliography

[1] C. Allain and L. Limat, *Regular patterns of cracks formed by directional drying of a colloidal suspension*, Phys. Rev. Lett. **74** (1995), 2981–2984.

[2] Atilla Aydin and James M. DeGraff, *Evolution of polygonal fracture patterns in lava flows*, Science **239** (1988), 471–476.

[3] Lloyd O. Bacon, *A method of determining dynamic tensile strength of rock at minimum loading*, US Dept. of Mines Report of Investigations **6067** (1962), 22pp.

[4] G. I. Barenblatt, *Scaling, self-similarity, and intermediate asymptotics*, Cambridge University Press, 1996.

[5] Jacob Bear, *Dynamics of fluids in porous media*, Dover, 1989.

[6] Maurice A. Biot, *General theory of three-dimensional consolidation*, J. App. Phys. **12** (1941), 155–164.

[7] Thomas Boeck, Hans-Achim Bahr, Stefan Lampenscherf, and Ute Bahr, *Self-driven propagation of crack arrays: A stationary two-dimensional model*, Phys. Rev. E **59** (1999), 1408.

[8] S. Bohn, L. Pauchard, and Y. Couder, *Hierarchical crack pattern as formed by successive domain divisions. I. Temporal and geometrical hierarchy*, Phys. Rev. E **71** (2005), 046214.

[9] S. Bohn, J. Platkiewicz, B. Andreotti, M. Adda-Bedia, and Y. Couder, *Hierarchical crack pattern as formed by successive domain divisions. II. From disordered to deterministic behavior*, Phys. Rev. E **71** (2005), 046215.

[10] Bruno A. Boley and Jerome H. Weiner, *Theory of thermal stresses*, Wiley, New York, 1960.

[11] J. Harlen Bretz, H. T. U. Smith, and George E. Neff, *Channeled Scabland of Washington: new data and interpretations*, J. Soc. Am. Bull. **67** (1956), 957–1049.

[12] Stephen R. Brown and Christopher H. Scholz, *Broad bandwidth study of the topography of natural rock surfaces*, J. Geophys. Res. **90** (1985), 12575–12582.

[13] Paul Budkewitsch and Pierre-Yves Robin, *Modelling the evolution of columnar joints*, J. Volcanol. Geotherm. Res. **59** (1994), 219–239.

[14] Richard Bulkeley, *Part of a letter from Sir R.B.S.R.S. to Dr. Lister, concerning the Giants Causway in the County of Atrim in Ireland*, Phil. Trans. R. Soc. Lond. **17** (1693), 708–710.

[15] A. Bye, B. R. Edwards, and C. J. Hickson, *Preliminary field, petrographic, and geochemical analysis of possible subglacial, dacite volcanism at the Watts Point volcanic centre, southwestern British Columbia*, Geol. Soc. Canada, Curr. Res. **A20** (2000), 9pp.

[16] Millard F. Coffin and Olav Eldholm, *Large igneous provinces: crustal structure, dimensions, and external consequences*, Rev. Geophys. **31** (1994), 1–36.

[17] B. Cotterell and J. R. Rice, *Slightly curved or kinked cracks*, Int. Jour. Frac. **16** (1980), 155–169.

[18] Robert D. Deegan, Shilpa Chheda, Lisa Patel, M. Marder, Harry L. Swinney, Jeehoon Kim, and Alex de Lozanne, *Wavy and rough cracks in silicon*, Phys. Rev. E **67** (2003), 066209.

[19] James M. DeGraff and Atilla Aydin, *Surface morphology of columnar joints and its significance to mechanics and direction of joint growth*, Geol. Soc. Am. **99** (1987), 605–617.

[20] ———, *Effect of thermal regime on growth increment and spacing of contraction joints in basaltic lava*, J. Geophys. Res. **98** (1993), 6411–6430.

[21] James M. DeGraff, Philip E. Long, and Atilla Aydin, *Use of joint-growth directions and rock textures to infer thermal regimes during solidification of basaltic lava flows*, J. Volcanol. Geotherm. Res. **38** (1989), 309–324.

[22] Aleksandar Donev, Ibrahim Cisse, David Sachs, Evan A. Variano, Frank H. Stillinger, Robert Connelly, Salvatore Torquato, and P. N. Chaikin, *Improving the density of jammed disordered packings using ellipsoids*, Science **303** (2004), 990–993.

[23] E. R. Dufresne, E. I. Corwin, N. A. Greenblatt, J. Ashmore, D. Y. Wang, A. D. Dinsmore, J. X. Cheng, X. S. Xie, J. W. Hutchinson, and D. A. Weitz, *Flow and fracture in drying nanoparticle suspensions*, Phys. Rev. Lett. **91** (2003), 224501.

[24] E. R. Dufresne, D. J. Stark, N. A. Greenblatt, J. X. Cheng, J. W. Hutchinson, L. Mahadevan, and D. A. Weitz, *Dynamics of fracture in drying suspensions*, Langmuir **22** (2006), 7144.

[25] R. A. Fisher and L. H. C. Tippett, *Limiting forms of the frequency distribution of the largest or smallest member of a sample*, Proc. Cambridge Phil. Soc. **24** (1927), 180–190.

[26] C. L. Flemmer, *On the regime boundaries of moisture in granular materials*, Powder Tech. **66** (1991), 191–194.

[27] Sam Foley and T. Molyneux, *An account of the Giants Caus-Way in the North of Ireland: by the Reverend Dr. Sam. Foley*, Phil. Trans. R. Soc. Lond. **18** (1694), 170–182.

[28] J. W. French, *The fracture of homogeneous media*, Trans. Geol. Soc. Glasgow **17** (1925), 50–68.

[29] Lucas Goehring, Zhenquan Lin, and Stephen W. Morris, *An experimental investigation of the scaling of columnar joints*, Phys. Rev. E **74** (2006), 036115.

[30] Lucas Goehring, L. Mahadevan, and Stephen W. Morris, *Non-equilibrium scale selection in columnar joints*, Unpublished (2007).

[31] Lucas Goehring and Stephen W. Morris, *Order and disorder in columnar joints*, Europhys. Lett. **69** (2005), 739–745.

[32] ———, *On the drying of colloidal starch*, Unpublished (2007).

[33] ———, *The scaling of columnar joints in basalt*, J. Geophys. Res. (Submitted Feb. 2007), 13 pp.

[34] Nathan L. Green, *Geology and petrology of Quaternary volcanic rocks, Garibaldi Lake area, Southwestern British Columbia: summary*, Geol. Soc. Am. Bull. **92** (1981), 697–702.

[35] A. A. Griffith, *The phenomena of rupture and flow in solids*, Phil. Trans. R. Soc. Lond. A **221** (1921), 163–198.

[36] A. Groisman and E. Kaplan, *An experimental study of cracking induced by desiccation*, Europhys. Lett. **25** (1994), 415–20.

[37] M. Groll and S. Rösler, *Operation principles and performance of heat pipes and closed two-phase thermosyphons*, J. Non-Equilib. Thermodyn. **17** (1992), 91–151.

[38] Kenneth A. Grossenbacher and Stephen M. McDuffie, *Conductive cooling of lava: columnar joint diameter and stria width as functions of cooling rate and thermal gradient*, J. Volcanol. Geotherm. Res. **69** (1995), 95–103.

[39] G. M. Grover, T. P. Cotter, and G. F. Erickson, *Structures of very high thermal conductance*, J. Appl. Phys. **35** (1964), 1990–1991.

[40] Xian-Zhong Han and Bruce R. Hamaker, *Functional and microstructural aspects of soluble corn starch in pastes and gels*, Starch **52** (2000), 76–80.

[41] Harry C. Hardee, *Solidification in Kilauea Iki lava lake*, J. Volcanol. Geotherm. Res. **7** (1980), 211–223.

[42] C. J. Hickson, J. K. Russell, and M. V. Stasiuk, *Volcanology of the 2350 B.P. eruption of Mount Meager Volcanic Complex, British Columbia, Canada: implications for hazards from eruptions in topographically complex terrain*, Bull. Volcanol. **60** (1999), 489–507.

[43] Anita M. Ho and Katharine V. Cashman, *Temperature constrains on the Ginko flow of the Columbia River Basalt Group*, Geology **25** (1997), 403–406.

[44] P. R. Hooper and C. J. Kawkesworth, *Isotopic and geochemical constraints on the origin and evolution of the Columbia River Basalt*, J. Petrology **34** (1993), 1203–1246.

[45] D. Hull and B. D. Caddock, *Simulation of prismatic cracking of cooling basalt lava flows by the drying of sol-gels*, J. Mat. Sci. **34** (1999), 5707–5720.

[46] J. W. Hutchinson and Z. Suo, *Mixed-mode cracking in layered materials*, Adv. Appl. Mech. **29** (1992), 63–191.

[47] T. H. Huxley, *Physiography: An introduction to the study of nature*, MacMillan and Co., London, 1881.

[48] G. R. Irwin, *Analysis of stresses and strains near the end of a crack traversing a plate*, J. App. Mech. **24** (1957), 361–364.

[49] E. A. Jagla, *Stable propagation of an ordered array of cracks during directional drying*, Phys. Rev. E **65** (2002), 046147.

[50] ———, *Maturation of crack patterns*, Phys. Rev. E **69** (2004), 056212.

[51] E. A. Jagla and A. G. Rojo, *Sequential fragmentation: The origin of columnar quasihexagonal patterns*, Phys. Rev. E **65** (2002), 026203.

[52] E. M. Jones, *Apollo 15 Lunar surface journal; Hadley Rille*, 1996, http://www.hq.nasa.gov/office /pao/History/alsj/a15/a15.rille.html.

[53] Andrew C. Kerr, *The geochemical stratigraphy, field relations and temporal variation of the Mull-Morvern Tertiary lava succession, NW Scotland*, Trans. R. Soc. Edinburgh **86** (1995), 35–47.

[54] ———, *On the nature of the parental magma of the Palaeogene Staffa Magma sub-type, Isle of Mull, Scotland*, Trans. R. Soc. Edinburgh **89** (1998), 87–93.

[55] Teruhisa S. Komatsu, *Toward a robust phenomenological expression of evaporation efficiency for unsaturated soil surfaces*, J. App. Meteor. **42** (2003), 1330–1334.

[56] Teruhisa S. Komatsu and Shin-Ichi Sasa, *Pattern selection of cracks in directionally drying fracture*, Jpn. J. Appl. Phys. **36** (1997), 391–395.

[57] A. H. Lachenbruch, *Mechanics of thermal contraction cracks and ice-wedge polygons in permafrost*, U. S. Geol. Surv. Spec. Paper **70** (1962), 69.

[58] L. D. Landau and E. M. Lifshitz, *Theory of elasticity*, 2nd ed., Pergamon press, Bristol, UK, 1970.

[59] Philip E. Long and Bernard J. Wood, *Structures, textures and cooling histories of Columbia River basalt flows*, Geol. Soc. Am. Bull. **97** (1986), 1144–1155.

[60] Jason Lore, Huajian Gao, and Atilla Aydin, *Viscoelastic thermal stress in cooling basalt flows*, J. Geophys. Res. **105** (2000), 23695–23709.

[61] Paul Lyle and John Preston, *Geochemistry and volcanology of the Tertiary basalts of the Giant's Causeway area, Northern Ireland*, J. Geol. Soc. London **150** (1993), 109–120.

[62] Robert Mallet, *On the origin and mechanism of production of the prismatic (or columnar) structure of basalt*, Phil. Mag. **50** (1875), 122–135 and 201–226.

[63] Bill Mathews and Jim Monger, *Roadside Geology of Southern British Columbia*, Mountain Press Publishing Company, Missoula, 2005.

[64] W. H. Mathews, *Geology of the Mount Garibaldi map-area, Southwestern British Columbia, Canada. Part II: geomorphology and Quaternary volcanic rocks.*, Bull. Geol. Soc. Am. **69** (1958), 179–198.

[65] Michael T. Mellon, *Small-scale polygonal features on Mars: Seasonal thermal contraction cracks in permafrost*, J. Geophys. Res. **102** (1997), 25617–25628.

[66] Fredric M. Menger, Hong Zhang, Kevin L. Caran, Victor A. Seredyuk, and Robert P. Apkarian, *Gemini-induced columnar jointing in vitreous ice. Cryo-HRSEM as a tool for discovering new colloidal morphologies*, J. Am. Chem. Soc. **124** (2002), 1140–1141.

[67] Tsuyoshi Mizuguchi, Akihiro Nishimoto, So Kitsunezaki, Yoshihiro Yamazaki, and Ichio Aoki, *Directional crack propagation of granular water systems*, Phys. Rev. E **71** (2005), 056122.

[68] Thomas Molyneux, *A letter from Dr. Thomas Molyneux, to Dr. Martin Lister, Fellow of the Colledge of Physicians, and of the Royal Society, in, London: Containing some additional observations on the Giants Causway in Ireland*, Phil. Trans. R. Soc. Lond. **20** (1698), 209–223.

[69] M. S. Mostafa, N. Afify, A. Gaber, and E. F. Abu Zaid, *Investigation of thermal properties of some basalt samples in egypt*, J. Therm. Anal. Cal. **75** (2004), 179–188.

[70] Gerhard Müller, *Experimental simulation of basalt columns*, J. Volcanol. Geotherm. Res. **86** (1998), 93.

[71] ———, *Starch columns: Analog model for basalt columns*, J. Geophys. Res. **103** (1998), 15239–15253.

[72] ———, *Experimental simulation of joint morphology.*, J. Struct. Geol. **23** (2001), 45.

[73] Tsutomu Murase and Alexander R. McBirney, *Properties of some common igneous rocks and their melts at high temperatures*, Geol. Soc. Am. Bull. **84** (1973), 3563–3592.

[74] Akihiho Nishimoto, Tsuyoshi Mizuguchi, and So Kitsunezaki, *Numerical study of drying process and columnar fracture process in granule-water mixtures*, Phys. Rev. E **76** (2007), 016102.

[75] J. P. O'Reilly, *Explanatory notes and discussion on the nature of the prismatic forms of a group of columnar basalts, Giant's Causeway*, Trans. R. Irish Acad. **26** (1879), 641–728.

[76] L. A. Ostrovsky and P. A. Johnson, *Dynamic nonlinear elasticity in geomaterials*, Rivista del Nuovo Cimento **24** (2001), 1–46.

[77] H. G. Patil, D. I. Deendar, and N. W. Gokhale, *Mini columnar joints in basalts, of Kodali village, Maharashtra*, Curr. Sci. **53** (1984), 1089–1090.

[78] L. Pauchard, M. Adda-Bedia, C. Allain, and Y. Couder, *Morphologies resulting from the directional propagation of fractures*, Phys. Rev. E **67** (2003), 027103.

[79] Dallas L. Peck and Takeshi Minakami, *The formation of columnar joints in the upper part of Kilauean lava lakes, Hawaii*, Geol. Soc. Am. Bull. **79** (1968), 1151–1168.

[80] L. Pel, K. . Landman, and E. F. Kaasschieter, *Analytic solution for the non-linear drying problem*, Int. J. Heat Mass Transfer **45** (2002), 3173–3180.

[81] G. I. Petrunin, V. G. Popov, and V. M. Ladygin, *Thermal properties of basalts from the Bouvet triple junction and their implications for petrophysical characteristics*, Izv. Phys. Solid Earth **37** (2001), 441–451.

[82] Stephen P. Reidel, *Emplacement of Columbia River basalt*, J. Geophys. Res. **103** (1998), 27393–27410.

[83] Stephen P. Reidel and Terry L. Tolan, *Eruption and emplacement of flood basalt: An example from the large-volume Teepee Butte Member, Columbia River Basalt Group*, Geol. Soc. Am. Bull. **104** (1992), 1650–1671.

[84] Stephen P. Reidel, Terry L. Tolan, Peter R. Hooper, Marvin H. Beeson, Karl R. Fecht, Robert D. Bentley, and James Lee Anderson, *The Grande Ronde Basalt, Columbia River Basalt Group; Stratigraphic descriptions and correlations in Washington, Oregon, and Idaho*, Geol. Soc. Am. Spec. Paper **239** (1989), 21–53.

[85] Marshall Reiter, Margaret W. Barroll, Jeffrie Minier, and Gerry Clarkson, *Thermo-mechanical model for incremental fracturing in cooling lava flows*, Tectonophysics **142** (1987), 241–260.

[86] O. Ronsin and B. Perrin, *Thermo-mechanical model for incremental fracturing in cooling lava flows*, Tectonophysics **142** (1987), 241–260.

[87] ———, *Thermo-mechanical model for incremental fracturing in cooling lava flows*, Tectonophysics **142** (1997), 241–260.

[88] J. K. Russell, C. J. Hickson, and Graham Andrews, *Canadian Cascade volcanism: Subglacial to explosive eruptions along the Sea to Sky Corridor, British Columbia*, Floods, Faults, and Fire: Geological field trips in Washington State and Southwest British Columbia: Geological Society of Americal Field Guide 9 (P. Stelling and D. S. Tucker, eds.), The Geological Society of America, 2007, pp. 1–29.

[89] Michael P. Ryan and Charles G. Sammis, *Cyclic fracture mechanisms in cooling basalt*, Geol. Soc. Am. Bull. **89** (1978), 1295–1308.

[90] ———, *The glass transition in basalt*, J. Geophys. Res. **86** (1981), 9519–9535.

[91] J. M. Salamanca, E. Ciampi, D. A. Faux, P. M. Glover, P. J. McDonald, A. F. Routh, A. C. I. A. Peters, R. Satguru, and J. L Keddie, *Lateral drying in thick films of waterborne colloidal particles*, Langmuir **17** (2001), 3202–3207.

[92] R. Saliba and E. A. Jagla, *Analysis of columnar joint patterns from three-dimesnional stress modeling*, J. Geophys. Res. **108** (2003), 2476.

[93] Jean Schmittbuhl, Francois Schmitt, and Christopher Scholz, *Scaling invariance of crack surfaces*, J. Geophys. Res. **100** (1995), 5953–5973.

[94] J. Sellés-Martínez, *Concretion morphology, classification and genesis*, Earth-Sci. Rev. **41** (1996), 177–210.

[95] K. V. Seshadri, *Columnar jointing in Mesozoic sandstone of Buhj series, Kutch Basin, Gujarat, India*, Jour. Geol. Soc. India **49** (1997), 452–453.

[96] H. R. Shaw and D. A. Swanson, *Eruption and flow rates of flood basalts*, Proceedings of the Second Columbia River Basalt Symposium (E. H. Gilmore and D. F. Stradling, eds.), East. Wash. State Coll. Press, 1970, pp. 271–299.

[97] Kelly A. Shorlin, John R. de Bruyn, Malcolm Graham, and Stephen W. Morris, *Development and geometry of isotropic and directional shrinkage crack patterns*, Phys. Rev. E. **61** (2000), 6950.

[98] Narpinder Singh, Jaspreet Singh, and Navdeep Singh Sodhi, *Morphological, thermal, rheological and noodle-making properties of potato and corn starch*, J. Sci. Food Agric. **82** (2002), 1376–1383.

[99] R. S. Sletten, B. Hallet, and R. C. Fletcher, *Resurfacing time of terrestrial surfaces by the formation and maturation of polygonal patterned ground*, J. Geophys. Res. **108** (2003), 8044.

[100] I. J. Smalley, *Contraction crack networks in basalt flows*, Geol. Mag. **103** (1966), 110–114.

[101] C. A. Tang, Y. B. Zhang, Z. Z. Liang, T. Xu, L. G. Tham, P.-A. Lindqvist, S. Q. Kou, and H. Y. Liu, *Fracture spacing in layered materials and pattern transition from parallel to polygonal fractures*, Phys. Rev. E **73** (2006), 056120.

[102] James A. TenCate, Eric Smith, and Robert A. Guyer, *Universal slow dynamics in granular solids*, Phys. Rev. Lett. **85** (2000), 1020–1023.

[103] R. N. Thompson, M. A. Morrison, A. P. Dickin, I. L. Gibson, and R. S. Harmon, *Two contrasting styles of interaction between basic magmas and continental crust in the British Tertiary volcanic province*, J. Geophys. Res. **91** (1986), 5985–5997.

[104] Terry L. Tolan, Stephen P. Reidel, Marvin H. Beeson, James Lee Anderson, Karl R. Fecht, and Donald A. Swanson, *Revisions to the estimates of the areal extent and volume of the Columbia River Basalt Group*, Geol. Soc. Am. Spec. Paper **239** (1989), 1–20.

[105] S. I. Tomkeieff, *The basalt lavas of the Giant's Causeway district of Northern Ireland*, Bull. Volcanol. **6** (1940), 89–146.

[106] A. Toramaru and T. Matsumoto, *Columnar joint morphology and cooling rate: A starch-water mixture experiment*, J. Geophys. Res. **109** (2004), B02205.

[107] S. Y. Touloukian, W. R. Judd, and R. F. Roy, *Physical properties of rocks and minerals*, Hemisphere, 1989.

[108] D. L. Turcotte and G. Schubert, *Geodynamics*, 2nd ed., Cambridge University Press, 2001.

[109] Richard B. Waitt, *Case for periodic collusal Jöulhlaups from Pleistocene glacial Lake Missoula*, Geol. Soc. Am. Bull. **96** (1985), 1271–1286.

[110] D. Weaire and C. O'Carroll, *A new model for the Giant's Causeway*, Nature **302** (1983), 240–241.

[111] D. Weaire and N. Rivier, *Soap, cells, and statistics – random patterns in two dimensions*, Contep. Phys. **25** (1984), 59–99.

[112] Denis Weaire and Stefan Hutzler, *The physics of foams*, Oxford University Press, 1999.

[113] Robert C. Weast (ed.), *CRC Handbook of Chemistry and Physics*, 51st ed., The Chemical Rubber Co., 1970.

[114] Waloddi Weibull, *A statistical distribution function of wide applicability*, J. App. Mech. **18** (1951), 293–297.

[115] R. S. White, *A hot-spot model for early Tertiary volcanism in the N Atlantic*, Geol. Soc. London Spec. Pub. **39** (1988), 3–13.

[116] Kenneth W. Winkler and Xingzhou Liu, *Measurements of third-order elastic constants in rocks*, J. Acoust. Soc. Am. **100** (1996), 1392–1398.

[117] A. Yuse and M. Sano, *Transition between crack patterns in quenched glass plates*, Nature **362** (1993), 329–331.